

**Dissertation**  
**submitted to the**  
**Combined Faculties for the Natural Sciences and for Mathematics**  
**of the Ruperto-Carola University of Heidelberg, Germany**  
**for the degree of**  
**Doctor of Natural Sciences**

Put forward by

**Diplom-Physiker Hans-Hermann Boie**

Born in Heilbronn

Oral examination: 03.06.2009



# Bremsstrahlung Emission Probability in the $\alpha$ Decay of $^{210}\text{Po}$

Referees: Prof. Dr. Dirk Schwalm  
Prof. Dr. Hans Emling



## Zusammenfassung

Mit dem vorliegende Experiment wurde zum ersten Mal die Emissionswahrscheinlichkeit von Bremsstrahlung während des  $\alpha$ -Zerfalls von  $^{210}\text{Po}$  bis zu  $\gamma$ -Energien von  $\sim 500\text{ keV}$  mit einer statistischen Genauigkeit gemessen, die Aussagen über die Gültigkeit verschiedener theoretischer Ansätze zur Beschreibung dieses Prozesses erlaubt. Es wurde gezeigt, dass Korrekturen zur E1-Winkelverteilung der Bremsstrahlungsphotonen berücksichtigt werden müssen, die durch eine Interferenz der Dipol- mit der Quadrupolstrahlung, sowie durch relativistische Effekte verursacht werden. Mit der experimentell ermittelten Winkelverteilung zeigt das gemessene Spektrum der differentiellen Emissionswahrscheinlichkeit der Bremsstrahlung eine hervorragende Übereinstimmung mit den theoretischen Vorhersagen einer vollständig quantenmechanischen Rechnung.

## Abstract

A high-statistics measurement of bremsstrahlung emitted in the  $\alpha$  decay of  $^{210}\text{Po}$  has been performed. The measured differential emission probabilities, which could be followed up to  $\gamma$ -energies of  $\sim 500\text{ keV}$ , allow for the first time for a serious test of various model calculations of the bremsstrahlung accompanied  $\alpha$  decay. It is shown that corrections to the  $\alpha$ - $\gamma$  angular correlation due to the interference between the electric dipole and quadrupole amplitudes and due to the relativistic character of the process have to be taken into account. With the experimentally derived angular correlation the measured energy-differential bremsstrahlung emission probabilities show excellent agreement with the fully quantum mechanical calculation.



*Emily, Giulia, Hanna*

*and Claudia*



# Contents

<b>1</b>	<b>Introduction</b>	<b>1</b>
<b>2</b>	<b>Theoretical Description</b>	<b>5</b>
2.1	$\alpha$ Decay . . . . .	5
2.2	Bremsstrahlung . . . . .	6
2.3	Coulomb Acceleration Model . . . . .	7
2.4	Quantum Mechanical Treatment . . . . .	10
2.5	The Semi-Classical Jentschura-Milstein-Terekhov Approach . . . . .	13
2.6	Summary . . . . .	15
<b>3</b>	<b>Experimental Setup</b>	<b>17</b>
3.1	Principle of Measurement . . . . .	17
3.2	$\alpha$ Source . . . . .	20
3.3	Detection of $\alpha$ Particles . . . . .	21
3.4	Detection of Bremsstrahlung . . . . .	23
3.5	Geometry of the Setup . . . . .	26
3.6	Data Acquisition . . . . .	29
<b>4</b>	<b>Simulation of the <math>\alpha</math>-<math>\gamma</math>-Detection Efficiency</b>	<b>31</b>
4.1	The Simulation package . . . . .	31
4.2	Efficiency Calibration . . . . .	33
4.3	The $\alpha$ - $\gamma$ Coincident Photon Detection Efficiency . . . . .	42
4.4	Accuracy of the Simulated Coincident Efficiency . . . . .	46
<b>5</b>	<b>Data Analysis</b>	<b>51</b>

---

5.1	$\alpha$ -Energy Spectra . . . . .	51
5.2	$\gamma$ -Energy Spectra . . . . .	54
5.3	Time Spectra . . . . .	55
5.4	Bremsstrahlung Analysis . . . . .	62
5.4.1	Modelling the Projected Energy Spectra . . . . .	68
5.5	The Down-scaled $\alpha$ -Singles Spectra . . . . .	77
5.6	Analysis of the Angular Distribution . . . . .	79
5.7	The Energy-Differential Bremsstrahlung Emission Probability . . . . .	88
<b>6</b>	<b>Results and Conclusion</b>	<b>93</b>
6.1	Discussion of the Experimental Results . . . . .	93
6.2	Summary and Outlook . . . . .	97
<b>A</b>	<b>Classical Treatment</b>	<b>99</b>
A.1	Bremsstrahlung . . . . .	99
A.1.1	The Bremsstrahlung Vector Potential . . . . .	99
A.1.2	Frequency Distribution and Angular Distribution of Bremsstrahlung	101
A.2	The Centre of Mass System . . . . .	104
A.3	Bremsstrahlung of two Charged Particles . . . . .	107
A.4	Coulomb Acceleration Model . . . . .	111
A.5	Strict Coulomb Acceleration Model . . . . .	115
<b>B</b>	<b>Quantum Mechanical Treatment</b>	<b>117</b>
B.1	Photon Emission Probability in the Dipole Approximation . . . . .	117
B.2	Spherically Symmetric Potentials . . . . .	120
B.2.1	The Coulomb Potential . . . . .	121
B.2.2	Constant Potential . . . . .	123
B.3	Description of the $\alpha$ Decay using Gamow Vectors . . . . .	124
B.3.1	Gamow Vectors . . . . .	125
B.3.2	Gamow Vector and Decay Rate for the $\alpha$ Decay . . . . .	126
B.4	The Initial Wave Function $ \Phi_i\rangle$ . . . . .	132
B.5	The Final Wave Function $ \Phi_f\rangle$ . . . . .	135
B.6	The Matrix Element $\langle\Phi_f  \partial_r U(r)  \Phi_i\rangle$ . . . . .	141

B.7 Bremsstrahlung Emission Probability . . . . .	143
B.8 Dependence of the Bremsstrahlung Emission Probability on the Choice of $r_0$ and $V_0$ . . . . .	146
B.9 Annotations . . . . .	153
B.9.1 Completeness of the Coulomb Wave Functions . . . . .	153
B.9.2 Numerical Integration of $\langle \Phi_f   \partial_r U(r)   \Phi_i \rangle$ . . . . .	154
B.9.3 Taylor-Expansion with a Complex Argument . . . . .	155
<b>C <math>\alpha</math>- and <math>\gamma</math>-Lineshape</b>	<b>157</b>
C.1 The $\alpha$ -Lineshape . . . . .	157
C.2 The $\gamma$ -Lineshape . . . . .	159
<b>D <math>\gamma</math> Spectra</b>	<b>163</b>
<b>List of Figures</b>	<b>169</b>
<b>List of Tables</b>	<b>173</b>
<b>Glossary</b>	<b>175</b>
Notations . . . . .	175
Abbreviations . . . . .	176
Constants . . . . .	176
<b>Bibliography</b>	<b>177</b>
<b>Danksagung</b>	<b>181</b>



# Chapter 1

## Introduction

When discussing the  $\alpha$  decay of a nucleus the "classical" picture one usually has in mind is that of an  $\alpha$  particle tunnelling through the Coulomb barrier and then being accelerated from the classical turning point to its final energy. Thus bremsstrahlung photons will be emitted during the process. But while the emission of soft photons during the Coulomb scattering of charged particles can be well described by classical electrodynamics (see e.g. [1, 2]), in the  $\alpha$  decay the implication of a trajectory partly located in a classically forbidden region immediately provokes the question: Do  $\alpha$  particles emit photons during tunneling?

Several remarks seem to be in place with regard to this question: As the wavelengths of the photons are much larger than the extend of the tunneling barrier and even much larger than the main classical acceleration region, it is in principle not possible to identify where the photon was emitted. This is clearly born out in the quantum mechanical perturbation approach. Here Fermi's Golden Rule provides a well defined way how to calculate the emission probability connected with the decay of the initial state (the mother nucleus) into the final state consisting of the daughter nucleus, an  $\alpha$  particle and a photon, and the calculation of the transition matrix element involves, of course, the integration over the full coordinate space. On the other hand, within the quasi-classical approximation, which is well justified as the Sommerfeld parameter  $\eta$  of the  $\alpha$  particle is large compared to unity ( $\eta = 22$  for the  $\alpha$  emitter  $^{210}\text{Po}$ ), different space regions can be connected to different time intervals. It is therefore tempting to split the transition matrix element into contributions from classically allowed and classically forbidden regions. However, such an interpretation can only have a restricted meaning because it is possible to rewrite the bremsstrahlung matrix element in different forms using operator identities. As a result, the integrand for the matrix element, as well as the relative contributions of the regions of integration, will be different though the final outcome will be the same. Nevertheless, the issue of the tunneling during the emission process was widely discussed [3–21]. These authors used different theoretical approaches leading, not surprisingly, to partly conflicting results as to the relative contribution of the tunneling, but more seriously also with regard to the total  $\gamma$  emission probabilities.

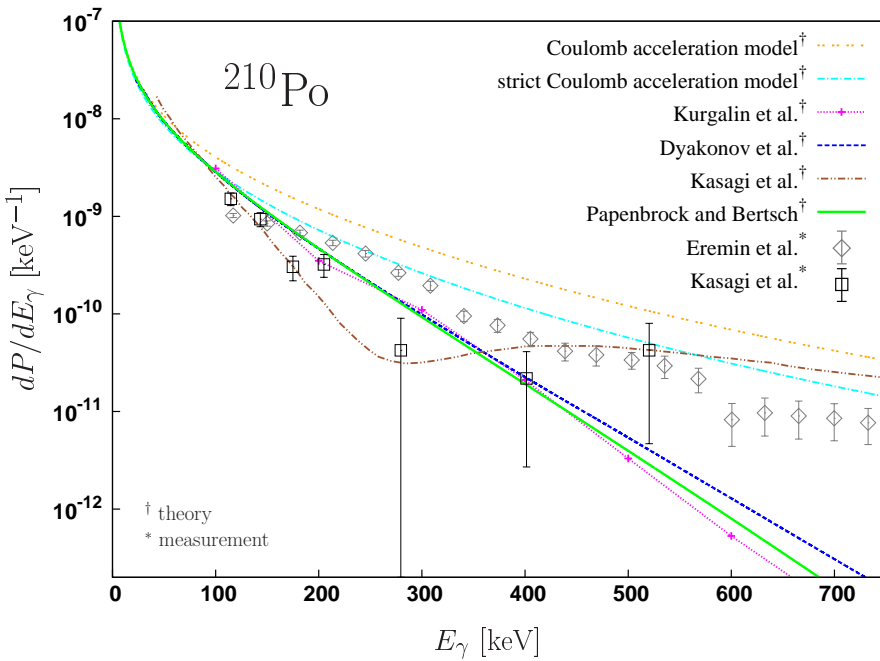


**Figure 1.1:** The measurement of Kasagi et al. [23] (black squares) and Eremin et al. [26] (grey diamonds) are plotted together with the theoretical predictions of the CA model (orange), the SCA model (cyan), the treatment by Kurgalin et al. [16] (magenta), the semi-classical treatments of Dyakonov et al. [10] (blue) and Kasagi et al. [23] (brown) and the quantum mechanical model by Papenbrock and Bertsch (green) [3].

The interest in the bremsstrahlung accompanied  $\alpha$  decay was actually stirred up in 1994 when a first attempt to observe this rare decay mode was published [22]. But this and later experimental attempts to measure these elusive decays [23–29] produced inconsistent results and did not reach the sensitivity to allow for a serious test of the various theoretical predictions. The unsatisfactory situation accounted prior to our investigations for the best studied case  $^{210}\text{Po}$  is displayed in figure 1.1: Kasagi et al. [23] were the first to measure the bremsstrahlung accompanied  $\alpha$  decay of  $^{210}\text{Po}$  and to calculate the emission probability in a quasi-classical approximation. While the kind of interference pattern implied by their results was neither observed in the quantum mechanical (QM) calculation of Papenbrock and Bertsch [3] nor in the quasi-classical (QC) approach of Dyakonov [10], all calculations are certainly not in conflict with the data given the large error bars. The picture was getting confused when Eremin et al. [26, 27] presented their data on  $^{210}\text{Po}$ , which is not only in contradiction with the previous data but also with all theoretical predictions, the exception being the classical Coulomb acceleration (CA) model (see e.g. [10]) expected to represent an absolute upper limit for the emission probabilities.

The aim of this thesis was to clarify the confusing situation by performing a high-statistics measurement of the bremsstrahlung emission probability in the  $\alpha$  decay of  $^{210}\text{Po}$  [30].

In chapter 2 a brief overview on some of the theoretical descriptions of the bremsstrahlung accompanied  $\alpha$  decay is given. The experimental setup is presented in chapter 3. The GEANT4 simulation of the setup and the derivation of the detection efficiency is discussed in chapter 4. Chapter 5 describes the data analysis and in chapter 6 the final results are presented and discussed.



# Chapter 2

## Theoretical Description

The theory of the bremsstrahlung emission probability accompanying an  $\alpha$  decay was discussed intensely in the literature in recent years [3–21]. The following discussion will be restricted to those approaches relevant for the interpretation of the present measurement. In particular we will discuss the Coulomb acceleration model (section 2.3), the quantum mechanical treatment (section 2.4) and the refined semi-classical approach of Jentschura-Milstein-Terekhov (section 2.5).

A detailed discussion of the Coulomb acceleration model and the quantum mechanical treatment can be found in the appendix A and B.

### 2.1 $\alpha$ Decay

An  $\alpha$  particle, a cluster of two protons and two neutrons, forming a helium-4 ( ${}^4\text{He}$ ) nucleus, is strongly bound (binding energy:  $B({}^4\text{He}) = 28.295 \text{ MeV}$ , separation energies:  $S_n = 20.578 \text{ MeV}$ ,  $S_p = 19.814 \text{ MeV}$ ). Thus for heavy nuclei it can be energetically favourable to split up into an  $\alpha$  particle and a daughter nucleus with mass  $(A - 4)$  and charge number  $(Z - 2)$ , with  $A$  and  $Z$  being the mass and charge of the parent nucleus.

$$m({}^A\text{Z}) > m({}^{A-4}\text{Z}-2) + m({}^4\text{He}) \quad (2.1)$$

$$\implies B({}^A\text{Z}) > B({}^{A-4}\text{Z}-2) + B({}^4\text{He}) \quad (2.2)$$

The  $\alpha$  particle is on the one hand bound inside the nucleus by the strong force on the other hand because of its charge ( $2^+$ ) repelled by the electromagnetic field of the remaining protons. The potential seen by the  $\alpha$  particle is the superposition of both potential, schematically drawn in figure 2.1 [31].

Due to the resulting potential barrier the  $\alpha$  decay is classically forbidden, viewed quantum mechanically though the  $\alpha$  particle has a certain probability to tunnel through the barrier and leave the nucleus. This process is called the  $\alpha$  decay. The theoretical description of the  $\alpha$  decay was one of the early successes of quantum mechanics [32–34].

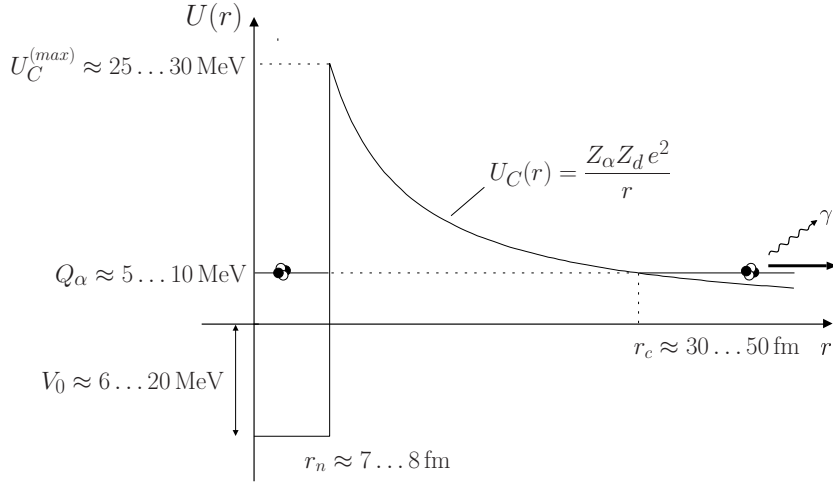


**Figure 2.1:** In the  $\alpha$  decay an  $\alpha$  particle is tunneling through the Coulomb-barrier and is accelerated in the field of the remaining nucleus. Typical values for the decay energy  $Q_\alpha$ , the height of the potential barrier  $U_C^{(\max)}$ , the radius of the nucleus  $r_n$  and the classical turning point  $r_c$  are given in the figure.

## 2.2 Bremsstrahlung

Bremsstrahlung is electromagnetic radiation which is emitted by an accelerated or decelerated charge. Classically an elementary charge  $e$  at the point  $\mathbf{r}$  which is accelerated by  $\dot{\beta} = \dot{\mathbf{v}}/c$  results in a vector potential  $\mathbf{A}$  at the point of the observer  $\mathbf{x}$  and at time  $t$  which is given by (see e.g. [1])

$$\mathbf{A}(\mathbf{x}, t) = \frac{e}{c} \left[ \frac{[\mathbf{n} \times [(\mathbf{n} - \dot{\beta}) \times \dot{\beta}]]}{(1 - \dot{\beta} \cdot \mathbf{n})^3} \right]_{\text{ret}} \quad (2.3)$$

for  $|\mathbf{r} - \mathbf{x}| \gg 1$ . Here  $\mathbf{n}$  is an unit vector in the direction of the observer ( $\mathbf{n} = (\mathbf{x} - \mathbf{r})/|\mathbf{x} - \mathbf{r}|$ ) and  $c$  is the speed of light.

Assuming that the acceleration  $\dot{\beta}$  act in the direction of motion  $\beta$  ( $\dot{\beta} \parallel \beta$ ) the probability for bremsstrahlung photons  $dP_\gamma$  emitted into the solid angle  $d\Omega$  with an energy in the interval  $dE_\gamma$  is given by (in the non-relativistic dipole approximation)

$$\frac{d^2 P}{dE_\gamma d\Omega} = \frac{\alpha}{4\pi^2 E_\gamma} \left| \int_{-\infty}^{+\infty} \dot{\beta}(t) \sin \vartheta(t) \exp \left( \frac{i}{\hbar} E_\gamma \left( t - \frac{\mathbf{n} \cdot \mathbf{r}(t)}{c} \right) \right) dt \right|^2, \quad (2.4)$$

with the fine structure constant  $\alpha = e^2/(\hbar c)$  and the angle  $\vartheta$  between the direction of motion and the direction to the observer. A detailed derivation and discussion of this classical result can be found in appendix A.1.

## 2.3 Coulomb Acceleration Model

The simplest model for the bremsstrahlung emission probability in the  $\alpha$  decay is the *Coulomb acceleration (CA) model*. Here the  $\alpha$  particle is viewed to tunnel through the classically forbidden region and materialise at the classical turning point  $r_c$  with zero velocity. It is then accelerated in the Coulomb field of the daughter nucleus. In this classical model the tunneling process is completely ignored.

In the non-relativistic limit and within the dipole approximation the expression for the probability of bremsstrahlung photons  $dP$  per energy interval  $dE_\gamma$  and solid angle  $d\Omega$  is given by (see appendix A.4)

$$\frac{d^2 P}{dE_\gamma d\Omega} \approx \frac{\alpha(Z_{\text{eff}}^{E1})^2}{4\pi^2 E_\gamma} \sin^2 \vartheta \left| \int_{r_c}^{+\infty} \beta'(r) e^{iE_\gamma t(r)/\hbar} dr \right|^2, \quad (2.5)$$

where  $\vartheta$  is the angle between the observer of the bremsstrahlung photon and the direction of motion of the  $\alpha$  particle. The effective dipole charge  $Z_{\text{eff}}^{E1}$  is defined by the relation

$$Z_{\text{eff}}^{E1} := \mu \left( \frac{Z_\alpha}{M_\alpha} - \frac{Z_d}{M_d} \right), \quad (2.6)$$

with the mass  $M_\alpha$  and the charge  $Z_\alpha$  of the  $\alpha$  particle and the mass  $M_d$  and the charge  $Z_d$  of the daughter nucleus. The *reduced mass*  $\mu$  is defined by  $\mu = M_\alpha \cdot M_d / (M_\alpha + M_d)$ . Moreover,  $\beta'(r) = d\beta(r)/dr$  is the derivative of the relative velocity between  $\alpha$  particle and daughter nucleus with respect to their relative distance.

With the equation of motion

$$\frac{1}{2} \mu c^2 \beta^2(r) = Q_\alpha - \frac{Z_\alpha Z_d e^2}{r}, \quad (2.7)$$

where  $Q_\alpha$  is the decay energy of the  $\alpha$  decay, the relation (2.5) can be easily integrated numerically. In appendix A.4 a detailed derivation is presented.

In equation (2.5) the integral spans over the whole acceleration process ( $r_c < r < \infty$ ). However from a classical point of view a bremsstrahlung photon of energy  $E_\gamma$  can only be emitted if the kinetic energy of relative motion is higher than  $E_\gamma$ . In the *strict Coulomb acceleration (SCA) model* this is taken into account by setting the lower limit of the integration in equation (2.5) to  $r_{\min}$  defined by

$$r_{\min} = \frac{Z_\alpha Z_d e^2}{Q_\alpha - E_\gamma}. \quad (2.8)$$

The predictions of the CA and SCA models for the angle-integrated bremsstrahlung emission probability in the  $\alpha$  decay of  $^{210}\text{Po}$  are plotted in figure 1.1 and figure 2.2.

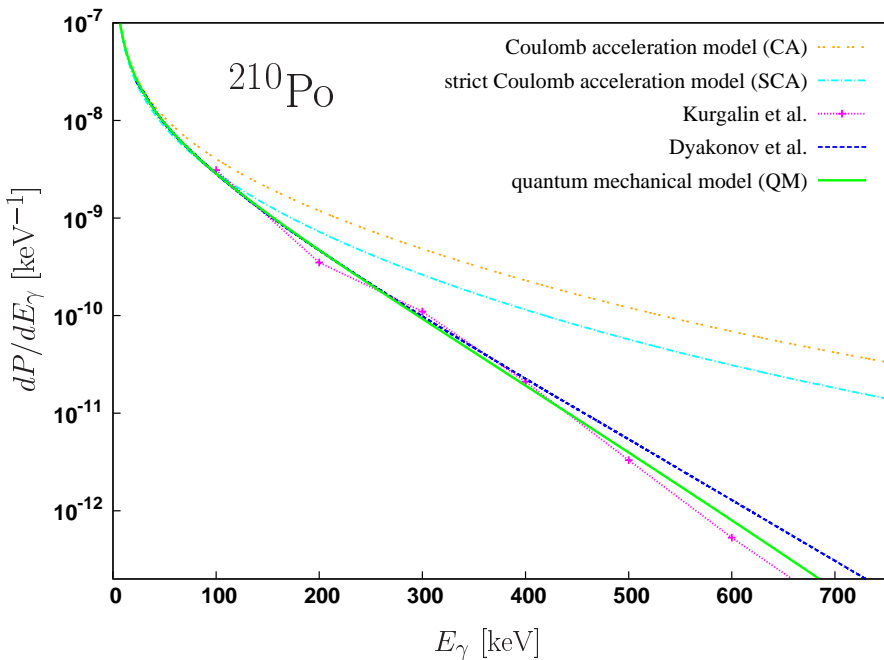


**Figure 2.2:** The theoretical predictions of the CA (orange), the SCA model (cyan), the semi-classical treatment of Dyakonov et al. [10] (blue) and the quantum mechanical model (QM, green) are plotted. The prediction of the semi-classical Jentschura-Milstein-Terekhov approach is not plotted separately as it is indistinguishable from the quantum mechanical result in this logarithmic plot (see also figure 2.5). Also shown is a numerical calculation of Kurgalin et al. [16] (magenta), where the square-well potential in  $U(r)$  (see equation (2.17)) was replaced by a Wood-Saxon type potential.

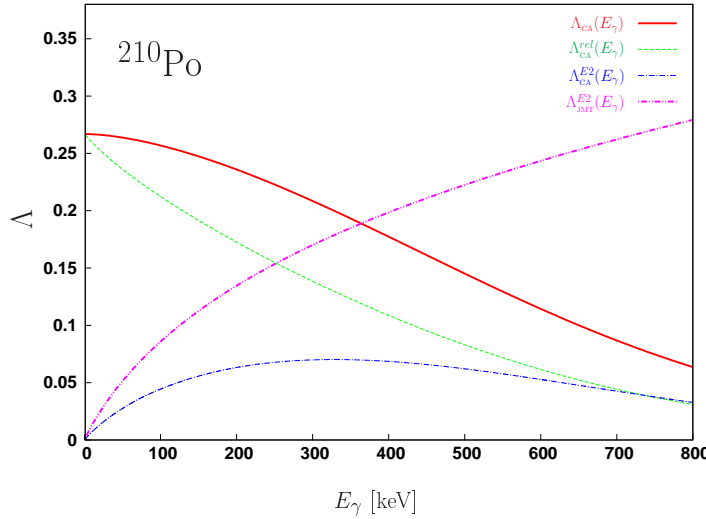


**Figure 2.3:** The interference term  $\Lambda_{CA}(E_\gamma)$  as function of the photon energy  $E_\gamma$  (red). In addition the contribution from the relativistic correction  $\Lambda_{CA}^{rel}(E_\gamma)$  (green) and the quadrupole contribution  $\Lambda_{CA}^{E2}(E_\gamma)$  (blue) in the CA model are plotted separately. The correction from the quadrupole contribution derived in the context of the Jentschura-Milstein-Terekhov approach  $\Lambda_{JMT}^{E2}(E_\gamma)$  is shown for comparison (magenta).

As to be expected, the emission probability predicted in the SCA model is getting smaller as compared to the CA probability with increasing  $\gamma$ -energy.

For the angular correlation between the direction of the  $\alpha$  particle and the bremsstrahlung photon the classical CA model equation (2.5) predicts a dipole distribution.

Looking at first order corrections to (2.5) we obtain contributions from the quadrupole term and relativistic contributions, which are of the same order of magnitude. As shown in more detail in appendix A.4 we find

$$\frac{d^2P}{dE_\gamma d\Omega} \approx \frac{\alpha}{4\pi^2 E_\gamma} \left| \int_{r_c}^{+\infty} \left( Z_{\text{eff}}^{E1} + Z_{\text{eff}}^{E2} \underbrace{\left( 2\beta(r) - i \frac{E_\gamma}{\hbar c} r \right)}_{\text{rel. corr.}} \cos \vartheta \right) \beta'(r) \sin \vartheta e^{iE_\gamma t(r)/\hbar} dr \right|^2. \quad (2.9)$$

The effective quadrupole charge  $Z_{\text{eff}}^{E2}$  is given by

$$Z_{\text{eff}}^{E2} = \mu^2 \left( \frac{Z_\alpha}{M_\alpha^2} + \frac{Z_d}{M_d^2} \right). \quad (2.10)$$

In the case of the  $\alpha$  decay of  $^{210}\text{Po}$  we find that the effective quadrupole charge ( $Z_{\text{eff}}^{E2} \approx 1.95$ ) is about five times bigger than the corresponding dipole charge ( $Z_{\text{eff}}^{E1} \approx 0.4$ ). Therefore it is important to take contributions from the electric quadrupole radiation into account.

This expression for  $d^2P/(dE_\gamma d\Omega)$  has the structure

$$\frac{d^2P}{dE_\gamma d\Omega} \approx C \left| (f_1(E_\gamma) + f_2(E_\gamma) \cos \vartheta) \sin \vartheta \right|^2 \quad (2.11)$$

and can be written as

$$\frac{d^2P}{dE_\gamma d\Omega} \approx C f_1^2(E_\gamma) \sin^2 \vartheta \left( 1 + \frac{2\text{Re}(f_1(E_\gamma)f_2^*(E_\gamma))}{f_1^2(E_\gamma)} \cos \vartheta + \frac{f_2^2(E_\gamma)}{f_1^2(E_\gamma)} \cos^2 \vartheta \right). \quad (2.12)$$

As the squared second order term  $f_2^2(E_\gamma)/f_1^2(E_\gamma) \cos^2 \vartheta$  is  $\ll 1$  it can thus be neglected. So the angular correlation can be written as

$$f_{\mathcal{A}}(E_\gamma, \vartheta) = \sin^2 \vartheta \left( 1 + 2\Lambda_{\text{CA}}(E_\gamma) \cos \vartheta \right) \quad (2.13)$$

where the function  $\Lambda_{\text{CA}}(E_\gamma)$  is defined by

$$\Lambda_{\text{CA}}(E_\gamma) := \frac{\text{Re}(f_1(E_\gamma)f_2^*(E_\gamma))}{f_1^2(E_\gamma)} = \Lambda_{\text{CA}}^{\text{rel}}(E_\gamma) + \Lambda_{\text{CA}}^{E2}(E_\gamma) \quad (2.14)$$

and describes the correction to the dipole distribution. Note that the interference term  $\Lambda_{\text{CA}}(E_\gamma)$  has two (additive) contributions, one due to the relativistic correction ( $\Lambda_{\text{CA}}^{\text{rel}}(E_\gamma)$ ), the other due to the quadrupole contribution ( $\Lambda_{\text{CA}}^{E2}(E_\gamma)$ ). They are plotted in figure 2.3 for the case of  $^{210}\text{Po}$ . (For a comparison with the result of the strict Coulomb acceleration model see figure A.5.) While the relativistic contribution dominates at  $E_\gamma \approx 0 \text{ keV}$ , they are both of equal size for  $E_\gamma \geq 500 \text{ keV}$ . Of course, when integrating equation (2.9) over  $\vartheta$  the contribution of the interference term vanishes.

## 2.4 Quantum Mechanical Treatment

A full (non-relativistic) quantum mechanical treatment for the bremsstrahlung emission probability has been presented by [3]. Here the perturbative quantum mechanical expression of the photon emission probability for the transition from the initial state  $|i\rangle$  to the final state  $|f\rangle$  is obtained from Fermi's golden rule

$$W_{i \rightarrow f} = \frac{2\pi}{\hbar} |\langle f | H_{\text{em}} | i \rangle|^2 \rho_f, \quad (2.15)$$

where  $\rho_f$  is the density of the final states and  $H_{\text{em}}$  is the interaction Hamiltonian of the electromagnetic field. Within the dipole approximation one obtains (see appendix B)

$$\frac{dP^2}{dE_\gamma d\Omega} = \frac{(Z_{\text{eff}}^{E1} e)^2}{2\pi \mu^2 c^3} \left| \langle \Phi_f | \partial_r U(r) | \Phi_i \rangle \right|^2 \frac{1}{E_\gamma} \sin^2 \vartheta. \quad (2.16)$$

Here  $\Phi_i(r)$  and  $\Phi_f(r)$  are the radial wave functions of the initial and final state, respectively, and  $U(r)$  is the potential between the  $\alpha$  particle and the daughter nucleus (see figure 2.1).

The potential  $U(r)$  is usually approximated by a Coulomb potential outside the radius  $r_0$  and a constant potential  $V_0$  inside

$$U(r) = \frac{Z_\alpha Z_d e^2}{r} \Theta(r - r_0) + V_0 \Theta(r_0 - r). \quad (2.17)$$

The initial wave function  $\Phi_i(r)$  has zero angular momentum and is given in terms of the Coulomb wave functions  $F_0$  and  $G_0$  outside  $r_0$  and proportional to the spherical Bessel function  $j_0$  inside

$$\Phi_i(r) = \begin{cases} A j_0(\kappa r) & \text{for } r < r_0 \\ C \frac{G_0(\eta, kr) + i F_0(\eta, kr)}{kr} & \text{for } r > r_0. \end{cases} \quad (2.18)$$

The Sommerfeld parameter  $\eta$  is defined by

$$\eta = \frac{\mu Z_\alpha Z_d e^2}{\hbar^2 k} \quad (2.19)$$

and the wave vectors  $k$  and  $\kappa$  are given by

$$k = \frac{1}{\hbar} \sqrt{2\mu Q_\alpha} \quad \kappa = \frac{1}{\hbar} \sqrt{2\mu(Q_\alpha - V_0)} \quad (2.20)$$

where  $Q_\alpha$  is the  $Q$ -value of the  $\alpha$  decay. The initial state is normalised to a unit outgoing flux of particles.

The radius  $r_0$  and the potential  $V_0$  are fixed by matching the wave function at  $r = r_0$  such that the decay energy and the mean life of the  $\alpha$  decay is reproduced. There are multiple discrete solution sets  $(r_0, V_0)$  distinguished by the number of nodes of the inner wave function. However the final bremsstrahlung emission probability is quite insensitive to the choice of the solution set  $(r_0, V_0)$ . The solution selected is  $r_0 = 7.96$  fm,  $V_0 = -13.42$  MeV (see also appendix B.8).

The final wave function  $\Phi_f(r)$  has an angular momentum of one and is therefore described by the Coulomb wave functions  $F_1$  and  $G_1$  outside  $r_0$  and by the spherical Bessel function  $j_1$  inside

$$\Phi_f(r) = \begin{cases} a j_1(\kappa' r) & \text{for } r < r_0 \\ c \frac{\sin(\alpha) G_1(\eta', k' r) + \cos(\alpha) F_1(\eta', k' r)}{k' r} & \text{for } r > r_0. \end{cases} \quad (2.21)$$

For the primed quantities  $\eta'$ ,  $k'$  and  $\kappa'$  the decay energy is reduced by the energy of the emitted bremsstrahlung photon  $E_\gamma$

$$k' = \frac{1}{\hbar} \sqrt{2\mu(Q_\alpha - E_\gamma)} \quad \kappa' = \frac{1}{\hbar} \sqrt{2\mu(Q_\alpha - E_\gamma - V_0)} \quad \eta' = \frac{\mu Z_\alpha Z_d e^2}{\hbar^2 k'} . \quad (2.22)$$

The angle  $\alpha$  is determined by matching the wave function at  $r = r_0$ . For  $^{210}\text{Po}$  the value of  $\tan(\alpha)$  is of the order of  $10^{-28}$  and therefore the irregular Coulomb wave function  $G_1$  is suppressed in  $\Phi_f$ . The final wave function is normalised requiring the completeness relation when integrated over the energy.

The matrix element  $\langle \Phi_f | \partial_r U(r) | \Phi_i \rangle$  is then given by

$$\begin{aligned} \langle \Phi_f | \partial_r U(r) | \Phi_i \rangle &\approx \sqrt{\frac{2m^2}{\pi\hbar^3 k k'}} \left[ \left( \frac{Z_\alpha Z_d e^2}{r_0} - V_0 \right) \left( F_1(\eta', k'r_0) + G_1(\eta', k'r_0) \tan(\alpha) \right) G_0(\eta, kr_0) \right. \\ &\quad \left. - zZe^2 \int_{r_0}^{\infty} dr \frac{1}{r^2} \left( F_1(\eta', k'r) + G_1(\eta', k'r) \tan(\alpha) \right) \left( G_0(\eta, kr) + iF_0(\eta, kr) \right) \right] \end{aligned} \quad (2.23)$$

which can be evaluated numerically. A detailed derivation of the quantum mechanical result can be found in appendix B. In figure 2.2 the result of our the quantum mechanical calculation (QM) for the angle-integrated bremsstrahlung emission probability for  $^{210}\text{Po}$  is plotted and compared to other theoretical predictions.

As expected, the quantum mechanical result (QM) agrees with the classical result for  $E_\gamma \rightarrow 0$ , but for higher  $\gamma$ -energies the classical results are overestimating the emission probability by orders of magnitude.

Note that there is a numerical difference between our quantum mechanical calculation and the result published in [3] because we used the correct decay energy  $Q_\alpha(^{210}\text{Po}) = 5.407 \text{ MeV}$  for the  $\alpha$  decay of  $^{210}\text{Po}$  in our numerical evaluation.

The imaginary part of the matrix element (2.23) is mainly an integral over a product of the two regular Coulomb wave functions  $F_0$  and  $F_1$ . Because the regular Coulomb wave functions nearly vanish inside the barrier, the imaginary part contains mainly contributions to the bremsstrahlung from the classical acceleration in the Coulomb field.

On the other hand the real part of  $\langle \Phi_f | \partial_r U(r) | \Phi_i \rangle$  is dominated by the irregular Coulomb wave functions  $G_0$  and  $G_1$  and therefore also contains contributions to the bremsstrahlung from the tunneling region.

So the comparison of the relative contribution from the real and imaginary part of the matrix element can be considered as an estimate of the role of the tunneling for the bremsstrahlung emission probability [3]. As shown in figure 2.4 the "tunneling" contribution is smaller than 5% at photon energies below 100 keV but rises considerably to reach values near 15% at  $E_\gamma = 600 \text{ keV}$ .

Unfortunately, a full quantum mechanical treatment of the quadrupole and of the relativistic contribution to the bremsstrahlung emission probability is not available. To obtain a quantum mechanical estimate of the E2-contribution a calculation within a semi-classical approach was initiated [21], the result of which will be presented in the following section.

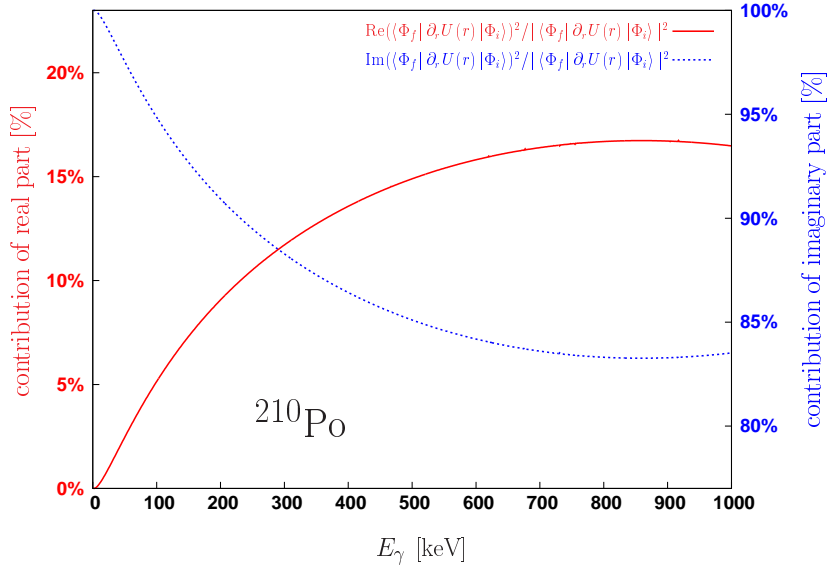


**Figure 2.4:** The contributions from the imaginary (blue) and real (red) part of the matrix element are compared. The imaginary part of the matrix element contains mainly the contribution to the bremsstrahlung from the classical acceleration in the Coulomb field, whereas the real part contains the contribution from the tunneling region.

## 2.5 The Semi-Classical Jentschura-Milstein-Terekhov Approach

In the semi-classical (non-relativistic) treatment by Jentschura, Milstein and Terekhov [21] the regular and irregular Coulomb wave functions in the matrix element are replaced by semi-classical approximations and the quadrupole contribution has been taken into account.

According to [21] the bremsstrahlung emission probability can then be written as

$$\frac{d^2P}{dE_\gamma d\Omega} = \frac{e^2}{\pi\mu^2 E_\gamma} \sin^2 \vartheta \left| Z_{\text{eff}}^{E1} e^{i\delta_1} \mathcal{M} + Z_{\text{eff}}^{E2} e^{i\delta_2} \mathcal{N} \cos \vartheta \right|^2 \quad (2.24)$$

The dipole contribution  $\mathcal{M}$  and the quadrupole contribution  $\mathcal{N}$  can be expressed by

$$\mathcal{M} = \sqrt{\frac{2k}{\pi k'}} \frac{k k'}{k+k'} \frac{\eta}{\bar{\eta}} \left[ J(\xi) + \frac{1}{\bar{\eta}} J_1(\xi) \right] \quad (2.25)$$

$$\mathcal{N} = \sqrt{\frac{2k}{\pi k'}} \frac{k k'}{k+k'} \frac{\eta}{\bar{\eta}} \left[ -\sqrt{\frac{2Q_\alpha}{\mu}} J_1(\xi) \right] \quad (2.26)$$

where  $\bar{\eta} = (\eta + \eta')/2$  is a "mean" Sommerfeld parameter and  $\xi = \eta' - \eta$  is the difference of the final and the initial Sommerfeld parameter. The values  $k$ ,  $k'$ ,  $\eta$  and  $\eta'$  are defined as

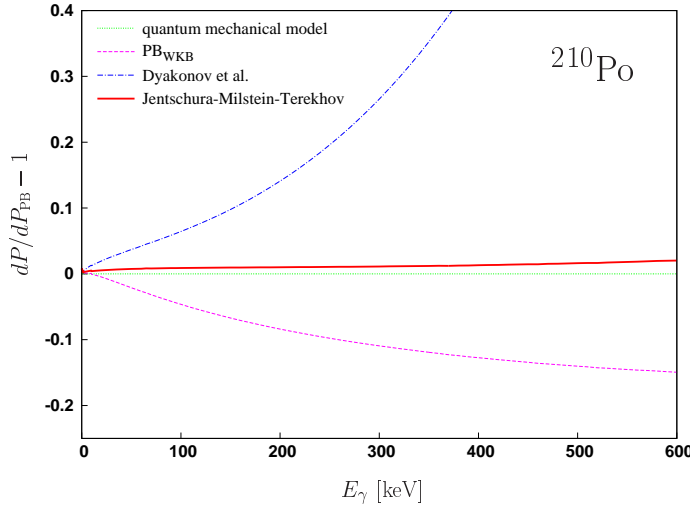


**Figure 2.5:** The deviation from the fully quantum mechanical result (QM, green) is plotted for the Jentschura-Milstein-Terekhov approach (red), the semiclassical WKB approximation given in [3] (magenta) and the semiclassical treatment by Dyakonov et al. [10] (blue).

above

$$k = \frac{1}{\hbar} \sqrt{2\mu Q_\alpha} \quad \eta = \frac{\mu Z_\alpha Z_d e^2}{\hbar^2 k} \quad k' = \frac{1}{\hbar} \sqrt{2\mu(Q_\alpha - E_\gamma)} \quad \eta' = \frac{\mu Z_\alpha Z_d e^2}{\hbar^2 k'} . \quad (2.27)$$

The functions  $J(\xi)$  and  $J_1(\xi)$  can be expressed in terms of simple integrals

$$J(\xi) = i \xi \exp(-\pi\xi) \int_0^\infty dt \sinh(t) \exp[i\xi(t - \sinh t)] \quad (2.28)$$

$$J_1(\xi) = -\xi \exp(-\pi\xi) \int_0^\infty dt \exp[i\xi(t - \sinh t)] . \quad (2.29)$$

Neglecting the E2-contribution the result of the semi-classical treatment is in excellent agreement with our quantum mechanical calculation. The percentage of deviation of the semi-classical result from the quantum mechanical result is shown for the case of  $^{210}\text{Po}$  in figure 2.5 together with the results from other semi-classical treatments; the improvement of the Jentschura-Milstein-Terekhov approach with respect to the quantum mechanical result is obvious.

To discuss the E2-correction to the angular correlation we define again a function  $\Lambda_{\text{JMT}}^{E2}(E_\gamma)$  by writing

$$\frac{dP_{\text{JMT}}}{dE_\gamma d\Omega} = \left. \frac{dP_{\text{JMT}}}{dE_\gamma d\Omega} \right|_{\text{dipole}} \cdot (1 + 2\Lambda_{\text{JMT}}^{E2}(E_\gamma) \cos \vartheta) . \quad (2.30)$$

From equation (2.24) we get

$$\Lambda_{\text{JMT}}^{E2}(E_\gamma) = \frac{Z_{\text{eff}}^{E2}}{Z_{\text{eff}}^{E1}} \text{Re} \left( \frac{\mathcal{M}\mathcal{N}^*}{|\mathcal{M}|^2} e^{i(\delta_1 - \delta_2)} \right). \quad (2.31)$$

In figure 2.3 the interference term  $\Lambda_{\text{JMT}}^{E2}(E_\gamma)$  is plotted for the case of  ${}^{210}\text{Po}$  in magenta. While the corresponding interference term  $\Lambda_{\text{CA}}(E_\gamma)$  from the classical Coulomb acceleration model approaches  $\Lambda_{\text{JMT}}^{E2}(E_\gamma)$  for  $E_\gamma \rightarrow 0$ , it considerably underestimates  $\Lambda_{\text{JMT}}^{E2}(E_\gamma)$  at higher photon energies;  $\Lambda_{\text{JMT}}^{E2}(E_\gamma)$  even dominates the classical relativistic term  $\Lambda_{\text{CA}}^{rel}(E_\gamma)$  for  $\gamma$ -energies  $\geq 250$  keV.

## 2.6 Summary

The preceding discussions have shown that the total (angle-integrated) bremsstrahlung emission probability  $dP/dE_\gamma$  in the  $\alpha$  decay of  ${}^{210}\text{Po}$  is dominated by the E1 dipole radiation. The probability is steeply decreasing with increasing  $E_\gamma$ , reaching values of  $10^{-12}$  keV $^{-1}$  for  $E_\gamma \approx 600$  keV. The quantum mechanical result for  $dP/dE_\gamma$  is expected to be accurate (within the underlying assumption for the  $\alpha$ -potential  $U(r)$ , see equation (2.17)) to within 1% (see appendix B.1), and is well represented by the semi-classical approach of Jentschura-Milstein-Terekhov [21]. The influence of the shape of  $U(r)$  on the emission probability is expected to be small. Kurgalin et al. [16] have performed a numerical calculation replacing the square well by a Wood-Saxon type potential; however the available information about this calculation does not allow to decide if the observed deviations (see figure 2.2) are in fact due to the different form of  $U(r)$  alone. E2 quadrupole contributions to the angle-integrated bremsstrahlung emission probability  $dP/dE_\gamma$  are estimated to be  $\leq 1.5\%$  for  $\gamma$ -energies up to 600 keV [21].

On the other hand, the  $\alpha$ - $\gamma$  angular distribution, which is  $\propto \sin^2 \vartheta$  for pure dipole radiation, is found to be considerably modified by quadrupole contributions and leads to an  $\alpha$ - $\gamma$  angular correlation  $f_{\times}(\vartheta) \propto \sin^2 \vartheta (1 + 2\Lambda^{E2} \cos \vartheta)$ . As shown within the semi-classical approach,  $\Lambda^{E2}$  reaches values up to 0.25 for  $\gamma$ -energies around 600 keV. The results obtained within the classical Coulomb acceleration model suggest, however, that a consistent treatment of the E2-contribution to the  $\alpha$ - $\gamma$  correlation has to include also first order relativistic contributions, i.e.  $f_{\times}(\vartheta) \propto \sin^2 \vartheta (1 + 2\Lambda \cos \vartheta)$  with  $\Lambda = \Lambda^{E2} + \Lambda^{rel}$  (see equations (2.13) and (2.14)), where  $\Lambda^{rel}$  is of the same size as  $\Lambda^{E2}$ . Unfortunately  $\Lambda^{rel}$  has not been calculated for the relevant  $\gamma$ -energies within a relativistic quantum mechanical framework; only for  $E_\gamma \rightarrow 0$  it has been shown [35] that  $\Lambda^{rel}$  is equal to  $\Lambda_{\text{CA}}^{rel}$ , i.e.  $\sim 0.27$ . Thus the  $\cos \vartheta$  term in the  $\alpha$ - $\gamma$  correlation function  $f_{\times}(\vartheta)$  is so far only known for  $E_\gamma \approx 0$  keV.



# Chapter 3

## Experimental Setup

In order to be able to measure the bremsstrahlung emitted during an  $\alpha$  decay it is important to distinguish the rare bremsstrahlung events from the ambient  $\gamma$ -background. As shown in chapter 2 typical emission probabilities integrated over the interesting energy region of 300–500 keV are in the order of  $10^{-10}$  bremsstrahlung photons per decay. With commercially available  $\alpha$  source activities of about 100 kBq a rate of about  $10^{-5}$  bremsstrahlung photons per second in this energy range is expected. Even with good background suppression the  $\gamma$ -background in the corresponding energy range would be about five orders of magnitude higher ( $\approx 1$  per second). The room background can further be suppressed by requiring the simultaneous detection of the bremsstrahlung photon and the  $\alpha$  particle. Assuming a time window of 100 ns and a source activity of 100 kBq the rate of background photons is reduced to  $10^{-2}$  per second. This is still three orders of magnitude larger than the bremsstrahlung rate. Therefore additional precautions have to be taken to measure this elusive process.

Below we will first discuss the basic principle of the measurement (section 3.1), which relies on an excellent energy and timing resolution of the detectors employed to record the  $\alpha$  particles and bremsstrahlung photons. Moreover, the measurement requires a strong  $\alpha$  source, which ideally should decay only into the ground state of a stable daughter nucleus to avoid any additional disturbing radiation. The selected  $\alpha$  source,  $\alpha$  detector and photon detector are shortly described in section 3.2, 3.3 and 3.4, while in section 3.5 and 3.6 the experimental setup and the data acquisition system are presented. For more details see [36].

### 3.1 Principle of Measurement

As mentioned above great care has to be taken to distinguish the bremsstrahlung photons from the background radiation. This can be accomplished by noting that the sum energy of all emitted particles ( $\alpha$  particle, daughter nucleus (with possible excitation energy) and

bremsstrahlung photon) has to be equal to the decay energy of the  $\alpha$  decay  $Q_\alpha$ .

The energy  $Q_\alpha$  released in the  $\alpha$  decay is equal to the mass difference between the decaying nucleus and the sum of the masses of the daughter nucleus and the  $\alpha$  particle. The released energy splits up into the kinetic energy of the  $\alpha$  particle  $E_\alpha$ , the kinetic energy of the daughter nucleus  $E_d$ , the excitation energy of the daughter nucleus  $E_{\text{ex}}$  and the energy of the bremsstrahlung photon  $E_\gamma$ :

$$Q_\alpha = E_\alpha + E_d + E_{\text{ex}} + E_\gamma. \quad (3.1)$$

Due to energy and momentum conservation the energy of the  $\alpha$  particle for a decay into the ground state of the daughter nucleus ( $E_{\text{ex}} = 0$ ) can be approximated by

$$E_\alpha \approx \frac{M_d}{M_\alpha + M_d} (Q_\alpha - E_\gamma), \quad (3.2)$$

with the mass of the daughter nucleus  $M_d$  and the mass of the  $\alpha$  particle  $M_\alpha$ . Note that in equation (3.2) the initial nucleus is assumed to be at rest and the small photon recoil momentum was neglected. Denoting the energy of the  $\alpha$  particle by  $E_{\alpha,0}$  when no bremsstrahlung photon is emitted, this can be written as

$$E_\alpha + \frac{M_d}{M_\alpha + M_d} E_\gamma \approx E_{\alpha,0} = \text{const.} \quad (3.3)$$

Therefore in a 2-dimensional plot of the  $\alpha$ -energy  $E_\alpha$  versus the  $\gamma$ -energy  $E_\gamma$ , bremsstrahlung events can be found on a straight line given by equation 3.3.

In the present experiment the  $\alpha$  decay of  $^{210}\text{Po}$  is investigated.  $^{210}\text{Po}$  decays into the stable daughter nucleus  $^{206}\text{Pb}$  with a weak  $\gamma$ -branch of order  $10^{-5}$ , leading to the emission of a  $\gamma$ -ray with an energy of  $E_\gamma = 803.1 \text{ keV}$ . The decay energy  $Q_\alpha^1$  has a value of  $5407.46 \text{ keV}$  which results in  $E_{\alpha,0} = 5304.38 \text{ keV}$  [37].

In figure 3.1 the schematic structure of the expected 2-dimensional  $E_\alpha$ - $E_\gamma$  plot of a coincidence measurement is illustrated. In the red region given by equation (3.3) the bremsstrahlung events are expected to show up. Chance coincidences of  $\alpha$  particles with  $\gamma$ -rays from the room background will mainly occur with  $\alpha$  particles of energy  $E_{\alpha,0}$ . These chance coincidences are therefore found in the green region. If the  $^{210}\text{Po}$  decays into the  $803.10 \text{ keV}$  excited state of  $^{206}\text{Pb}$  the emitted  $\alpha$  particle has an energy of  $4516.58 \text{ keV}$ . The excited state of the daughter nucleus decays by emitting a coincident  $\gamma$ -ray with an energy of  $803.10 \text{ keV}$ . These events will produce a full-energy peak in the  $E_\alpha$ - $E_\gamma$  plot at  $E_{\alpha,803} = 4516.58 \text{ keV}$  and  $E_\gamma = 803.10 \text{ keV}$ , and its corresponding Compton-background will contribute to the region marked blue in the figure.

Thus by measuring with good resolution the energies of the coincidentally measured  $\alpha$  particle and bremsstrahlung photon can be distinguished efficiently from the background as shown in figure 3.1.

---

<sup>1</sup>In the literature sometimes  $E_{\alpha,0}$  and  $Q_\alpha$  are not distinguished.

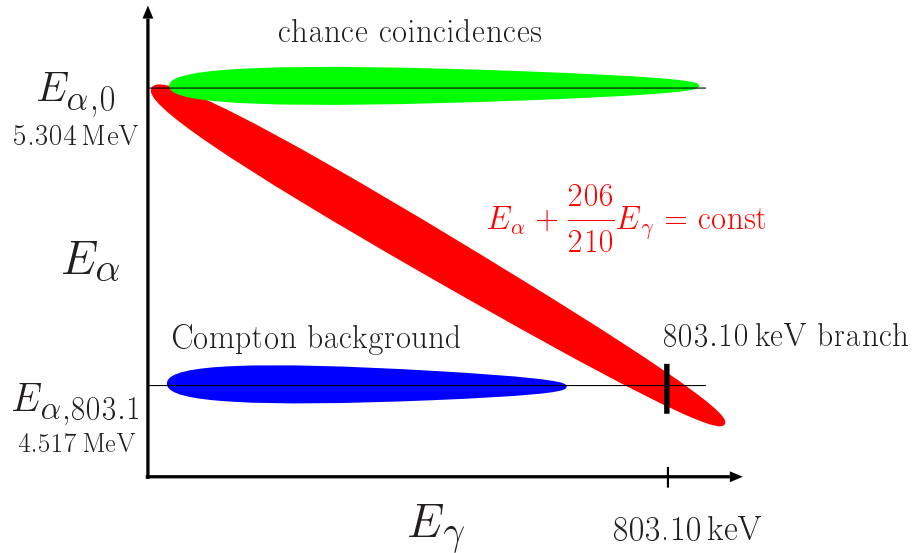


**Figure 3.1:** Schematic structure of a 2-dimensional plot of the coincidentally measured  $\alpha$ -energy versus  $\gamma$ -energy. The bremsstrahlung events are expected to be found in the red region given by equation (3.3). Chance coincidence from room background  $\gamma$ -rays with  $\alpha$  decays are contributing to the green region. At  $E_{\alpha,803}$  and  $E_\gamma = 803.10 \text{ keV}$  the full-energy peak of the 803 keV  $\gamma$ -branch can be found with its Compton-background in the blue region.

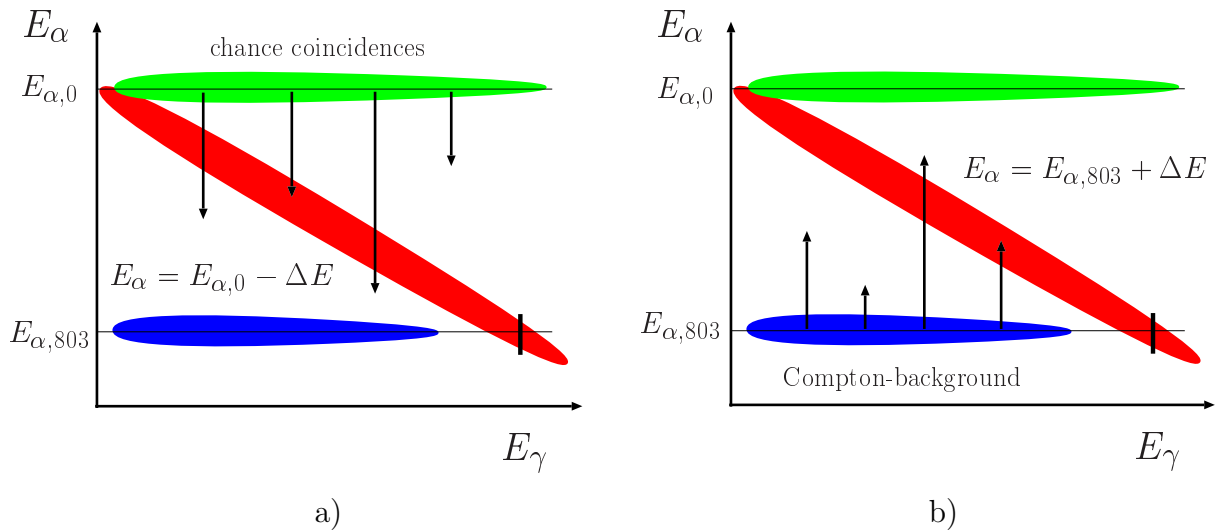


**Figure 3.2:** Coincident background in the region of the expected bremsstrahlung events arises either from chance coincidences with background  $\gamma$ -rays and an  $\alpha$  particle that lost energy by scattering or one whose energy was measured to low (a) or from a photon out of the 803 keV  $\gamma$ -branch Compton-background, where the energy of the coincidentally measured  $\alpha$  particle was measured to high, e.g. by pile-up.

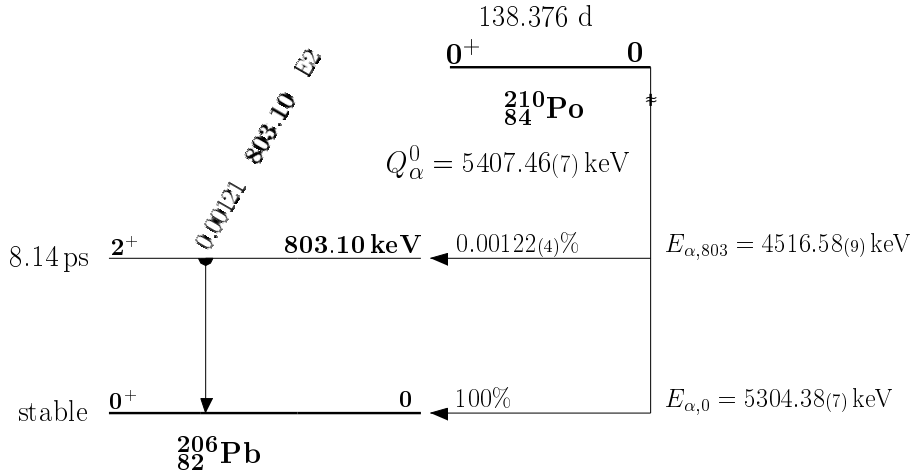


**Figure 3.3:**  $\alpha$  decay scheme of  $^{210}\text{Po}$  [37].

Nevertheless, the region where the bremsstrahlung events are expected will not be free of chance coincidences. These may arise from chance coincidences of background  $\gamma$ -rays with  $\alpha$  particles that either lost energy, e.g. by scattering, energy loss in the source material or in the dead-layer of the detector, or whose energy was measured too low (e.g. due to incomplete charge collection). Another source of coincident background are events from the Compton background of the  $803\text{ keV}$   $\gamma$ -branch where the measured value of the energy of the corresponding  $\alpha$  particle is too high, e.g. because of pile-up. Both background sources have to be minimised by appropriate measures, in particular by optimising the  $\alpha$ - and  $\gamma$ -energy as well as the time resolution.

Another possible coincident background, which has the same  $E_\alpha$ - $E_\gamma$  dependence as the bremsstrahlung emitted in an  $\alpha$  decay, is due to an external bremsstrahlung process, which might occur while the  $\alpha$  particle is slowed down in the  $\alpha$ -detector. These contributions can be estimated to be orders of magnitude smaller in particular when Si-detectors are used to record the  $\alpha$  particles, as here the E1-radiation is strongly reduced due to the similar  $N/Z$ -ratios of natural Si and  $^4\text{He}$ .

### 3.2 $\alpha$ Source

For the present experiment the  $\alpha$ -decaying  $^{210}\text{Po}$  isotope was selected (see figure 3.3). This isotope is especially suited for this experiment as it decays predominantly into the  $0^+$  ground state of the stable daughter nucleus  $^{206}\text{Pb}$ , and only with a weak  $\gamma$ -branch of  $0.00122(4)\%$  in the first excited  $2^+$  state at  $803.1\text{ keV}$  [37]. Thus only few  $\gamma$ -rays are emitted by the source itself. This allows to measure bremsstrahlung photons up to  $800\text{ keV}$  without interference with photons emitted after the  $\alpha$  decay of  $^{210}\text{Po}$ . On the other hand,

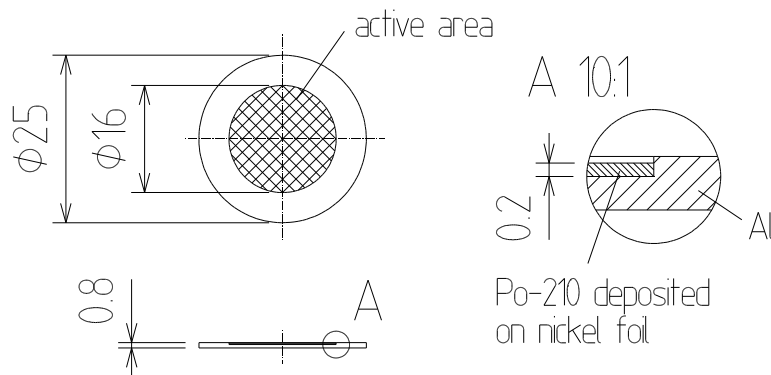


**Figure 3.4:** Dimensions of the  $^{210}\text{Po}$  source obtained from AEA Technology QSA.

the 803 keV branch is very useful for energy and efficiency calibrations (see sections 4.2 and 5.1). Moreover,  $^{210}\text{Po}$  has a half-life of  $T_{1/2} = 138.4$  d, which is convenient for high statistic measurements.

Commercial sources with an open active area are normally limited to an activity of about 100 kBq to limit the sputtering rate; because the binding of the atoms in the material is quite weak, the recoil energy released in the  $\alpha$  decay can break out clusters of source material and thereby contaminate the surrounding.

A high activity is needed to achieve high statics data, but on the other hand the source material must be thin to reduce the energy spread of the  $\alpha$  particles due to energy loss in the source material. Therefore two independent sources<sup>2</sup> of an activity of 100 kBq each were used for the experiment. The sources had an active area of 16 mm diameter and were deposited on a 0.2 mm thick nickel foil with an aluminium backing of 0.5 mm thickness (see figure 3.4). The  $\gamma$ -detector was placed beneath the two sources, so the  $\gamma$ -radiation had to travel through the disk. Therefore the thickness of the nickel foil and the material of the backing was minimised to lower the absorption for the bremsstrahlung photons.

The areal uniformity of the activity within the active area of the source was tested using an autoradiography. The result is shown in Figure 3.5, no spatial variation of the activity could be seen.

### 3.3 Detection of $\alpha$ Particles

Two single-sided silicon strip detectors (SSSD) of type W(SS)-300 from micron semiconductor<sup>3</sup> were used to detect the  $\alpha$  particles. These silicon strip detectors had an active area of  $5\text{ cm} \times 5\text{ cm}$ , a thickness of  $300\text{ }\mu\text{m}$  and the electrode on one side of the detec-

<sup>2</sup>AEA Technology QSA GmbH, Gieselweg 1, D-38110 Braunschweig, Germany

<sup>3</sup>Micron Semiconductor Limited, 1 Royal Buildings, Marlborough Road, Lancing, Sussex BN 15 8UN, UK

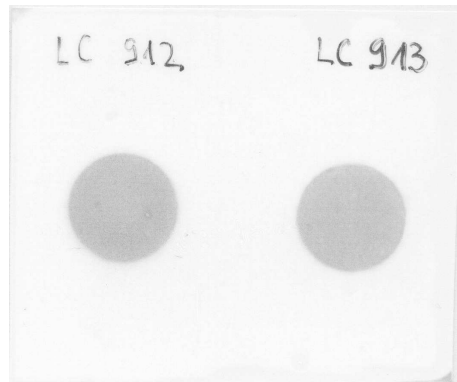


**Figure 3.5:** The uniformity of the  $\alpha$  sources was tested by an autoradiography. No areal spread of the activity could be detected.

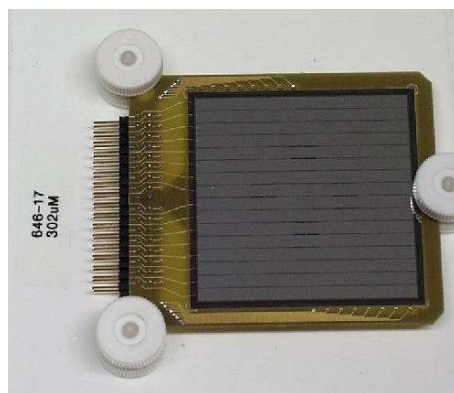


**Figure 3.6:** Picture of the silicon strip detector.

crystal	length	total weight	relative efficiency
A	76.3 mm	1555 g	55%
B	77 mm	1527 g	55%
C	76 mm	1581 g	59.1%

**Table 3.1:** Lengths, total weights and relative efficiencies of the HPGe crystals as given in the specifications by the manufacturer.

tor was segmented into 16 strips (see figure 3.6). Due to the high activity of the sources the segmentation was needed to reduce the rate for the data acquisition and the pile-up probability.

The  $\alpha$  particles were incident on the unsegmented side of the detector to avoid events with incomplete charge collection from  $\alpha$ -hits in the area between the strips. For the same reason events where the  $\alpha$  particle has deposited energy in two neighbouring strips were rejected from the analysis (by this measure  $\approx 2.5\%$  of the events were rejected).

The silicon detectors are mounted on a copper plate cooled to about  $-20^\circ\text{C}$ . By cooling the detectors the energy resolution is improved ( $\sim 28\text{ keV FWHM}$  for  $E_\alpha = 5.304\text{ MeV}$ ) and the damage of the silicon due to the implanted  $\alpha$  particles is reduced.

## 3.4 Detection of Bremsstrahlung

For the detection of the  $\gamma$ -rays a highly efficient, high-purity germanium (HPGe) cluster detector of the MINIBALL type [38] was used. The cluster detector consists out of three encapsulated semi-hexagonal germanium crystals. The outer electrode of each crystal is electronically segmented into six segments. The capsules are housed in a common cryostat and cooled to liquid nitrogen temperature ( $-195.8^\circ\text{C}$ ). A picture of the triple cryostat from CTT<sup>4</sup> is shown in figure 3.7.

The encapsulated HPGe crystals were produced by Canberra Eurisys<sup>5</sup>. Figure 3.8 shows the design of the crystals and the segmentation. The length, weight and relative efficiency [39] of each crystal as given in the specifications by Canberra Eurisys can be found in table 3.1, figure 3.9 shows pictures of one capsule.

The efficiency of the cluster detector can be raised by adding up the energy signals recorded in the three detectors for each event (addback mode). Simulation show that in this way the efficiency of the cluster detector can be raised by about 23% at 800 keV.

The detectors were operated with about +4 kV on the inner contact provided by iseg<sup>6</sup> power supplies. For the cooling of the detectors with liquid nitrogen ( $\text{LN}_2$ ) an automatic

<sup>4</sup>Cryostat and Detector Technique Thomas, Tonnerrestr. 5, D-56410 Montabaur, Germany

<sup>5</sup>CANBERRA Eurisys GmbH, Walter-Flex-Str. 66, D-65428 Rüsselsheim, Germany

<sup>6</sup>iseg Spezialelektronik GmbH, Bautzner Landstr. 23, D-01454 Radeberg, Germany

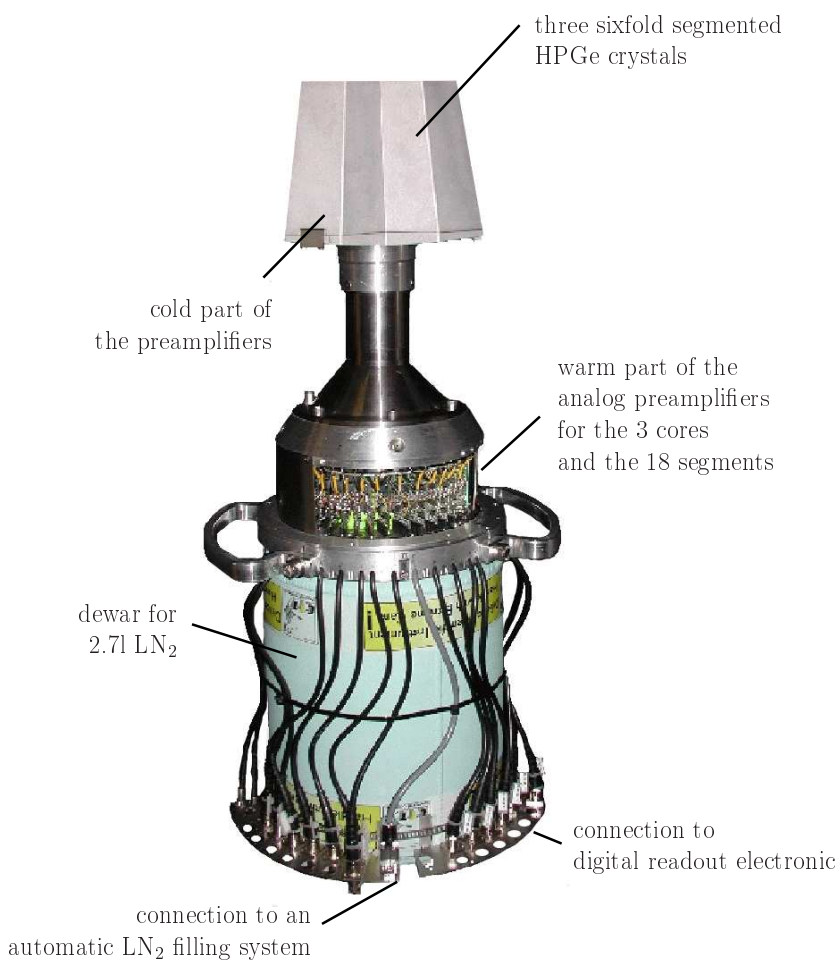


**Figure 3.7:** Picture of the MINIBALL cluster detector.

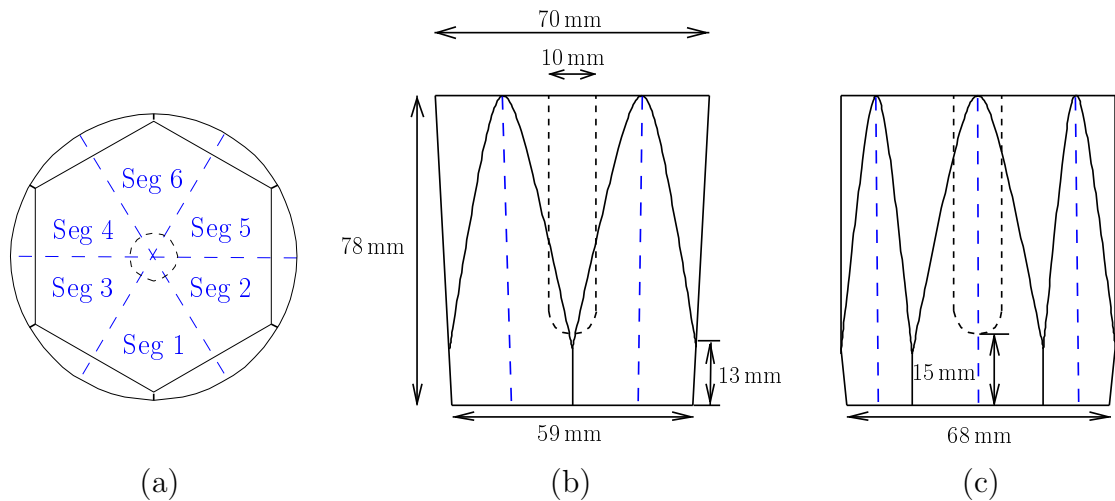


**Figure 3.8:** Segmentation of the outer contact (a) and dimensions (b),(c) of the HPGe crystals.



**Figure 3.9:** Pictures of an encapsulated, sixfold segmented HPGe MINIBALL detector.

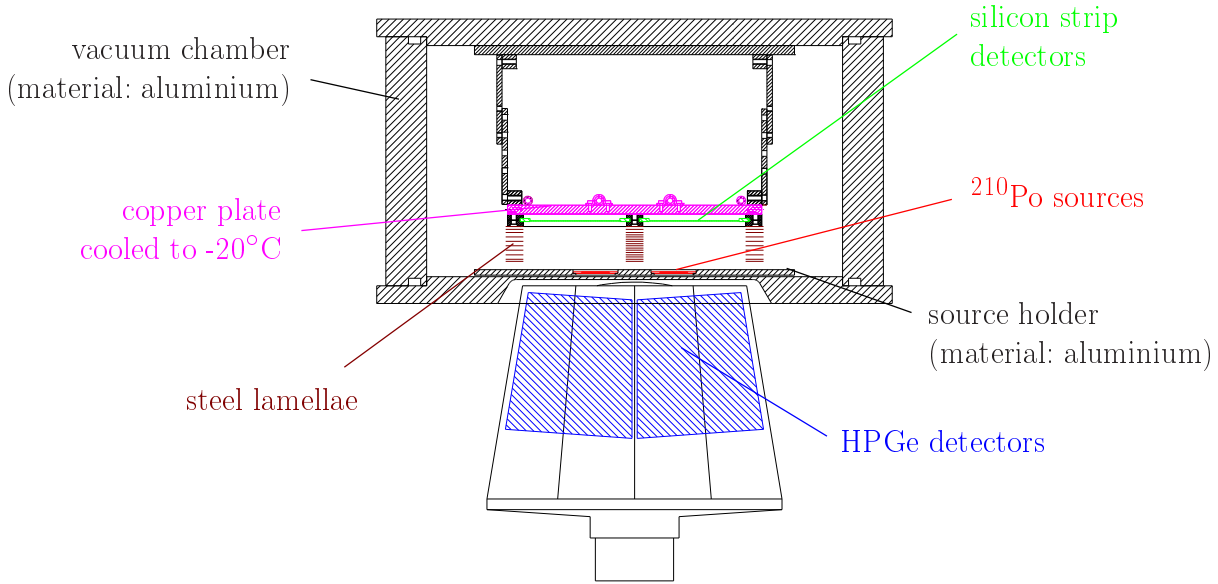


**Figure 3.10:** Schematic drawing of the experimental setup.

filling system with a 160 l LN<sub>2</sub> tank was used (electronics by Ortec<sup>7</sup>). Both the LN<sub>2</sub> filling system and the high voltage were controlled and monitored by a software designed for this experiment and now partly used also for the MINIBALL detector array.

The detector signals were pre-amplified by analog electronics. The first amplification stage was mounted directly on the capsules and was therefore also cooled to LN<sub>2</sub> temperature. The remaining parts of the preamplifiers were integrated in the cluster cryostat (see figure 3.7).

After the preamplifiers the readout was provided by fully digital electronics (see 3.6). The electronic allowed not only to record the deposited energy but also the shapes of the signals of the cores and of all segments as a function of time. By pulse shape analysis (PSA) the position of the main interaction within the crystal could be determined and the time resolution could be improved (see also section 5.3).

### 3.5 Geometry of the Setup

In the design of the setup the efficiency of  $\alpha$ - and  $\gamma$ -detection had to optimised while keeping the count-rates of the silicon detectors in a reasonable range and the energy resolutions as good as possible. Different setups were analysed using a simulation (see also chapter 4). Figure 3.10 shows a schematic drawing of the experimental setup realised.

<sup>7</sup>German contact: AMETEK GmbH, Rudolf-Diesel-Str. 16, D-40670 Meerbusch, Germany

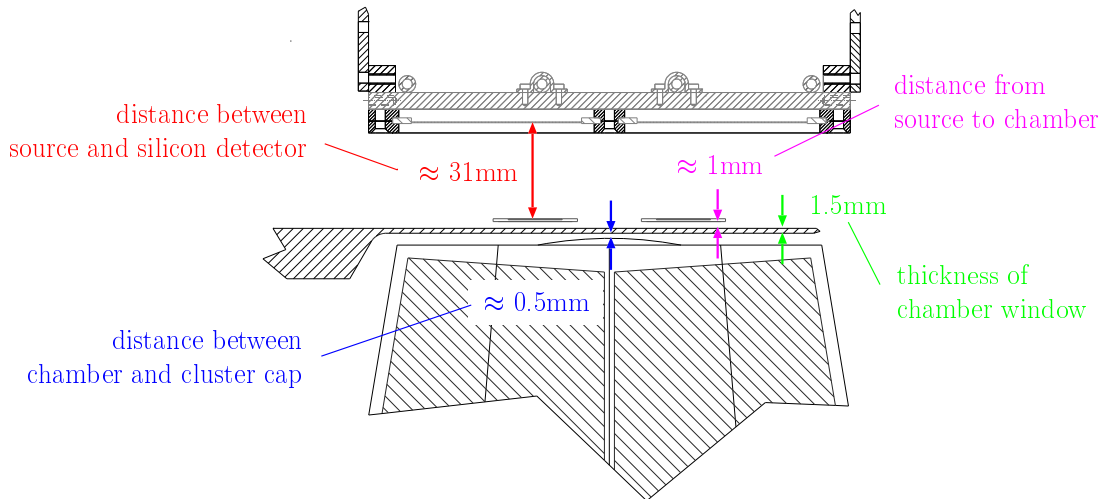


**Figure 3.11:** Distances between the sources, the silicon detectors and the HPGe detector, respectively (the source holder is not shown).

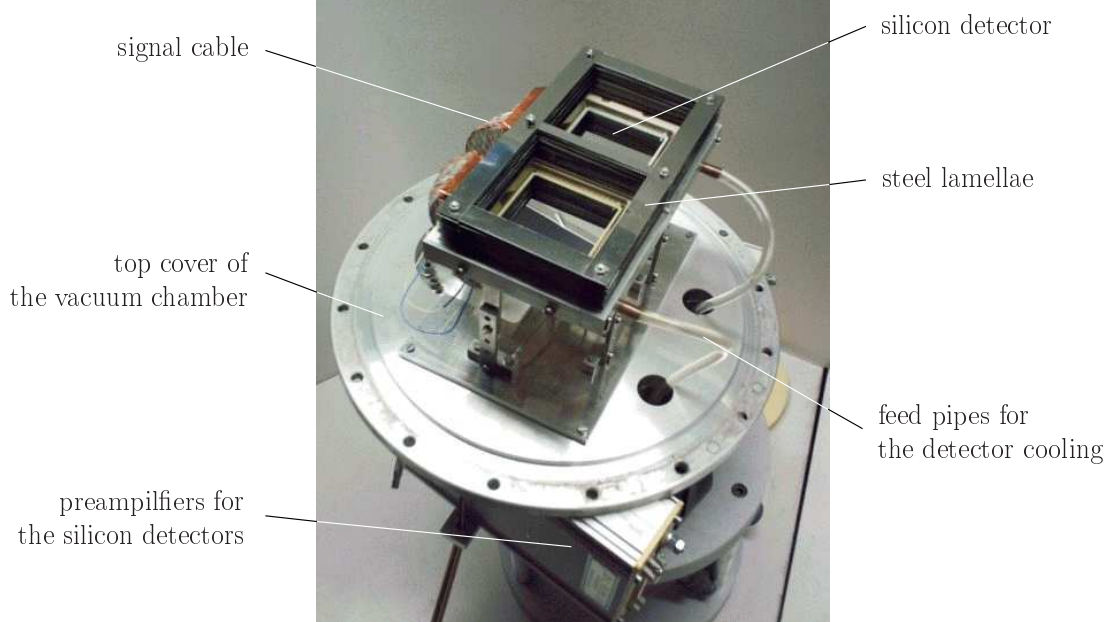


**Figure 3.12:** Picture of the silicon detector mounted on the top cover of the vacuum chamber.

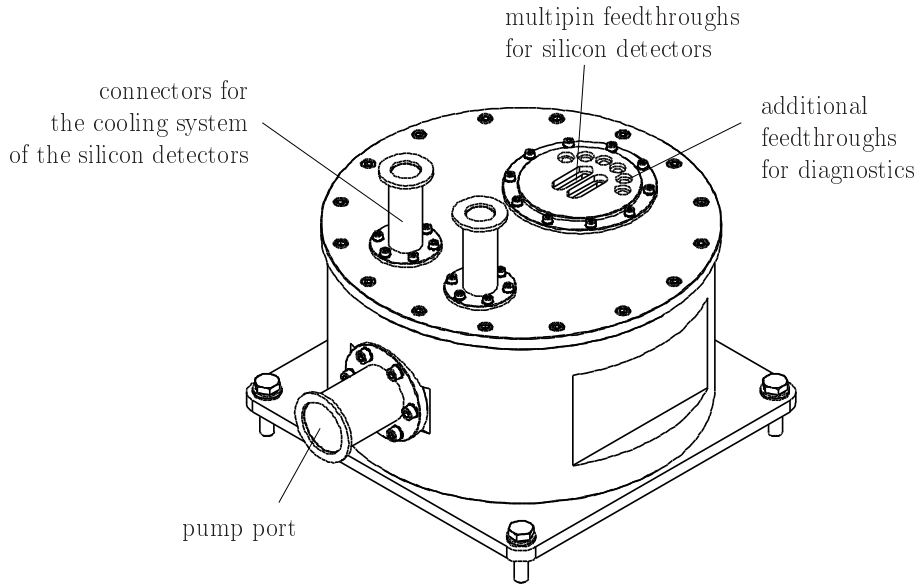


**Figure 3.13:** Schematic drawing of the vacuum chamber with the feedthroughs for the electronics, the pump port and the connectors for the cooling system of the silicon detectors.

The two  $\alpha$  sources were placed directly above the HPGe cluster detector within the vacuum chamber. In this area the thickness of the vacuum chamber was reduced to 1.5 mm to keep the attenuation of  $\gamma$  radiation low. Above each source a silicon detector was placed at a distance of 31 mm. The silicon detectors were mounted on a solid copper plate cooled to  $-20^\circ\text{ C}$ , which was attached to the top cover of the vacuum chamber with a stainless steel stage to reduce the heat flux. The steel lamellae were used to hinder scattered  $\alpha$  particles to be detected and in particular to avoid that  $\alpha$  particles emitted from the left (right) source are seen by the right (left) Si-detector;  $\alpha$  particles emitted and detected under small angles with respect to the surface of the source or detector would suffer large energy losses in the source material or the dead layers of the Si-detector, which would lead to deterioration of the  $\alpha$ -energy resolution.

The distances between the sources, the silicon detectors and the HPGe cluster detector are given in figure 3.11, while figure 3.12 shows a picture of the silicon detectors mounted in the chamber.

The  $\alpha$  sources and the silicon detectors had to be operated in vacuum to ensure that  $\alpha$  particles could reach the detectors. The chamber was pumped to  $5 \cdot 10^{-6}$  mbar with a turbo molecular pump. A schematical drawing of the vacuum chamber is presented in figure 3.13.

The setup was surrounded with a 10 cm thick lead layer to shield the  $\gamma$ -detector from the room background. To shield the X-rays from the lead induced by background  $\gamma$ -rays and by cosmic radiation the HPGe cluster detector was additionally covered with 12 mm of copper [40] as shown in figure 3.14. With this combined shield the rate of background

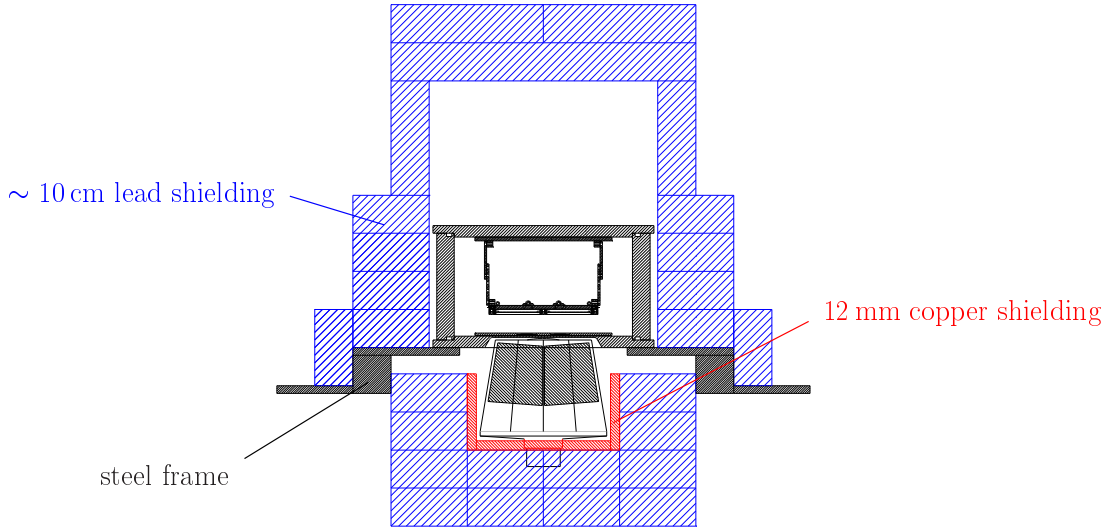


**Figure 3.14:** To reduce ambient  $\gamma$ -background the setup was shielded with 10 cm of lead. The germanium detector was additionally shielded with 12mm of copper to screen X-rays from the lead.

events detected in the cluster detector could be reduced from  $\sim 300$  Hz to about 20 Hz for  $\gamma$ -energies  $\geq 40$  keV.

A more detailed description of the experimental setup can be found in reference [36].

## 3.6 Data Acquisition

To readout the  $2 \times 16$  strips of the silicon detectors analog electronic from mesytec<sup>8</sup> was used. The electronic is split into two components: the MPR-16 preamplifier unit and the STM-16 unit incorporating the main amplifier, timing filter amplifier (TFA), and leading-edge discriminator (LE). Each component contains 16 channels, so two MPR-16 and two STM-16 units were used. The preamplifiers were mounted directly on top of the vacuum chamber to keep the signal cables as short as possible.

The energy signal from the main amplifiers in the STM-16 were digitised using 12 bit, peak-sensing analog-to-digital converters (ADC) of type V556S manufactured by CAEN<sup>9</sup>. The timing signals from the discriminators were read out by 12 bit, multi-event time-to-digital converters (TDC) of type CAEN V775S.

The signals from the cluster detector were pre-amplified by analog preamplifiers included in

<sup>8</sup>mesytec Gbr, Wernher-von-Braun-str. 1, D-85640 Putzbrunn, Germany

<sup>9</sup>CAEN S.p.A. Via Vetraia, 11, 55049, Viareggio (LU), Italy

the cryostat and then read out with digital electronics from XIA<sup>10</sup>. In the XIA DGF-4C<sup>11</sup> module the charge signals from the preamplifiers are first filtered and amplified in analog signal-conditioning units (ASC) and then digitised by 12 bit flash ADCs with a sampling rate of 40 MHz (25 ns per sample). 1024 samples are stored in a FIFO and first analysed with a digital leading edge trigger algorithm to obtain a timing signal. Then the digital pulses are further analysed in an FPGA<sup>12</sup> and a DSP<sup>13</sup>, which allow to perform also user defined pulse shape analysis algorithms in real-time [41, 42]. The low counting rate from the  $\gamma$ -detector in the present experiment allowed us to store not only the energy and timing signals but also the full pulse traces. This allowed to analyse the shape of the pulses offline as described in section 5.3.

The XIA DGF-4C modules contain four channels each and can be connected via a PECL<sup>14</sup> bus to synchronise the readout of two or more modules. The seven channels needed for the readout of one segmented HPGe detector (one channel for the core and six for the segments) are provided by two DGF-4C modules; to readout the cluster detector six modules were used.

The trigger output of DGF-4C modules is delayed by about 600 ns and can therefore not be used for a coincidence trigger with the fast trigger signal from the silicon detectors. Therefore an analog trigger signal from each core was generated in addition using timing filter amplifiers and constant fraction discriminators (CFD). These timing signals were recorded in the same TDCs as used for the silicon detectors.

The fast timing signals from the  $\alpha$ - and  $\gamma$ -detectors were used to select coincident  $\alpha$ - $\gamma$ -events using a standard trigger-electronic. Moreover,  $\gamma$ -singles and down-scaled  $\alpha$ -singles were recorded.

The cbdaq data acquisition software [43] has been used with an implementation for the XIA DGF-4C card [41]. For details see also [36].

---

<sup>10</sup>XIA LLC, 31057 Genstar Rd., Hayward CA 94544, USA

<sup>11</sup>Digital Gamma Finder

<sup>12</sup>Field Programmable Gate Array

<sup>13</sup>Digital Signal Processor

<sup>14</sup>Positive Emitter Collector Logic

# Chapter 4

## Simulation of the $\alpha$ - $\gamma$ -Detection Efficiency

To derive the total energy-differential bremsstrahlung emission probability accompanying the  $\alpha$  decay of  $^{210}\text{Po}$  from the measured data the efficiency of the setup for detecting a bremsstrahlung photon in the  $\gamma$ -detector in coincidence with an  $\alpha$  particle,  $\varepsilon_{\gamma}^c(E_{\gamma})$ , has to be known. This efficiency depends not only on the energy  $E_{\gamma}$  of the photon, but also on the  $\alpha$ - $\gamma$ -angular correlation, which cannot easily be taken into account analytically due to the compactness of the experimental setup. Therefore the whole setup was implemented in a Monte-Carlo simulation to study the influence of the angular correlation on the efficiency in more detail and to determine the efficiency  $\varepsilon_{\gamma}^c(E_{\gamma})$  over the relevant  $\gamma$ -energy range.

### 4.1 The Simulation package

The simulation program used is basically based on two simulation packages:

**GEANT4:** GEANT4 (GEometry ANd Tracking) is an object-oriented simulation toolkit for high energy physics [44]. It simulates the passage of particles through matter including tracking, geometry, physics models and hits. GEANT4 is implemented in the C++ programming language and was designed by a worldwide collaboration of physicists and software engineers. It has been used in applications in particle physics, nuclear physics, accelerator design, space engineering and medical physics.

**g4miniball:** The g4miniball simulation package [45] developed as part of this dissertation provides a library for the simulation of one or more MINIBALL cluster detectors within an GEANT4 environment. Figure 4.1 shows the visualisation of a simulated MINIBALL cluster detector (cut open).

The simulation provides a detailed implementation of the geometry of the HPGe

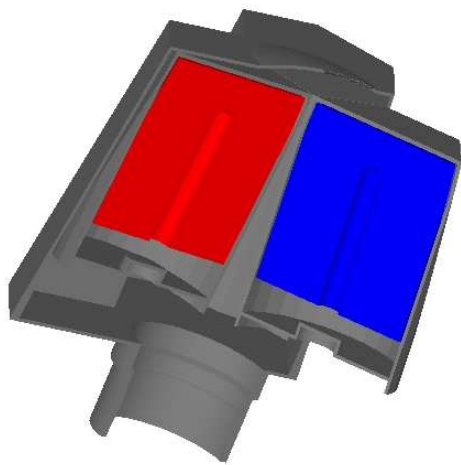


**Figure 4.1:** Visualisation of the simulated MINIBALL cluster detector with the g4miniball package. For the visualisation the cryostat and the detectors are cut open.

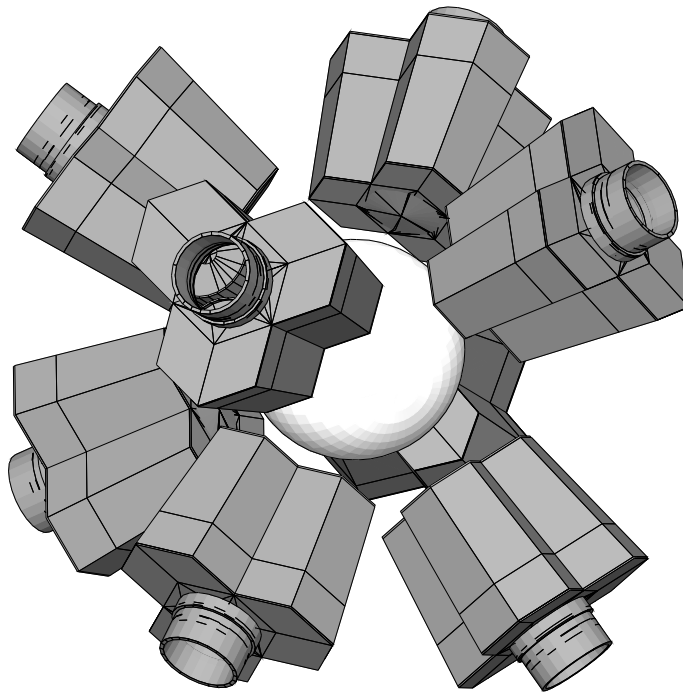


**Figure 4.2:** Visualisation of a standard setup of MINIBALL consisting of eight MINIBALL cluster detectors together with a vacuum chamber in the simulation.

crystals, the capsules of the crystals and the cryostat wall. The electronics and the LN<sub>2</sub> dewar are not included.

The `g4miniball` library was originally developed for simulating only one MINIBALL cluster detector for the experiment described here. However, it was designed such that it is an easy to use toolkit for the simulation of all possible setups of the MINIBALL detector array. The library contains class-objects to include the detailed geometry of the crystals and cluster detectors, for the determination of the deposited energy in an event and a flexible interface for the readout, which allows e.g. to further process the data using the ROOT analysis software [46]. An event generator for calibration sources (<sup>60</sup>Co and <sup>152</sup>Eu) is also provided.

There are also examples included in the `g4miniball` package to illustrate the handling and the implemented features. Figure 4.2 shows a standard setup of MINIBALL with eight MINIBALL cluster detectors and an aluminum detector chamber.

A visualisation of the simulated experimental setup of the present experiment is show in figure 4.3 and 4.4.

Included into the simulation are the MINIBALL cluster detector, the two silicon strip detectors, the two  $\alpha$  sources with backing and source holder, the detector support for the silicon detector, the vacuum chamber, the steel lamellae, the copper shielding of the MINIBALL cluster detector and the lead shielding of the experiment.

## 4.2 Efficiency Calibration

Although the geometry of the setup and its components has been included into the simulation as careful as possible, there remain some uncertainties concerning the full-energy peak efficiency of the MINIBALL cluster detector. These are caused by (partly unknown) tolerances of the crystal sizes, the thickness of the dead-layers, the composition of the material of the detector capsules (kept secret by the manufacturer of the detector), the charge collection efficiency, simplification of the simulated geometry, etc. Several auxiliary measurements were therefore performed in addition to the calibration points supplied by the <sup>210</sup>Po source itself to check the results obtained from the simulation of the MINIBALL detector: some of the input measures were slightly adjusted to properly reproduce the result of these calibration measurements.

These adjustments are compiled in table 4.1. The relative efficiency (with respect to a standard NaI detector [39]) is a measure of the active volume of the Ge-crystal. The dimensions of the simulated crystal (taken to be the design values) were scaled with an appropriate factor to end up with an crystal of the matching relative efficiency. The required adjustments of the thicknesses of the dead-layers and Al capsules act as a compensation for effects not included in the simulation (e.g. regions of incomplete charge collection, unknown materials, . . . ), for insufficiencies of the simulated setup and of the simulation itself.

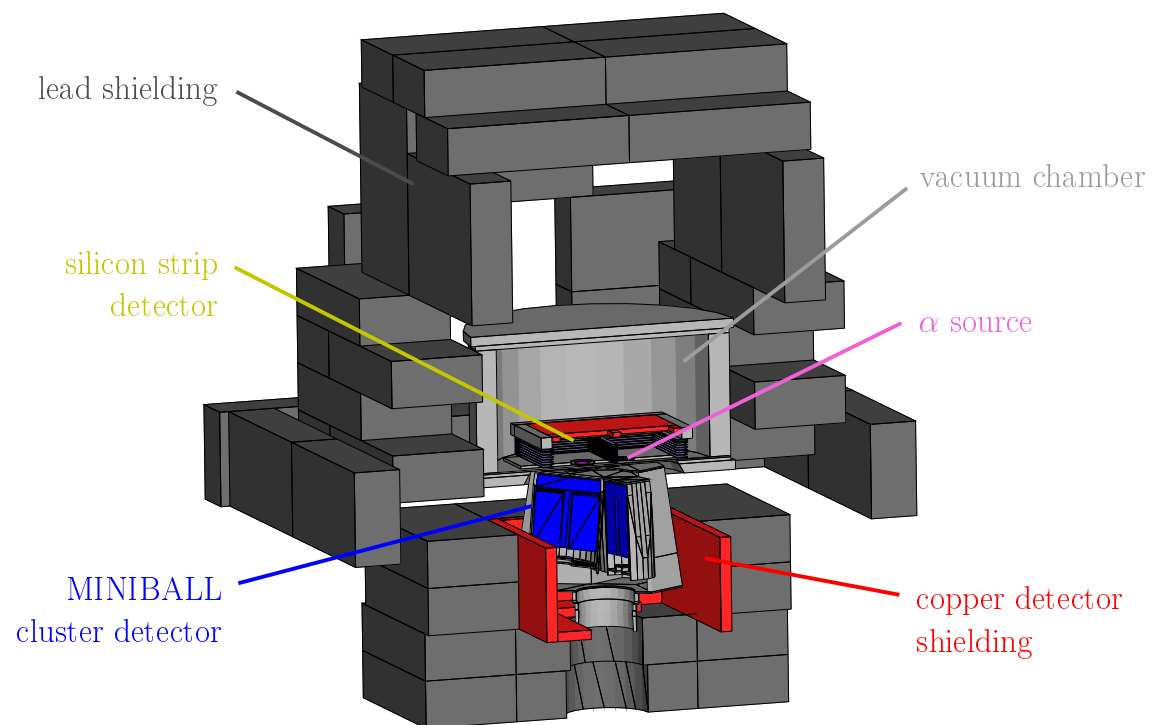


**Figure 4.3:** Visualisation of the simulated experimental setup cut open.

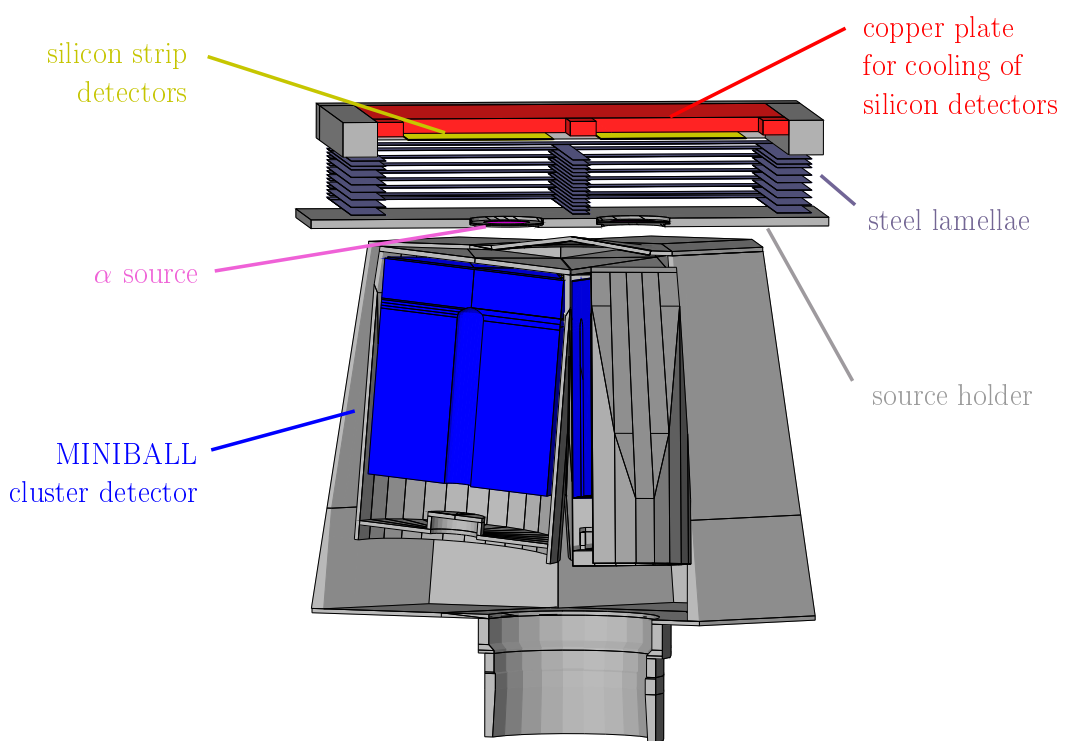


**Figure 4.4:** A more detailed visualisation of the simulated experimental setup (the lead shielding, the copper shielding for the MINIBALL cluster detector and the vacuum chamber are not visualised)

value	datasheet	simulation
relative efficiency module A	55.0%	58.3%
relative efficiency module B	55.0%	56.5%
relative efficiency module C	59.1%	60.7%
dead-layer module A	5 $\mu\text{m}$	0.4 mm
dead-layer module B	5 $\mu\text{m}$	0.3 mm
dead-layer module C	5 $\mu\text{m}$	0.6 mm
capsule thickness (side)	0.7 mm	1.6 mm
capsule thickness (front)	1 mm	1.8 mm

**Table 4.1:** The relative efficiencies of the crystals, the thicknesses of the dead-layers and the capsules have been adapted in the simulation to give a good agreement with the measurements of the reference sources. To achieve a suitable relative efficiency the dimensions of the simulated crystal were scaled with an appropriate factor. The required adjustments of the thicknesses of the dead-layers and the capsules function as a compensation for effects not included in the simulation and for insufficiencies of the simulated setup.

	$N_{803}$ [counts]	error	$\varepsilon_{803}^c$ data	error	$\varepsilon_{803}^c$ simulation
addback	425394	688	8.09 %	$\pm 0.26 \%$	8.08 %
module A	87101	300	1.66 %	$\pm 0.05 \%$	1.64 %
module B	129631	393	2.46 %	$\pm 0.08 \%$	2.49 %
module C	126962	361	2.41 %	$\pm 0.08 \%$	2.43 %

$$N_\alpha = 4.311(2) \cdot 10^{11}, f_{803} = 1.22(4) \cdot 10^{-5}$$

**Table 4.2:** The measured coincident full-energy peak efficiencies for the 803 keV  $\gamma$ -ray following the  $\alpha$  decay of  $^{210}\text{Po}$  to the first excited  $2^+$  state of  $^{206}\text{Pb}$  are compared to the results of the simulation. ( $N_\alpha$  is the number of  $\alpha$  particles detected,  $f_{803}$  is the  $\alpha$ -branching ratio to  $^{206}\text{Pb}(2^+)$ , see figure 3.3)

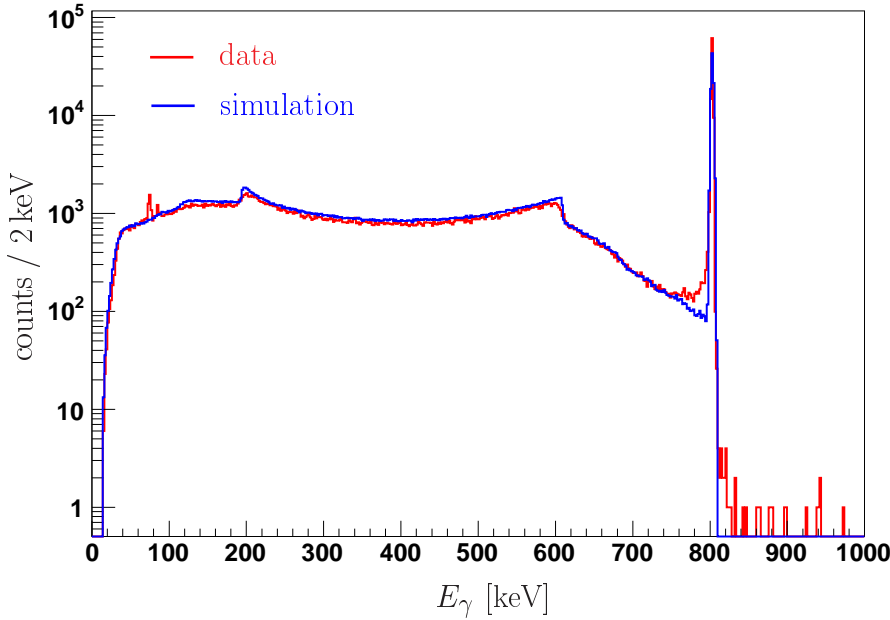


**Figure 4.5:** The spectrum of the coincident 803 keV  $\gamma$ -branch (module B) with its Compton background ( $4.3 \text{ MeV} < E_\alpha < 4.6 \text{ MeV}$ ) from the data is compared with the simulation (scaled according to the full-energy peak area). The lead X-rays are not included in the simulation, therefore the peaks are not present in the simulated spectrum. The electronic cutoff at  $\gamma$  energies  $\leq 40 \text{ keV}$  is artificially added into the simulation.

As mentioned already in section 3.2, the 803 keV  $\gamma$ -branch of the  $^{210}\text{Po}$  source is a very convenient "build-in" calibration source. The coincident detection efficiency for the 803 keV  $\gamma$ -ray is deduced from the data using the relation (discussed in more detail in chapter 5)

$$\varepsilon_{803}^c = \frac{N_{803}}{f_{803} \cdot N_\alpha} \quad (4.1)$$

with the number of coincident detected (full-energy) photons from the 803 keV  $\gamma$ -branch  $N_{803}$ , the branching ratio  $f_{803}$  and the number of detected  $\alpha$  particles  $N_\alpha$  (see section 5.5). The measured coincident detection efficiency for the setup used in the bremsstrahlung measurement at 803 keV is presented in table 4.2 and compared to the result of the simulation. The error of the measured efficiency is dominated by the uncertainty of the branching ratio  $f_{803}$ . In the simulation the E2 angular correlation between the direction of the  $\alpha$  particle and the 803 keV  $\gamma$ -ray was taken into account. The efficiencies are measured and simulated for observing the full-energy of the 803 keV  $\gamma$ -ray a) in one of the three individual modules of the MINIBALL detector or b) in the addback mode, where the energy signals of the individual modules are added up. Note that the gain in the full-energy peak efficiency when using the addback mode amounts to 23%.

Figure 4.5 shows the spectrum of the coincident 803 keV  $\gamma$ -branch with its Compton back-

---

type	energy	intensity $I_\mu$
$K_{\alpha 1}$	74.969 keV	0.462(9)
$K_{\alpha 2}$	72.805 keV	0.277(6)
$K_{\alpha 3}$	72.144 keV	0.00043(1)
$K_{\beta 1}$	84.938 keV	0.107(2)
$K_{\beta 2}$	87.300 keV	0.0391(8)
$K_{\beta 3}$	84.450 keV	0.056(1)
$K_{\beta 4}$	87.580 keV	0.0009(4)
$K_{\beta 5}$	85.470 keV	0.0031(1)

**Table 4.3:** *X-ray energies and intensities (per 1 K-shell vacancies) for lead (Pb) [37]*

ground (module B,  $4.3 \text{ MeV} < E_\alpha < 4.6 \text{ MeV}$ ) from the data (red) and from the simulation (blue) in comparison. Both spectra are scaled according to the full-energy peak area. The main features of the spectrum are very well reproduced (the background from the lead X-rays is not present in the spectrum of the simulation because they are not included in the simulation). The electronic cutoff at  $\gamma$  energies  $\leq 40 \text{ keV}$  is artificially added into the simulation.

A  $^{60}\text{Co}$  and a  $^{152}\text{Eu}$  calibration source was used to check the simulated efficiencies over a wide energy range. Both sources were placed in nearly the same position as one of the  $^{210}\text{Po}$  sources, close to crystal B of the HPGe cluster detector.

Because of the close distance of the  $\gamma$  source to the cluster detector summing effects had to be taken into account. To do so the calibration sources are simulated in case of  $^{60}\text{Co}$  including to well known  $\gamma$ - $\gamma$  angular correlation. In case of  $^{152}\text{Eu}$ , as the decay scheme is quite complicated, only approximations for the  $\gamma$ - $\gamma$  angular correlation were used. The results from the simulations were then used to correct for summing effects in the data.

The relative efficiencies are directly taken from the intensities of the lines compared with the intensities given in the literature [37].

The absolute full-energy  $\gamma$ -detection efficiencies are deduced from the data by looking at coincident decays recorded in two different crystals. Requiring one  $\gamma$ -ray from a  $\gamma$ -cascade to be detected in say module A, the measured probability that the second cascade  $\gamma$ -ray with energy  $E_{\gamma_2}$  is observed in module B or C can be used to extract the absolute  $\gamma$ -detection efficiencies of module B and C for  $\gamma$ -rays of energy  $E_{\gamma_2} \dots$  etc.

In figure 4.6 the measured efficiencies from the  $^{60}\text{Co}$  source are compared with the simulated isotropic photon detection efficiency. The same is presented in figure 4.7 for the  $^{152}\text{Eu}$  source.

Below  $\approx 200 \text{ keV}$  the  $\gamma$  efficiencies are getting very sensitive to the precise description of the inactive materials between source and active volume of the  $\gamma$ -detector. To check the quality of the simulation at these low  $\gamma$ -energies we used the X-rays emitted by the daughter atom  $^{206}\text{Pb}$  after the  $\alpha$  decay. With a small probability an electron may be ejected by the  $\alpha$

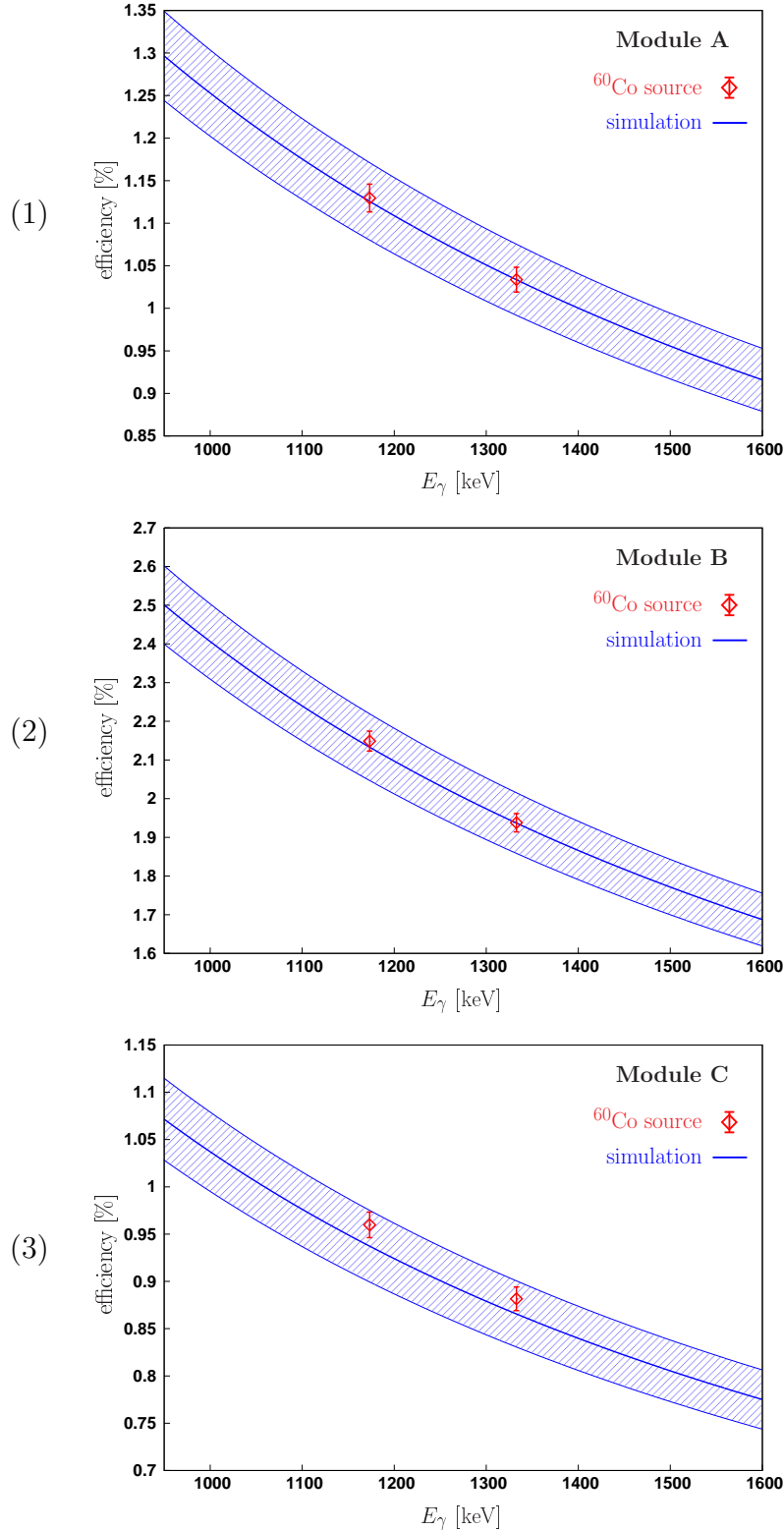


**Figure 4.6:** The measured full-peak energy efficiencies from the  $^{60}\text{Co}$  reference source located near module B for module A (1), module B (2) and module C (3) are compared to the simulated isotropic photon detection efficiency (summing effects have been corrected). The shown error band reflects the accuracy of the simulated efficiency (see section 4.4).

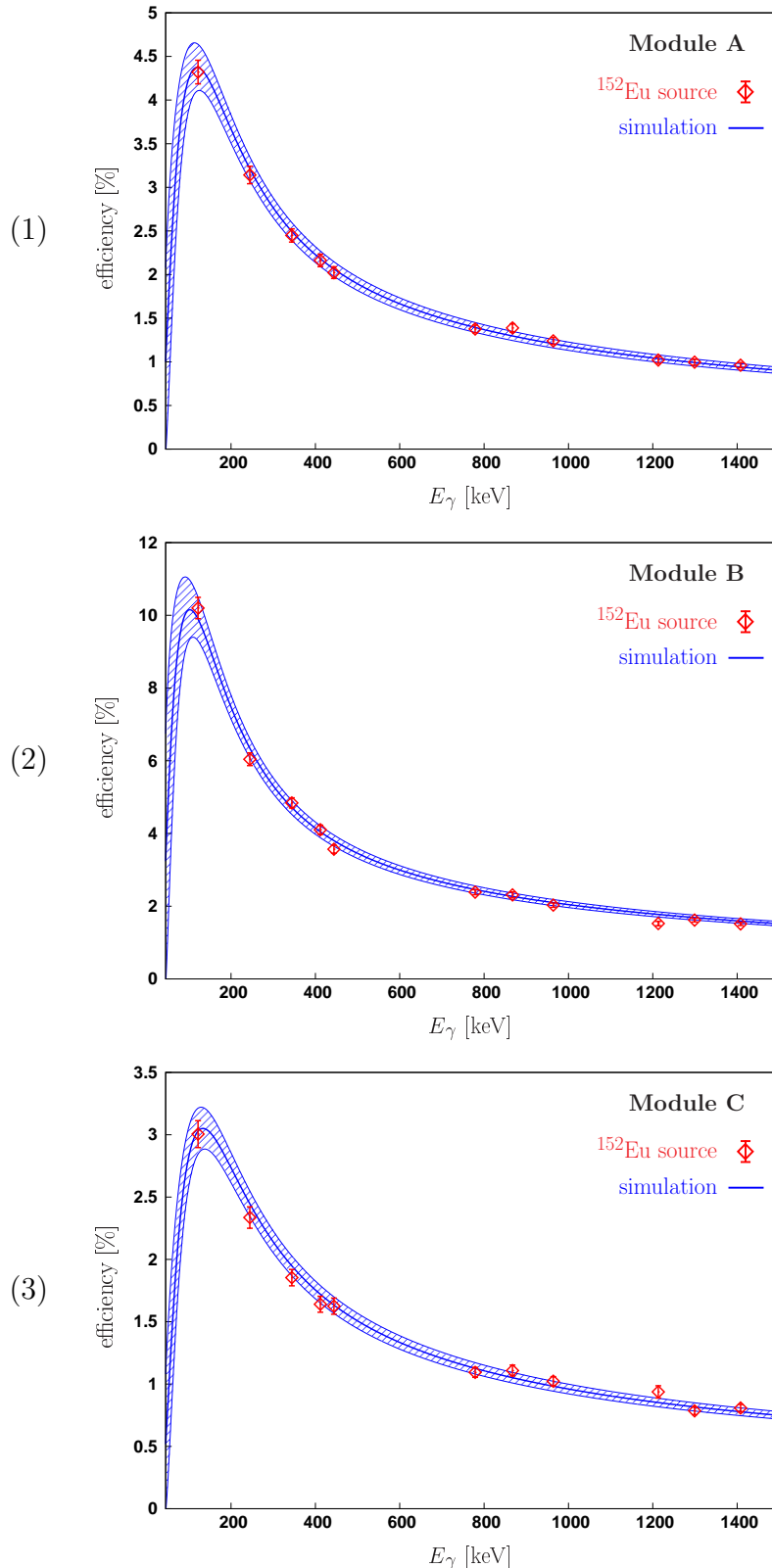


**Figure 4.7:** The measured full-energy peak efficiencies from the  $^{152}\text{Eu}$  reference source located near module B for module A (1), module B (2) and module C (3) are compared with the simulated isotropic photon detection efficiency (summing effects have been corrected). The shown error band reflects the accuracy of the simulated efficiency (see section 4.4).

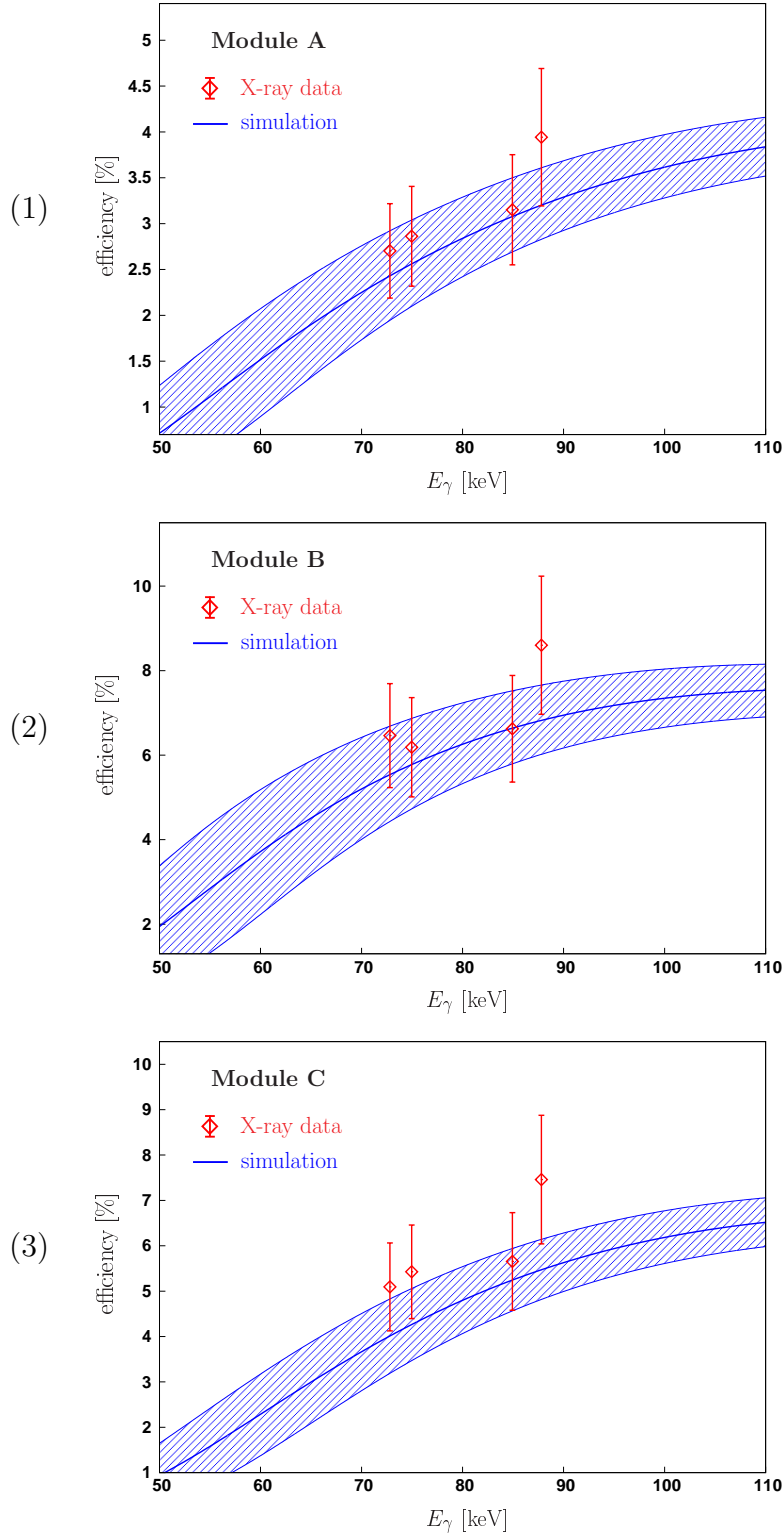


**Figure 4.8:** With a small probability X-ray radiation from the source is produced by an inner shell electron knockout reaction during the  $\alpha$  decay. The detection efficiencies of X-rays measured in coincidence with the  $\alpha$  particle in module A (1), module B (2) and module C (3) are compared with the simulated coincident isotropic efficiency. The error band reflects the accuracy of the simulation (see section 4.4).

particle from an inner shell of the atom. The resulting gap is filled by an electron from an upper shell producing the characteristic X-ray radiation of the daughter nucleus. In table 4.3 the X-ray energies and relative intensities  $I_\mu$  in the daughter nucleus  $^{206}\text{Pb}$  are listed [37]. In this knockout reaction the energy of the  $\alpha$  particle is reduced by the electron binding energy and the kinetic energy of the ejected electron. By a coincident measurement of the X-ray photons and the  $\alpha$  particles these photons can be easily distinguished from the X-ray radiation caused by background reactions with the lead shielding of the setup.

To measure the coincident detection efficiency the number of coincidentally detected X-rays  $N_{\text{X-ray}}$  is compared to the number of produced X-rays in the  $\alpha$  decay. The K-electron emission probability  $P_K$  per  $\alpha$  decay of  $^{210}\text{Po}$  has been measured [47] and also been calculated [48, 49]. Here the value  $P_K = 2.6(5) \cdot 10^{-6}$  determined in [47] in a  $\alpha$ - $\gamma$  coincidence measurement is used. Then the coincident detection efficiency is given by

$$\varepsilon_{\text{X-ray}}^c = \frac{N_{\text{X-ray}}}{P_K \cdot I_\mu \cdot N_\alpha} \quad (4.2)$$

where  $N_\alpha = 4.311(2) \cdot 10^{11}$  is the total number of detected  $\alpha$  particles (section 5.5).

In figure 4.8 the measured coincident detection efficiencies for X-ray radiation following the  $\alpha$  decay of  $^{210}\text{Po}$  is compared with the simulation assuming an isotropic angular distribution of the photons. Within the systematic uncertainty given by the error of  $P_K$  the agreement between the data and simulation is satisfactory.

### 4.3 The $\alpha$ - $\gamma$ Coincident Photon Detection Efficiency

In order to determine the energy-differential bremsstrahlung emission probability  $dP(E_\gamma)/dE_\gamma$  from the measured number of  $\alpha$ - $\gamma$  coincidences  $dN_{br}^c(E_\gamma)/dE_\gamma$ , the efficiency  $\varepsilon_\gamma^c(E_\gamma)$  of the set-up for detecting a bremsstrahlung photon of energy  $E_\gamma$  in coincidence with an  $\alpha$  particle has to be known. In fact, with  $N_\alpha$  being the total number of  $\alpha$  particles detected in the Si-detectors we obtain  $dP(E_\gamma)/dE_\gamma$  from

$$\frac{dP(E_\gamma)}{dE_\gamma} = \frac{1}{\varepsilon_\gamma^c(E_\gamma) \cdot N_\alpha} \cdot \frac{dN_{br}^c(E_\gamma)}{dE_\gamma}. \quad (4.3)$$

The coincident photon detection efficiency  $\varepsilon_\gamma^c(E_\gamma)$  will depend on the  $\alpha$ - $\gamma$  angular distribution  $f_{\not\propto}(E_\gamma, \vartheta)$  as the acceptance of the setup is limiting  $\vartheta$  to  $\sim 60^\circ < \vartheta \leq 180^\circ$ .

In the following we want to illustrate the effect of the angular correlation  $f_{\not\propto}$  on the coincident photon detection efficiency. As an example the acceptance of the setup for a photon energy of 100 keV and 500 keV is compared with an isotropic, a pure E1 dipole and a pure E2 quadrupole distribution in figure 4.9, i.e.

$f_{\not\propto}(E_\gamma, \vartheta) = \text{const.}$	isotropic
$f_{\not\propto}(E_\gamma, \vartheta) = \sin^2 \vartheta$	pure E1 dipole
$f_{\not\propto}(E_\gamma, \vartheta) = \sin^2 \vartheta \cdot \cos^2 \vartheta$	pure E2 quadrupole

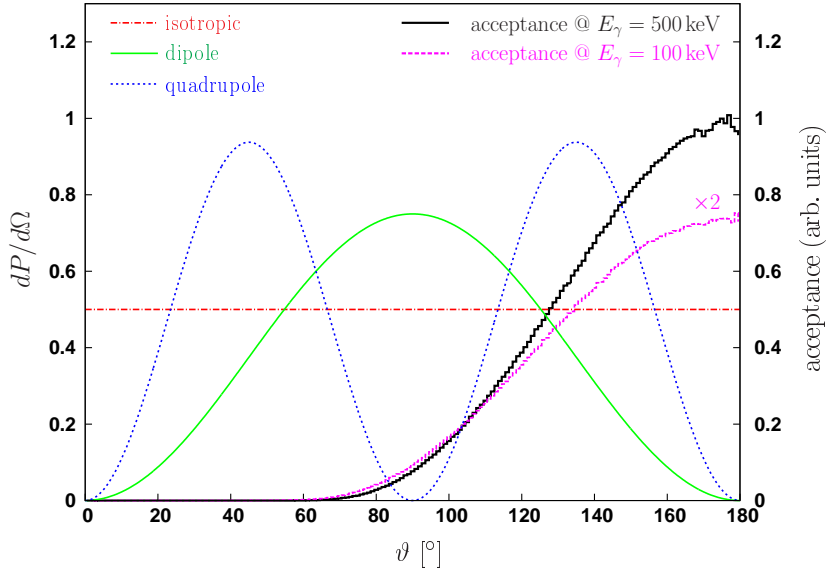


**Figure 4.9:** The simulated acceptance of the setup at  $E_\gamma = 100$  keV and 500 keV is compared with an isotropic (red), a pure E1 dipole (green) and a pure E2 quadrupole correlation (blue).

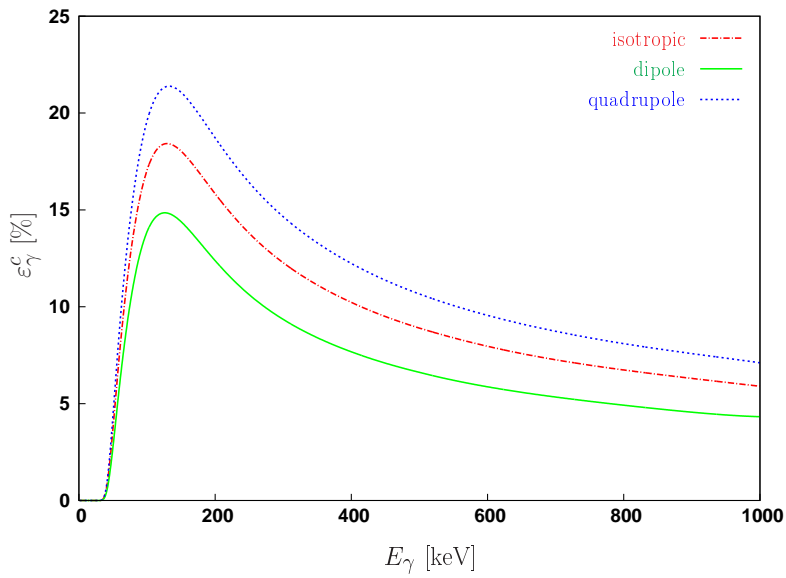


**Figure 4.10:** The simulated coincident photon detection efficiency  $\varepsilon_\gamma^c$  of the setup (addback mode) is shown for an isotropic (red), for a pure E1 dipole (green) and a pure E2 quadrupole correlation (blue).

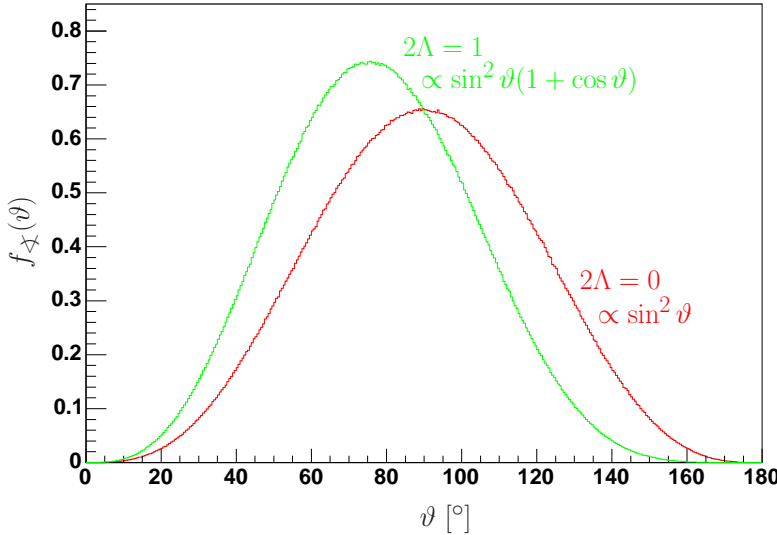


**Figure 4.11:** The angular distribution generated in the event generation of the GEANT4 simulation for  $2\Lambda = 0$  (red) and  $2\Lambda = 2$  (green) are plotted versus the angle  $\vartheta$  between the direction of motion of the generated  $\alpha$ -particle and the propagation direction of the generated bremsstrahlung photon.

The resulting coincident photon detection efficiencies of the setup are shown in figure 4.10. As mentioned in section 2.5 for the bremsstrahlung emission during the  $\alpha$  decay of  $^{210}\text{Po}$  the interference between the electric dipole and quadrupole distribution as well as the relativistic correction has to be taken into account.

Considering only first order correction terms, the angular correlation is given by (see equation (2.13))

$$f_{\chi}(E_{\gamma}, \vartheta) = \sin^2 \vartheta (1 + 2\Lambda(E_{\gamma}) \cos \vartheta). \quad (4.4)$$

Theoretically we so far only know  $\Lambda(E_{\gamma})$  in the limit  $E_{\gamma} \rightarrow 0$ , while for  $E_{\gamma} > 0$  we only have the prediction of the semi-classical model of Jentschura-Milstein-Terekhov [21], which does include the quadrupole interference but not the relativistic correction.

In order to enable calculation of the coincidence efficiency  $\varepsilon_{\gamma}^c(E_{\gamma})$  for any value of  $\Lambda(E_{\gamma})$  we rewrite equation (4.4) in the form

$$f_{\chi}(\vartheta) = \sin^2 \vartheta (1 + 2\Lambda \cos \vartheta) \quad (4.5)$$

$$= \sin^2 \vartheta + 2\Lambda \sin^2 \vartheta \cos \vartheta \quad (4.6)$$

$$= \sin^2 \vartheta + 2\Lambda \sin^2 \vartheta \cos \vartheta + 2\Lambda \sin^2 \vartheta - 2\Lambda \sin^2 \vartheta \quad (4.7)$$

$$= (1 - 2\Lambda) \cdot \sin^2 \vartheta + 2\Lambda \cdot \sin^2 \vartheta (1 + \cos \vartheta). \quad (4.8)$$

$E_\gamma$ range [keV]	$\varepsilon_{\gamma,2\Lambda=0}^c$ [%]	$\varepsilon_{\gamma,2\Lambda=1}^c$ [%]	rel. err.	$E_\gamma$ range [keV]	$\varepsilon_{\gamma,2\Lambda=0}^c$ [%]	$\varepsilon_{\gamma,2\Lambda=1}^c$ [%]	rel. err.
50 ... 60	4.15	2.19	7.0%	430 ... 440	7.22	3.63	4.0%
60 ... 70	7.35	4.03	5.6%	440 ... 450	7.11	3.59	4.0%
70 ... 80	10.1	5.57	5.0%	450 ... 460	7.02	3.51	4.0%
80 ... 90	12.0	6.76	4.7%	460 ... 470	6.95	3.50	4.0%
90 ... 100	13.3	7.44	4.5%	470 ... 480	6.78	3.44	4.0%
100 ... 110	14.1	7.90	4.3%	480 ... 490	6.72	3.37	4.0%
110 ... 120	14.6	8.13	4.2%	490 ... 500	6.61	3.28	4.0%
120 ... 130	14.8	8.14	4.2%	500 ... 510	6.52	3.26	4.0%
130 ... 140	14.8	8.11	4.1%	510 ... 520	6.50	3.21	4.0%
140 ... 150	14.5	7.89	4.1%	520 ... 530	6.39	3.16	4.0%
150 ... 160	14.1	7.58	4.1%	530 ... 540	6.29	3.14	4.0%
160 ... 170	13.7	7.33	4.1%	540 ... 550	6.30	3.12	4.0%
170 ... 180	13.3	7.08	4.1%	550 ... 560	6.10	3.08	4.0%
180 ... 190	12.9	6.90	4.1%	560 ... 570	6.11	3.00	4.0%
190 ... 200	12.6	6.63	4.1%	570 ... 580	6.05	2.98	4.0%
200 ... 210	12.1	6.40	4.0%	580 ... 590	6.02	2.93	4.0%
210 ... 220	11.8	6.20	4.0%	590 ... 600	5.92	2.91	4.0%
220 ... 230	11.5	5.98	4.0%	600 ... 610	5.87	2.89	4.0%
230 ... 240	11.2	5.82	4.0%	610 ... 620	5.77	2.87	4.0%
240 ... 250	10.9	5.57	4.0%	620 ... 630	5.76	2.87	4.0%
250 ... 260	10.5	5.43	4.0%	630 ... 640	5.64	2.85	4.0%
260 ... 270	10.2	5.33	4.0%	640 ... 650	5.59	2.81	4.0%
270 ... 280	9.96	5.06	4.0%	650 ... 660	5.51	2.69	4.0%
280 ... 290	9.75	5.03	4.0%	660 ... 670	5.55	2.73	4.0%
290 ... 300	9.53	4.87	4.0%	670 ... 680	5.44	2.71	4.0%
300 ... 310	9.28	4.75	4.0%	680 ... 690	5.37	2.67	4.0%
310 ... 320	9.11	4.61	4.0%	690 ... 700	5.37	2.67	4.0%
320 ... 330	8.78	4.49	4.0%	700 ... 710	5.30	2.58	4.0%
330 ... 340	8.75	4.42	4.0%	710 ... 720	5.34	2.65	4.0%
340 ... 350	8.53	4.28	4.0%	720 ... 730	5.19	2.56	4.0%
350 ... 360	8.37	4.24	4.0%	730 ... 740	5.13	2.55	4.0%
360 ... 370	8.17	4.18	4.0%	740 ... 750	5.17	2.51	4.0%
370 ... 380	8.07	4.06	4.0%	750 ... 760	5.14	2.47	4.0%
380 ... 390	7.86	3.98	4.0%	760 ... 770	5.08	2.46	4.0%
390 ... 400	7.69	3.86	4.0%	770 ... 780	5.01	2.47	4.0%
400 ... 410	7.60	3.83	4.0%	780 ... 790	4.98	2.42	4.0%
410 ... 420	7.42	3.71	4.0%	790 ... 800	4.92	2.42	4.0%
420 ... 430	7.28	3.66	4.0%				

**Table 4.4:** The simulated coincident photon detection efficiencies  $\varepsilon_{\gamma,2\Lambda=0}^c$  for the  $\alpha$ - $\gamma$  angular correlation  $f_{2\Lambda=0} = \sin^2 \vartheta$  and  $\varepsilon_{\gamma,2\Lambda=1}^c$  for  $f_{2\Lambda=1} = \sin^2 \vartheta(1 + \cos \vartheta)$  are listed for 10 keV energy bins up to a  $\gamma$ -energy of 800 keV (addback mode).

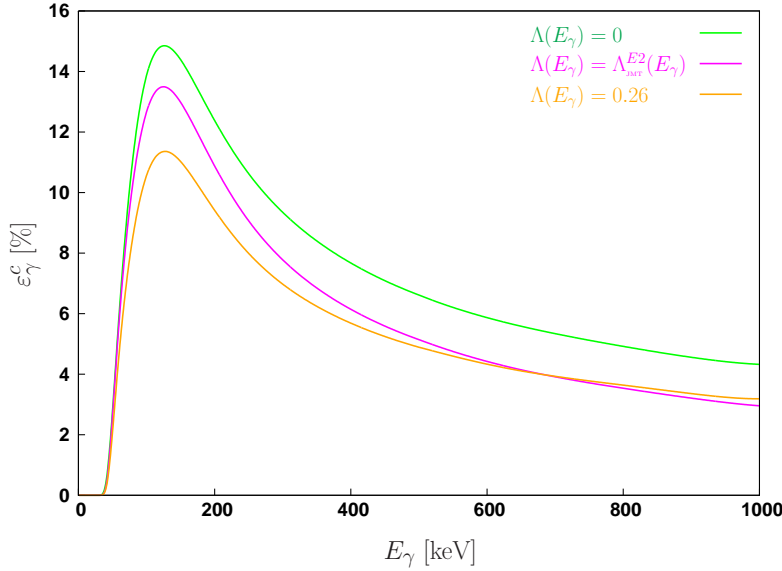


**Figure 4.12:** The simulated coincident photon detection efficiency (addback mode) for the bremsstrahlung emission assuming the  $\alpha$ - $\gamma$  angular correlation to be given by equation (4.4) with  $\Lambda(E_\gamma) = 0$  (non-relativistic pure dipole, green),  $\Lambda(E_\gamma) = \Lambda_{\text{JMT}}^{E2}(E_\gamma)$  (non-relativistic semi-classical result of Jentschura-Milstein-Terekhov [21], magenta), and assuming a constant  $\Lambda$  value  $\Lambda(E_\gamma) = 0.26$  (orange) are shown.

Thus by knowing the coincident photon detection efficiencies  $\varepsilon_{\gamma,2\Lambda=0}^c$  for a pure dipole (E1)  $\alpha$ - $\gamma$  angular correlation  $f_{2\Lambda=0} = \sin^2 \vartheta$  and  $\varepsilon_{\gamma,2\Lambda=1}^c$  for the angular correlation  $f_{2\Lambda=1} = \sin^2 \vartheta(1 + \cos \vartheta)$ , the coincident photon detection efficiency for a given  $\Lambda$  value can be derived by

$$\varepsilon_{\gamma,\Lambda}^c = (1 - 2\Lambda) \cdot \varepsilon_{\gamma,2\Lambda=0}^c + 2\Lambda \cdot \varepsilon_{\gamma,2\Lambda=1}^c. \quad (4.9)$$

The values of  $\varepsilon_{\gamma,2\Lambda=0}^c$  and  $\varepsilon_{\gamma,2\Lambda=1}^c$  were simulated using the corresponding angular correlation  $f_{2\Lambda=0} = \sin^2 \vartheta$  and  $f_{2\Lambda=1} = \sin^2 \vartheta(1 + \cos \vartheta)$  in the event generation. The angular distribution generated in the simulation for  $2\Lambda = 0$  and  $2\Lambda = 1$  are shown in figure 4.11. The resulting coincident photon detection efficiencies  $\varepsilon_{\gamma,2\Lambda=0}^c$  and  $\varepsilon_{\gamma,2\Lambda=1}^c$  for an energy range upto 800 keV binned in 10 keV energy bins are listed in table 4.4 (addback mode).

In figure 4.12 the resulting efficiency curves  $\varepsilon_\gamma^c(E_\gamma)$  assuming the  $\alpha$ - $\gamma$  angular correlation (see equation (4.4)) with  $\Lambda(E_\gamma) = 0$  (non-relativistic pure dipole),  $\Lambda(E_\gamma) = \Lambda_{\text{JMT}}^{E2}(E_\gamma)$  (non-relativistic semi-classical result [21]) and a constant  $\Lambda$  value  $\Lambda(E_\gamma) = 0.26$  are shown.

## 4.4 Accuracy of the Simulated Coincident Efficiency

In the following section the accuracy of the simulated coincident photon efficiency  $\varepsilon_\gamma^c$  is estimated.

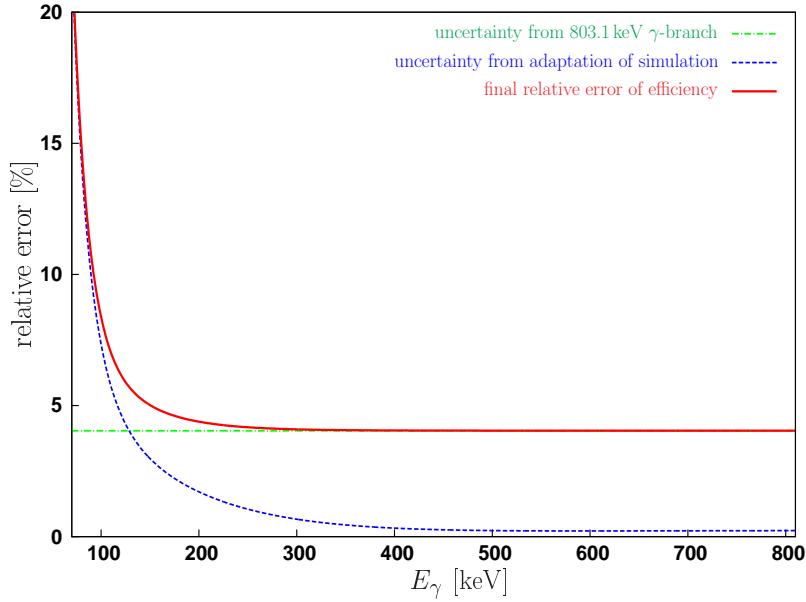


**Figure 4.13:** The relative error from the 803 keV  $\gamma$ -branch (green) and the error from the adaptation of the simulation (blue) are combined to the final relative error of the simulated efficiency (red).

There are many parameters that influence the accuracy of the simulation, such as the dimensions of the detectors, the chamber and the  $\alpha$  sources, the thicknesses of the different materials, the composition of the materials, the distances between the sources, the chamber and the detectors. All of these parameters have uncertainties which in principle have to be taken into account.

In the present case, however, the 803 keV  $\gamma$ -ray following the  $\alpha$  decay of  $^{210}\text{Po}$  in the first excited  $2^+$  state of the daughter nucleus  $^{206}\text{Pb}$  could be used as a build-in calibration source to determine the absolute detection efficiency of the setup at  $\sim 800$  keV. This information together with  $\gamma$ -calibration sources covering the  $\gamma$ -energy range between  $\sim 100$  keV and  $\sim 1.5$  MeV was used to adjust some of the input data of the simulation (see table 4.1). We therefore have two main contributions to the error budget: The measurement of the 803 keV  $\gamma$ -ray is subject to an relative error of  $\sim 4\%$ , which is mainly caused by the uncertainty of the branching ratio  $f_{803}$  (see table 4.1). The second error contribution is estimated from the required adjustment of the simulation by comparing the relative efficiencies obtained with the adapted parameters to the efficiencies with the original parameters taken from the data sheets.

In figure 4.13 the relative error from the 803 keV  $\gamma$ -branch is plotted in green and the relative error from the adaptation of the simulation is plotted in blue. The resulting combined error taking into account both contributions is shown in red.

Note that the reference sources were point-like whereas the  $^{210}\text{Po}$  sources have active areas

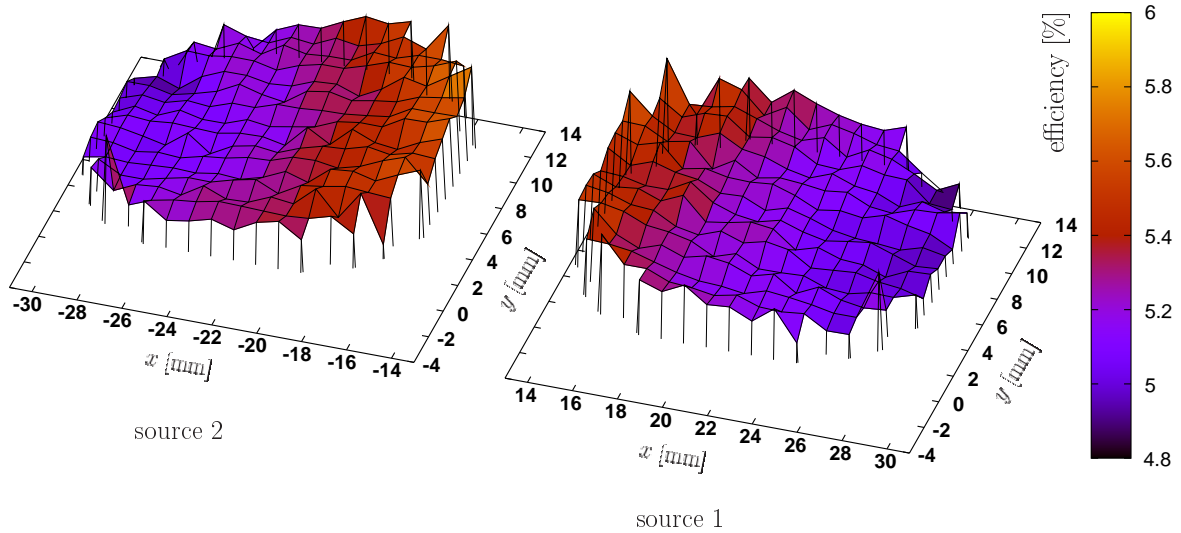


**Figure 4.14:** The simulated coincident photon detection efficiency is plotted for the active area of the two  $\alpha$  sources in a 2-dimensional surface plot. The variation in the coincident efficiency is in the order of  $\pm 7\%$ . The uncertainty due to the inhomogeneity of the sources is neglected because the uniformity of the sources has been shown (see section 3.2).

of  $\sim 4 \text{ cm}^2$  each. Therefore the variation of the detection efficiency over the active area of the source was investigated. Figure 4.14 shows the variation in the simulated coincident photon detection efficiency over the source area of both sources at  $E_\gamma = 500 \text{ keV}$ . The variation of the efficiency is in the order of  $\pm 7\%$ . But because the uniformity of the source has been shown (see section 3.2, figure 3.5) no uncertainty of the simulated efficiency due to the spreading of the source has to be considered.

The slight difference of the activities of the two sources by 17%, however, was taken into account in the simulation.

The resulting relative errors of  $\varepsilon_{\gamma,2\Lambda=0}^c(E_\gamma)$  and  $\varepsilon_{\gamma,2\Lambda=1}^c(E_\gamma)$  are given in table 4.4. Moreover, the coincident detection efficiencies for  $\Lambda(E_\gamma) = \Lambda_{\text{JMT}}^{E^2}(E_\gamma)$  and for  $\Lambda(E_\gamma) = 0.26$  are plotted with the corresponding error bands in figure 4.15.

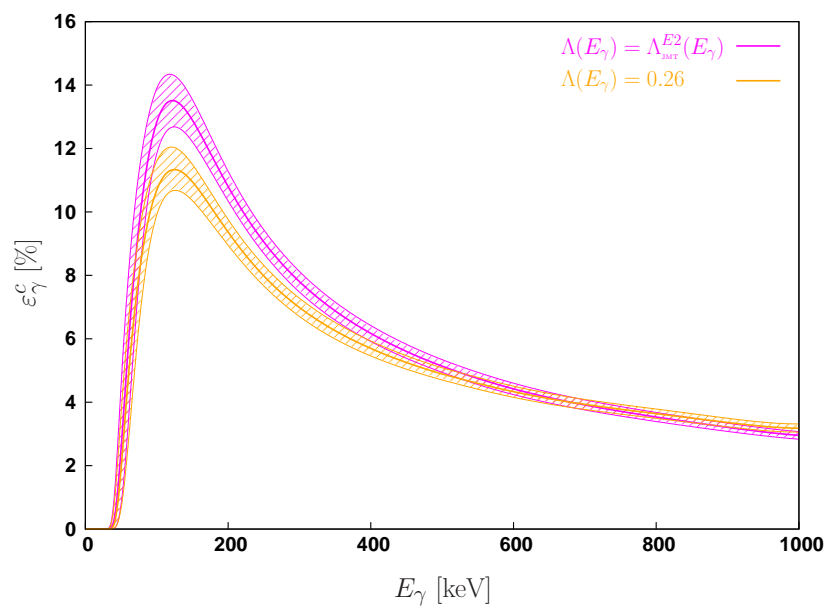


**Figure 4.15:** The coincident photon detection efficiency (addback) for  $\Lambda(E_\gamma) = \Lambda_{JMT}^{E2}(E_\gamma)$  (magenta) and  $\Lambda(E_\gamma) = 0.26$  (orange) are plotted with the corresponding error bands.



# Chapter 5

## Data Analysis

The production run lasted more than a year and the analysed data corresponds to 270 days of data taking (about 70% up time).

Within that period  $4.3 \cdot 10^{11}$   $\alpha$ -particles were incident on the detector. In the energy region above 300 keV about 160 bremsstrahlung events have been recorded while in the same time  $1.4 \cdot 10^8$  background photons were detected.

A detailed description of the analysis of the experimental data is presented in this chapter.

### 5.1 $\alpha$ -Energy Spectra

Figure 5.1 shows an  $\alpha$ -energy spectrum from one strip of the silicon detector. Shown in black are the down-scaled  $\alpha$ -singles. The spectrum displays an asymmetric Gaussian peak, corresponding to the detection of  $\alpha$  particles of energy  $E_{\alpha,0} = 5304$  keV from the ground state decay of  $^{210}\text{Po}$  to  $^{206}\text{Pb}$ , together with a long low-energy tail caused mainly by scattered  $\alpha$  particles. Note that the tail is completely covering up the  $\alpha$ -line expected at  $E_{\alpha,803} = 4517$  keV due to the  $10^{-5}$  branch of  $^{210}\text{Po}$  to the  $2^+$  state of  $^{206}\text{Pb}$ . A detailed discussion of the peak form and a suitable fit function for describing the shape of the peak will be given in section 5.4.1 and appendix C.1.

The red curve in figure 5.1 shows  $\alpha$  particles recorded in coincidence with a photon ( $E_\gamma \gtrsim 40$  keV). While the peak at  $E_{\alpha,0} = 5304.38$  keV is now strongly suppressed it is still prominent due to random coincidences with room background. The signature of the  $\alpha$  branch to  $^{206}\text{Pb}(2^+)$  can now be clearly seen at  $E_{\alpha,803} = 4517$  keV.

The resolution of the  $\alpha$  detection varies from strip to strip. This is caused by varying properties of the silicon detector and the electronics and by the geometry of the setup. Due to the geometry the range of the emission and detection angles as well as the count rates are different for each strip of a detector, resulting in different energy losses in the source material and in the dead-layer of the silicon detector.

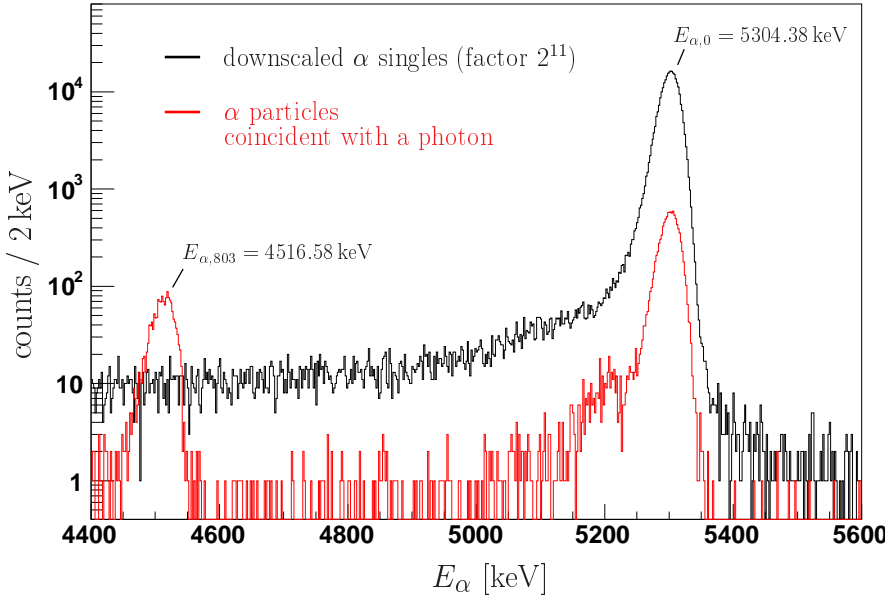


**Figure 5.1:**  $\alpha$ -energy spectrum of down-scaled  $\alpha$ -singles (black) and  $\alpha$  particles coincident with a photon (red). The data shown were detected by strip number seven of the silicon detector within a period of five days.

In figure 5.2 the resolution (FWHM) of the 5304 keV  $\alpha$ -line at the beginning of the production run is plotted for each strip in red. The outer strips (strip 1...5 of detector 1 and strip 12...16 of detector 2) cover a wider spread of the emission and detection angels than the central strips and therefore exhibit a slightly higher FWHM. The same holds for the inner strips (strip 15 and 16 of detector 1 and strip 1 and 2 of detector 2). The resolution at the end of the production run (green) and the count rate of each strip (blue) are also plotted in figure 5.2. The loss in resolution is likely due to the radiation damage of the detectors; the detected  $\alpha$ -particles are implanted into the detector material and damage the crystal structure of the silicon. A discussion of these effects can be found in the literature [39, 50, 51].

For the analysis of the data only the energy region between  $E_{\alpha,803}$  and  $E_{\alpha,0}$  is relevant, as beyond  $E_{\gamma} \approx 700$  keV the emission probability of bremsstrahlung is too low to be observed in this experiment.

In the  $\alpha$ - $\gamma$  coincidence spectrum as shown figure 5.1 (red) the  $E_{\alpha,803}$  and  $E_{\alpha,0}$  peaks are prominent and are used for the energy calibration. Between these energies the response of the detectors and the electronics can be considered to be linear.

The energy spectra of each strip are calibrated separately. For the calibration the data is grouped into groups of three to six days of data taking to provide enough statistic for each strip.

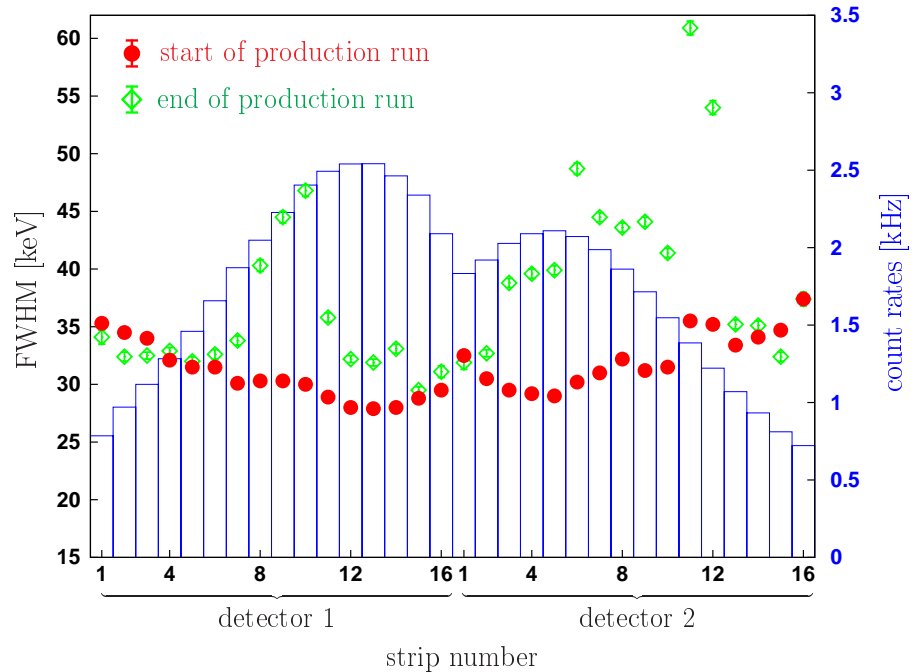


**Figure 5.2:** The energy resolution of the individual strips of the silicon detectors is plotted versus the strip number. The resolution at the beginning of the production run is plotted in red, the resolution at the end is plotted in green. The loss in resolution over the time is likely due to the radiation damage in the silicon detector. The count rate for each strip at the beginning of the production run is plotted in blue (right axis).

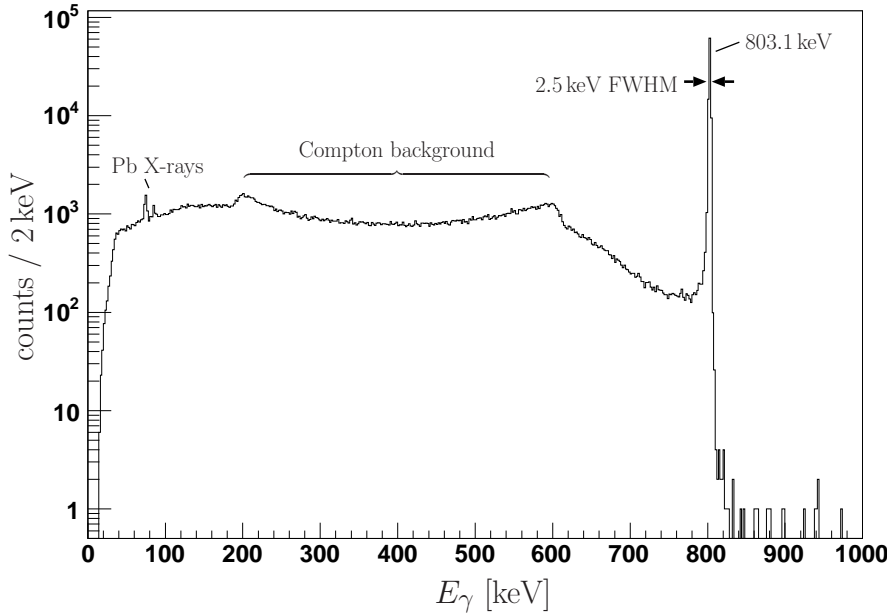


**Figure 5.3:** The  $\gamma$ -energy spectrum measured in coincidence with  $\alpha$  particles selecting the  $\alpha$ -branch of  $^{210}\text{Po}$  to the first excited  $2^+$  state of  $^{206}\text{Pb}$  shows the full-energy peak at 803 keV, which has a FWHM of about 2.5 keV and a long tail towards lower  $\gamma$ -energies due to incomplete detection of the 803 keV photon (partly caused by Compton-scattering in the active volume of the Ge-detectors, with the scattered photon leaving the active volume undetected). X-rays following the  $\alpha$  decay of  $^{210}\text{Po}$  to  $^{206}\text{Pb}(2^+)$  measured in coincidence with the  $\alpha$  particle are also present in the spectrum at the corresponding  $\gamma$ -energies.

## 5.2 $\gamma$ -Energy Spectra

In figure 5.3 the  $\gamma$ -energy spectrum measured in coincidence with  $\alpha$ 's selecting the  $\alpha$  branch of  $^{210}\text{Po}$  to the  $2^+$  state of  $^{206}\text{Pb}$  of module A is shown.

Besides the full-energy peak at 803 keV, which has a FWHM of about 2.5 keV, the spectrum displays a long tail towards lower  $\gamma$ -energies due to the incomplete detection of the 803 keV photon. While this tail, which extends down to the electronic threshold of  $\sim 40$  keV, might cause coincident background due to pile-up events in the region where bremsstrahlung events are expected (see figure 3.1), they do allow, on the other hand, for a careful investigation and optimisation of the time-correlation of  $\alpha$ 's and  $\gamma$ -rays for  $\gamma$ -energies between  $\sim 80$  keV and  $\sim 800$  keV as discussed in section 5.3.

For the energy calibration of the  $\gamma$ -energy spectra  $\gamma$ -lines from the room background are used. A detailed background spectrum with the classification of the background lines can be found in appendix D.

Each HPGe crystal of the cluster detector is calibrated separately and the data is again grouped to provide enough statistic. For the calibration of the  $\gamma$  energy spectra a linear function is used which has been shown to be a good approximation of the response of the HPGe crystals and the electronics [36] between  $80 \text{ keV} < E_\gamma < 1300 \text{ keV}$ .

## 5.3 Time Spectra

To reduce background it is important to distinguish coincident events from random events. To be able to do so the difference between the time when the  $\alpha$  particle was detected and the time of the photon detection is used. For each accepted event (downscaled single- $\alpha$ -, single- $\gamma$ -, and coincident  $\alpha$ - $\gamma$ -events) the timing signal of each strip of the silicon detector and of the core of each crystal and of each of the segments of the cluster detector was recorded. In all cases the recorded time is the time difference between the master trigger and the delayed trigger signal of the strip, core or segment (see section 3.6).

The spectrum of time differences between the time of the master trigger,  $t_{\text{trig}}$ , and the delayed trigger signal of a strip of the silicon detector,  $t_\alpha$ , is shown in figure 5.4. There are two classes of events contributing to the spectrum. First there are down-scaled  $\alpha$ -singles with no photon detected in the same event (blue curve in the inset of figure 5.4). Down-scaled  $\alpha$ -singles recorded in the chosen strip which gives also rise to the master trigger can be found in the self trigger peak. If the master trigger was produced by an  $\alpha$  particle in a different strip the event contributes to the broad background on the right of the self trigger peak. The second contribution comes from events in which an  $\alpha$  particle was recorded together with a photon (red curve in the inset of figure 5.4). On a background from chance coincidences a prominent peak of the coincident  $\alpha$ - $\gamma$  events can be seen.

Two different times from the HPGe detector were recorded: The time  $t_\gamma^{\text{CFD}}$  was taken from the analog timing branch. Here the preamplifier signal of the core of the responding module was shaped in a timing filter amplifier (TFA) and then a constant fraction discriminator (CFD) was used to produce the trigger output. Also the “fast trigger” output of the XIA DGF-4C cards was recorded as  $t_\gamma^{\text{XFT}}$ . This output is generated by the digital leading edge (LE) discriminator and therefore the time resolution is restricted by the sampling rate of the flash ADC of 40 MHz (2 ns per sample).

For the investigating and optimising the coincidence time information  $\alpha$ - $\gamma$  coincidences with  $E_\alpha$  restricted to  $E_{\alpha,803}$  are considered. These events are dominated by the full energy peak of 803 keV  $\gamma$ -branch and its Compton-background and 2-dimensional  $E_\gamma$  versus  $t_\alpha - t_\gamma$  plots allow to analyse the dependence of the time resolution from the detected photon energy.

Figures 5.5 and 5.6 show such a 2-dimensional plot for the analog CFD time  $t_\gamma^{\text{CFD}}$  and the XIA Fast Trigger time  $t_\gamma^{\text{XFT}}$ , respectively together with its projection on the time axis. For the XIA Fast Trigger time  $t_\gamma^{\text{XFT}}$  the centre of the coincidence peak moves to earlier times with lower  $\gamma$ -energies. This is a well known behaviour of a leading edge trigger, the so called “amplitude walk” [36, 39]. For very small energies also  $t_\gamma^{\text{CFD}}$  shows such an amplitude

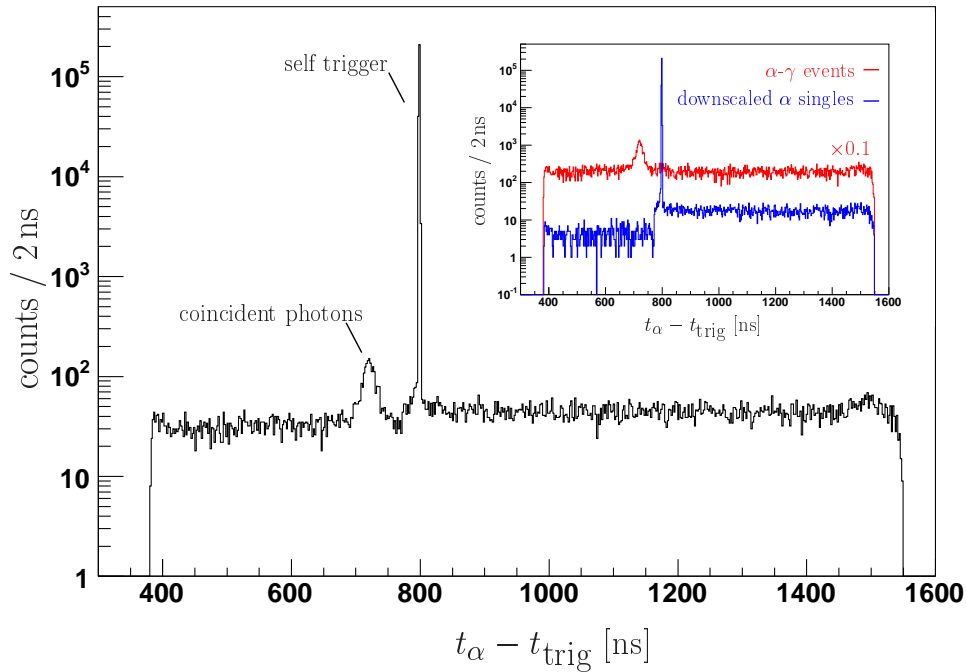


**Figure 5.4:** The spectrum of the time difference between the master trigger  $t_{\text{trig}}$  and the delayed trigger signal of a single strip of the silicon detector is shown (strip 12 of detector 1). Events in which only a down-scaled  $\alpha$  particle is recorded and the selected strip generated the master trigger give rise to the self trigger peak. A photon which is detected in coincidence with the  $\alpha$  particle and produced the master trigger can be found in the coincidence peak. In the inset the corresponding spectra of down-scaled  $\alpha$ -singles (blue) and events in which both an  $\alpha$  particle and a photon was recorded (red) are shown separately.

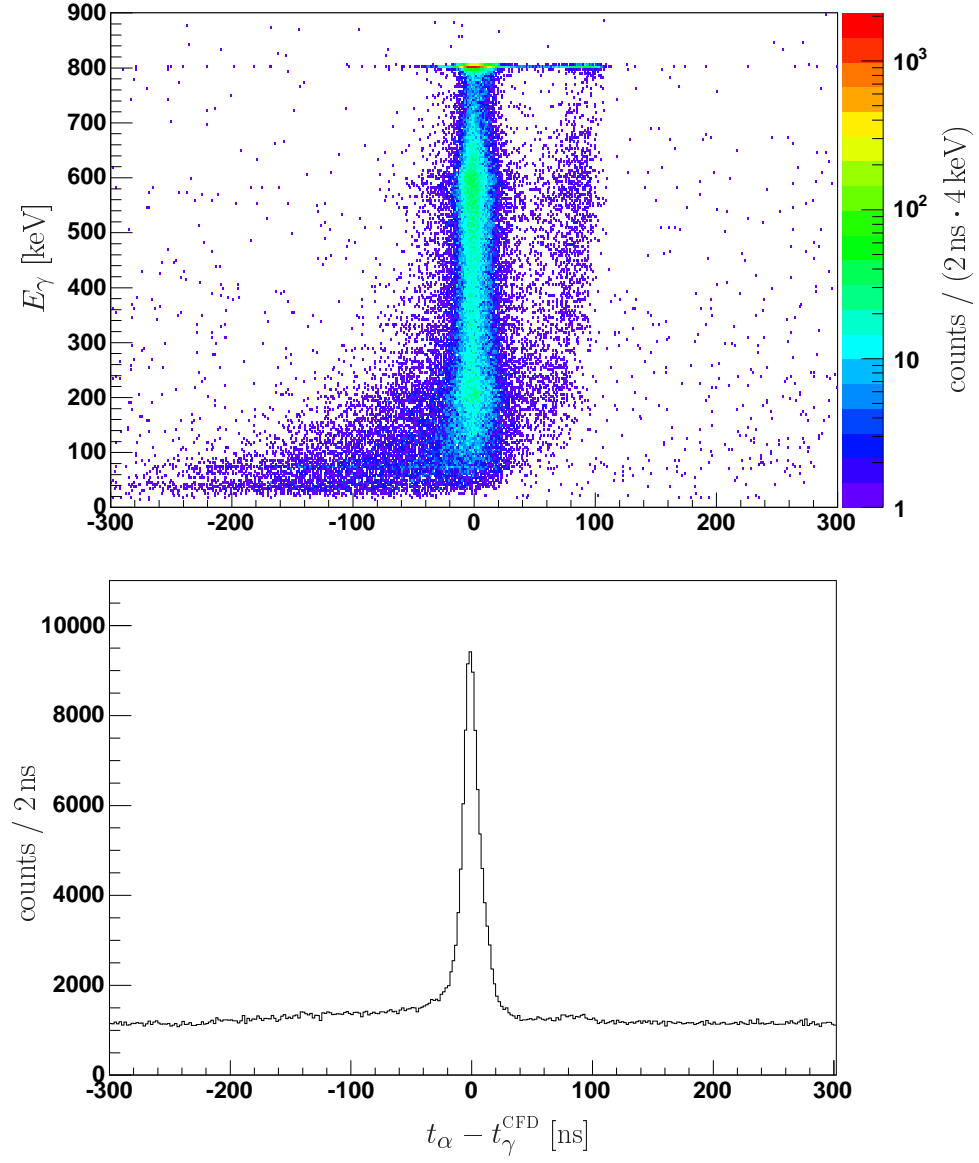


**Figure 5.5:** In the upper panel the detected energy of the 803 keV  $\gamma$ -ray from the  $\alpha$  decay to  $^{206}\text{Pb}(2^+)$  is plotted versus the time difference between the detection time of the  $\alpha$  particle,  $t_\alpha$ , and the photon time from the analog timing branch  $t_\gamma^{\text{CFD}}$  (sum of all modules, addback mode). In the lower panel the projection on the time axis is shown. The time resolution is getting worse for lower  $\gamma$ -energies, moreover, for very low  $\gamma$ -energies a slight amplitude walk can been seen. The origin of the small second coincidence peak at 100 ns is unclear.

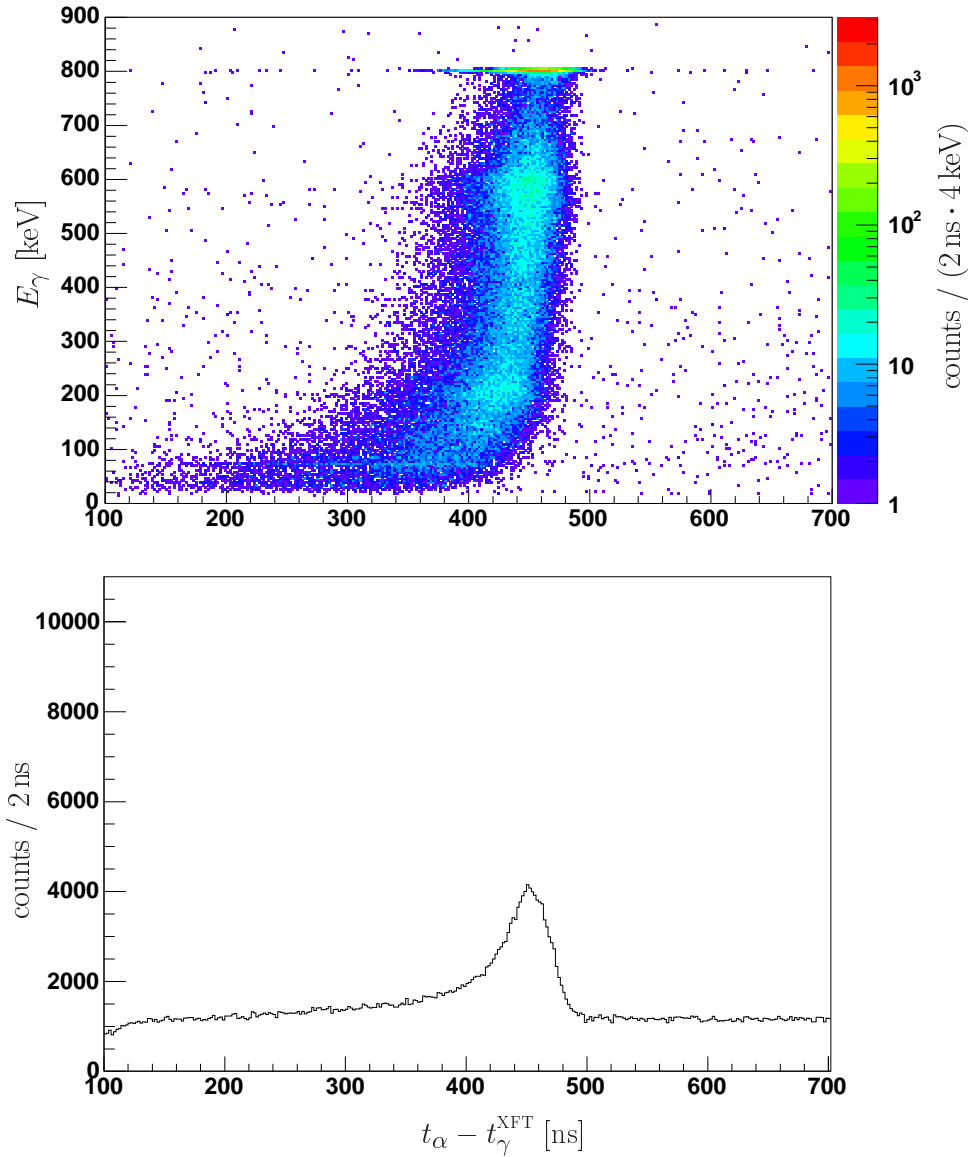


**Figure 5.6:** In the upper panel the detected energy of the 803 keV  $\gamma$ -ray from the  $\alpha$  decay to  $^{206}\text{Pb}(2^+)$  is plotted versus the time difference between the detection time of the  $\alpha$  particle,  $t_\alpha$ , and the photon time  $t_\gamma^{\text{XFT}}$  derived from the digital leading edge trigger integrated in the XIA DGF-4C cards (sum of all modules, addback mode). In the lower panel the projection onto the time axis is shown. For lower  $\gamma$ -energies the centre of the coincidence peak is shifted to earlier times. This feature is known as “amplitude walk” and is typical for a leading edge trigger. Because of the sampling rate of the flash ADC (1 sample = 25 ns) the resolution of the timing is limited to about 50 ns.

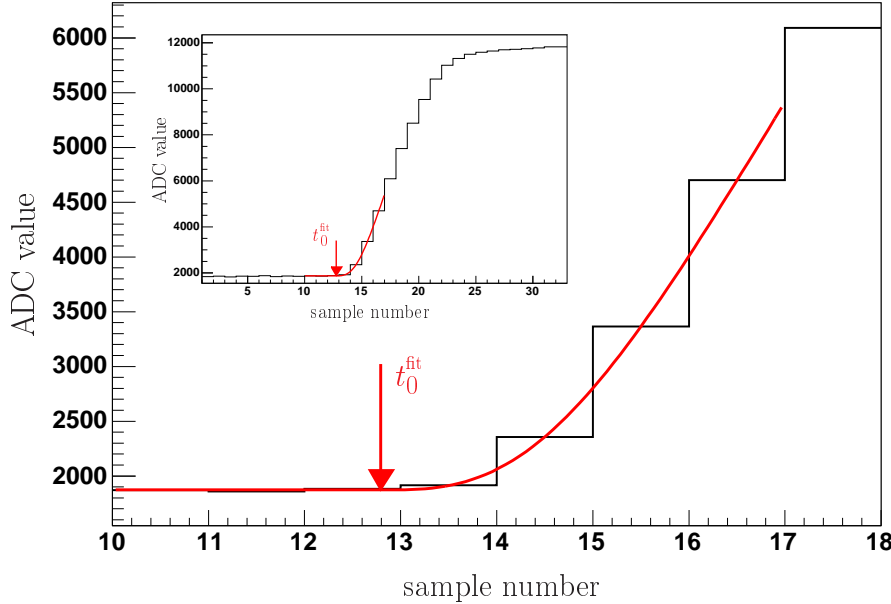


**Figure 5.7:** Trace of a charge pulse from a detector segment in which an energy of 2.4 MeV was deposited. The response function of the preamplifier  $R(t)$  (red) is fitted to 7 samples from the trace including  $\sim 4$  samples from the start of the pulse and  $\sim 3$  samples from the baseline. The value  $t_0^{\text{fit}}$  indicates the fitted start time of the pulse. In the inset the total pulse trace is shown.

walk, which is due to the fact that for such low energies the CFD starts to behave like a LE trigger.

As noted in section 3.6, due to the low counting rate of the germanium detectors it was possible to store the pulse traces digitised in the XIA DGF-4C cards; a typical trace of a (current integrated) charge pulse corresponding to a deposited  $\gamma$ -energy of 2.4 MeV is shown in the inset of figure 5.7. The recorded signal traces allow for a detailed off-line pulse shape analysis (PSA), which can be used to determine more careful the start time  $t_0$  of the signal and thereby to improve the timing information on an event by event basis.

Different algorithms to determine the start time  $t_0$  of the pulse from such traces have been discussed [36, 42, 52, 53]. We used the following procedure [54]:

Approximating the beginning of the current pulse, induced by an energy deposition in the detector at time  $t_0$ , by a step function  $\Theta(t - t_0)$ , the resulting charge pulse  $R(t)$  for  $t \gtrsim t_0$  is given by a convolution of the response function of the preamplifier with a step function, which leads to ([54], note that an obvious misprint has been corrected)

$$R(t) = A_p \left( t - t_0 - \frac{\sqrt{\pi} \tau_r}{2\sqrt{1.3}} \operatorname{erf} \left( \frac{\sqrt{1.3}(t - t_0)}{\tau_r} \right) \right) \Theta(t - t_0) + B_p . \quad (5.1)$$

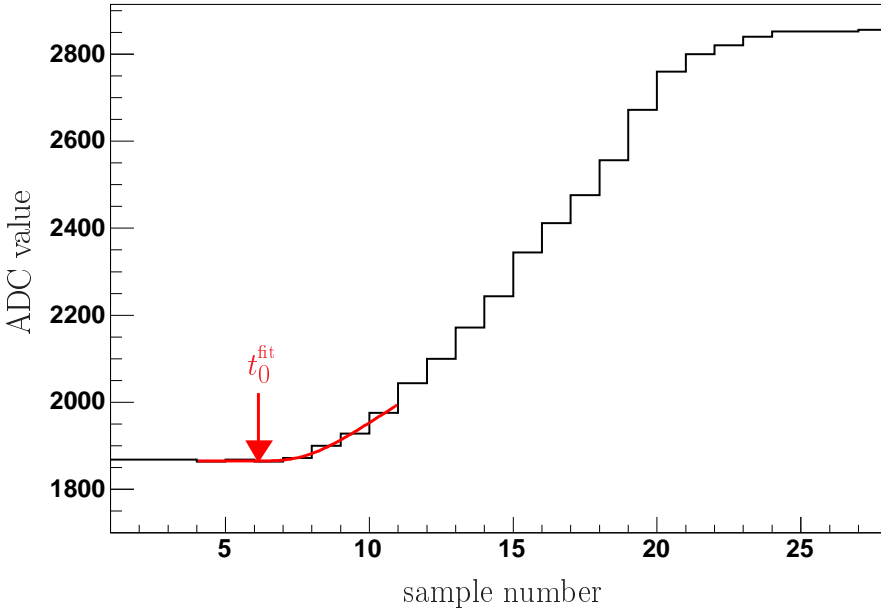


**Figure 5.8:** Trace of a charge pulse from a detector segment in which an energy of 240 keV was recorded, together with the best fit (red curve) using equation (5.1) and the resulting start time  $t_0^{\text{fit}}$ .

The value  $\tau_r$  describes the rise time of the preamplifier, the value  $B_p$  corresponds to the baseline before the start of the signal.

The function  $R(t)$  is only a good approximation of the first 50-100 ns of the charge pulse. For this work 7 samples of the trace are used to fit  $R(t)$  to the beginning of the trace covering 3 samples of the baseline and 4 of the beginning of the trace. The rise time of the preamplifier was optimised to a value of  $\tau_r = 2.3$  samples = 57.5 ns. In figure 5.7 an example for a fitted function  $R(t)$  and the resulting start time  $t_0^{\text{fit}}$  is given.

The signal of a 240 keV photon which rises slowly in the beginning is presented in figure 5.8. The fitted response function  $R(t)$  with the fitted start time  $t_0^{\text{fit}}$  is plotted in red. This illustrates that the fit of the start of the pulse with the response function  $R(t)$  also gives realistic values for  $t_0^{\text{fit}}$  for events with low  $\gamma$ -energy.

The fitted start time  $t_0^{\text{fit}}$  is used to correct the the XIA Fast Trigger time  $t_\gamma^{\text{XFT}}$ . As  $t_\gamma^{\text{XFT}}$  determines the readout of the trace, the corrected trigger time  $t_\gamma^{\text{XTC}}$  is defined by

$$t_\gamma^{\text{XTC}} = t_\gamma^{\text{XFT}} + t_0^{\text{fit}} \cdot 25 \text{ ns} . \quad (5.2)$$

As already shown in [36], the timing information from PSA the segment traces is more precise than that derived from the core trace. So the evaluation of  $t_\gamma^{\text{XTC}}$  was based on  $t_0^{\text{fit}}$  from the trace of the hit segment with the largest deposited energy fraction.

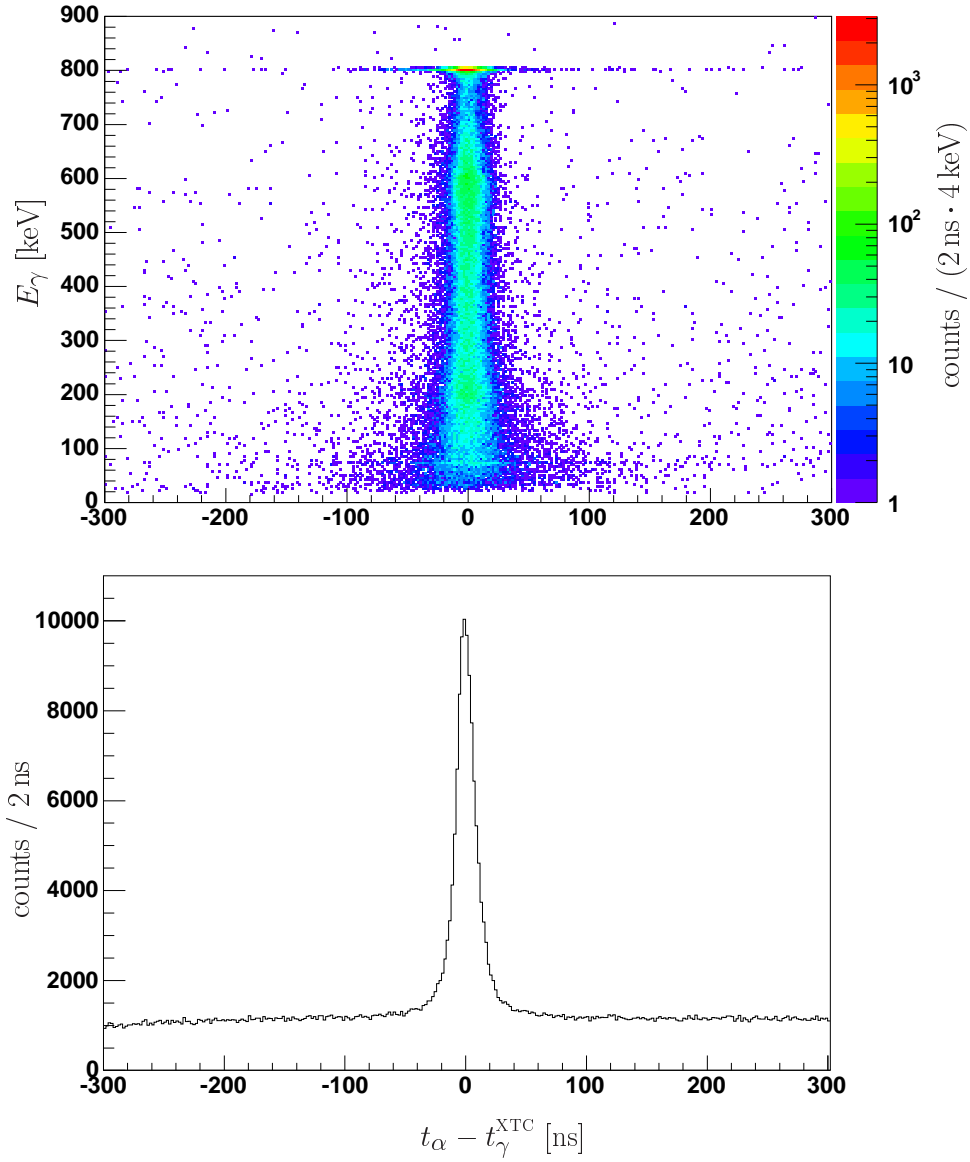


**Figure 5.9:** In the upper panel the detected energy of the 803 keV  $\gamma$ -ray from the  $\alpha$  decay to  $^{206}\text{Pb}(2^+)$  is plotted versus the time difference between the detection time of the  $\alpha$  particle,  $t_\alpha$ , and the photon time  $t_\gamma^{\text{XTC}}$  derived using PSA of the segment signals (sum of all modules, addback mode). In the lower panel the projection onto the time axis is shown. In comparison the XIA fast trigger time the amplitude walk has been cancelled and in comparison to the analog timing the shape of the coincidence peak and the background has been improved.

$E_\gamma$	CFD time		corrected XFT time		gain
	FWHM [ns]	area <sup>†</sup> [counts]	FWHM [ns]	area <sup>†</sup> [counts]	
100 keV...200 keV	29.4	7283	29.3	8643	18.7%
200 keV...300 keV	21.9	8065	24.6	8556	6.1%
300 keV...400 keV	18.6	6263	20.7	6594	5.3%
400 keV...500 keV	17.0	6680	18.7	6972	4.4%
500 keV...600 keV	15.2	9572	19.0	10048	5.0%
600 keV...700 keV	15.1	6055	16.6	6309	4.2%
700 keV...800 keV	14.7	3496	14.9	3636	4.0%
800 keV...900 keV	13.2	24182	14.5	24962	3.2%

<sup>†</sup> integral of the spectrum from  $-4.5 \cdot \sigma$  to  $4.5 \cdot \sigma$  (background subtracted)

**Table 5.1:** The time resolution and the area under the coincidence peak are compared for the two timing methods applying the corrected XIA time  $t_\gamma^{XTC}$  and the analog time  $t_\gamma^{CFD}$ , respectively. While the resolution is comparable, the shape of the coincidence peak and the number of coincident events within the interval from  $-4.5 \cdot \sigma$  to  $4.5 \cdot \sigma$  is improved. The last column shows the relative gain in area.

The resulting 2-dimensional  $E_\gamma$  versus  $t_\alpha - t_\gamma^{XTC}$  plot is presented in figure 5.9. With this correction the amplitude walk is corrected and also the time resolution at low energies is considerably improved compared to the XFT timing. In table 5.1 the timing resolution obtained with the corrected XIA timing is compared to the CFD timing for different energy regions. Also the number of counts within a window of  $-4.5 \cdot \sigma$  to  $4.5 \cdot \sigma$  (the interval used for the analysis, see also section 5.4.1) are given for both timing method.

Note that the coincidence time resolution as measured by the FWHM is similar for both methods, but that the number of events within the accepted time window is larger (in particular in the low energy window from 100 – 200 keV) when using the corrected XFT timing.

During the period of data taking several time calibrations of the TDCs were performed using an Ortec 462 time calibrator. The TDCs were found to be linear and stable. The time offset of each silicon strip were calibrated using the self trigger peak, grouping the data as described in section 5.1. For the calibration of the offset of the corrected XIA time of each segment the coincidence peak in the  $t_\alpha - t_\gamma^{XTC}$  spectrum was used.

## 5.4 Bremsstrahlung Analysis

The spectrum of the time difference between the detection time of the  $\alpha$  particle  $t_\alpha$  and the  $\gamma$ -ray  $t_\gamma$ , which is given by the corrected XFT time  $t_\gamma^{XTC}$  (see section 5.3), is plotted in figure 5.10. It shows a prominent coincidence peak riding on a broad distribution of random coincidences.

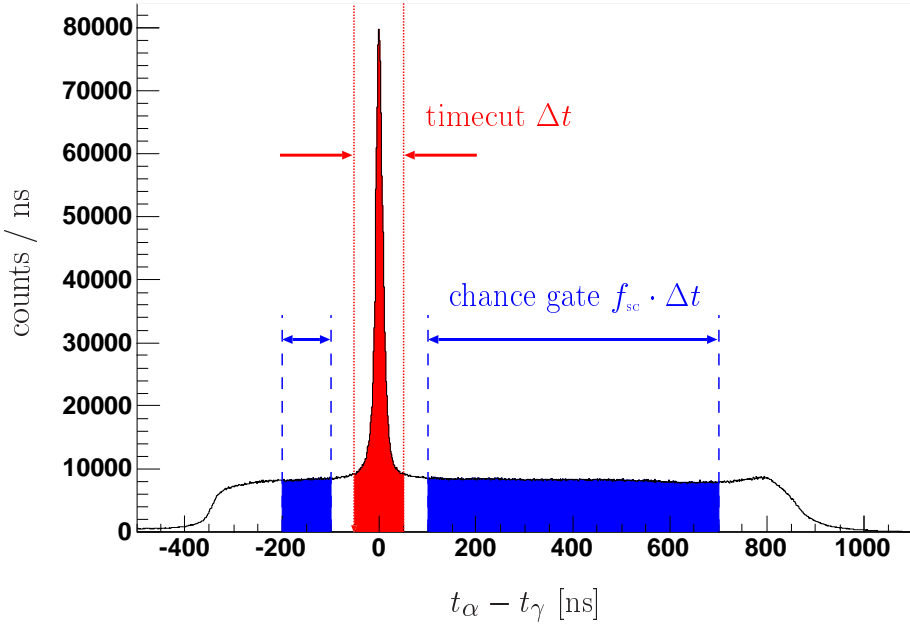


**Figure 5.10:** Spectrum of  $t_\alpha - t_\gamma$  with time-cut and chance gate

To observe the bremsstrahlung emitted in the  $\alpha$  decay of  $^{210}\text{Po}$  coincident events have to be selected by a time-cut. Figure 5.11 shows the 2-dimensional  $E_\alpha$  versus  $E_\gamma$  plot for a time-cut on the coincidence peak with a width of  $\Delta t = 100\text{ ns}$ . A more careful choice of the time-cut, which depends on  $E_\gamma$  and which is used later in the analysis is discussed in detail in section 5.4.1.

In the upper part of the resulting  $E_\alpha$  versus  $E_\gamma$  plot (compare also to figure 3.1) a horizontal band of random coincidences of  $\alpha$  particles from the  $\alpha$  decay to the ground state of  $^{206}\text{Pb}$  and photons from the room background can be seen. The 803 keV gamma branch is prominent in the lower right corner with its Compton background forming the lower horizontal band on its left. If the  $\alpha$  particle knocks out an electron during the decay part of its energy is taken away by the electron. The remaining gap in the electron shell is filled by an electron from an upper shell producing X-ray radiation. These X-rays have the typical X-ray  $\gamma$ -energy of the daughter nucleus and the corresponding  $\alpha$  particle has a smaller energy. Thus these events form the vertical lines on the left side of the spectrum. On the diagonal of the  $E_\alpha$  versus  $E_\gamma$  plot the bremsstrahlung events are clearly visible.

The 2-dimensional  $E_\alpha$  versus  $E_\gamma$  spectrum obtained by selecting events in the chance coincidence gate (see figure 5.10) is displayed in figure 5.12.

Remember that there are two sources of background in the region of the bremsstrahlung as already noted in section 3.1: (a) Background arises from random coincidences of photons

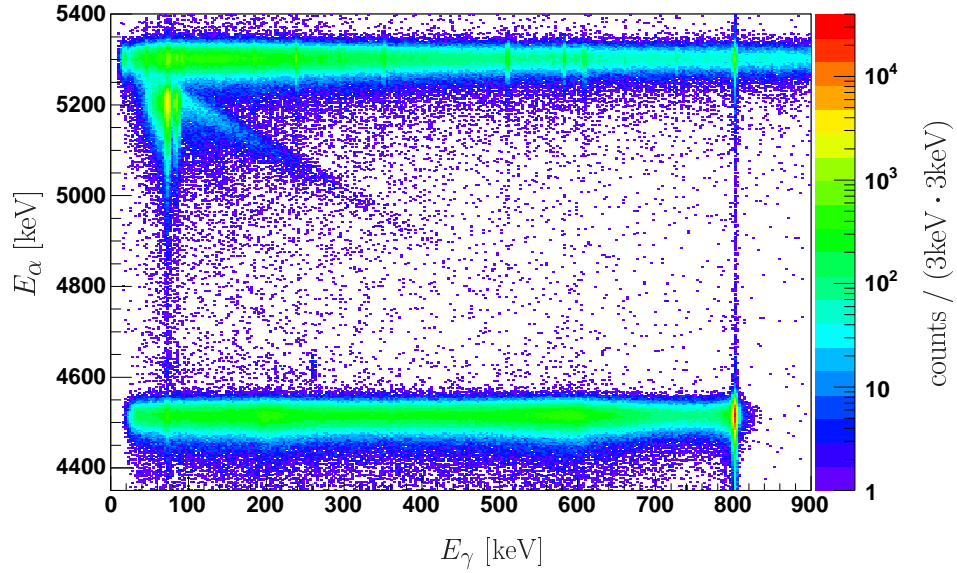


**Figure 5.11:** 2-dimensional  $E_\alpha$  versus  $E_\gamma$  plot of events within a coincidence time-cut of  $-50 \text{ ns} < \Delta t < 50 \text{ ns}$ .

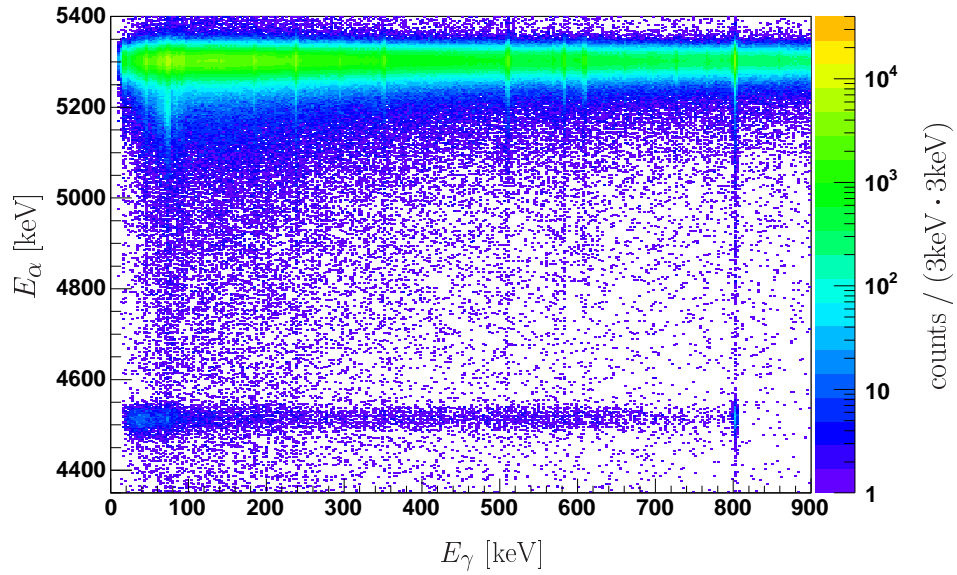


**Figure 5.12:** 2-dimensional  $E_\alpha$  versus  $E_\gamma$  plot of events from the chance gate on the coincidence time spectrum ( $-200 \text{ ns} < \Delta t < -100 \text{ ns}$  or  $100 \text{ ns} < \Delta t < 700 \text{ ns}$ ). The colour table is scaled by the ratio of the width of the prompt gate to that of the chance gate. (see figure 5.11).

bin number	$E_\gamma$ range	$\Delta E_\gamma$
0	90 keV ... 110 keV	20 keV
1	110 keV ... 130 keV	20 keV
2	130 keV ... 150 keV	20 keV
3	150 keV ... 170 keV	20 keV
4	170 keV ... 190 keV	20 keV
5	190 keV ... 210 keV	20 keV
6	210 keV ... 240 keV	30 keV
7	240 keV ... 270 keV	30 keV
8	270 keV ... 300 keV	30 keV
9	300 keV ... 350 keV	50 keV
10	350 keV ... 400 keV	50 keV
11	400 keV ... 450 keV	50 keV
12	450 keV ... 550 keV	100 keV

**Table 5.2:** Binning of the data in  $E_\gamma$ . Because the bremsstrahlung emission probability decreases exponentially with  $E_\gamma$ , wider bins were used at higher  $\gamma$ -energies.

from the room background with  $\alpha$  particles from the  $\alpha$  decay to the ground state of  $^{206}\text{Pb}$  that lost part of their energy, e.g. by scattering, energy loss in the source material, in the dead-layer of the detector, etc. This background is also present in the random spectrum. (b) Photons from the Compton background of the 803 keV  $\gamma$ -branch may be measured in coincidence with a prompt  $\alpha$  particle whose energy is detected to high, e.g. due to pile-up. This background is not present in random spectrum. Therefore a simple background subtraction of the random spectrum as used in [23, 24, 36] does only take into account part of the background. The high statistics of the present data allowed us to perform a more advanced analysis taking into account both kinds of backgrounds.

For the further analysis the data is split into several bins in the  $\gamma$ -energy. Because the bremsstrahlung probability decreases exponentially with  $E_\gamma$ , wider bins were used at higher  $\gamma$ -energies. Table 5.2 shows the  $E_\gamma$  bins used in the analysis.

The prompt events for each  $\gamma$ -energy bin are then projected along the diagonal in the  $E_\alpha$  versus  $E_\gamma$  plot by plotting them as a function of  $\tilde{E} = E_\alpha + 206/210 \cdot E_\gamma$  (see section 3.1). In these spectra the bremsstrahlung events should result in a peak at  $\tilde{E} = E_{\alpha,0} = 5304$  keV. An example is shown in figure 5.13. By this procedure the peaks from the chance coincidences and from the Compton background of the 803.1 keV branch are getting broader, but at the same time the width of the bremsstrahlung peak is optimised.

The same projection is applied to the data obtained with the chance gate (see figure 5.14). The resulting spectrum, scaled with the width of the chance gate in comparison to the prompt gate gives a good reference for the random background in the corresponding prompt coincidence spectrum.

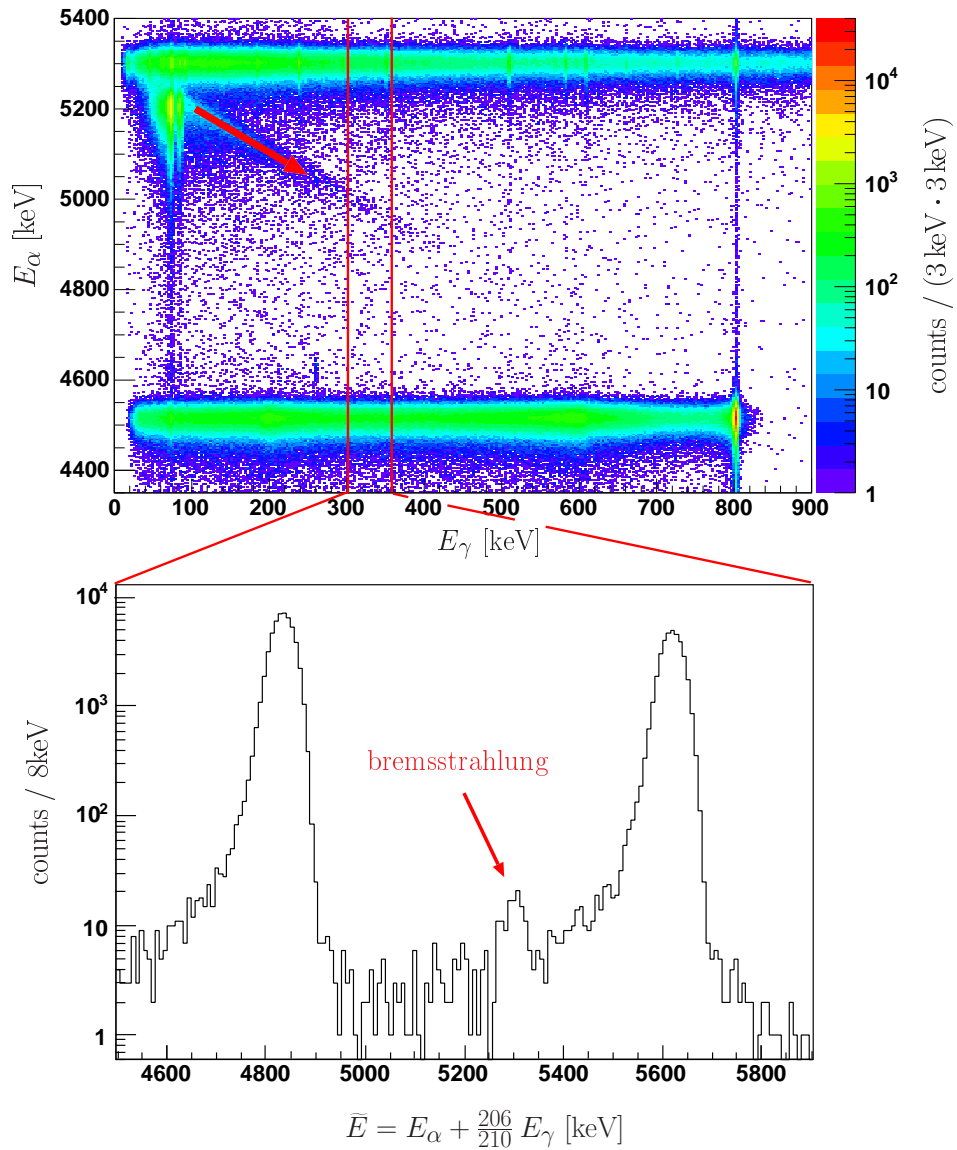


**Figure 5.13:** Prompt data from the  $\gamma$ -energy bin 9 ( $300 \text{ keV} < E_\gamma < 350 \text{ keV}$ ) projected along the expected bremsstrahlung diagonal.

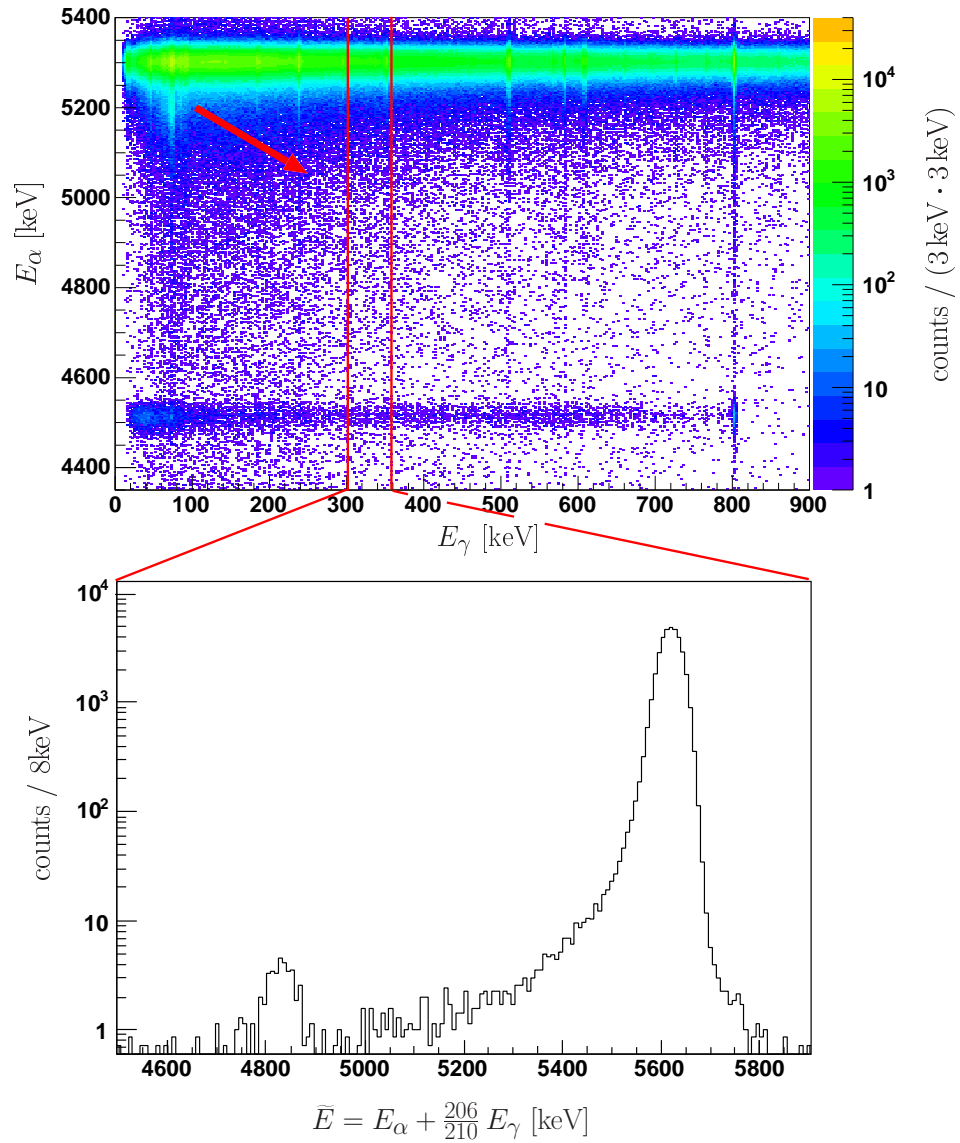


**Figure 5.14:** Random data from the  $\gamma$ -energy bin 9 ( $300 \text{ keV} < E_\gamma < 350 \text{ keV}$ ) projected along the expected bremsstrahlung diagonal. The projected spectrum is scaled with the ratio of the widths of the time windows applied to obtain the prompt and random spectra.

### 5.4.1 Modelling the Projected Energy Spectra

To extract the number of bremsstrahlung photons from the projected spectra it is necessary to understand the shape of the underlying random background and to model the various coincident contributions to the spectra.

#### Modelling the $\alpha$ -Lineshape

The response of the Si-detector to an impinging monoenergetic  $\alpha$  particle of 5304 keV from the  $\alpha$  decay of  $^{210}\text{Po}$  has a characteristic form. Its shape is influenced by various effects, e.g. incomplete charge collection in the detector, energy loss of the  $\alpha$  particle in the dead layer of the silicon detector, pile-up effects, etc. All these effects are characteristic of the detection of the  $\alpha$  particle or of the geometry of the setup but do not depend on the choice of the time-cut. Therefore the peak form can be deduced from the random (non-projected)  $\alpha$  spectrum.

Several methods to fit an  $\alpha$  spectrum have been proposed in the literature [55–58]. In this work a fit function  $f(x)$  is used consisting out of a Gaussian  $g(x)$ , a function for the approximation of the low energy tail  $t_l(x)$  and one for the high energy tail  $t_h(x)$ .

$$f(x, x_0) = g(x, x_0) + t_l(x, x_0) + t_h(x, x_0). \quad (5.3)$$

The modelling of the  $\alpha$ -lineshape is discussed in detail in appendix C.1.

#### Modelling the Background due to Chance Coincidences

The peak at  $\tilde{E} = 5304 \text{ keV} + 206/210 \cdot \overline{E_\gamma}$  and its low energy tail is due to random coincidences between the  $\alpha$  particle from the decay of  $^{210}\text{Po}$  to the ground state of  $^{206}\text{Pb}$  and the ambient  $\gamma$  background. For a given energy bin the projected spectrum obtained with the random gate gives a good approximation of the background contribution.

Due to the projection the peak form is broadened in comparison to the  $\alpha$ -lineshape discussed above. In principle the  $\alpha$ -lineshape folded with the characteristic function of the background spectrum should reproduce the peak form of the projected spectrum. For simplification, the broadened peak in the projected random spectrum is approximated by six equidistant Gaussian with each amplitude fitted freely. To each of the six Gaussians a low energy tail and a high energy tail of similar structure as mentioned above was attached, shifted with the position of the Gaussian, and scaled by its area. All parameters of the tails are identical for each Gaussian and are allowed to vary freely during the fit. By this procedure the peak form in the projected random spectrum is described very well; scaled with the widths of the respective time-cuts it describes the background from chance coincidences in the prompt spectrum without any further fitting. In figure 5.15 the so derived function  $b_{cc}(\tilde{E})$  modelling this background contribution is plotted in cyan for the energy bin  $190 \text{ keV} < E_\gamma < 210 \text{ keV}$ .

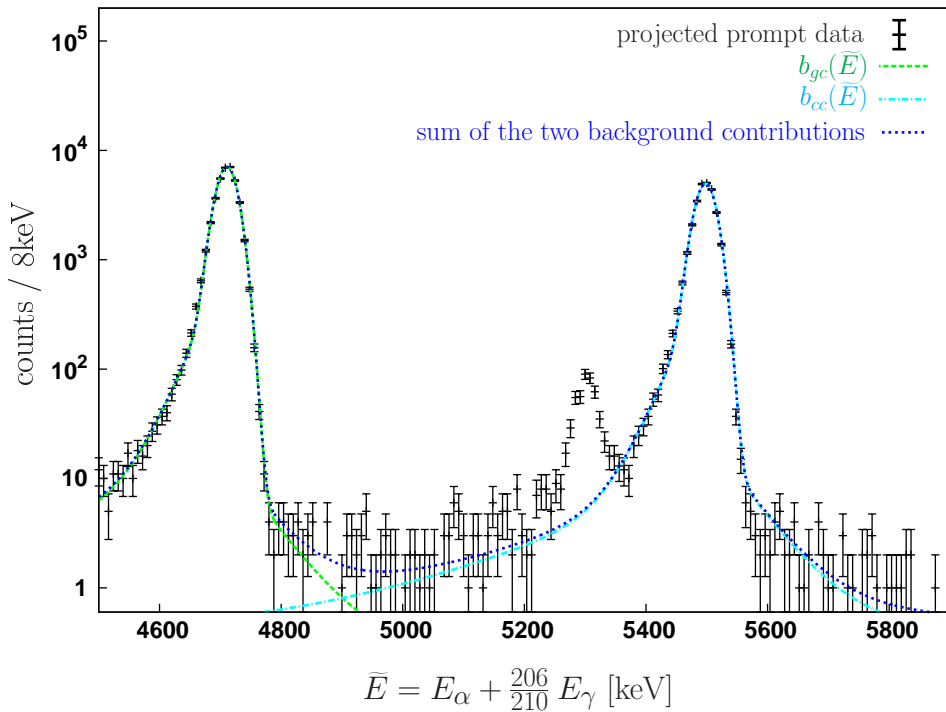


**Figure 5.15:** Background contributions in the projected prompt energy spectrum due to  $\alpha$  particles which were detected in coincidence with photons from the room background and due to the Compton background from the 803 keV  $\gamma$ -branch. The function  $b_{cc}(\bar{E})$  models the background from the chance coincidences (cyan), the function  $b_{gc}(\bar{E})$  that from the Compton background of the  $\gamma$ -branch (green). The sum of both contributions results in the dotted curve (blue). The shown spectrum is the projected  $190 \text{ keV} < E_\gamma < 210 \text{ keV}$  energy bin for a 100 ns wide prompt time-gate.

### Modelling the Background due to the 803 keV $\gamma$ -Branch

The second main feature in the prompt projected energy spectra at  $\tilde{E} < 5304 \text{ keV}$  is due to the Compton background from the 803 keV  $\gamma$ -branch. Because the photons from the 803 keV branch are detected in coincidence with the corresponding  $\alpha$  particles they are strongly suppressed in the random spectra. Therefore a different method has to be applied in order to model this contribution.

The peak from the 803 keV  $\gamma$ -branch is again broadened due to the projection but it has a slightly different form than the peak from the chance coincidences. Again a fit function consisting of six equidistant Gaussian with their corresponding low and high energy tails is used. The absolute areas of the Gaussians are fitted to the spectrum whereas the structure of tails is taken from the fit of the random spectrum and held constant.

The resulting function  $b_{gc}(\tilde{E})$  again describes the contribution very well as shown figure 5.15 (green line).

### Modelling of the Compton Background due to Higher Energy Bremsstrahlung

The upper part of figure 5.16 displays the 2-dimensional  $E_\alpha$  versus  $E_\gamma$  plot of simulated bremsstrahlung events using the quantum mechanical model. The projection on the  $\tilde{E}$  axis is shown for a specific energy bin (here  $190 \text{ keV} < E_\gamma < 210 \text{ keV}$ ) in the lower part of figure 5.16.

Using ideal detectors all bremsstrahlung events would lie on the  $E_\alpha + 206/210 \cdot E_\gamma = E_{\alpha,0}$  diagonal in the the 2-dimensional  $E_\alpha$  versus  $E_\gamma$  plot. The simulated bremsstrahlung events displayed in the upper panel of figure 5.16 show that one expects a considerable number of events below this diagonal. These counts are due to (A) events in which the full  $\gamma$ -energy was detected, but the measured  $\alpha$ -energy is lower due to the effects that lead to the typical peak-form in the  $E_\alpha$  spectrum, and (B) due to events with the correct  $\alpha$ -energy, but a lower measured  $\gamma$ -energy, because the bremsstrahlung photon left the active volume of the germanium detector after Compton scattering and thus deposited only part of its energy. The comparison of the emitted bremsstrahlung energy, which is known for each event in the simulation, with the energy detected by the germanium detector allows to distinguish these effects. In the projected spectrum shown in the lower panel of figure 5.16 those bremsstrahlung events in which the full photon energy was detected are plotted in blue. The projected spectrum for these events shows the typical peak-form of the  $\alpha$ -energy peak. The red histogram shows bremsstrahlung events where the emitted energy was higher but only part of it was detected in the active volume of the detector.

To determine the number of bremsstrahlung events the first effect (A) is taken into account by fitting the bremsstrahlung peak in the projected spectrum with the  $\alpha$ -lineshape discussed above (blue spectrum in figure 5.17). To include also the second effect (B) the simulation is used to determine the function  $f_{bc}(\tilde{E})$  describing the Compton background of higher energy bremsstrahlung, and scaling it with the area of the full energy bremsstrahlung

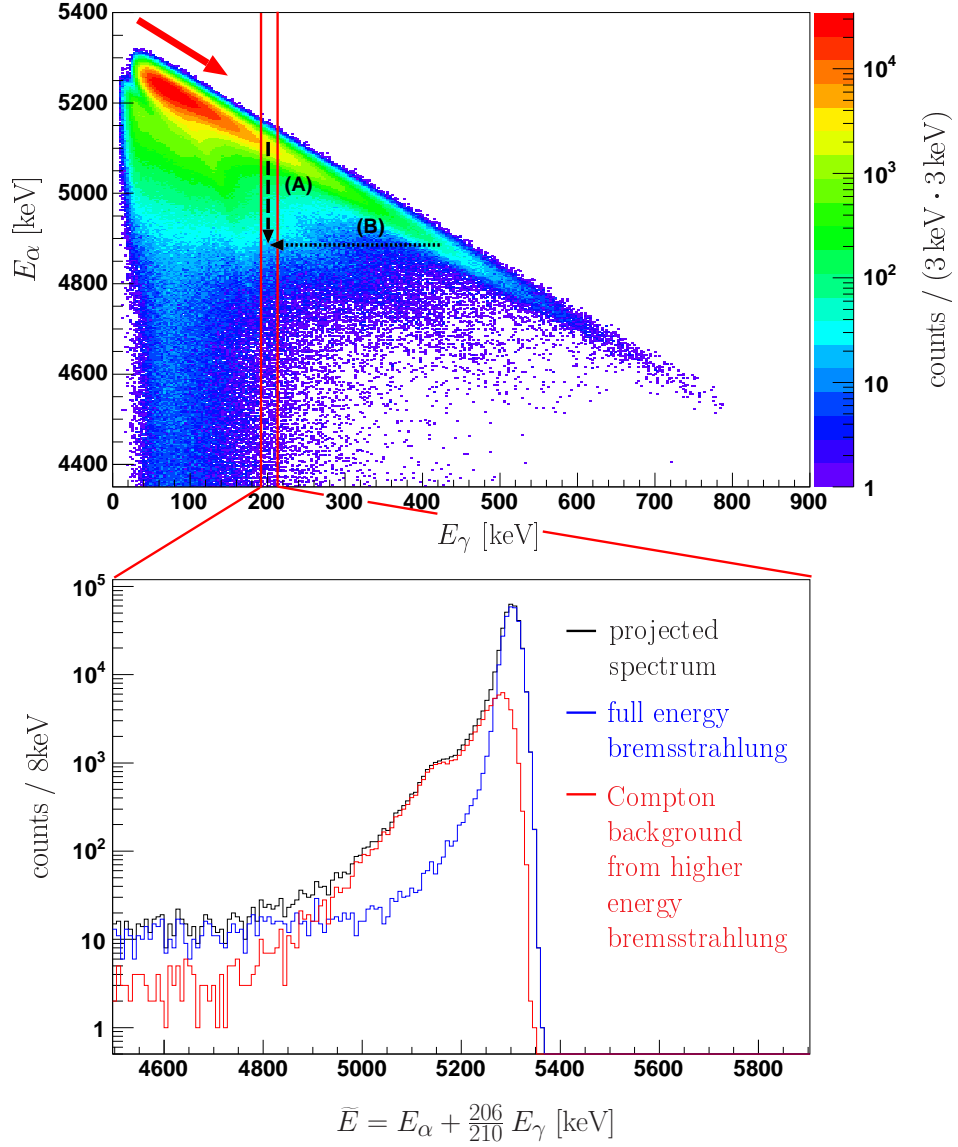


**Figure 5.16:** In the upper panel the  $E_\alpha$  versus  $E_\gamma$  plot for  $8 \cdot 10^9$  simulated bremsstrahlung events is shown. The lower panel shows the projected energy spectrum for an  $\gamma$ -energy bin of  $190 \text{ keV} < E_\gamma < 210 \text{ keV}$ . The projected energy spectrum is a superposition of bremsstrahlung events recorded in the  $\gamma$ -detector with its full  $\gamma$ -energy (blue) and of Compton events from higher energy bremsstrahlung (red).

peak (magenta spectrum in figure 5.17). This is done separately for each  $E_\gamma$  bin.

### Fitting of the Bremsstrahlung Peak

The fit function  $f_{fit}$  for the projected prompt spectrum is the sum of the four mentioned contributions. The functions  $b_{cc}(\tilde{E})$  describing the background from the chance coincidences, and the function  $b_{gc}(\tilde{E})$  describing the Compton background caused by the 803 keV  $\gamma$ -branch. The Gaussian  $g_{br}(\tilde{E}, \tilde{E}_{br})$  models the full energy bremsstrahlung events with the corresponding tails from the  $\alpha$ -lineshape scaled with the area of the Gaussian. The function  $f_{bc}(\tilde{E}, \tilde{E}_{br})$  for the Compton background from higher energy bremsstrahlung is scaled with the area  $A_{sim}$  of the fitted full energy bremsstrahlung events in the simulation.

The function  $f_{fit}$  is then given by

$$\begin{aligned} f_{fit}(\tilde{E}) = & A_{br} \left( g_{br}(\tilde{E}, \tilde{E}_{br}) + \frac{1}{A_{ref}} t_l(\tilde{E}, \tilde{E}_{br}) + \frac{1}{A_{ref}} t_h(\tilde{E}, \tilde{E}_{br}) \right. \\ & \left. + \frac{1}{A_{sim}} f_{bc}(\tilde{E}, \tilde{E}_{br}) \right) + b_{cc}(\tilde{E}) + b_{gc}(\tilde{E}) \end{aligned} \quad (5.4)$$

with the position of the bremsstrahlung peak in the projected spectrum  $\tilde{E}_{br}$  and the Gaussian  $g_{br}(\tilde{E})$

$$g_{br}(\tilde{E}, \tilde{E}_{br}) = \frac{1}{\sigma \sqrt{2\pi}} \exp \left( -\frac{1}{2} \frac{(\tilde{E} - \tilde{E}_{br})^2}{\sigma^2} \right). \quad (5.5)$$

All parameters of the  $\alpha$ -lineshape including the width  $\sigma$  are kept constant. Only the area  $A_{br}$  of the full energy bremsstrahlung and the position  $\tilde{E}_{br}$  of the peak are free fitting parameters.

Figure 5.17 shows the projected data for the  $190 \text{ keV} < E_\gamma < 210 \text{ keV}$  energy bin and a prompt time cut of  $\Delta t = 100 \text{ ns}$ . The fitted function  $f_{fit}(\tilde{E})$  describes the spectrum very well.

### Optimising the Prompt Time Window

The spectrum of the time difference  $t_\alpha - t_\gamma$  as shown in 5.10 is dominated by the coincident events from the 803 keV  $\gamma$ -branch. To analyse the shape of the coincidence peak in the time spectrum for bremsstrahlung events it is therefore necessary to constrain it to bremsstrahlung events. This done by applying the condition

$$5234 \text{ keV} < E_\alpha + \frac{210}{206} E_\gamma < 5374 \text{ keV} \wedge E_\alpha < 5220 \text{ keV}. \quad (5.6)$$

This condition selects events within a 140 keV broad band around the diagonal on which full-energy bremsstrahlung events are expected to show up.

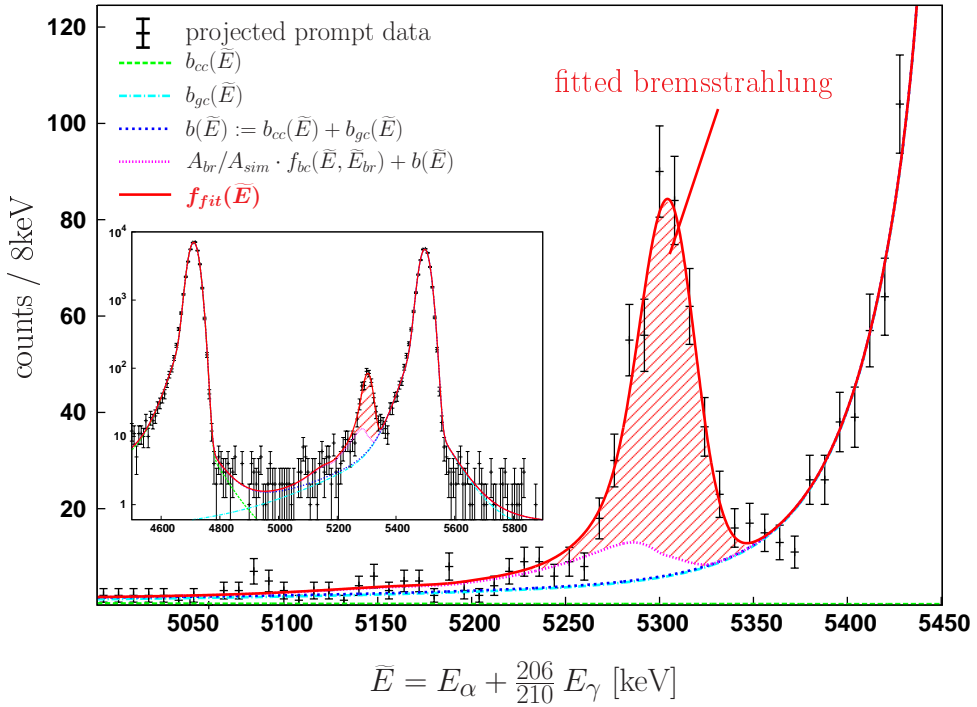


**Figure 5.17:** The projected data is fitted with the function  $f_{fit}(\tilde{E})$  ( $190 \text{ keV} \leq E_\gamma \leq 210 \text{ keV}$ ,  $\Delta t = 100 \text{ ns}$ ). This function is the sum of the bremsstrahlung peak (Gaussians with tails), the contribution of the Compton background of higher energy bremsstrahlung  $f_{bc}(\tilde{E})$  and the functions modelling the background from the chance coincidences  $b_{cc}(\tilde{E})$  and the Compton background from the 803 keV  $\gamma$ -branch  $b_{gc}(\tilde{E})$ .

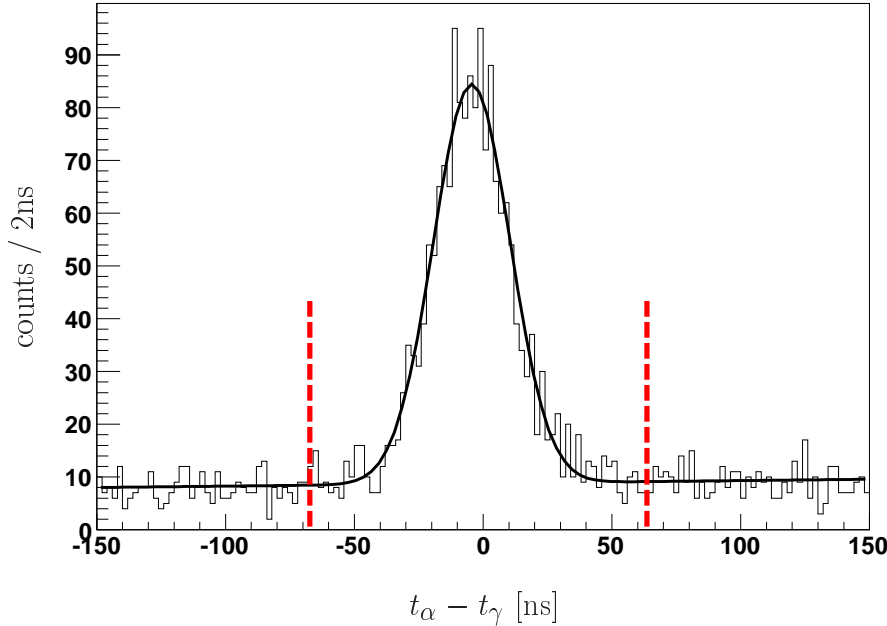


**Figure 5.18:** The spectrum of the time difference  $t_\alpha - t_\gamma$  for events in the bremsstrahlung region (equation (5.6)) and with a  $\gamma$ -energy of  $130 \text{ keV} < E_\gamma < 150 \text{ keV}$  is fitted with a Gaussian and a linear background.

As mentioned in section 5.3 the coincidence time resolution depends on the photon energy. So the prompt gate for the different  $E_\gamma$  energy bins should be adjusted individually to (A) minimise the contribution of random coincidences and to (B) avoid any efficiency losses due to too narrow gates.

The spectrum of the time difference for the energy bin  $130 \text{ keV} < E_\gamma < 150 \text{ keV}$  and condition (5.6) is shown in figure 5.18. The coincidence peak is fitted with a Gaussian and a linear background. The width  $\Delta t$  of the prompt gate used in the analysis of the corresponding energy bin is chosen to be proportional to the fitted standard deviation  $\sigma$

$$t_0 - 4.5\sigma < t_\alpha - t_\gamma < t_0 + 4.5\sigma, \quad (5.7)$$

i.e.  $\Delta t = 9\sigma$ , with  $t_0$  being the fitted position of the Gaussian. (Although  $t_0$  varies slightly with the energy bin a constant value is chosen for all energy bins). This choice of the gate window ensures that more than 99.9% of the area of the Gaussian lies within the time-cut.

Because the statistic in the region defined by equation (5.6) is very low for higher photon energies some energy bins are grouped together for the fitting procedure. In these cases for the lower energy bins within a group the gate of the preceding lower energy group is applied to ensure no bremsstrahlung events are lost. The fitted values and the gate widths chosen for each energy bin are presented in figure 5.19.

To verify the choice of the gate widths the resulting number of bremsstrahlung events was

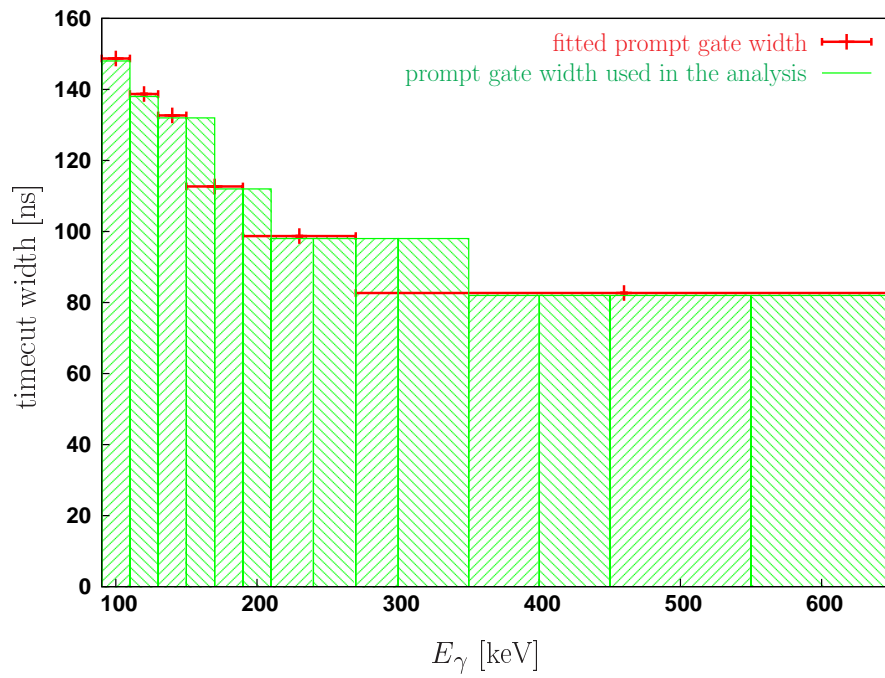


**Figure 5.19:** The red points show the  $\Delta t = 9\sigma$  prompt gate width resulting from the fitting procedure with the horizontal bars indicating the energy bins that were grouped together in the fit. The green lines show the width of the prompt gate which was used in the analysis of each of the 14 energy bins.

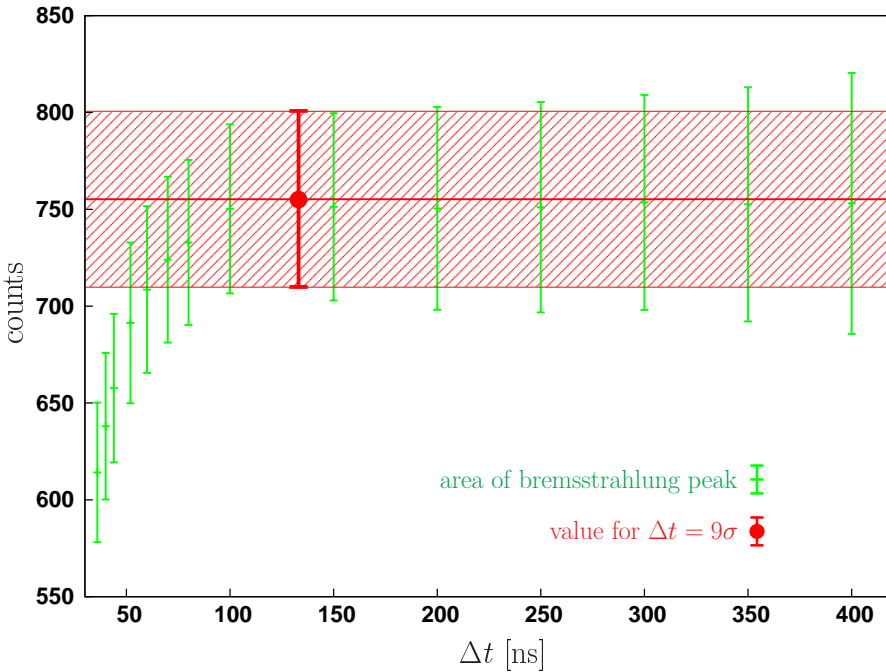


**Figure 5.20:** The area of the bremsstrahlung peak for the  $150 \text{ keV} < E_\gamma < 170 \text{ keV}$  energy bin is plotted versus the width of the prompt time gate. The red point is the number of bremsstrahlung events using a prompt time gate of  $\Delta t = 9\sigma$ .

analysed over a range of different gate widths. In Figure 5.20 the area of the bremsstrahlung peak is plotted versus the width of the prompt gate. Using  $\Delta t = 9\sigma$  is certainly sufficient to ensure that the efficiency loss due to the time cut is much smaller than the statistical error.

### Number of Observed Bremsstrahlung Events per $E_\gamma$ -Energy Bin

The fitting procedure described above was applied to each energy bin separately with the corresponding prompt gate widths. In table 5.3 the fitted bremsstrahlung area is listed for each energy bin together with the reduced  $\chi^2$  of the fit.

The number of bremsstrahlung events  $A_n^{br}$  observed in the energy bin  $n$  is connected to the total energy-differential bremsstrahlung emission probability  $(dP/dE_\gamma)_n$  by

$$\left( \frac{dP}{dE_\gamma} \right)_n = \frac{1}{\Delta E_{\gamma,n}} \cdot \frac{A_n^{br}}{\varepsilon_{\gamma,n}^c \cdot N_\alpha}, \quad (5.8)$$

where  $\Delta E_{\gamma,n}$  is the width of the energy bin  $n$ ,  $\varepsilon_{\gamma,n}^c$  is the coincident photon detection efficiency averaged over the bin  $n$ , and  $N_\alpha$  is the number of  $\alpha$  particles detected in the Si-detector. While  $N_\alpha$  can be extracted in a straight forward way from the down-scaled  $\alpha$ -singles spectra (see the following section 5.5),  $\varepsilon_{\gamma,n}^c$  can only be taken from the simulation

$E_\gamma$ bin [keV]	$A_n^{br}$	$\chi^2$
90 ... 110	2455	2.0
110 ... 130	1719	1.7
130 ... 150	1223	1.8
150 ... 170	755	1.7
170 ... 190	588	1.5
190 ... 210	368	1.6
210 ... 240	371	1.3
240 ... 270	196	1.6
270 ... 300	127	1.2
300 ... 350	93	1.2
350 ... 400	45	1.0
400 ... 450	15	1.1
450 ... 550	11	1.1

**Table 5.3:** The fitted number of bremsstrahlung events  $A_n^{br}$  is listed for each energy bin together with the reduced  $\chi^2$  of the fit (addback mode). For the error evaluation see section 5.7.

once the  $\alpha$ - $\gamma$  angular correlation is known (see section 4.3); information about the  $\alpha$ - $\gamma$  angular correlation is deduced from the present measurement in section 5.6.

## 5.5 The Down-scaled $\alpha$ -Singles Spectra

The number of down-scaled  $\alpha$  singles detected in the two silicon detectors is used to deduce the total number of  $\alpha$  particles incident on the silicon detectors. The  $\alpha$ -energy spectrum of the down-scaled  $\alpha$  singles is fitted using the  $\alpha$ -lineshape derived from the random spectrum. (see section 5.4.1 and appendix C.1).

During the time of data taking the down-scale factor was changed from time to time because of the exponential decay of the  $\alpha$  source. Therefore the data is grouped according to the down-scale factor and fitted separately.

Figure 5.21 shows the fit of the first group of data with down-scale factor  $2^{11}$ . Table 5.4 compiles the resulting values. The total number of  $\alpha$  particles which were recorded by the two Si-detectors is  $4.311(2) \cdot 10^{11}$ .

With a detection efficiency of the Si-detectors of about 12% the total number of  $\alpha$  decays is  $\sim 3.59 \cdot 10^{12}$ .

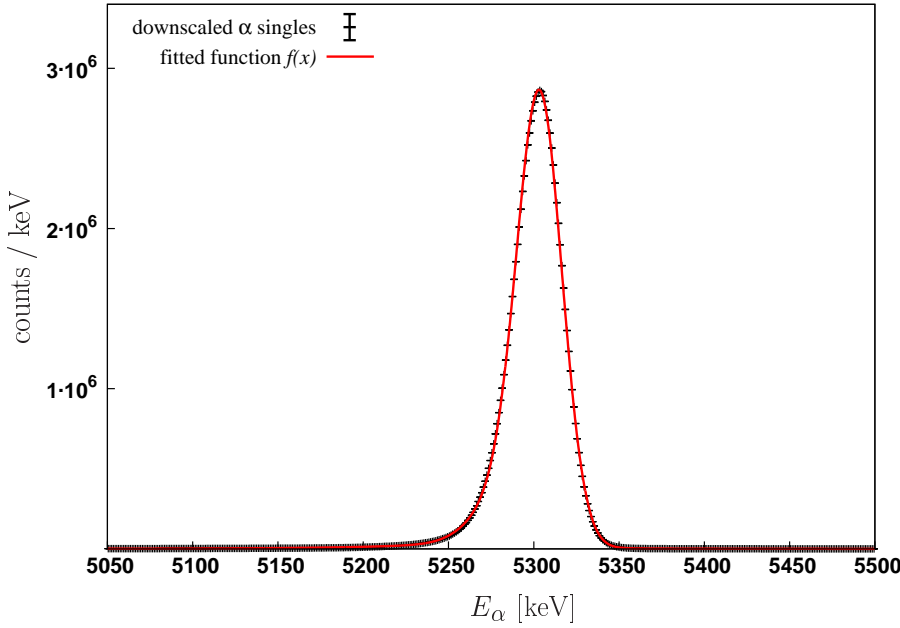


**Figure 5.21:** The  $\alpha$ -energy spectrum of the down-scaled  $\alpha$ -singles is fitted using the reference  $\alpha$ -lineform. The fitted area multiplied with the down-scale factor gives total number of  $\alpha$  particles incident on the detector.

run number	ds factor	ds $\alpha$ singles	fit error	$\alpha$ singles	fit error
406 ... 500	$2^{11}$	$1.053 \cdot 10^8$	$7.9 \cdot 10^4$	$2.157 \cdot 10^{11}$	$1.6 \cdot 10^8$
504 ... 562	$2^{10}$	$1.120 \cdot 10^8$	$6.5 \cdot 10^4$	$1.147 \cdot 10^{11}$	$6.7 \cdot 10^7$
616 ... 765	$2^6$	$1.574 \cdot 10^9$	$1.5 \cdot 10^6$	$1.007 \cdot 10^{11}$	$9.4 \cdot 10^7$
sum				$4.311 \cdot 10^{11}$	$2.0 \cdot 10^8$

**Table 5.4:** The number of  $\alpha$  particles recorded by the silicon detectors is given by the fitted area of detected down-scaled (ds)  $\alpha$ -singles multiplied by the down-scale factor.

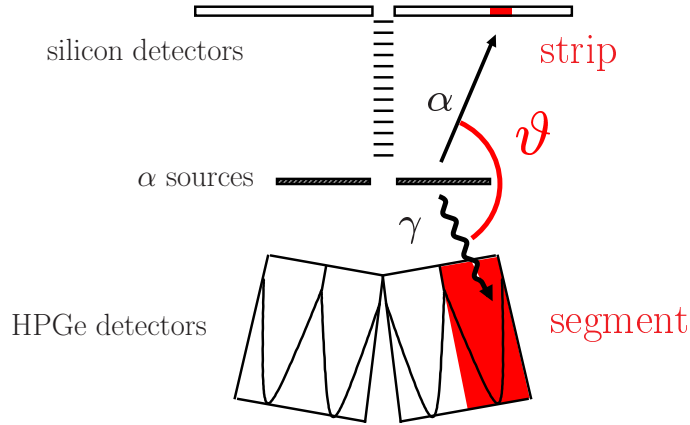


**Figure 5.22:** Through the segmentation of the silicon detectors and the HPGe cluster detector the angle  $\vartheta$  between the direction of the  $\alpha$  particle and the photon can be deduced.

## 5.6 Analysis of the Angular Distribution

The present setup was not designed to measure the angular correlation  $f_{\gamma}(E_{\gamma}, \vartheta)$  between the direction of the  $\alpha$  particle and the direction of the bremsstrahlung photon; in fact, the setup was optimised to follow the bremsstrahlung emission probability up to the highest possible  $\gamma$ -energies. Nevertheless, the segmentation of the  $\alpha$ - and  $\gamma$ -detectors allow together with the simulation program (discussed in section 4.1) to draw some conclusions about  $f_{\gamma}(E_{\gamma}, \vartheta)$ . This analysis became necessary as it turned out during the course of the present experiment that only a non-relativistic calculation of the  $\alpha$ - $\gamma$  angular correlation will be available, which is not sufficient to describe correctly the  $\alpha$ - $\gamma$  angular correlation as discussed in chapter 2.

Figure 5.22 shows how the angle  $\vartheta$  between the direction of the  $\alpha$  particle and the photon can be estimated from the strip of the silicon detector hit by the  $\alpha$  particle and from the segment of the HPGe cluster detector containing the largest energy deposition of the  $\gamma$ -ray (main interaction approximation [59]). Combining the 18 segments of the HPGe cluster detector ( $h_m$ ,  $m = 1 \dots 18$ ) and the 32 strips of the silicon detectors ( $s_n$ ,  $n = 1 \dots 32$ ) we obtain 576 individual segment-strip pairs ( $P_{m,n}$ ,  $m = 1 \dots 18$ ,  $n = 1 \dots 32$ ) covering a  $\vartheta$ -range of  $60^\circ \lesssim \vartheta \leq 180^\circ$  (note that each Si-detector only sees one of the  $\alpha$ -sources).

To obtain information about the  $\alpha$ - $\gamma$  angular correlation we compare the number of events detected per segment-strip pair,  $N_{m,n}^{exp}$ , to the number of simulated events,  $N_{m,n}^{sim(iso)}$ , assuming in the simulation an isotropic  $\alpha$ - $\gamma$  angular correlation.

Using the simulated contribution to  $P_{m,n}$ , we can define an average angle of isotropic emission  $\vartheta_{m,n}^{sim}$  between the direction of the simulated  $\alpha$  particle and the corresponding photon for this segment-strip pair, defined as the angle between the averaged direction of

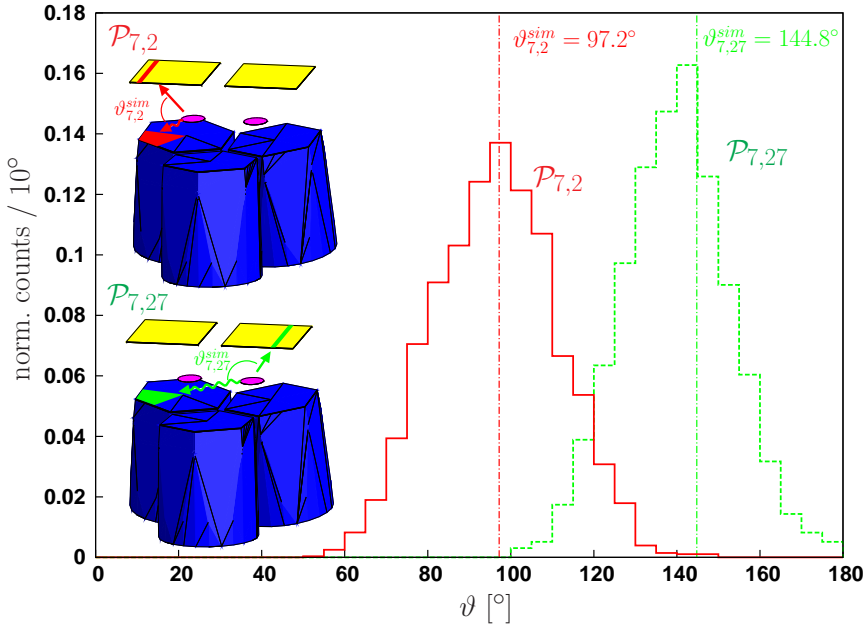


**Figure 5.23:** The simulated  $\vartheta$ -distributions and the corresponding average angle are shown for the segment-strip pairs  $\mathcal{P}_{7,2}$  and  $\mathcal{P}_{7,27}$  ( $E_\gamma = 803$  keV).

the  $\alpha$  particles  $\overline{\mathbf{p}}^\alpha_{m,n}$  and the averaged direction of the photons  $\overline{\mathbf{p}}^\gamma_{m,n}$

$$\vartheta_{m,n}^{\text{sim}} := \angle(\overline{\mathbf{p}}^\alpha_{m,n}, \overline{\mathbf{p}}^\gamma_{m,n}) . \quad (5.9)$$

In figure 5.23 the simulated  $\vartheta$ -distributions are shown for the segment-strip pairs  $\mathcal{P}_{7,2}$  and  $\mathcal{P}_{7,27}$  together with the corresponding average angle  $\vartheta_{7,2}^{\text{sim}}$  and  $\vartheta_{7,27}^{\text{sim}}$ .

Due to the close geometry of the present setup the  $\vartheta$ -resolution per segment-strip pair is only moderate ( $\text{FWHM} \sim 30^\circ - 40^\circ$ ), but should be still sufficient to gain information on the  $\alpha$ - $\gamma$  angular correlation function.

In view of the limited statistic and the moderate  $\vartheta$ -resolution of the  $\mathcal{P}_{m,n}$  we further combine the segment-strip pairs according to the average angle  $\vartheta_{m,n}^{\text{sim}}$  into  $\vartheta$ -bins  $\mathcal{B}_i$  of  $10^\circ$  width. The number of segment-strip pairs grouped together varies for the different bins and is shown in figure 5.24. Figure 5.25 shows the simulated  $\vartheta$ -distribution for four of the  $\vartheta$ -bins  $\mathcal{B}_i$ ; note that the resolution is only slightly deteriorated compared to that of the corresponding segment-strip pairs shown in figure 5.23.

We define the simulated isotropic detection ratio  $r_i^{\text{sim(iso)}}$  for bin  $\mathcal{B}_i$  as

$$r_i^{\text{sim(iso)}} := \frac{N_i^{\text{sim(iso)}}}{N^{\text{sim(iso)}}} , \quad (5.10)$$

where  $N^{\text{sim(iso)}}$  is the total number of simulated events assuming an isotropic  $\alpha$ - $\gamma$  angular

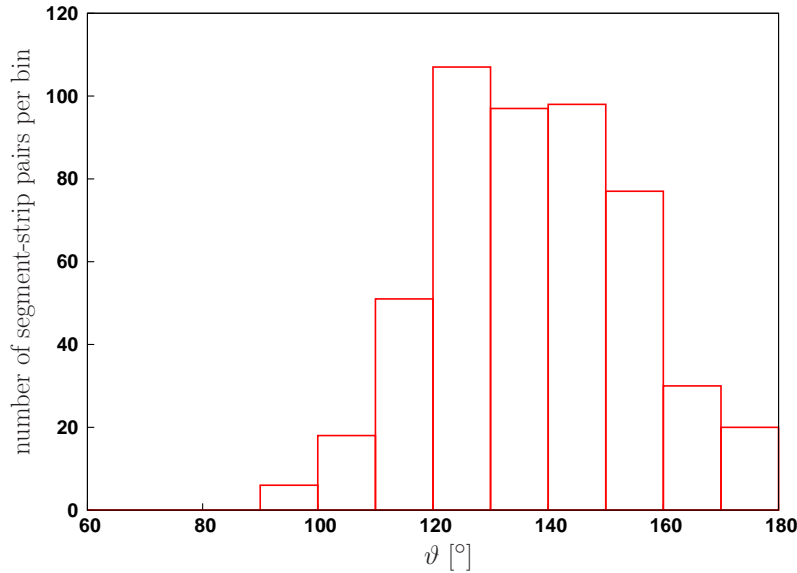


**Figure 5.24:** The segment-strip pairs are grouped according to their average angle  $\vartheta_{m,n}^{\text{sim}}$  into  $10^\circ$  wide bins. The number of segment-strip pairs per bin is shown for an simulation assuming an isotropic  $\alpha$ - $\gamma$  angular correlation and a photon energy of  $E_\gamma = 803$  keV.

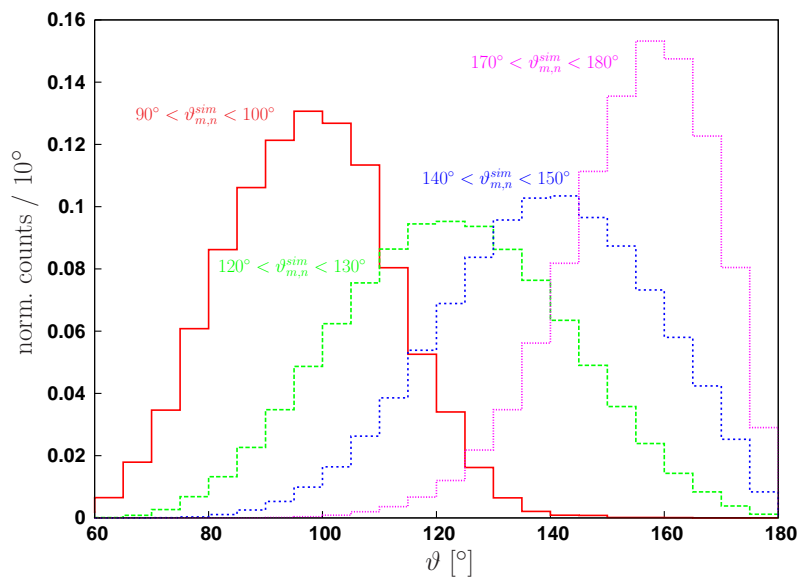


**Figure 5.25:** The simulated  $\vartheta$ -distributions for four segment-strip bins  $\mathcal{B}_i$  are shown ( $E_\gamma = 803$  keV).

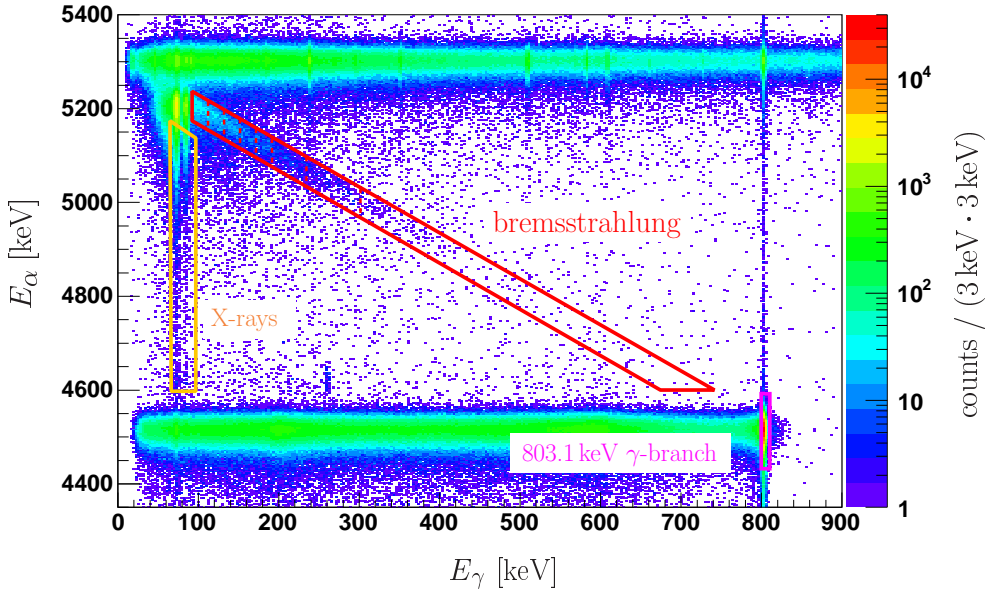


**Figure 5.26:** The data for the analysis of the angular correlation of the 803 keV  $\gamma$ -branch, the X-rays from the source and the bremsstrahlung events is selected from the prompt data by cuts in the  $\gamma$ - and  $\alpha$ -energy. The bremsstrahlung data is grouped into  $\gamma$ -energy bins. The background is corrected using the same energy cuts in the random data scaled with the widths of the prompt and the random time window.

correlation and  $N_i^{sim(iso)}$  is the number of simulated events contributing to the segment-strip bin  $\mathcal{B}_i$

$$N_i^{sim(iso)} := \sum_{\mathcal{P}_{m,n} \in \mathcal{B}_i} \mathcal{N}_{m,n}^{sim(iso)}. \quad (5.11)$$

The measured ratio  $r_i^{exp}$  is defined accordingly as the number of events detected in bin  $\mathcal{B}_i$ , divided by the total number of detected events  $N^{exp}$ , that is

$$r_i^{exp} := \frac{N_i^{exp}}{N^{exp}} \quad , \text{ with} \quad N_i^{exp} := \sum_{\mathcal{P}_{m,n} \in \mathcal{B}_i} \mathcal{N}_{m,n}^{exp}. \quad (5.12)$$

The angular correlation averaged over the  $\vartheta$ -distribution of bin  $\mathcal{B}_i$  is then given by

$$\overline{f_{\not\propto}(\vartheta_i)} = \left( \frac{d\overline{P}}{d\Omega} \right)_i \propto \frac{r_i^{exp}}{r_i^{sim(iso)}}. \quad (5.13)$$

### Test of the Angular Correlation Extraction Procedure

The above procedure to extract the  $\alpha$ - $\gamma$  angular correlation from the data was first checked using (a) the K X-rays emitted after the kick-out of the K-electron from  $^{206}\text{Pb}$  by the

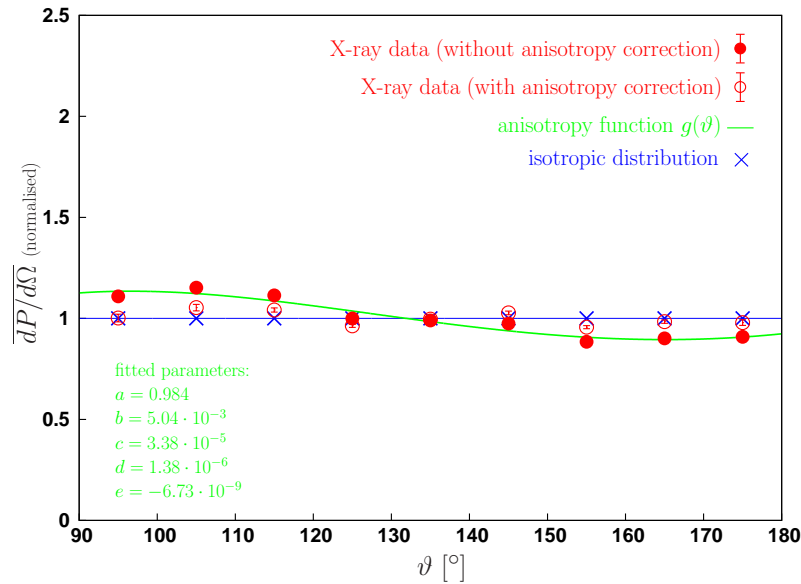


**Figure 5.27:** The X-rays following the  $\alpha$  decay of  $^{210}\text{Po}$  are expected to be emitted isotropically. Therefore the X-ray data is used to correct for the anisotropy of the setup. A polynomial function  $g(x) = a + b(\vartheta - \xi) + c(\vartheta - \xi)^2 + d(\vartheta - \xi)^3 + e(\vartheta - \xi)^4$  is fitted to the data ( $\xi$  is chosen to be  $135^\circ$ ) and used to correct the simulated detection ratios  $r_i^{\text{sim(iso)}}$ . The corrected data is shown by the open symbols.

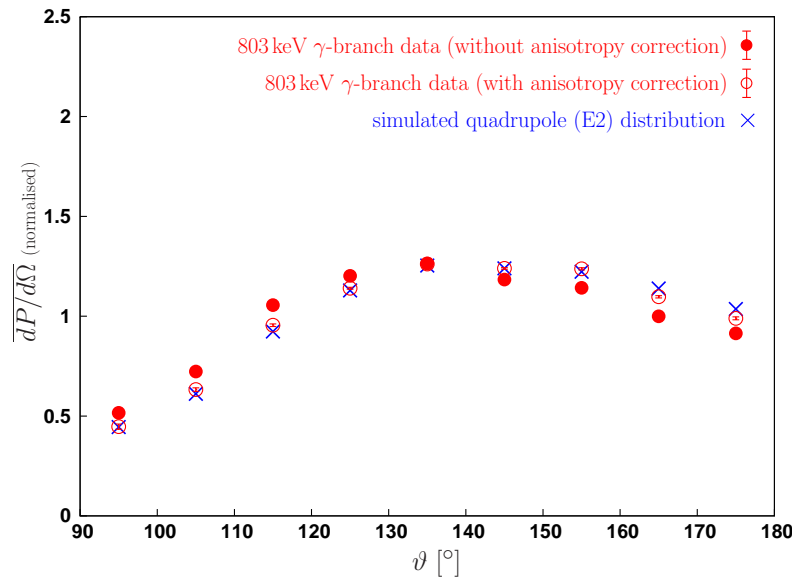


**Figure 5.28:** The angular correlation for the 803 keV  $\gamma$ -branch is compared to a simulated quadrupole distribution. The anisotropy corrected data is in excellent agreement with the simulated quadrupole distribution.

emitted  $\alpha$ , and (b) using the 803 keV transition following the  $\alpha$  decay of  $^{210}\text{Po}$  to  $^{206}\text{Pb}(2^+)$ . As the recoil velocity of  $^{206}\text{Pb}$  is very small, we expect for the sum over all K X-rays an isotropic  $\alpha$ - $\gamma$  angular correlation in the laboratory system, while the correlation of the 803 keV transition will be governed by a pure E2 quadrupole distribution of the form  $\cos^2 \vartheta \cdot \sin^2 \vartheta$ .

Figure 5.27 and 5.28 show the measured correlation functions for the X-rays and the 803 keV transition, respectively. The selection energy cuts are shown in figure 5.26; in both cases the random background from the random time gate is subtracted scaled with the widths of the prompt and random time window.

As displayed in figure 5.27 the deduced correlation for the X-rays slightly deviate ( $< 10\%$ ) from the expected isotropic distribution. These deviations are attributed to deficiencies of the simulations, which were found to be very sensitive to small deviations of the geometry of the simulated from the real setup. To correct for it we define an anisotropy function  $g(\vartheta)$  by

$$g(\vartheta) = a + b(\vartheta - \xi) + c(\vartheta - \xi)^2 + d(\vartheta - \xi)^3 + e(\vartheta - \xi)^4. \quad (5.14)$$

where  $\xi$  was chosen to be  $135^\circ$ . The parameters of which were determined by fitting  $g(\vartheta)$  to the measured X-ray correlation as shown in figure 5.27. In the following we will apply this function to correct all simulated detection ratios  $r_i$ . For the K X-rays data this results in the open symbols, which scatter only within their error margins around the isotropic distribution.

The validity of the anisotropy correction is further tested using the 803 keV transition. Applying the same anisotropy factor in the extraction of the measured  $\alpha$ - $\gamma$  correlation, the resulting distribution is in perfect agreement with the simulated distribution assuming a pure E2 quadrupole correlation, which is calculated, in analogy to equation (5.13), by  $r_i^{sim(E2)} / r_i^{sim(iso)}$ . This gives confidence that the extraction procedure should be well under control also for  $\gamma$ -energies between 80 keV and 800 keV.

### Angular Correlation of the Bremsstrahlung

To get information about the angular correlation of the bremsstrahlung in dependence of the  $\gamma$ -energy the bremsstrahlung data is grouped into  $\gamma$ -energy bins as illustrated in figure 5.26. For each of these bins the angular correlation is analysed separately.

The background is corrected using the same energy gates in the  $E_\alpha$  versus  $E_\gamma$  matrix for the random data scaled with the widths of the prompt time window  $\Delta t^{exp}$  and the random time window  $\Delta t^{bg}$

$$r_i^{br} := \frac{N_i^{exp} - g \cdot N_i^{bg}}{N_i^{exp} - g \cdot N_i^{bg}} \quad , \text{ with} \quad g = \frac{\Delta t^{exp}}{\Delta t^{bg}}. \quad (5.15)$$

In figure 5.29 the distribution  $r_i^{exp} / r_i^{sim(iso)}$  and the resulting background free correlation

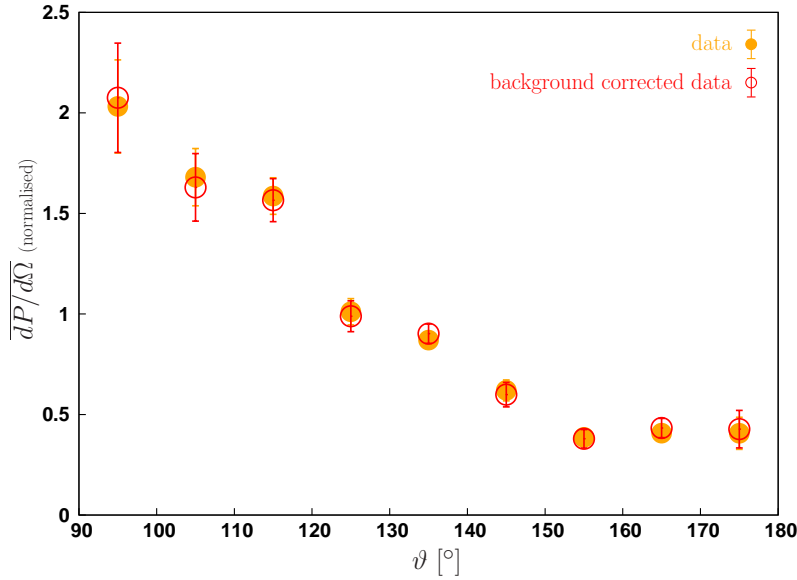


**Figure 5.29:** Experimental angular correlation for bremsstrahlung events with  $130 \text{ keV} < E_\gamma < 150 \text{ keV}$  (orange points) and the resulting background free correlation (red circles) are shown in comparison (without anisotropy correction).

$(\overline{dP/d\Omega})_i^{br} = r_i^{br}/r_i^{sim(iso)}$  for bremsstrahlung events with  $130 \text{ keV} < E_\gamma < 150 \text{ keV}$  are displayed.

The background free, anisotropy corrected and normalised angular correlations are then compared to simulations assuming an  $\alpha$ - $\gamma$  angular correlation function of the form (see sections 2.3 and 2.5)

$$f_{\mathcal{A}}(E_\gamma, \vartheta) = \sin^2 \vartheta (1 + 2\Lambda(E_\gamma) \cos \vartheta). \quad (5.16)$$

For each bin the angular distribution is simulated for a set of different values for  $\Lambda$ . In figure 5.30 the angular correlation data for bremsstrahlung in the energy region  $130 \text{ keV} < E_\gamma < 150 \text{ keV}$  is compared to simulated distributions for 5 different  $\Lambda$  values.

The best value for  $\Lambda$  is determined by a chi-square minimising algorithm. The reduced chi-square  $\chi_{red}^2$  here is given by

$$\chi_{red,\Lambda}^2 = \frac{\chi_\Lambda^2}{\nu}, \quad \text{with} \quad \chi_\Lambda^2 = \sum_{i=1}^n \frac{\left( \left( \overline{dP/d\Omega} \right)_i^{br} - \zeta \cdot \left( \overline{dP/d\Omega} \right)_i^{sim(\Lambda)} \right)^2}{\left( \sigma_i^{br} \right)^2}, \quad (5.17)$$

where  $(\overline{dP/d\Omega})_i^{br}$  is the angular correlation of the bremsstrahlung data,  $\sigma_i^{br}$  the corresponding uncertainty, and  $(\overline{dP/d\Omega})_i^{sim(\Lambda)}$  is the simulated angular correlation with the value  $\Lambda$ . The normalisation factor  $\zeta$  is a free parameter optimised in the fit. The number of degrees of freedom  $\nu$  is equal to the number of bins  $n$  minus two.

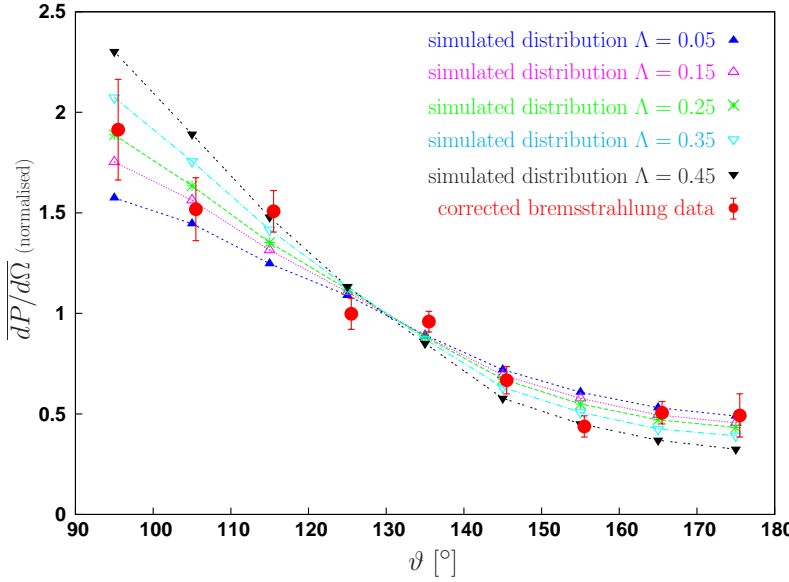


**Figure 5.30:** The background and anisotropy corrected angular correlation for bremsstrahlung events in the  $\gamma$ -energy bin  $130 \text{ keV} < E_\gamma < 150 \text{ keV}$  is compared to the simulated angular distribution assuming  $f_{\mathcal{A}}(E_\gamma, \vartheta) = \sin^2 \vartheta (1 + 2\Lambda \cos \vartheta)$  and five different values for  $\Lambda$ .

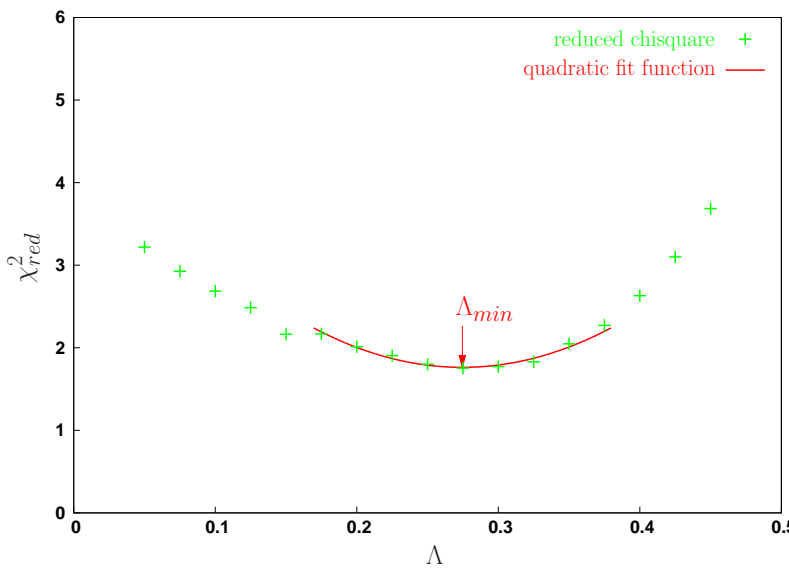


**Figure 5.31:** The reduced chi-square defined in equation (5.17) is plotted in dependence of the parameter  $\Lambda$  (here the data for the  $\gamma$ -energy bin  $130 \text{ keV} < E_\gamma < 150 \text{ keV}$  is shown). The value  $\Lambda_{min}$  minimising  $\chi^2_{red}$  is determined by the fit of a quadratic polynomial.

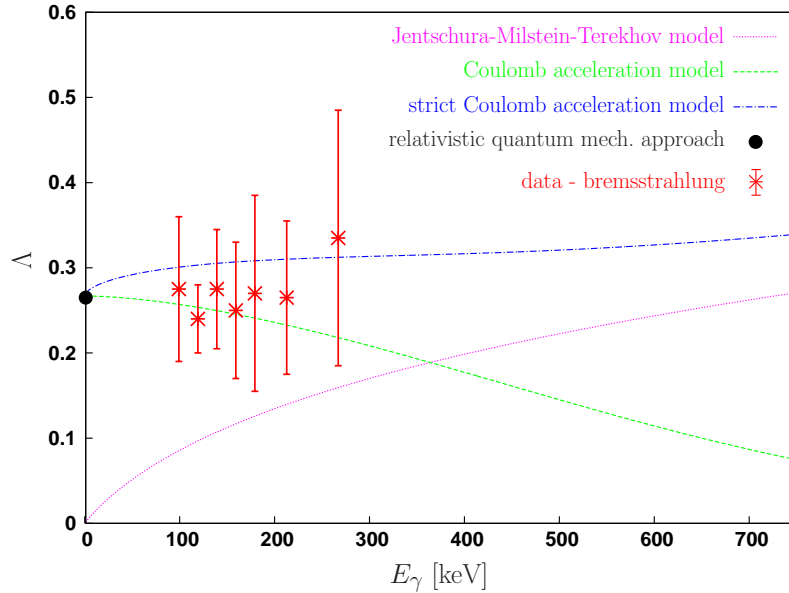


**Figure 5.32:** The parameter  $\Lambda$  derived from the experimental data of the bremsstrahlung is plotted versus the  $\gamma$ -energy. The theoretical predictions of the Jentschura-Milstein-Terekhov model (magenta), of the Coulomb acceleration model (green), of the strict Coulomb acceleration model (blue), and of the relativistic quantum mechanical approach valid for  $E_\gamma \rightarrow 0$  [35] (black point) are shown in comparison to the data.

In figure 5.31 the reduced chi-square is plotted in dependence of the parameter  $\Lambda$  for the  $\gamma$ -energy bin  $130 \text{ keV} < E_\gamma < 150 \text{ keV}$ . The  $\Lambda$  value minimising  $\chi^2_{\text{red}}$  is determined by the fit of a quadratic polynomial.

The derived  $\Lambda$  values for the bremsstrahlung are plotted versus the  $\gamma$ -energy  $E_\gamma$  in figure 5.32. The uncertainties are taken from the  $\chi^2_{\text{red}}$  minimisation algorithm. These uncertainties are estimated in a standard procedure [60], where  $\Delta\Lambda$  is given by

$$\Delta\Lambda = \sqrt{\chi^2_{\text{red}}(\Lambda_{\min})} \cdot \delta\Lambda \quad (5.18)$$

and  $\delta\Lambda$  is defined by the condition

$$\chi^2(\Lambda_{\min} + \delta\Lambda) = \chi^2(\Lambda_{\min}) + 1. \quad (5.19)$$

In figure 5.32 the experimental results for  $\Lambda(E_\gamma)$  are also compared to various theoretical predictions. In the non-relativistic semi-classical calculation of Jentschura-Milstein-Terekhov [21]  $\Lambda(E_\gamma)$  is only due to the E2-quadrupole amplitude in the bremsstrahlung emission probability, which is expected to vanish for  $E_\gamma \rightarrow 0$ . This is clearly falling short to explain the measured values of  $\Lambda$ . The data rather seem to approach the  $\Lambda$ -value of 0.27, that is the  $E_\gamma \rightarrow 0$  limit of the classical relativistic calculations (Coulomb acceleration and strict Coulomb acceleration model), which was shown to be identical to the  $E_\gamma \rightarrow 0$  limit

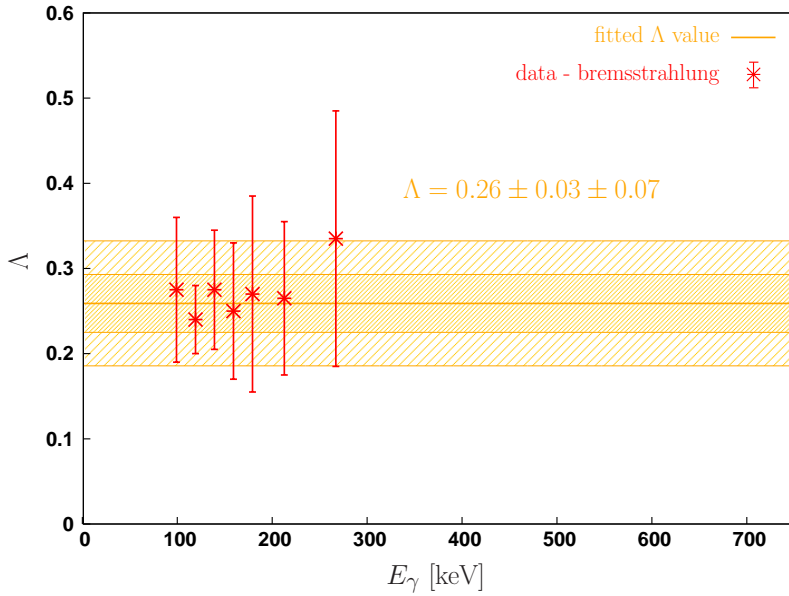


**Figure 5.33:** The experimental data does not allow to draw a sustainable conclusions on the  $\gamma$ -energy dependence of the  $\Lambda$  value. Therefore a constant was fitted to the data. The shown error is the combined of the error of the data points and an estimated systematical error of 25%.

of a relativistic quantum mechanical calculation [35]. Unfortunately the experimental  $\Lambda$  values are not accurate enough to draw any sustainable conclusion on their  $E_\gamma$ -dependence. Therefore a constant value was fitted to the data as shown in figure 5.33. The error band is given by the error of the data points and an additional systematical error estimated to 25%.

## 5.7 The Energy-Differential Bremsstrahlung Emission Probability

We have now determined all ingredients required to calculate the energy-differential bremsstrahlung emission probability  $dP/dE_\gamma$  according to equation (5.8) from the number of bremsstrahlung events given in table 5.3.

The total number of  $\alpha$  particles detected was determined in section 5.5 to be

$$N_\alpha = 4.311(2) \cdot 10^{11} .$$

The coincident photon detection efficiency  $\varepsilon_\gamma^c(E_\gamma)$  was simulated for  $\Lambda(E_\gamma) = \Lambda_{exp} = 0.26 \pm 0.07$ . The result is plotted in figure 5.34 together with its error band, which is determined by the estimated error of the simulation and the error of  $\Lambda_{exp}$ . The coincident

$E_\gamma$ range [keV]	$\Delta E_\gamma$ [keV]	$\overline{E_\gamma}$ [keV]	counts	$\varepsilon_{\gamma, \Lambda(\text{exp})}^c$	$(dP/dE_\gamma)_n$ [keV $^{-1}$ ]
90 ... 110	20	99	2455	10.6	2.68(8)(34) 10 $^{-9}$
110 ... 130	20	119	1719	11.3	1.76(5)(20) 10 $^{-9}$
130 ... 150	20	139	1223	11.2	1.27(4)(13) 10 $^{-9}$
150 ... 170	20	159	755	10.6	8.24(35)(87) 10 $^{-10}$
170 ... 190	20	179	588	9.9	6.89(33)(72) 10 $^{-10}$
190 ... 210	20	199	368	9.3	4.61(28)(48) 10 $^{-10}$
210 ... 240	30	224	371	8.7	3.31(20)(34) 10 $^{-10}$
240 ... 270	30	254	196	7.9	1.92(16)(20) 10 $^{-10}$
270 ... 300	30	284	127	7.3	1.35(13)(14) 10 $^{-10}$
300 ... 350	50	323	93	6.6	6.51(78)(69) 10 $^{-11}$
350 ... 400	50	373	45	5.9	3.51(63)(38) 10 $^{-11}$
400 ... 450	50	423	15	5.4	1.28(43)(15) 10 $^{-11}$
450 ... 550	100	493	11	4.9	5.2(26)(7) 10 $^{-12}$

**Table 5.5:** The bremsstrahlung emission probability evaluated with the coincident photon detection efficiency  $\varepsilon_{\gamma, \Lambda_{\text{exp}}}^c(E_\gamma)$  (addback mode) assuming  $\Lambda(E_\gamma) = \Lambda_{\text{exp}} = 0.26 \pm 0.07$ .  $\overline{E_\gamma}$  denotes the weighted energy of the  $\gamma$ -energy bin discussed in the main text. In brackets the statistical error (first bracket) and the systematic error (second bracket) are given. For details of the error evaluation see table 5.6.

**Table 5.6:** The statistical error is derived from the number of counts in the bremsstrahlung peak and the background below. For the systematic error the contributions from the background modelling and the detection efficiency is taken into account.

$E_\gamma$ range [keV]	90 · 110	110 · 130	130 · 150	150 · 170	170 · 190	190 · 210	210 · 240	240 · 270	270 · 300	300 · 350	350 · 400	400 · 450	450 · 550
<b>statistical error</b>													
bremsstrahlung $\mathcal{B}$	2455	1719	1223	755	588	368	371	196	127	93	45	15	11
Compton contrib. $\mathcal{C}$	829	498	289	142	97	48	46	18	8.4	5.4	1.7	0.4	0.3
random background $\mathcal{R}$	1274	654	368	180	112	79	80	44	21	29	18	10	19
absolute error $\Delta\mathcal{B}$	68	54	43	33	28	22	22	16	13	11	8.0	5.0	5.5
rel. statistical error $\Delta\mathcal{B}/\mathcal{B}$	<b>2.8%</b>	<b>3.1%</b>	<b>3.5%</b>	<b>4.3%</b>	<b>4.8%</b>	<b>6.0%</b>	<b>6.0%</b>	<b>8.2%</b>	<b>9.8%</b>	<b>12%</b>	<b>18%</b>	<b>34%</b>	<b>50%</b>
<b>systematic error from the background modelling</b>													
bremsstrahlung $\mathcal{B}$	2455	1719	1223	755	588	368	371	196	127	93	45	15	11
Compton $\mathcal{C}$	829	498	289	142	97	48	46	18	8.4	5.4	1.7	0.4	0.3
estimated uncertainty $\Delta\mathcal{C}/\mathcal{C}$	10%	10%	10%	10%	10%	10%	10%	10%	10%	10%	10%	10%	10%
absolute error $\Delta\mathcal{C}$	83	50	29	14	9.7	4.8	4.6	1.8	0.8	0.5	0.2	0.04	0.03
background $\mathcal{R}$	1274	654	368	180	112	79	80	44	21	29	18	10	19
estimated uncertainty $\Delta\mathcal{R}/\mathcal{R}$	5%	5%	5%	5%	5%	5%	5%	5%	5%	5%	5%	5%	5%
absolute error $\Delta\mathcal{R}$	64	33	18	9.0	5.6	4.0	4.0	2.2	1.1	1.5	0.90	0.50	0.95
combined abs. err. $\Delta(\mathcal{C} + \mathcal{R})/\mathcal{B}$	105	60	34	17	11	6.3	6.1	2.8	1.4	1.6	0.92	0.5	0.95
combined rel. err. $\Delta(\mathcal{C} + \mathcal{R})/\mathcal{B}$	4.3%	3.5%	2.8%	2.2%	1.9%	1.7%	1.6%	1.5%	1.1%	1.7%	2.0%	3.3%	8.6%
<b>systematic error from the efficiency simulation</b>													
$\varepsilon_\gamma^c(\Lambda_{\text{exp}})$	10.6	11.3	11.2	10.6	9.9	9.3	8.7	7.9	7.3	6.6	5.9	5.4	4.9
absolute error $\Delta\varepsilon$	1.3	1.2	1.1	1.1	1.0	0.94	0.88	0.81	0.76	0.69	0.63	0.59	0.52
relative error $\Delta\varepsilon/\varepsilon$	12%	11%	10%	10%	10%	10%	10%	10%	10%	10%	11%	11%	11%
<b>combined systematic error</b>													
rel. system. error	<b>12.8%</b>	<b>11.1%</b>	<b>10.5%</b>	<b>10.5%</b>	<b>10.4%</b>	<b>10.3%</b>	<b>10.3%</b>	<b>10.4%</b>	<b>10.5%</b>	<b>10.6%</b>	<b>10.8%</b>	<b>11.4%</b>	<b>13.7%</b>

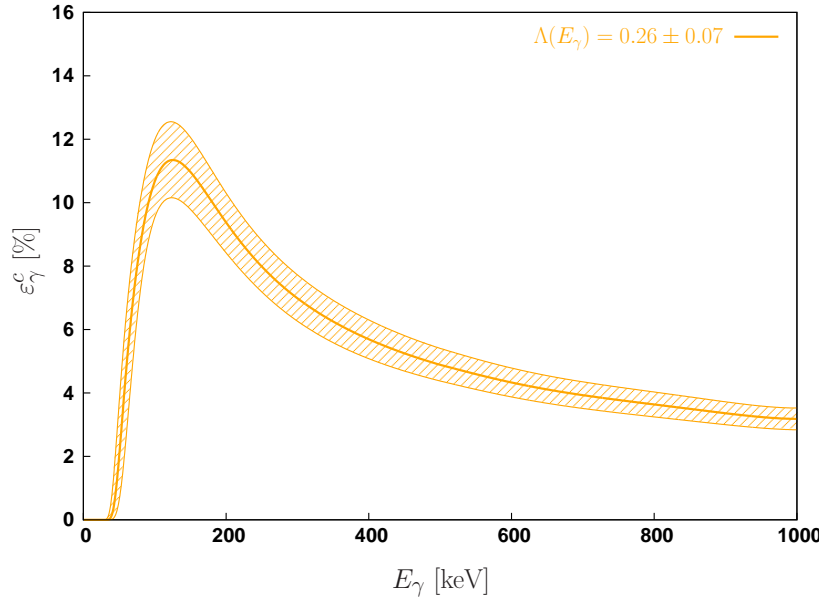


**Figure 5.34:** The simulated coincident photon detection efficiency (addback mode) assuming  $\Lambda(E_\gamma) = \Lambda_{exp} = 0.26 \pm 0.07$ . The shown error band is determined by the uncertainty of the simulation (see section 4.4) and the error of  $\Lambda_{exp}$ .

photon detection efficiencies, averaged over the  $\gamma$ -energy bins are compiled in table 5.5, while their uncertainties are given in table 5.6.

Using this input data together with equation (5.8) we obtain the bremsstrahlung emission probabilities compiled together with their statistical and systematic errors in table 5.5.

The statistical error is derived from the total number of counts in the peak area including the background beneath the peak. The background is the sum of the Compton background caused by higher energy bremsstrahlung events and the background from chance coincidences. For the background evaluation the energy range is used where the bremsstrahlung peak is above the error level of the background. The bremsstrahlung peak area, the background contributions and the resulting estimated statistical error are listed in table 5.6.

The systematic errors are due to

- (a) the modelling of the Compton contribution from higher energetic bremsstrahlung events and the description of the random background using the events from the random coincidence gate; these contributions are estimated to have an uncertainty of 10% and 5%, respectively,

and (b) due to the coincident photon detection efficiency  $\varepsilon_\gamma^c$  as discussed above.

A detailed error budget for each  $\gamma$ -energy bin is given in table 5.6.

As the emission probabilities  $dP(E_\gamma)/dE_\gamma$  are exponentially falling off with increasing  $\gamma$ -energies and the  $\gamma$ -bins used in the analysis have increasing widths  $\Delta E_\gamma$ , we also give in table 5.5 the weighted bin energies  $\overline{E}_\gamma$ . Plotting the measured emission probabilities  $(dP/dE_\gamma)_n$  at  $\overline{E}_\gamma$ , they can be directly compared to theoretical predictions calculated at  $\overline{E}_\gamma$  for an infinitesimal small energy bin  $dE_\gamma$ .  $\overline{E}_\gamma$  was determined using an exponential adjusted to the measured probabilities close to the bin of interest.

# Chapter 6

## Results and Conclusion

### 6.1 Discussion of the Experimental Results

The final experimental result for the energy-differential bremsstrahlung emission probability accompanying the  $\alpha$  decay of  $^{210}\text{Po}$ , evaluated with the experimentally derived  $\alpha$ - $\gamma$  angular correlation function as discussed in section 5.6 and listed in table 5.5, is shown in figure 6.1. The  $1\sigma$  errors shown compromise the statistical and the systematic uncertainties; they are dominated by systematic uncertainties of the detection efficiency at small and by statistical errors at high  $\gamma$ -energies. Note that the external bremsstrahlung contribution, which stems from the slowing down of  $\alpha$ -particles in the Si-detector are orders of magnitude smaller than the measured probabilities.

Also shown in figure 6.1 are the earlier experimental results obtained by Kasagi et al. [23–25]; within their errors they are consistent with the present high statistic data. However, the previous data of Eremin et al. [26, 27] are inconsistent with the present findings.

Our high statistic data also allow for a detailed comparison with theoretical calculations (see figure 6.2). Since the first order E2-contribution as well as the first order relativistic correction, which lead to the  $\cos\vartheta$  term in the  $\alpha$ - $\gamma$  angular correlation (see equation 2.13) do not contribute when integrated over the total solid angle, non-relativistic theories considering only E1 dipole radiation should give an excellent approximation for the energy differential emission probability. In fact we have shown within the semi-classical approach [21] that higher order E2 contributions to the angle-integrated emission probabilities are < 1.5% up to  $\gamma$ -energies of 500 keV, and higher order relativistic corrections are expected to be at most of the same size. Performing the non-relativistic QM calculation of Papenbrock and Bertsch [3] with the proper  $Q_\alpha$  value (see section 2.4) we obtain the solid curve in figure 6.2, which is in good agreement with our data over the full  $\gamma$ -energy range covered. Also shown is the (non-relativistic) semi-classical calculation of Dyakonov et al. [10] valid for small  $\gamma$ -energies only. We revisited this semi-classical approach [21] to enlarge its range of applicability to  $\gamma$ -energies reached in the present investigation. As discussed

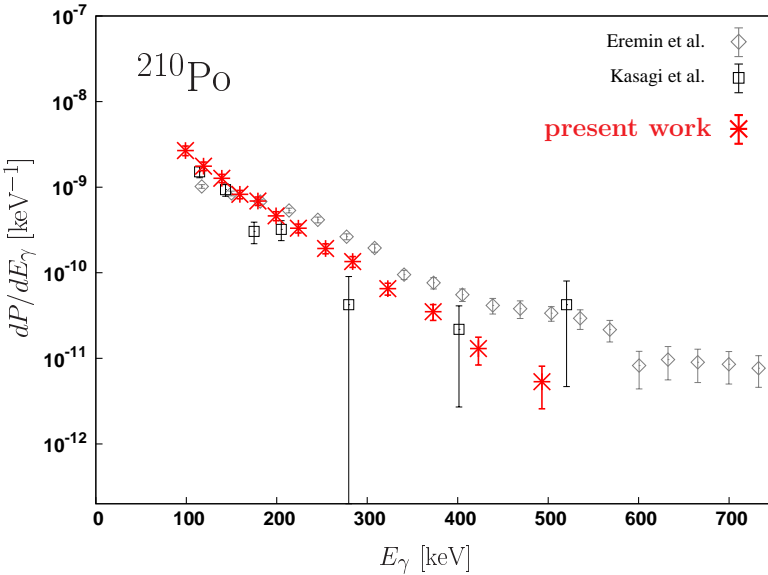


**Figure 6.1:** The measured energy-differential bremsstrahlung emission probability accompanying the  $\alpha$  decay of  $^{210}\text{Po}$  (red crosses: present work) compared to previous measurements (open squares: Kasagi et al. [23], open diamonds: Eremin et al. [26])

in section 2.5 we find the result of our improved approach to agree with the quantum mechanical prediction to better than 2% even at energies as high as 500 keV. Figure 6.2 also displays the results of two classical bremsstrahlung calculations using the Coulomb acceleration (CA) and the strict Coulomb acceleration (SCA) model (see section 2.3). While they agree as expected with the quantum mechanical calculations at small  $\gamma$ -energies, they considerably overestimate the emission probabilities at higher energies.

The evaluation of the emission probabilities from the measured data required the input of the  $\alpha$ - $\gamma$  angular correlation into the calculation of the coincident detection efficiency  $\varepsilon_\gamma^c(E_\gamma)$  of the setup. The model calculations show that the dipole correlation function, which is proportional to  $\sin^2 \vartheta$ , is considerably modified by E2- and relativistic contributions and lead to an  $\alpha$ - $\gamma$  angular correlation of the form  $\sin^2 \vartheta(1 + 2\Lambda(E_\gamma) \cos \vartheta)$ . We were able to deduce an average value for  $\Lambda$  of  $\Lambda_{exp} = 0.26 \pm 0.07$  from our data, which we used in the simulation of  $\varepsilon_\gamma^c(E_\gamma)$ . To elucidate in more detail the accuracy of the present data and its sensitivity to the  $\alpha$ - $\gamma$  angular correlation, the deviation of our data from the quantum mechanical expectation is plotted in figure 6.3 together with the corresponding difference when assuming  $\Lambda(E_\gamma) = \Lambda_{JMT}^{E2}(E_\gamma)$  (see figure 4.15) from the non-relativistic semiclassical approach of Jentschura-Milstein-Terekhov [21]. This comparison shows, in agreement with the measured value for  $\Lambda_{exp}$ , that the relativistic contribution to  $\Lambda(E_\gamma)$  is mandatory to achieve reasonable agreement between theory and experiment to an overall precision of  $\sim 10\%$ .

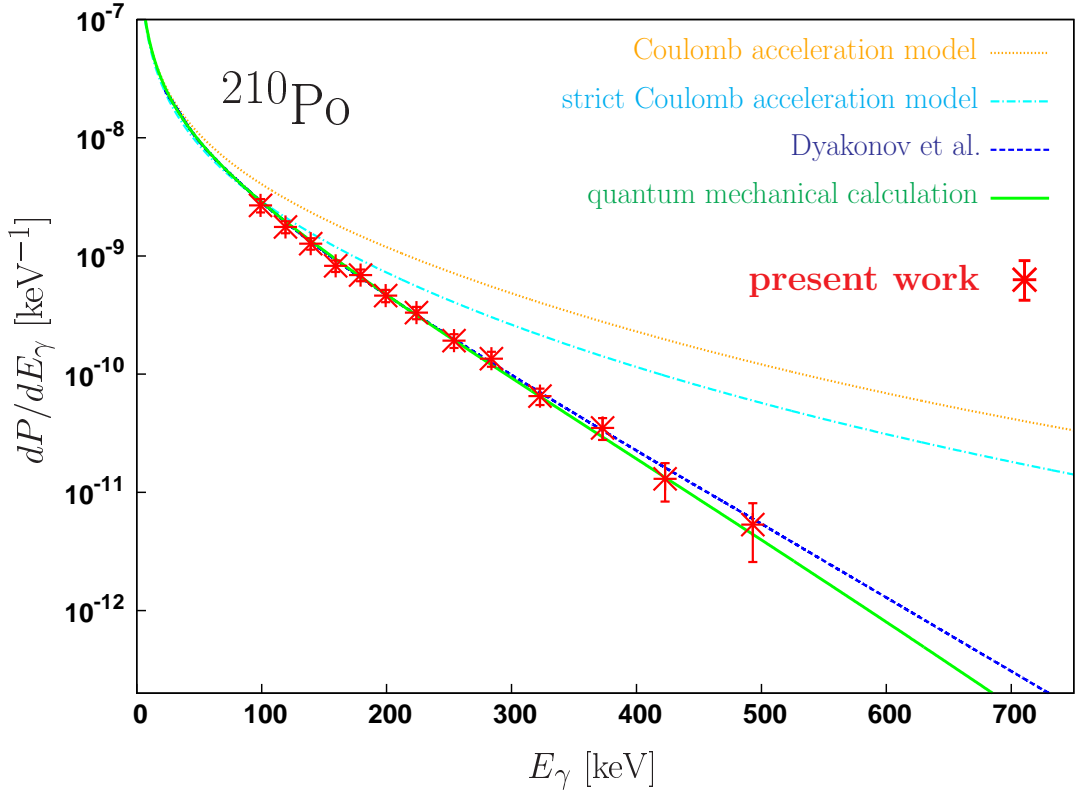


**Figure 6.2:** The energy-differential bremsstrahlung emission probability accompanying the  $\alpha$  decay of  $^{210}\text{Po}$  determined in the present work is compared to the theoretical predictions of the CA (orange) and the SCA model (cyan), of the semi-classical treatment of Dyakonov et al. [10] (blue) and of the quantum mechanical calculation (green). The predictions of the refined semi-classical Jentschura-Milstein-Terekhov model [21] are not plotted separately because they are indistinguishable from the result of the quantum mechanical calculation in this logarithmic plot.

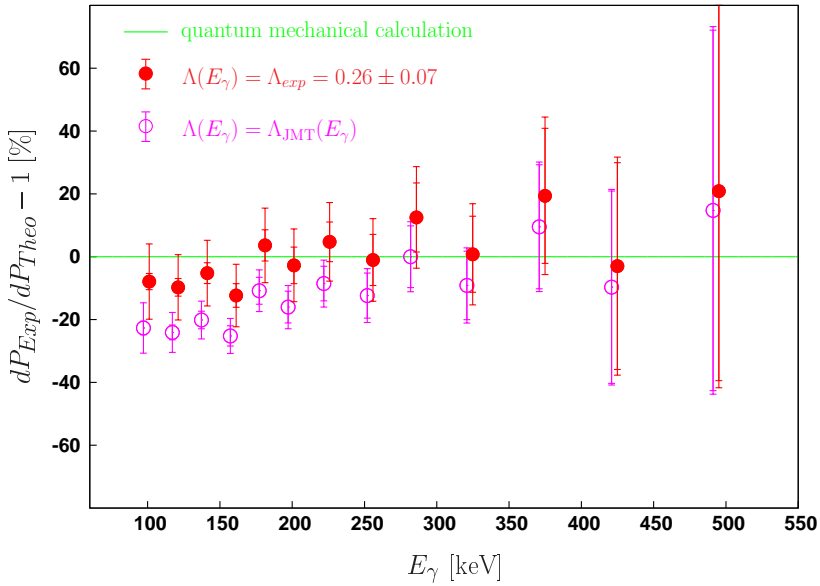


**Figure 6.3:** The deviation from the quantum mechanical calculation is plotted for the final experimental result evaluated with  $\Lambda(E_\gamma) = \Lambda_{exp} = 0.26 \pm 0.07$  (red points). The experimental data evaluated with  $\Lambda(E_\gamma) = \Lambda_{JMT}(E_\gamma)$  from the refined (non-relativistic) semi-classical Jentschura-Milstein-Terekhov model [21] are shown by the open (magenta) circles. The small error-bars correspond to the statistical error, the big error-bars represent the combined statistical and systematic error.

## 6.2 Summary and Outlook

In the present experiment the energy differential bremsstrahlung emission probability accompanying the  $\alpha$  decay of  $^{210}\text{Po}$  was measured with high statistics. In comparison to the previous measurement by Kasagi et al. [23–25] an improvement in statistics by almost two orders of magnitude has been achieved. This was accomplished by using two strong  $\alpha$  sources, an efficient  $\gamma$ -detection with a HPGe cluster detector of the MINIBALL type, and a measuring period of more 270 days. Through the segmentation of the silicon detectors and the MINIBALL cluster detector information could be gained on the  $\alpha$ - $\gamma$  angular correlation. The analysis of the data supports the existence of a non-vanishing correction factor  $\Lambda$  in the angular correlation  $f_{\alpha\gamma} = \sin^2 \vartheta(1 + 2\Lambda \cos \vartheta)$  with  $\Lambda^{\exp}(E_\gamma) = 0.26 \pm 0.07$ .

The final result on the bremsstrahlung is in good agreement with the quantum mechanical calculation (see section 2.4) and demonstrates that the classical Coulomb acceleration model and the strict Coulomb acceleration model overestimate the bremsstrahlung emission probability by more than an order of magnitude at  $\gamma$ -energies of  $> 400$  keV. Also other theoretical suggestions put forward, e.g. by Kasagi et al. [23–25] and Maydanyuk et al. [17, 18] are clearly ruled out by our high statistic data.

Together with U. D. Jentschura, A. I. Milstein and I. S. Terekhov a refined (non-relativistic) semi-classical approach has been developed which agrees with the quantum mechanical model [3, 7, 8] within 2% up to an energy of 800 keV. Within this framework the  $E1/E2$  interference contribution to the  $\alpha$ - $\gamma$  angular correlation for bremsstrahlung in the  $\alpha$ -decay was studied. Usually bremsstrahlung is assumed to be pure E1 radiation as the wavelength of the emitted radiation is much larger than the dimension of the radiating system. However, in the case of  $^{210}\text{Po}$  the effective quadrupole charge  $Z_{\text{eff}}^{E2} = 1.95$  is almost a factor of 5 larger than the effective dipole charge  $Z_{\text{eff}}^{E1} = 0.40$ . Though the E2 radiation does not contribute sizably to the total, angle-integrated emission probability, we found that it affects the  $\alpha$ - $\gamma$  angular correlation by leading to sizable values for  $\Lambda(E_\gamma)$  at  $E_\gamma > 0$ . However for  $E_\gamma \rightarrow 0$  the E2-contribution to the angular correlation vanishes, i.e.  $\Lambda(E_\gamma) \rightarrow 0$ , in contrast to our experimental finding.

On the other hand, the classical relativistic Coulomb acceleration model (CA) reveals that there are two contributions to  $\Lambda(E_\gamma)$ : one arising from the quadrupole interference which vanishes as in the semi-classical model for  $E_\gamma \rightarrow 0$ , and a second contribution connected to the relativistic nature of the problem. This relativistic contribution is non-zero for  $E_\gamma \rightarrow 0$  (see figure 2.3) and results in  $\Lambda(E_\gamma = 0) \approx 0.27$ , in agreement with our experimental value of  $0.26 \pm 0.07$ . Obviously, a theoretical treatment taking into account the quantum mechanical as well as the relativistic nature of the process is needed to fully understand the  $\alpha$ - $\gamma$  angular correlation in the bremsstrahlung accompanying the  $\alpha$  decay. Such a calculation was beyond the scope of this work, however, using Low's low-energy theorem [61] it was shown [35] that for  $E_\gamma \rightarrow 0$  the classical result for  $\Lambda(E_\gamma = 0)$  is regained in such a treatment.

An interesting goal for a future experiment would be to perform a more precise measure-

ment of the  $\alpha$ - $\gamma$  angular correlation.

A promising candidate for such a further measurement would be  $^{214}\text{Po}$ . With a decay energy  $Q_\alpha = 7833.26 \text{ keV}$  a 65 times higher bremsstrahlung emission probability is expected for this isotope at 600 keV. The drawback is that  $^{214}\text{Po}$  with a half-life of  $164.3 \mu\text{s}$  has to be produced either via the decay chain of  $^{226}\text{Ra}$  or using an online isotope separator.

# Appendix A

## Classical Treatment

### A.1 Bremsstrahlung

#### A.1.1 The Bremsstrahlung Vector Potential

The electromagnetic field at the point  $\mathbf{x}$  and the time  $t$  results from the motion of an elementary charge  $e$  at the point  $\mathbf{r}$  and the previous time  $t'$ . We define  $\mathbf{R}(t) = \mathbf{x} - \mathbf{r}(t)$  and get for the *retarded time*  $t'$

$$t' + \frac{R(t')}{c} = t, \quad (\text{A.1})$$

where  $c$  is the speed of light.

The 4-vector potential at the point  $\mathbf{x}$  is then given by Liénard-Wiechert potential [1, 2]

$$A^\mu(x) = \frac{e u^\mu(t')}{u_\nu \cdot [x^\nu - r^\nu(t')]} , \quad (\text{A.2})$$

where  $u^\mu$  is the 4-velocity of the charge. From equation (A.2) the electric and magnetic fields of a moving elementary charge  $e$  can be derived

$$\mathbf{E}(\mathbf{x}, t) = e \left[ \frac{\mathbf{n} - \boldsymbol{\beta}}{\gamma^2(1 - \boldsymbol{\beta} \cdot \mathbf{n})^3 R^2} \right]_{\text{ret}} + \frac{e}{c} \left[ \frac{[\mathbf{n} \times ((\mathbf{n} - \boldsymbol{\beta}) \times \dot{\boldsymbol{\beta}})]}{(1 - \boldsymbol{\beta} \cdot \mathbf{n})^3 R} \right]_{\text{ret}} \quad (\text{A.3})$$

$$\mathbf{B}(\mathbf{x}, t) = \left[ [\mathbf{n} \times \mathbf{E}] \right]_{\text{ret}} . \quad (\text{A.4})$$

On the right hand side the retarded time  $t'$  from equation (A.1) has to be used indicated by the subscript "ret". For  $\boldsymbol{\beta}$  and  $\gamma$  we have the common relativistic definitions

$$\beta = \frac{\mathbf{v}}{c} \quad \text{and} \quad \gamma = \frac{1}{\sqrt{1 - \beta^2}}, \quad (\text{A.5})$$

and  $\mathbf{n}$  is a unit vector pointing in the direction of  $\mathbf{x} - \mathbf{r}(t')$ .

The electric and magnetic fields  $\mathbf{E}(\mathbf{x}, t)$  and  $\mathbf{B}(\mathbf{x}, t)$  split up into *velocity fields* which are independent of the acceleration and a *acceleration fields*. The velocity fields are falling off with  $R^{-2}$  and may be neglected in the case of an accelerated charge ( $\dot{\beta} > 0$ ) at large distances  $R$

$$\mathbf{E}(\mathbf{x}, t) \approx \frac{e}{c} \left[ \frac{\left[ \mathbf{n} \times [(\mathbf{n} - \beta) \times \dot{\beta}] \right]}{(1 - \beta \cdot \mathbf{n})^3 R} \right]_{\text{ret}}. \quad (\text{A.6})$$

For the vector potential  $\mathbf{A}(\mathbf{x}, t)$  we choose the gauge

$$\mathbf{A}(\mathbf{x}, t) = R \mathbf{E}, \quad (\text{A.7})$$

which is a valid gauge because with the magnetic field (A.4) we have

$$\text{rot } \mathbf{A}(\mathbf{x}, t) = [(\nabla R) \times \mathbf{E}] + R \text{ rot } \mathbf{E} = [\mathbf{n} \times \mathbf{E}] = \mathbf{B}(\mathbf{x}, t). \quad (\text{A.8})$$

With (A.6) and (A.7) we get the expression for the vector potential of an accelerated charge

$$\mathbf{A}(\mathbf{x}, t) = \frac{e}{c} \left[ \frac{\left[ \mathbf{n} \times [(\mathbf{n} - \beta) \times \dot{\beta}] \right]}{(1 - \beta \cdot \mathbf{n})^3} \right]_{\text{ret}}, \quad (\text{A.9})$$

or for its Fourier transform

$$\mathbf{A}(\mathbf{x}, \omega) = \frac{1}{\sqrt{2\pi}} \int_{-\infty}^{+\infty} \mathbf{A}(t) e^{i\omega t} dt \quad (\text{A.10})$$

$$= \frac{e}{c} \sqrt{\frac{1}{2\pi}} \int_{-\infty}^{+\infty} \left[ \frac{\left[ \mathbf{n} \times [(\mathbf{n} - \beta) \times \dot{\beta}] \right]}{(1 - \beta \cdot \mathbf{n})^3} \right]_{\text{ret}} e^{i\omega t} dt. \quad (\text{A.11})$$

Replacing the time  $t$  using the definition of the retarded time (A.1)

$$t = t' + \frac{R(t')}{c} = t' + \frac{\mathbf{R}(t') \cdot \mathbf{n}}{c} = t' + \frac{\mathbf{x} \cdot \mathbf{n} - \mathbf{n} \cdot \mathbf{r}(t')}{c} \quad (\text{A.12})$$

and changing the variable of integration to  $t'$  leads to the expression for the vector potential from equation (A.11) (except for a phase factor which may be dropped due to local gauge invariance)

$$\mathbf{A}(\mathbf{x}, \omega) = \frac{e}{c} \sqrt{\frac{1}{2\pi}} \int_{-\infty}^{+\infty} \frac{\left[ \mathbf{n} \times [(\mathbf{n} - \beta) \times \dot{\beta}] \right]}{(1 - \beta \cdot \mathbf{n})^3} \exp \left( i\omega(t' - \frac{\mathbf{n} \cdot \mathbf{r}(t')}{c}) \right) \frac{dt}{dt'} dt' \quad (\text{A.13})$$

$$= \frac{e}{c} \sqrt{\frac{1}{2\pi}} \int_{-\infty}^{+\infty} \frac{\left[ \mathbf{n} \times [(\mathbf{n} - \beta) \times \dot{\beta}] \right]}{(1 - \beta \cdot \mathbf{n})^2} \exp \left( i\omega(t' - \frac{\mathbf{n} \cdot \mathbf{r}(t')}{c}) \right) dt'. \quad (\text{A.14})$$

### A.1.2 Frequency Distribution and Angular Distribution of Bremsstrahlung

The energy flux of the emitted radiation is given by the Poynting-vector [1]

$$\mathbf{S} = \frac{c}{4\pi} [\mathbf{E} \times \mathbf{B}] . \quad (\text{A.15})$$

The radiated power  $d\mathcal{P}$  per solid angle  $d\Omega$  is given by

$$|\mathbf{S}| = \frac{d\mathcal{P}}{R^2 d\Omega} . \quad (\text{A.16})$$

With the expression for the magnetic field  $\mathbf{B}$  from equation (A.4) and the transversality of the electric field for  $r \gg 1$  we get

$$\frac{d\mathcal{P}(t)}{d\Omega} = R^2 |\mathbf{S}| = R^2 \frac{c}{4\pi} |[\mathbf{E} \times \mathbf{B}]| \quad (\text{A.17})$$

$$= R^2 \frac{c}{4\pi} |[\mathbf{E} \times [\mathbf{n} \times \mathbf{E}]]| \quad (\text{A.18})$$

$$= \frac{c}{4\pi} R^2 \mathbf{E}^2 . \quad (\text{A.19})$$

With the gauge of (A.7) this leads to

$$\frac{d\mathcal{P}(t)}{d\Omega} = \frac{c}{4\pi} R^2 \mathbf{E}^2 = \frac{c}{4\pi} \mathbf{A}^2 . \quad (\text{A.20})$$

The total energy  $d\mathcal{W}$  radiated per solid angle  $d\Omega$  is given by the time integral

$$\frac{d\mathcal{W}}{d\Omega} = \frac{c}{4\pi} \int_{-\infty}^{\infty} |\mathbf{A}(t)|^2 dt \quad (\text{A.21})$$

$$= \frac{c}{4\pi} \int_{-\infty}^{\infty} dt \frac{1}{\sqrt{2\pi}} \int_{-\infty}^{\infty} d\omega \frac{1}{\sqrt{2\pi}} \int_{-\infty}^{\infty} d\omega' \mathbf{A}^*(\omega') \cdot \mathbf{A}(\omega) e^{i(\omega'-\omega)t} \quad (\text{A.22})$$

$$= \frac{c}{4\pi} \int_{-\infty}^{\infty} d\omega \int_{-\infty}^{\infty} d\omega' \mathbf{A}^*(\omega') \cdot \mathbf{A}(\omega) \frac{1}{2\pi} \int_{-\infty}^{\infty} dt e^{i(\omega'-\omega)t} \quad (\text{A.23})$$

$$= \frac{c}{4\pi} \int_{-\infty}^{\infty} d\omega \int_{-\infty}^{\infty} d\omega' \mathbf{A}^*(\omega') \cdot \mathbf{A}(\omega) \cdot \delta(\omega' - \omega) \quad (\text{A.24})$$

$$= \frac{c}{4\pi} \int_{-\infty}^{\infty} |\mathbf{A}(\omega)|^2 d\omega \quad (\text{A.25})$$

The gauge of  $\mathbf{A}(\mathbf{x}, t)$  was chosen such that  $\mathbf{A}(\mathbf{x}, t)$  is real, so it is evident that  $\mathbf{A}(-\omega) = \mathbf{A}^*(\omega)$  holds for the Fourier transform. This leads to

$$\frac{d\mathcal{W}}{d\Omega} = \frac{c}{4\pi} \int_{-\infty}^{\infty} |\mathbf{A}(\omega)|^2 d\omega \quad (\text{A.26})$$

$$= \frac{c}{4\pi} \int_{-\infty}^0 |\mathbf{A}(\omega)|^2 d\omega + \int_0^{\infty} |\mathbf{A}(\omega)|^2 d\omega \quad (\text{A.27})$$

$$= \frac{c}{2\pi} \int_0^{\infty} |\mathbf{A}(\omega)|^2 d\omega . \quad (\text{A.28})$$

For the energy  $\mathcal{I}$  radiated per solid angle  $d\Omega$  and per unit frequency interval  $d\omega$  we have the relation

$$\frac{d\mathcal{W}}{d\Omega} = \int_0^{\infty} \frac{d^2\mathcal{I}(\omega, \mathbf{n})}{d\omega d\Omega} d\omega . \quad (\text{A.29})$$

Hence with equation (A.28) we get

$$\frac{d^2\mathcal{I}(\omega, \mathbf{n})}{d\omega d\Omega} = \frac{c}{2\pi} |\mathbf{A}(\omega)|^2 . \quad (\text{A.30})$$

Using expression (A.14) for the vector potential leads to

$$\frac{d^2\mathcal{I}}{d\omega d\Omega} = \frac{e^2}{4\pi^2 c} \left| \int_{-\infty}^{+\infty} \frac{[\mathbf{n} \times [(\mathbf{n} - \boldsymbol{\beta}(t)) \times \dot{\boldsymbol{\beta}}(t)]]}{(1 - \boldsymbol{\beta}(t) \cdot \mathbf{n})^2} \exp\left(i\omega\left(t - \frac{\mathbf{n} \cdot \mathbf{r}(t)}{c}\right)\right) dt \right|^2 . \quad (\text{A.31})$$

Dividing this expression by the energy of a bremsstrahlung photon  $\hbar\omega$  gives the expression for the number of bremsstrahlung photons per solid angle, and per frequency interval, i.e. the bremsstrahlung emission probability

$$\frac{d^2P}{d\omega d\Omega} = \frac{e^2}{4\pi^2 \hbar c \omega} \left| \int_{-\infty}^{+\infty} \frac{[\mathbf{n} \times [(\mathbf{n} - \boldsymbol{\beta}(t)) \times \dot{\boldsymbol{\beta}}(t)]]}{(1 - \boldsymbol{\beta}(t) \cdot \mathbf{n})^2} \exp\left(i\omega\left(t - \frac{\mathbf{n} \cdot \mathbf{r}(t)}{c}\right)\right) dt \right|^2 , \quad (\text{A.32})$$

or per solid angle and per bremsstrahlungphoton energy interval  $dE_\gamma$

$$\frac{d^2P}{dE_\gamma d\Omega} = \frac{\alpha}{4\pi^2 E_\gamma} \left| \int_{-\infty}^{+\infty} \frac{[\mathbf{n} \times [(\mathbf{n} - \boldsymbol{\beta}(t)) \times \dot{\boldsymbol{\beta}}(t)]]}{(1 - \boldsymbol{\beta}(t) \cdot \mathbf{n})^2} \exp\left(i\frac{E_\gamma}{\hbar}\left(t - \frac{\mathbf{n} \cdot \mathbf{r}(t)}{c}\right)\right) dt \right|^2 \quad (\text{A.33})$$

with the fine structure constant  $\alpha = e^2(\hbar c)^{-1}$ .

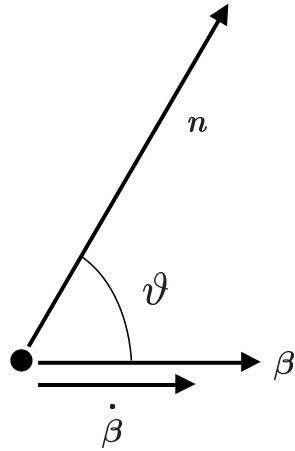


**Figure A.1:** The angle  $\vartheta$  is the angle between the direction of observation  $\mathbf{n} \parallel \mathbf{R}$  and the direction of motion of the particle  $\boldsymbol{\beta}$ . In the considered case of linear motion  $\boldsymbol{\beta}$  and  $\dot{\boldsymbol{\beta}}$  are parallel.

### Linear Motion

We now want to consider the simple case of a linear motion in which  $\boldsymbol{\beta}$  and  $\dot{\boldsymbol{\beta}}$  are parallel ( $\boldsymbol{\beta} \parallel \dot{\boldsymbol{\beta}}$ ).

Let  $\vartheta$  be the angle of observation measured from the direction of motion, see figure A.1. Then we see

$$\mathbf{n}(t) \cdot \boldsymbol{\beta}(t) = |\boldsymbol{\beta}(t)| \cos \vartheta(t) \quad (\text{A.34})$$

and get for the denominator

$$1 - \mathbf{n}(t) \cdot \boldsymbol{\beta}(t) = 1 - |\boldsymbol{\beta}(t)| \cos \vartheta(t) \quad (\text{A.35})$$

For the nominator we get

$$[\mathbf{n}(t) \times [(\mathbf{n}(t) - \boldsymbol{\beta}(t)) \times \dot{\boldsymbol{\beta}}(t)]] = [\mathbf{n}(t) \times ([\mathbf{n}(t) \times \dot{\boldsymbol{\beta}}(t)] - [\boldsymbol{\beta}(t) \times \dot{\boldsymbol{\beta}}(t)])] \quad (\text{A.36})$$

$$= [\mathbf{n}(t) \times [\mathbf{n}(t) \times \dot{\boldsymbol{\beta}}(t)]] \quad (\text{A.37})$$

where we have used  $[\boldsymbol{\beta}(t) \times \dot{\boldsymbol{\beta}}(t)] = 0$  because  $\boldsymbol{\beta}$  and  $\dot{\boldsymbol{\beta}}$  are parallel. Let  $\mathbf{e}_\perp(t)$  be the unit vector perpendicular to  $\mathbf{n}(t)$  and  $\dot{\boldsymbol{\beta}}(t)$ , then we can write

$$[\mathbf{n}(t) \times [\mathbf{n}(t) \times \dot{\boldsymbol{\beta}}(t)]] = |\dot{\boldsymbol{\beta}}(t)| \sin \vartheta(t) \mathbf{e}_\perp(t) \quad (\text{A.38})$$

If the distance of observation is big compared to the region of interaction,  $\mathbf{n}$  and  $\vartheta$  are approximately constant (therefore also  $\mathbf{e}_\perp$  is constant). Then equation (A.35) and (A.38)

simplify to

$$\left[ \mathbf{n} \times [(\mathbf{n} - \boldsymbol{\beta}(t)) \times \dot{\boldsymbol{\beta}}(t)] \right] = |\dot{\boldsymbol{\beta}}(t)| \sin \vartheta \mathbf{e}_\perp \quad (\text{A.39})$$

$$1 - \mathbf{n} \cdot \boldsymbol{\beta}(t) = 1 - |\boldsymbol{\beta}(t)| \cos \vartheta \quad (\text{A.40})$$

For the bremsstrahlung emission probability per solid angle and photon energy interval we get from (A.33)

$$\frac{d^2P}{dE_\gamma d\Omega} = \frac{\alpha}{4\pi^2 E_\gamma} \left| \int_{-\infty}^{+\infty} \frac{|\dot{\boldsymbol{\beta}}(t)| \sin \vartheta}{(1 - |\boldsymbol{\beta}(t)| \cos \vartheta)^2} \exp \left( i \frac{E_\gamma}{\hbar} \left( t - \frac{\mathbf{n} \cdot \mathbf{r}(t)}{c} \right) \right) dt \right|^2. \quad (\text{A.41})$$

In the non-relativistic limit ( $\beta \ll 1$ ) we get the normal  $\sin^2 \vartheta$  behaviour of the dipole radiation

$$\frac{d^2P}{dE_\gamma d\Omega} \approx \frac{\alpha}{4\pi^2 E_\gamma} \sin^2 \vartheta \left| \int_{-\infty}^{+\infty} |\dot{\boldsymbol{\beta}}(t)| \exp \left( i \frac{E_\gamma}{\hbar} \left( t - \frac{\mathbf{n} \cdot \mathbf{r}(t)}{c} \right) \right) dt \right|^2. \quad (\text{A.42})$$

The Integration over  $4\pi$  gives

$$\int_{4\pi} \sin^2 \vartheta d\Omega = \int_0^{2\pi} d\varphi \int_0^\pi \sin^3 \vartheta d\vartheta = 2\pi \int_0^\pi \sin^3 \vartheta d\vartheta = \frac{8\pi}{3} \quad (\text{A.43})$$

and leads to

$$\frac{dP}{dE_\gamma} = \frac{2\alpha}{3\pi E_\gamma} \left| \int_{-\infty}^{+\infty} |\dot{\boldsymbol{\beta}}(t)| \exp \left( i \frac{E_\gamma}{\hbar} \left( t - \frac{\mathbf{n} \cdot \mathbf{r}(t)}{c} \right) \right) dt \right|^2. \quad (\text{A.44})$$

## A.2 The Centre of Mass System

Considering two particles 1 and 2 at the points  $\mathbf{r}_1$  and  $\mathbf{r}_2$  with the masses  $m_1$  and  $m_2$  with the momenta  $\mathbf{p}_1$  and  $\mathbf{p}_2$  and the charges  $q_1$  and  $q_2$  it is convenient to discuss the system in the *centre of mass system*.

In the centre of mass system the relative motion and the motion of the centre of mass are distinguished. For the centre of mass we have

$$M_{cm} = m_1 + m_2 \quad (\text{A.45})$$

$$\mathbf{R}_{cm} = \frac{m_1 \mathbf{r}_1 + m_2 \mathbf{r}_2}{M_{cm}} \quad (\text{A.46})$$

$$\mathbf{V}_{cm} = \frac{\partial \mathbf{R}_{cm}}{\partial t} = \frac{m_1 \mathbf{v}_1 + m_2 \mathbf{v}_2}{M_{cm}} \quad (\text{A.47})$$

$$\mathbf{P}_{cm} = M_{cm} \mathbf{V}_{cm} = \mathbf{p}_1 + \mathbf{p}_2. \quad (\text{A.48})$$

For the relative motion of particle 1 and 2 we define the relative coordinate  $\mathbf{r}$  and get the relative velocity  $\mathbf{v}$

$$\mathbf{r} = \mathbf{r}_1 - \mathbf{r}_2 \quad (\text{A.49})$$

$$\Rightarrow \mathbf{v} = \frac{\partial \mathbf{r}}{\partial t} = \mathbf{v}_1 - \mathbf{v}_2. \quad (\text{A.50})$$

The non-relativistic kinetic energy of the two particles can then be written as

$$E_{\text{kin}} = \frac{1}{2}m_1\mathbf{v}_1^2 + \frac{1}{2}m_2\mathbf{v}_2^2 \quad (\text{A.51})$$

$$= \frac{1}{2}\frac{m_1^2 + m_1m_2}{m_1 + m_2}\mathbf{v}_1^2 + \frac{1}{2}\frac{m_2^2 + m_1m_2}{m_1 + m_2}\mathbf{v}_2^2 \quad (\text{A.52})$$

$$= \frac{1}{2}M_{cm}\frac{m_1^2\mathbf{v}_1^2 + m_2^2\mathbf{v}_2^2}{M_{cm}^2} + \frac{1}{2}\frac{m_1m_2}{m_1 + m_2}\mathbf{v}_1^2 + \frac{1}{2}\frac{m_1m_2}{m_1 + m_2}\mathbf{v}_2^2 \quad (\text{A.53})$$

$$= \frac{1}{2}M_{cm}\mathbf{V}_{cm}^2 + \frac{1}{2}\frac{m_1m_2\mathbf{v}_1^2}{m_1 + m_2} - \frac{m_1m_2\mathbf{v}_1\mathbf{v}_2}{m_1 + m_2} + \frac{1}{2}\frac{m_1m_2\mathbf{v}_2^2}{m_1 + m_2} \quad (\text{A.54})$$

$$= \frac{1}{2}M_{cm}\mathbf{V}_{cm}^2 + \frac{1}{2}\frac{m_1m_2}{m_1 + m_2}(\mathbf{v}_1 - \mathbf{v}_2)^2 \quad (\text{A.55})$$

$$= \frac{1}{2}M_{cm}\mathbf{V}_{cm}^2 + \frac{1}{2}\mu\mathbf{v}^2, \quad (\text{A.56})$$

where the *reduced mass*

$$\mu = \frac{m_1m_2}{m_1 + m_2} \quad (\text{A.57})$$

has been introduced. For the relative momentum  $\mathbf{p}$  we get

$$\mathbf{p} = \mu\mathbf{v} \quad (\text{A.58})$$

$$= \frac{m_1m_2}{m_1 + m_2}(\mathbf{v}_1 - \mathbf{v}_2) \quad (\text{A.59})$$

$$= \frac{1}{M_{cm}}(m_2\mathbf{p}_1 - m_1\mathbf{p}_2). \quad (\text{A.60})$$

We now want to move to the centre of mass system, i.e. we choose a coordinate system in which the centre of mass is at rest in the origin

$$R_{cm} = 0 \implies m_1\mathbf{r}_1 + m_2\mathbf{r}_2 = 0 \quad (\text{A.61})$$

$$V_{cm} = 0 \implies m_1\mathbf{v}_1 + m_2\mathbf{v}_2 = 0 \quad (\text{A.62})$$

$$P_{cm} = 0 \implies \mathbf{p}_1 + \mathbf{p}_2 = 0. \quad (\text{A.63})$$

In this system we get

$$\mathbf{r}_1 = -\frac{m_2}{m_1}\mathbf{r}_2 = \frac{m_2}{m_1}\mathbf{r} - \frac{m_2}{m_1}\mathbf{r}_1 \implies \mathbf{r}_1 = \frac{\mu}{m_1}\mathbf{r} \quad (\text{A.64})$$

$$\mathbf{r}_2 = -\frac{m_1}{m_2}\mathbf{r}_1 = -\frac{m_1}{m_2}\mathbf{r} - \frac{m_1}{m_2}\mathbf{r}_2 \implies \mathbf{r}_2 = -\frac{\mu}{m_2}\mathbf{r}. \quad (\text{A.65})$$

and

$$\mathbf{p}_1 = -\mathbf{p}_2 = \mathbf{p} \quad (\text{A.66})$$

The interaction with the electromagnetic field for two particles is given by the interaction Hamiltonian (see section B.1 for more details)

$$H_{\text{em}} = -\frac{q_1}{m_1 c} \mathbf{p}_1 \mathbf{A}(\mathbf{r}_1, t) - \frac{q_2}{m_2 c} \mathbf{p}_2 \mathbf{A}(\mathbf{r}_2, t) \quad (\text{A.67})$$

with the charge  $q_1$  and  $q_2$  of particle 1 and 2, respectively. If we use the first two terms of the expansion of the vector potential  $\mathbf{A}$

$$\mathbf{A}(\mathbf{r}, t) = \epsilon e^{i(\omega t - \mathbf{k}\mathbf{r})} \approx \epsilon (1 - i\mathbf{k}\mathbf{r} + \dots) e^{i\omega t} \quad (\text{A.68})$$

we get (dropping  $e^{i\omega t}$ )

$$H_{\text{em}} \approx -\frac{q_1}{m_1 c} \mathbf{p}_1 \epsilon (1 - i\mathbf{k}\mathbf{r}_1) - \frac{q_2}{m_2 c} \mathbf{p}_2 \epsilon (1 - i\mathbf{k}\mathbf{r}_2) \quad (\text{A.69})$$

$$= -\frac{q_1}{m_1 c} \mathbf{p} \epsilon (1 - i\mathbf{k} \frac{\mu}{m_1} \mathbf{r}) - \frac{q_2}{m_2 c} (-\mathbf{p}) \epsilon (1 - i\mathbf{k}(-\frac{\mu}{m_2} \mathbf{r})) \quad (\text{A.70})$$

$$= -\frac{\mathbf{p} \epsilon}{c} \left[ \left( \frac{q_1}{m_1} - \frac{q_2}{m_2} \right) - i \left( \frac{\mu q_1}{m_1^2} + \frac{\mu q_2}{m_2^2} \right) \mathbf{k} \mathbf{r} \right] \quad (\text{A.71})$$

$$= -\frac{\mathbf{p} \epsilon}{\mu c} \left[ \frac{m_2 q_1 - m_1 q_2}{m_1 + m_2} - i \frac{m_2^2 q_1 + m_1^2 q_2}{(m_1 + m_2)^2} \mathbf{k} \mathbf{r} \right] \quad (\text{A.72})$$

$$= -\frac{\mathbf{p} \epsilon}{\mu c} (q_{\text{eff}}^{E1} - i q_{\text{eff}}^{E2} \mathbf{k} \mathbf{r}) \quad (\text{A.73})$$

where we introduced the *effective dipole charge*

$$q_{\text{eff}}^{E1} = \frac{m_2 q_1 - m_1 q_2}{m_1 + m_2} = \mu \left( \frac{q_1}{m_1} - \frac{q_2}{m_2} \right) \quad (\text{A.74})$$

and the *effective quadrupole charge*

$$q_{\text{eff}}^{E2} = \frac{m_2^2 q_1 + m_1^2 q_2}{(m_1 + m_2)^2} = \mu^2 \left( \frac{q_1}{m_1^2} + \frac{q_2}{m_2^2} \right). \quad (\text{A.75})$$

If we use the charge numbers  $q = Z_{\text{eff}} e$ ,  $q_1 = Z_1 e$  and  $q_2 = Z_2 e$  the effective charge numbers are given by

$$Z_{\text{eff}}^{E1} = \frac{m_2 Z_1 - m_1 Z_2}{m_1 + m_2} = \mu \left( \frac{Z_1}{m_1} - \frac{Z_2}{m_2} \right) \quad (\text{A.76})$$

$$Z_{\text{eff}}^{E2} = \frac{m_2^2 Z_1 + m_1^2 Z_2}{(m_1 + m_2)^2} = \mu^2 \left( \frac{Z_1}{m_1^2} + \frac{Z_2}{m_2^2} \right). \quad (\text{A.77})$$

In the case of the  $\alpha$ -decay of  ${}^{210}\text{Po}$  we find

$$Z_{\text{eff}}^{E1} \approx \frac{206 \cdot 2 - 4 \cdot 82}{4 + 206} \approx 0.4 \quad (\text{A.78})$$

$$Z_{\text{eff}}^{E2} \approx \frac{206^2 \cdot 2 + 4^2 \cdot 82}{(4 + 206)^2} \approx 1.95 \quad (\text{A.79})$$

It is important to note, that in the case of  $^{210}\text{Po}$  the effective quadrupole charge is approximately five times bigger than the corresponding dipole charge. Therefore it is important to take contributions from the electric quadrupole radiation into account.

### A.3 Bremsstrahlung of two Charged Particles

In the following we will consider a system of two particles in the centre of mass system (see A.2). Let 1 be the first particle with the charge  $q_1 = Z_1 \cdot e$ , the masses  $m_1$  at the point  $\mathbf{r}_1(t)$ . For the second particle we define  $q_2$ ,  $m_2$  and  $\mathbf{r}_2(t)$  analogous.

Both particles are accelerated in the Coulomb field of the other particle and therefore emit interfering bremsstrahlung. From equation (A.30) we get for the bremsstrahlung emission probability per solid angle and per frequency interval

$$\frac{d^2P}{d\omega d\Omega} = \frac{c}{2\pi\hbar\omega} |\mathbf{A}_1(\omega) + \mathbf{A}_2(\omega)|^2. \quad (\text{A.80})$$

Using the expression (A.14) for the vector potential leads to

$$\begin{aligned} \frac{d^2P}{d\omega d\Omega} &= \frac{e^2}{4\pi^2\hbar\omega} \left| \int_{-\infty}^{+\infty} Z_1 \frac{\left[ \mathbf{n}_1(t) \times [(\mathbf{n}_1(t) - \boldsymbol{\beta}_1(t)) \times \dot{\boldsymbol{\beta}}_1(t)] \right]}{(1 - \boldsymbol{\beta}_1(t) \cdot \mathbf{n}_1(t))^2} \exp \left( i\omega(t - \frac{\mathbf{n}_1(t) \cdot \mathbf{r}_1(t)}{c}) \right) \right. \\ &\quad \left. + Z_2 \frac{\left[ \mathbf{n}_2(t) \times [(\mathbf{n}_2(t) - \boldsymbol{\beta}_2(t)) \times \dot{\boldsymbol{\beta}}_2(t)] \right]}{(1 - \boldsymbol{\beta}_2(t) \cdot \mathbf{n}_2(t))^2} \exp \left( i\omega(t - \frac{\mathbf{n}_2(t) \cdot \mathbf{r}_2(t)}{c}) \right) dt \right|^2. \end{aligned} \quad (\text{A.81})$$

In the two particle case without outer fields we have a linear motion where  $\boldsymbol{\beta}_1$ ,  $\boldsymbol{\beta}_2$ ,  $\dot{\boldsymbol{\beta}}_1$  and  $\dot{\boldsymbol{\beta}}_2$  are parallel. So we can use the relations (A.39) and (A.40) and get

$$\begin{aligned} \frac{d^2P}{d\omega d\Omega} &= \frac{\alpha}{4\pi^2\omega} \left| \int_{-\infty}^{+\infty} \frac{Z_1 |\dot{\boldsymbol{\beta}}_1(t)| \sin \vartheta_1(t) \mathbf{e}_{\perp,1}(t)}{(1 - |\boldsymbol{\beta}_1(t)| \cos \vartheta_1(t))^2} \exp \left( i\omega(t - \frac{\mathbf{n}_1(t) \cdot \mathbf{r}_1(t)}{c}) \right) \right. \\ &\quad \left. + \frac{Z_2 |\dot{\boldsymbol{\beta}}_2(t)| \sin \vartheta_2(t) \mathbf{e}_{\perp,2}(t)}{(1 - |\boldsymbol{\beta}_2(t)| \cos \vartheta_2(t))^2} \exp \left( i\omega(t - \frac{\mathbf{n}_2(t) \cdot \mathbf{r}_2(t)}{c}) \right) dt \right|^2 \end{aligned} \quad (\text{A.82})$$

If the distance of observation is big in comparison to the relative distance of the two particles ( $R \gg r$ ) the  $\mathbf{n}_1$  and  $\mathbf{n}_2$  and the angles  $\vartheta_1$  and  $\vartheta_2$  may be approximated to be

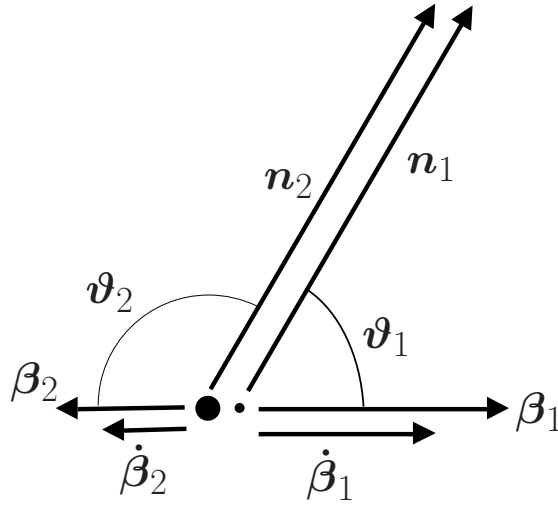


**Figure A.2:** For two interacting particles with no outer fields the resulting motion is linear, i.e. that  $\beta_1$ ,  $\beta_2$ ,  $\dot{\beta}_1$  and  $\dot{\beta}_2$  are parallel. If the distance of observation is big compared to the relative distance the angles  $\vartheta_1$  and  $\vartheta_2$  of the direction of observation  $n_1$  and  $n_2$  measured from the direction of motion are correlated by the relation  $\vartheta_2 = \pi - \vartheta_1$ .

constant and we have (see figure A.2)

$$\mathbf{n}_1(t) = \mathbf{n}_1 \quad (\text{A.83})$$

$$\mathbf{n}_2(t) = \mathbf{n}_2 = \mathbf{n}_1 \quad (\text{A.84})$$

$$\vartheta_1(t) = \vartheta_1 \quad (\text{A.85})$$

$$\vartheta_2(t) = \vartheta_2 = \pi - \vartheta_1 \quad (\text{A.86})$$

$$\mathbf{e}_{\perp,1}(t) = \mathbf{e}_{\perp,1} \quad (\text{A.87})$$

$$\mathbf{e}_{\perp,2}(t) = \mathbf{e}_{\perp,2} = -\mathbf{e}_{\perp,1} \quad (\text{A.88})$$

The unit vectors  $\mathbf{e}_{\perp,1}$  and  $\mathbf{e}_{\perp,2}$  are antiparallel because  $\dot{\beta}_1$  and  $\dot{\beta}_2$  are antiparallel.

We define

$$\mathbf{n} := \mathbf{n}_1 = \mathbf{n}_2 \quad (\text{A.89})$$

$$\vartheta := \vartheta_1 = \pi - \vartheta_2 \quad (\text{A.90})$$

$$\mathbf{e}_{\perp} := \mathbf{e}_{\perp,1} = -\mathbf{e}_{\perp,2} \quad (\text{A.91})$$

so equation (A.82) can be simplified to

$$\begin{aligned} \frac{d^2P}{d\omega d\Omega} &= \frac{\alpha}{4\pi^2\omega} \left| \int_{-\infty}^{+\infty} \frac{Z_1 |\dot{\beta}_1(t)| \sin \vartheta \mathbf{e}_{\perp}}{(1 - |\beta_1(t)| \cos \vartheta)^2} \exp \left( i\omega(t - \frac{\mathbf{n} \cdot \mathbf{r}_1(t)}{c}) \right) \right. \\ &\quad \left. - \frac{Z_2 |\dot{\beta}_2(t)| \sin \vartheta \mathbf{e}_{\perp}}{(1 + |\beta_2(t)| \cos \vartheta)^2} \exp \left( i\omega(t - \frac{\mathbf{n} \cdot \mathbf{r}_2(t)}{c}) \right) dt \right|^2. \end{aligned} \quad (\text{A.92})$$

We recall from equations (A.64) and (A.65)

$$\mathbf{r}_1(t) = \frac{\mu}{m_1} \mathbf{r}(t) \quad \mathbf{r}_2(t) = -\frac{\mu}{m_2} \mathbf{r}(t). \quad (\text{A.93})$$

If we define  $\beta$  in an analogous way to  $\mathbf{r}$

$$\beta = \frac{\dot{\mathbf{r}}}{c} = \frac{\dot{\mathbf{r}}_1 - \dot{\mathbf{r}}_2}{c} = \beta_1 - \beta_2 \quad (\text{A.94})$$

we get similar relations for  $\beta$  and  $\dot{\beta}$

$$\begin{aligned} \beta_1(t) &= \frac{\mu}{m_1} \beta(t) & \beta_2(t) &= -\frac{\mu}{m_2} \beta(t) \\ \dot{\beta}_1(t) &= \frac{\mu}{m_1} \dot{\beta}(t) & \dot{\beta}_2(t) &= -\frac{\mu}{m_2} \dot{\beta}(t). \end{aligned} \quad (\text{A.95})$$

The substitution of these relations into (A.92) leads to

$$\frac{d^2P}{d\omega d\Omega} = \frac{\alpha}{4\pi^2\omega} \left| \int_{-\infty}^{+\infty} \mu \left( \frac{Z_1}{m_1} \frac{1}{(1 - \frac{\mu}{m_1} |\beta(t)| \cos \vartheta)^2} e^{-i\omega \frac{\mu}{m_1} \frac{\mathbf{n} \cdot \mathbf{r}(t)}{c}} \right. \right. \\ \left. \left. - \frac{Z_2}{m_2} \frac{1}{(1 + \frac{\mu}{m_2} |\beta(t)| \cos \vartheta)^2} e^{i\omega \frac{\mu}{m_2} \frac{\mathbf{n} \cdot \mathbf{r}(t)}{c}} \right) |\dot{\beta}(t)| \sin \vartheta e^{i\omega t} dt \right|^2 \quad (\text{A.96}) \right.$$

where the unit vector  $\mathbf{e}_\perp$  was dropped in the integrant.

### Dipole Approximation

The Taylor expansion for the exponential factors leads to

$$e^{-i\omega \frac{\mu}{m_1} \frac{\mathbf{n} \cdot \mathbf{r}(t)}{c}} \approx 1 - i\omega \frac{\mu}{m_1} \frac{\mathbf{n} \cdot \mathbf{r}(t)}{c} \quad \text{and} \quad e^{-i\omega \frac{\mu}{m_2} \frac{\mathbf{n} \cdot \mathbf{r}(t)}{c}} \approx 1 - i\omega \frac{\mu}{m_2} \frac{\mathbf{n} \cdot \mathbf{r}(t)}{c}. \quad (\text{A.97})$$

In the *dipole approximation* only the first term of this expansion is taken into account. So the dipole approximation of equation (A.96) is given by

$$\frac{d^2P}{d\omega d\Omega} \approx \frac{\alpha}{4\pi^2\omega} \left| \int_{-\infty}^{+\infty} \mu \left( \frac{Z_1}{m_1} \frac{1}{(1 - \frac{\mu}{m_1} |\beta(t)| \cos \vartheta)^2} \right. \right. \\ \left. \left. - \frac{Z_2}{m_2} \frac{1}{(1 + \frac{\mu}{m_2} |\beta(t)| \cos \vartheta)^2} \right) |\dot{\beta}(t)| \sin \vartheta e^{i\omega t} dt \right|^2 \quad (\text{A.98}) \right.$$

Using the approximation

$$\frac{1}{(1-x)^2} \approx 1 + 2x + \dots \quad \text{and} \quad \frac{1}{(1+x)^2} \approx 1 - 2x + \dots \quad (\text{A.99})$$

leads to

$$\frac{d^2P}{d\omega d\Omega} \approx \frac{\alpha}{4\pi^2\omega} \left| \int_{-\infty}^{+\infty} \mu \left( \frac{Z_1}{m_1} \left( 1 + 2\frac{\mu}{m_1} |\boldsymbol{\beta}(t)| \cos \vartheta \right) - \frac{Z_2}{m_2} \left( 1 - 2\frac{\mu}{m_2} |\boldsymbol{\beta}(t)| \cos \vartheta \right) \right) |\dot{\boldsymbol{\beta}}(t)| \sin \vartheta e^{i\omega t} dt \right|^2 \quad (\text{A.100})$$

$$= \frac{\alpha}{4\pi^2\omega} \left| \int_{-\infty}^{+\infty} \left( \mu \left( \frac{Z_1}{m_1} - \frac{Z_2}{m_2} \right) + 2\mu^2 \left( \frac{Z_1}{m_1^2} + \frac{Z_2}{m_2^2} \right) |\boldsymbol{\beta}(t)| \cos \vartheta \right) |\dot{\boldsymbol{\beta}}(t)| \sin \vartheta e^{i\omega t} dt \right|^2. \quad (\text{A.101})$$

With the effective dipole and quadrupole charge from equations (A.76) and (A.77) we get finally

$$\frac{d^2P}{d\omega d\Omega} \approx \frac{\alpha}{4\pi^2\omega} \left| \int_{-\infty}^{+\infty} \left( Z_{\text{eff}}^{E1} + 2Z_{\text{eff}}^{E2} |\boldsymbol{\beta}(t)| \cos \vartheta \right) |\dot{\boldsymbol{\beta}}(t)| \sin \vartheta e^{i\omega t} dt \right|^2. \quad (\text{A.102})$$

## Quadrupole Contribution

In the following we want to consider the contribution from the second term in the expansion of the exponential factor from equation (A.97) which corresponds to the electric quadrupole. For the contribution of particle 1 in expression (A.96) we find

$$\begin{aligned} & \mu \frac{Z_1}{m_1} \frac{1}{(1 - \frac{\mu}{m_1} |\boldsymbol{\beta}(t)| \cos \vartheta)^2} e^{-i\omega \frac{\mu}{m_1} \frac{\mathbf{n} \cdot \mathbf{r}(t)}{c}} \\ & \approx \mu \frac{Z_1}{m_1} \left( 1 + 2\frac{\mu}{m_1} |\boldsymbol{\beta}(t)| \cos \vartheta \right) \left( 1 - i\omega \frac{\mu}{m_1} \frac{\mathbf{n} \cdot \mathbf{r}(t)}{c} \right) \end{aligned} \quad (\text{A.103})$$

$$= \mu \frac{Z_1}{m_1} \left( 1 + 2\frac{\mu}{m_1} |\boldsymbol{\beta}(t)| \cos \vartheta \right) \left( 1 - i\omega \frac{\mu}{m_1} \frac{|\mathbf{r}(t)|}{c} \cos \vartheta \right) \quad (\text{A.104})$$

$$= \mu \frac{Z_1}{m_1} + \mu^2 \frac{Z_1}{m_1^2} \left( 2|\boldsymbol{\beta}(t)| - i\frac{\omega}{c} |\mathbf{r}(t)| \right) \cos \vartheta - i\frac{2\mu^3 \omega}{c} \frac{Z_1}{m_1^3} |\mathbf{r}(t)| |\boldsymbol{\beta}(t)| \cos^2 \vartheta. \quad (\text{A.105})$$

In an analog way we find for the contribution of particle 2

$$\begin{aligned} & -\mu \frac{Z_2}{m_2} \frac{1}{(1 + \frac{\mu}{m_2} |\boldsymbol{\beta}(t)| \cos \vartheta)^2} e^{i\omega \frac{\mu}{m_2} \frac{\mathbf{n} \cdot \mathbf{r}(t)}{c}} \\ & \approx -\mu \frac{Z_2}{m_2} + \mu^2 \frac{Z_2}{m_2^2} \left( 2|\boldsymbol{\beta}(t)| - i\frac{\omega}{c} |\mathbf{r}(t)| \right) \cos \vartheta + i\frac{2\mu^3 \omega}{c} \frac{Z_2}{m_2^3} |\mathbf{r}(t)| |\boldsymbol{\beta}(t)| \cos^2 \vartheta. \end{aligned} \quad (\text{A.106})$$

We neglect the third term proportional to  $\cos^2\vartheta$  and get for the bremsstrahlung emission probability per solid angle and frequency

$$\frac{d^2P}{d\omega d\Omega} \approx \frac{\alpha}{4\pi^2\omega} \left| \int_{-\infty}^{+\infty} \left( Z_{\text{eff}}^{E1} + Z_{\text{eff}}^{E2} \left( 2|\beta(t)| - i\frac{\omega}{c}|\mathbf{r}(t)| \right) \cos\vartheta \right) |\dot{\beta}(t)| \sin\vartheta e^{i\omega t} dt \right|^2. \quad (\text{A.107})$$

### Angular Correlation

From equation (A.107) we find that the expression for the number of emitted bremsstrahlung photon per solid angle and frequency has the structure

$$\frac{d^2P}{d\omega d\Omega} \approx |(f_1(\omega) + f_2(\omega) \cos\vartheta) \sin\vartheta|^2 \quad (\text{A.108})$$

$$= f_1^2(\omega) \sin^2\vartheta + 2\text{Re}(f_1(\omega)f_2^*(\omega)) \sin^2\vartheta \cos\vartheta + f_2^2(\omega) \sin^2\vartheta \cos^2\vartheta \quad (\text{A.109})$$

$$= f_1^2(\omega) \sin^2\vartheta \left( 1 + \frac{2\text{Re}(f_1(\omega)f_2^*(\omega))}{f_1^2(\omega)} \cos\vartheta + \frac{f_2^2(\omega)}{f_1^2(\omega)} \cos^2\vartheta \right) \quad (\text{A.110})$$

The third term is small and might be neglected but the second interference term has to be taken into account. As we can see from equation (A.107) in comparison with equation (A.102) this second term has two contributions: one from the relativistic character of the problem, which vanishes for  $\beta \ll 1$ , and one from the electric quadrupole.

## A.4 Coulomb Acceleration Model

In the Coulomb-acceleration model (CA) the  $\alpha$  particle is assumed to materialise at the classical turning point with zero velocity and is then accelerated in the Coulomb field of the daughter nucleus.

Let  $Z_\alpha$  and  $Z_d$  be the charge of the  $\alpha$  particle and the daughter nucleus, respectively. Then the Coulomb potential at a relative distance  $r$  of the  $\alpha$  particle and the daughter nucleus is given by

$$V(r) = \frac{Z_\alpha Z_d e^2}{r}. \quad (\text{A.111})$$

Then the classical turning point  $r_c$  is given by the condition  $V(r_c) = Q_\alpha$  where  $Q_\alpha$  is the  $Q$ -value of the  $\alpha$ -decay, i.e. the total kinetic energy released, which is shared by the  $\alpha$ -particle and the daughter nucleus. So one gets

$$r_c = \frac{Z_\alpha Z_d e^2}{Q_\alpha} \quad (\text{A.112})$$

The equation of motion is given by Newton's law

$$\mu \ddot{r}(t) = -\frac{\partial}{\partial r} V(r) = \frac{Z_\alpha Z_d e^2}{r^2(t)} \implies \ddot{r}(t) = \frac{Z_\alpha Z_d e^2}{\mu r^2(t)} \quad (\text{A.113})$$

where  $\mu$  is the reduced mass given by equation (A.57).

At the beginning of the acceleration ( $t_0 = 0$ ) the  $\alpha$  particle is at rest at the classical turning point  $r_c$ . From energy conservation we get

$$\frac{1}{2}\mu v^2(r) = Q_\alpha - \frac{Z_\alpha Z_d e^2}{r} \quad (\text{A.114})$$

$$\Rightarrow v(r) = \frac{dr}{dt} = \sqrt{\frac{2}{\mu} \left( Q_\alpha - \frac{Z_\alpha Z_d e^2}{r} \right)} = \sqrt{\frac{2Z_\alpha Z_d e^2}{\mu}} \sqrt{\frac{1}{r_c} - \frac{1}{r}}. \quad (\text{A.115})$$

Or looking at  $\beta(r)$  and  $\dot{\beta}(r)$  as defined in (A.94) we get

$$\beta(r) = \sqrt{\frac{2Z_\alpha Z_d e^2}{\mu c^2}} \sqrt{\frac{1}{r_c} - \frac{1}{r}} \quad (\text{A.116})$$

$$\dot{\beta}(r) = \frac{Z_\alpha Z_d e^2}{\mu c} \frac{1}{r^2} \quad \text{for } r > r_c \quad (\text{A.117})$$

To evaluate equation (A.80) we substitute the integration over time by the integration over the relative distance  $r$  by

$$\dot{\beta} dt = \frac{d\beta}{dt} dt = \frac{d\beta}{dt} \frac{dt}{dr} dr = \frac{d\beta}{dr} dr. \quad (\text{A.118})$$

From equation (A.116) we get

$$\frac{d\beta}{dr} = \beta'(r) = \sqrt{\frac{Z_\alpha Z_d e^2}{2\mu c^2}} \left( \frac{1}{r_c} - \frac{1}{r} \right)^{-\frac{1}{2}} \frac{1}{r^2}. \quad (\text{A.119})$$

The resulting expression for the bremsstrahlung emission probability per energy interval and solid angle derived from equation (A.107) is then given by

$$\frac{d^2P}{d\omega d\Omega} \approx \frac{\alpha}{4\pi^2\omega} \left| \int_{r_c}^{+\infty} \left( Z_{\text{eff}}^{E1} + Z_{\text{eff}}^{E2} \left( 2\beta(r) - i\frac{\omega}{c}r \right) \cos\vartheta \right) \beta'(r) \sin\vartheta e^{i\omega t(r)} dr \right|^2. \quad (\text{A.120})$$

To get an expression for  $t(r)$  the differential equation (A.114) might be solved by standard techniques [62]. Equation (A.114) can be written as

$$\dot{r}^2(t) + \frac{\zeta}{r} = \Omega \quad (\text{A.121})$$

with

$$\zeta = \frac{2Z_\alpha Z_d e^2}{\mu} \quad \text{and} \quad \Omega = \frac{2Q_\alpha}{\mu} \quad (\text{A.122})$$

For the differential equation (A.121) we find the solution

$$t(r) = \left[ \frac{\zeta \ln(\sqrt{\Omega\rho} + \sqrt{\Omega\rho - \zeta})}{\Omega^{\frac{3}{2}}} + \frac{\sqrt{\Omega\rho^2 - \zeta\rho}}{\Omega} \right]_{\rho=r_c}^{\rho=r} \quad (\text{A.123})$$

or with  $r_c = \zeta/\Omega$  we get

$$t(r) = \left[ \sqrt{\frac{\mu}{2Q_\alpha}} \left( r_c \ln(\sqrt{\rho} + \sqrt{\rho - r_c}) + \sqrt{\rho(\rho - r_c)} \right) \right]_{\rho=r_c}^{\rho=r}. \quad (\text{A.124})$$

Equation (A.120) can be evaluated numerically. In figure A.3 the velocity  $\beta(r)$ , its derivative  $\beta'(r)$ , the acceleration  $\dot{\beta}(r)$  and the time  $t(r)$  is plotted for the case of  $^{210}\text{Po}$ . The resulting emission probability is given in figure A.4.

### Angular Correlation

As stated above equation (A.120) has the form

$$\frac{d^2P}{d\omega d\Omega} \approx C |(f_1(\omega) + f_2(\omega) \cos \vartheta) \sin \vartheta|^2 \quad (\text{A.125})$$

$$= C f_1^2(\omega) \sin^2 \vartheta \left( 1 + \frac{2\text{Re}(f_1(\omega)f_2^*(\omega))}{f_1^2(\omega)} \cos \vartheta + \frac{f_2^2(\omega)}{f_1^2(\omega)} \cos^2 \vartheta \right) \quad (\text{A.126})$$

with

$$f_1(\omega) = \int_{r_c}^{+\infty} Z_{\text{eff}}^{E1} \beta'(r) e^{i\omega t(r)} dr \quad (\text{A.127})$$

$$f_2(\omega) = \int_{r_c}^{+\infty} Z_{\text{eff}}^{E2} \left( 2\beta(r) - i\frac{\omega}{c}r \right) \beta'(r) e^{i\omega t(r)} dr \quad (\text{A.128})$$

The equation (A.125) can be approximated by

$$\frac{d^2P}{d\omega d\Omega} \approx C f_1^2(\omega) \sin^2 \vartheta (1 + 2\Lambda(\omega) \cos \vartheta). \quad (\text{A.129})$$

with the correction function  $\Lambda$  is defined by

$$\Lambda(\omega) = \frac{\text{Re}(f_1(\omega)f_2^*(\omega))}{f_1^2(\omega)}. \quad (\text{A.130})$$

In figure A.5 the correction function  $\Lambda$  is plotted. From equation (A.120) we see that this correction function has two contributions. The contribution from the term  $2\beta(r)$  in the integrant is referred to as the "relativistic correction" and the correction from the term  $-i\frac{\omega}{c}r$  as the "quadrupole correction".

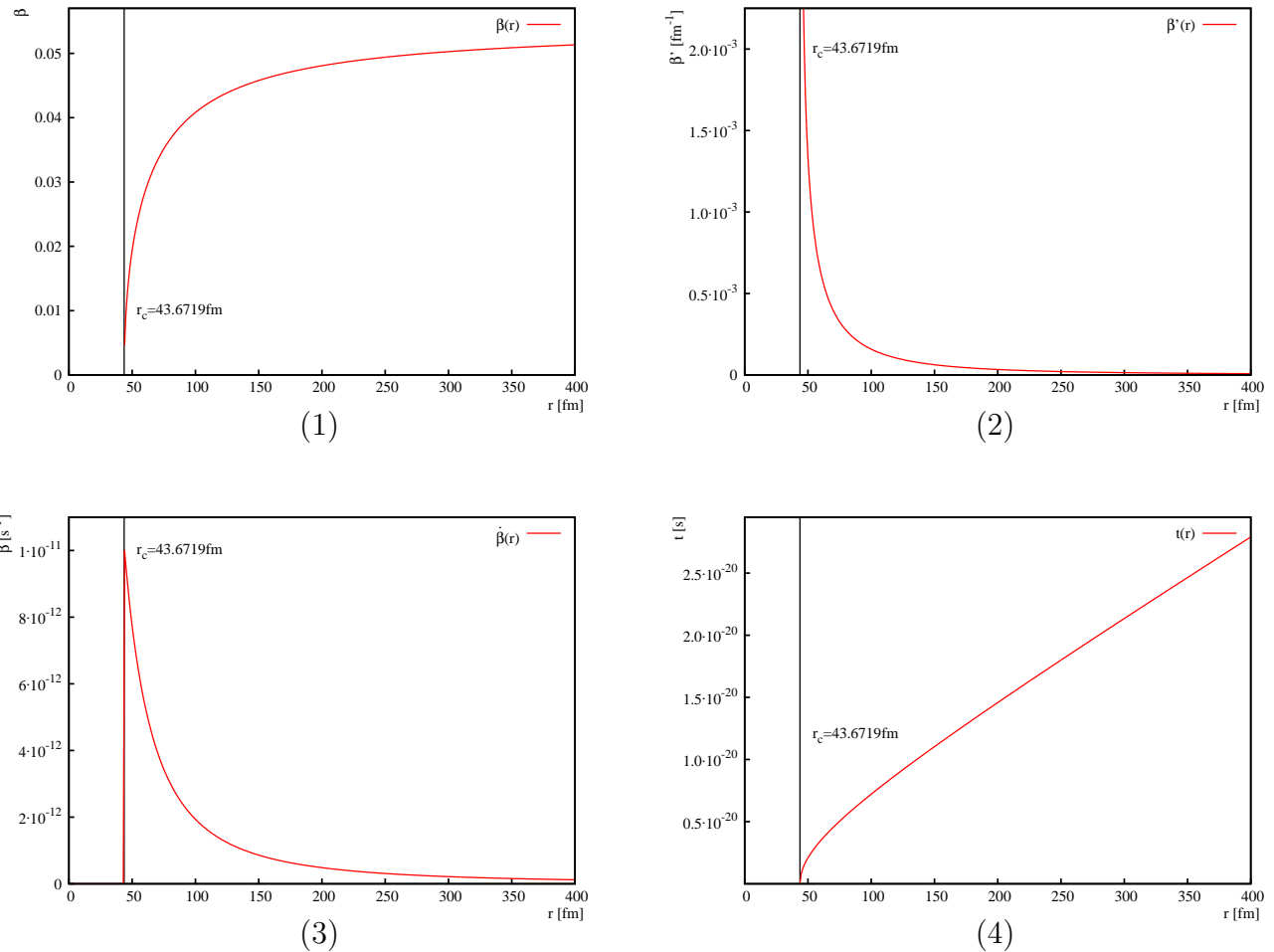


**Figure A.3:** The relative velocity  $\beta$  (1), its derivative with respect to  $r$  (2), the acceleration  $\dot{\beta}$  (3) and the time  $t$  (4) as functions of  $r$  for the case of  $^{210}\text{Po}$

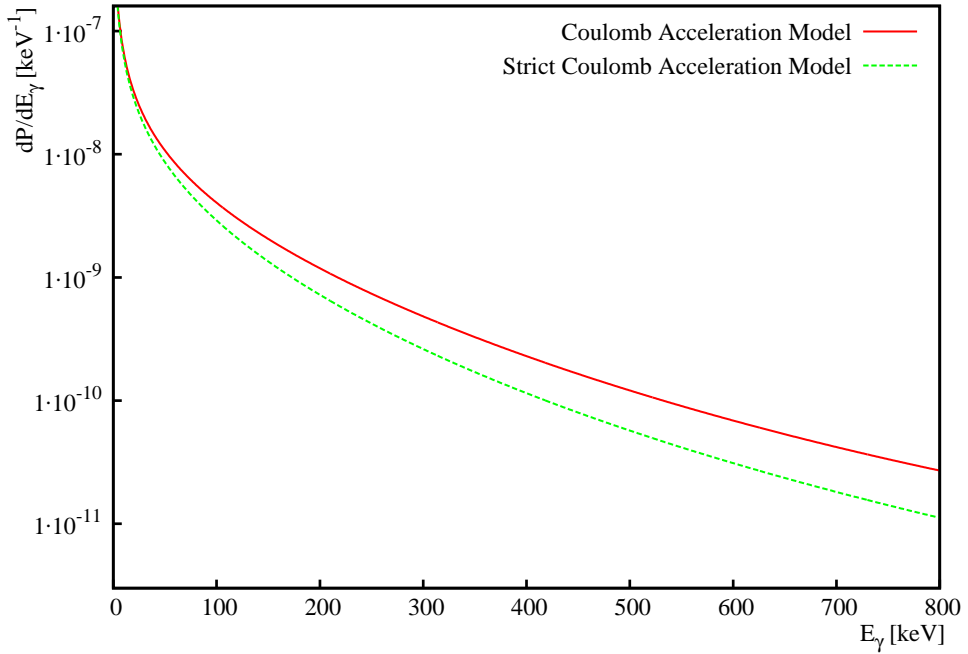


**Figure A.4:** The resulting bremsstrahlung emission probability of  $^{210}\text{Po}$  is shown for the Coulomb acceleration model (red) and the strict Coulomb acceleration model (green).

## A.5 Strict Coulomb Acceleration Model

In the *strict Coulomb acceleration model* (SCA) it is taken into account that from a classical point of view an bremsstrahlung photon of energy  $E_\gamma$  can only be emitted by an  $\alpha$ -particle which kinetic is bigger than  $E_\gamma$ . So the integration of equation (A.120) starts from the point  $r_{\min}$  with

$$r_{\min} = \frac{Z_\alpha Z_d e^2}{Q_\alpha - E_\gamma} \quad (\text{A.131})$$

The bremsstrahlung emission probability of  $^{210}\text{Po}$  in the strict Coulomb acceleration model is plotted in green in figure A.4. In figure A.5 the corresponding corrections  $\Lambda(E_\gamma)$  to the angular correlation are plotted. Note the large differences between the CA and SCA model for the relativistic as well as the E2 contribution to the interference term.

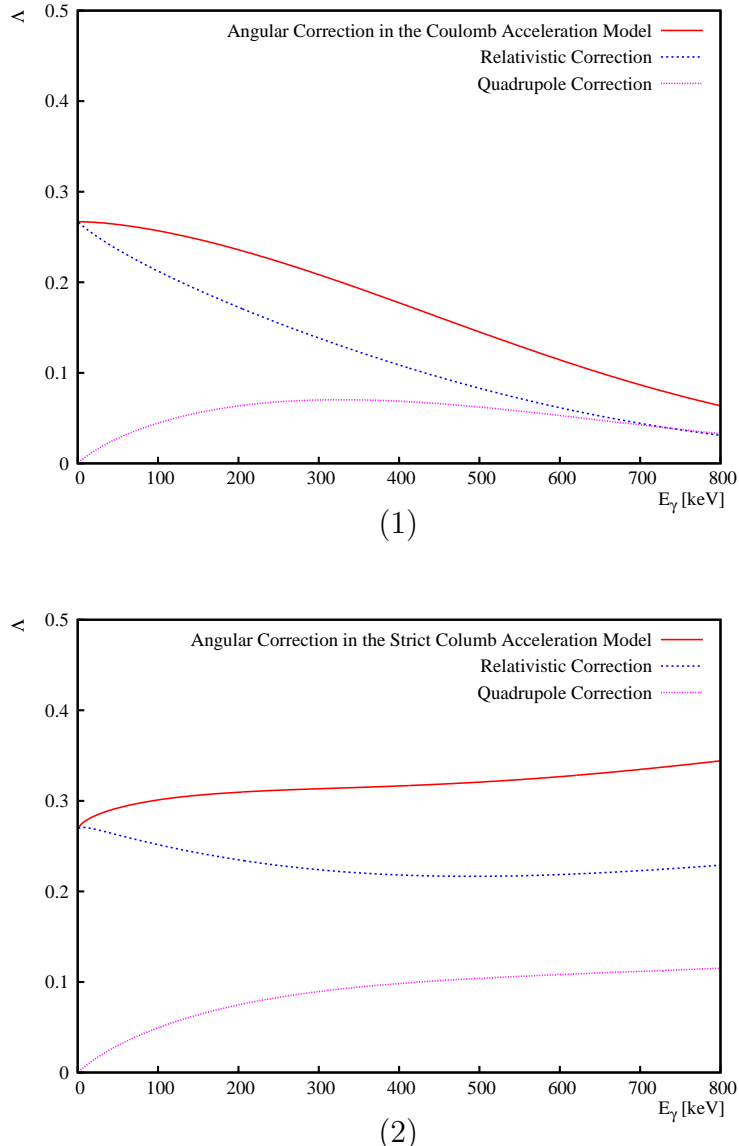


**Figure A.5:** The correction of the angular distribution described by the function  $\Lambda$  given by equation (A.130) is plotted for the Coulomb acceleration model (1) and the strict Coulomb acceleration model (2). In both cases the contribution from the relativistic character of the problem (blue) and the electric quadrupole (magenta) is also plotted separately.

## Appendix B

# Quantum Mechanical Treatment

In this chapter we follow the quantum mechanical calculation by Papenbrock and Bertsch [3].

As discussed in appendix A.2 the system of the  $\alpha$  particle and the daughter nucleus can be viewed as a *relative particle* with the *reduced mass*

$$\mu = \frac{M_\alpha \cdot M_d}{M_\alpha + M_d} \quad (\text{B.1})$$

in a potential  $U(r)$ , where  $r$  is the relative coordinate of the two particles ( $M_\alpha$  is the mass of the  $\alpha$  particle,  $M_d$  the mass of the daughter nucleus).

In the following sections we will discuss the photon emission probability (section B.1) and the solutions of the Schrödinger equation in a Coulomb potential and a constant potential (section B.2) for a general particle of mass  $m$ , charge  $q$  in a potential  $U(r)$ .

In sections B.3-B.8 the quantum mechanical description of bremsstrahlung emission probability in the  $\alpha$  decay is derived.

### B.1 Photon Emission Probability in the Dipole Approximation

According to Fermi's golden rule the photon emission probability for the transition from the initial state  $|i\rangle$  to the final state  $|f\rangle$  is

$$W_{i \rightarrow f} = \frac{2\pi}{\hbar} |\langle f | H_{\text{em}} | i \rangle|^2 \rho_f , \quad (\text{B.2})$$

where  $\rho_f$  is the density of the final states. The interaction Hamiltonian of the electromagnetic field  $H_{\text{em}}$  is given by

$$H_{\text{em}} = -\frac{q}{mc} \mathbf{p} \cdot \mathbf{A}(\mathbf{r}, t), \quad (\text{B.3})$$

where  $q$ ,  $m$  and  $\mathbf{p}$  are the charge, the mass and the momentum of the particle, respectively. With the quantisation of the electromagnetic field the vector potential  $\mathbf{A}$  can be written as (e.g. [63])

$$\mathbf{A}(\mathbf{r}, t) = \sum_{k_\gamma, \lambda} \sqrt{\frac{2\pi\hbar c}{k_\gamma V}} \left( a_{k_\gamma, \lambda} \boldsymbol{\epsilon}_{k_\gamma, \lambda} e^{i\mathbf{k}_\gamma \cdot \mathbf{r} - i\omega_\gamma t} + a_{k_\gamma, \lambda}^\dagger \boldsymbol{\epsilon}_{k_\gamma, \lambda}^* e^{-i\mathbf{k}_\gamma \cdot \mathbf{r} + i\omega_\gamma t} \right). \quad (\text{B.4})$$

In equation (B.4) the usual definition of the ladder operators

$$\begin{aligned} a_{k_\gamma, \lambda} |\dots, n_{k_\gamma, \lambda}, \dots\rangle &= \sqrt{n_{k_\gamma, \lambda}} |\dots, n_{k_\gamma, \lambda} - 1, \dots\rangle \\ a_{k_\gamma, \lambda}^\dagger |\dots, n_{k_\gamma, \lambda}, \dots\rangle &= \sqrt{n_{k_\gamma, \lambda} + 1} |\dots, n_{k_\gamma, \lambda} + 1, \dots\rangle \end{aligned}$$

is used. The wave-vector  $\mathbf{k}_\gamma$  points in the direction of the propagation of the photon, the polarisation vectors  $\boldsymbol{\epsilon}_{k_\gamma, \lambda}$  ( $\lambda = 1, 2$ ) are perpendicular to  $\mathbf{k}_\gamma$  and to each other. The volume  $V$  introduced in (B.4) is defined to have periodical boundary conditions, the frequency  $\omega_\gamma$  is given by

$$|\mathbf{k}_\gamma| = \frac{\omega_\gamma}{c}. \quad (\text{B.5})$$

The initial and final states can be written as the direct product of the initial and final states  $|\Phi_i\rangle$  and  $|\Phi_f\rangle$  of the particle and the photon states  $|0\rangle$  and  $|1_{k_\gamma, \lambda}\rangle = a_{k_\gamma, \lambda}^\dagger |0\rangle$ , respectively

$$\langle f | = \langle \Phi_f | \langle 1_{k_\gamma, \lambda} | = \langle \Phi_f | \langle 0 | a_{k_\gamma, \lambda} \quad | i \rangle = |0\rangle |\Phi_i\rangle. \quad (\text{B.6})$$

Using the equations (B.4), (B.3) and (B.2) the emission probability of a photon with wave-vector  $\mathbf{k}_\gamma$  can be expressed by

$$W_{i \rightarrow f, k_\gamma} = \frac{(2\pi)^2 q^2}{m^2 c k V} \sum_{\lambda} \left| \langle \Phi_f | \langle 1_{k_\gamma, \lambda} | \mathbf{p} \cdot \boldsymbol{\epsilon}_{k_\gamma, \lambda}^* e^{-i\mathbf{k}_\gamma \cdot \mathbf{r}} |0\rangle |\Phi_i\rangle \right|^2 \rho_f. \quad (\text{B.7})$$

Because of  $a_{k_\gamma, \lambda} |0\rangle = |0\rangle$  only the second part of equation (B.4) contributes to  $W_{i \rightarrow f, k_\gamma}$ .

In the  $\mathbf{k}_\gamma$ -space there are  $d^3 k_\gamma V / (2\pi)^3$  states in the volume element  $d^3 k_\gamma$ , which is given by  $d^3 k_\gamma = k_\gamma^2 dk_\gamma d\Omega$ . The photon emission probability is then given by

$$\begin{aligned} \frac{dP}{dE_\gamma d\Omega} &= \int \frac{k_\gamma^2 dk_\gamma V}{(2\pi)^3} \frac{(2\pi)^2 q^2}{m^2 c k_\gamma V} \sum_\lambda \left| \langle \Phi_f | \mathbf{p} \cdot \boldsymbol{\epsilon}_{k_\gamma, \lambda}^* e^{-i\mathbf{k}_\gamma \cdot \mathbf{r}} | \Phi_i \rangle \right|^2 \delta(E_i - E_f - \hbar k_\gamma c) \\ &= \int dk_\gamma k_\gamma \frac{q^2}{2\pi m^2 c} \sum_\lambda \left| \langle \Phi_f | \mathbf{p} \cdot \boldsymbol{\epsilon}_{k_\gamma, \lambda}^* e^{-i\mathbf{k}_\gamma \cdot \mathbf{r}} | \Phi_i \rangle \right|^2 \delta(E_i - E_f - \hbar k_\gamma c). \quad (\text{B.8}) \end{aligned}$$

We use the Taylor expansion for  $e^{-i\mathbf{k}_\gamma \cdot \mathbf{r}}$

$$e^{-i\mathbf{k}_\gamma \cdot \mathbf{r}} = 1 - i\mathbf{k}_\gamma \cdot \mathbf{r} + \frac{1}{2}(i\mathbf{k}_\gamma \cdot \mathbf{r})^2 + \dots \quad (\text{B.9})$$

and get in the *dipole approximation*  $e^{-i\mathbf{k}_\gamma \cdot \mathbf{r}} \approx 1$

$$\frac{dP}{dE_\gamma d\Omega} = \int dk_\gamma k_\gamma \frac{q^2}{2\pi m^2 c} \sum_\lambda \left| \langle \Phi_f | \mathbf{p} \cdot \boldsymbol{\epsilon}_{k_\gamma, \lambda}^* | \Phi_i \rangle \right|^2 \delta(E_i - E_f - \hbar k_\gamma c). \quad (\text{B.10})$$

Let  $\vartheta$  be the angle between  $\mathbf{p}$  and  $\mathbf{k}_\gamma$ ,  $\theta_1$  and  $\theta_2$  the angle between  $\mathbf{p}$  and  $\boldsymbol{\epsilon}_{k_\gamma, 1}$ ,  $\boldsymbol{\epsilon}_{k_\gamma, 2}$ , respectively. Then it is easy to see that

$$\cos \theta_1 = \sin \vartheta \cos \vartheta \quad \cos \theta_2 = \sin \vartheta \sin \vartheta. \quad (\text{B.11})$$

With  $\mathbf{p} \cdot \boldsymbol{\epsilon}_{k_\gamma, \lambda} = p \cos \theta_\lambda$  we can perform the summation over  $\lambda = 1, 2$  as  $\cos^2 \theta_1 + \cos^2 \theta_2 = \sin^2 \vartheta$  and obtain

$$\frac{dP}{dE_\gamma d\Omega} = \frac{q^2}{2\pi m^2 c} \int dk_\gamma k_\gamma \left| \langle \Phi_f | p | \Phi_i \rangle \right|^2 \delta(E_i - E_f - \hbar k_\gamma c) \cdot \sin^2 \vartheta. \quad (\text{B.12})$$

Performing the integration over  $k_\gamma$  with  $\delta(ax) = \frac{1}{|a|} \delta(x)$  and  $k_\gamma = \omega_\gamma/c = E_\gamma/(\hbar c)$  leads to

$$\frac{dP}{dE_\gamma d\Omega} = \frac{q^2 E_\gamma}{2\pi m^2 \hbar^2 c^3} \left| \langle \Phi_f | p | \Phi_i \rangle \right|^2 \cdot \sin^2 \vartheta. \quad (\text{B.13})$$

With the Hamiltonian

$$H = \frac{\mathbf{p}^2}{2m} + U(\vec{r}) \quad (\text{B.14})$$

and a spherically symmetric potential  $U(r)$ , the matrix element can also be written as

$$\langle \Phi_f | p | \Phi_i \rangle = \frac{1}{E_i - E_f} \langle \Phi_f | [H, p] | \Phi_i \rangle = \frac{1}{E_\gamma} \langle \Phi_f | [H, p] | \Phi_i \rangle = \frac{i\hbar}{E_\gamma} \langle \Phi_f | \partial_r U(r) | \Phi_i \rangle. \quad (\text{B.15})$$

So the emission probability for an photon of energy  $E_\gamma$  is given by

$$\frac{dP}{dE_\gamma d\Omega} = \frac{q^2}{2\pi m^2 c^3} \left| \langle \Phi_f | \partial_r U(r) | \Phi_i \rangle \right|^2 \frac{1}{E_\gamma} \cdot \sin^2 \vartheta . \quad (\text{B.16})$$

and since

$$\int d\Omega \sin^2 \vartheta = \int_0^{2\pi} d\varphi \int_0^\pi d\vartheta \sin^3 \vartheta = \frac{8\pi}{3} \quad (\text{B.17})$$

we find for the angle-integrated emission probability

$$\frac{dP}{dE_\gamma} = \frac{4 q^2}{3 m^2 c^3} \left| \langle \Phi_f | \partial_r U(r) | \Phi_i \rangle \right|^2 \frac{1}{E_\gamma} . \quad (\text{B.18})$$

## B.2 Time-independent Schrödinger Equation of Spherically Symmetric Potentials

The time-independent Schrödinger equation for a spherically symmetric potential  $U(r)$  is given by

$$\left( -\frac{\hbar^2}{2m} \Delta + U(r) \right) \varphi(\mathbf{r}) = E \varphi(\mathbf{r}) . \quad (\text{B.19})$$

The Laplace-Operator  $\Delta$  is given by

$$\Delta = \frac{1}{r} \frac{\partial^2}{\partial r^2} r + \frac{1}{r^2} \left( \frac{\partial^2}{\partial \theta^2} + \frac{1}{\tan \theta} \frac{\partial}{\partial \theta} + \frac{1}{\sin^2 \theta} \frac{\partial^2}{\partial \varphi^2} \right) \quad (\text{B.20})$$

using the polar coordinates  $r$ ,  $\theta$  and  $\phi$ . With the operator for the square of the angular momentum  $\mathbf{L}^2$

$$\mathbf{L}^2 = -\hbar^2 \left( \frac{\partial^2}{\partial \theta^2} + \frac{1}{\tan \theta} \frac{\partial}{\partial \theta} + \frac{1}{\sin^2 \theta} \frac{\partial^2}{\partial \varphi^2} \right) , \quad (\text{B.21})$$

the equation (B.19) can be written as

$$\left( -\frac{\hbar^2}{2m} \frac{1}{r} \frac{\partial^2}{\partial r^2} r + \frac{\mathbf{L}^2}{2mr^2} + U(r) \right) \varphi(\mathbf{r}) = E \varphi(\mathbf{r}) . \quad (\text{B.22})$$

Splitting up the wave function into a product of a radial part  $R(r)$  and the spherical harmonics  $Y_L^m(\theta, \varphi)$

$$\varphi(\mathbf{r}) = R(r) Y_L^m(\theta, \varphi) \quad (\text{B.23})$$

gives the differential equation for the radial function  $R_L(r)$

$$\left( -\frac{\hbar^2}{2m} \frac{1}{r} \frac{\partial^2}{\partial r^2} r + \frac{L(L+1)\hbar^2}{2mr^2} + U(r) \right) R_L(r) = ER_L(r). \quad (\text{B.24})$$

Here  $L(L+1)\hbar$  is the eigenvalue of the operator  $\mathbf{L}^2$  for the functions  $Y_L^m$

$$\mathbf{L}^2 Y_L^m(\theta, \varphi) = L(L+1)\hbar^2 Y_L^m(\theta, \varphi). \quad (\text{B.25})$$

Introducing the functions  $u_L(r)$  as

$$R_L(r) = \frac{u_L(r)}{r} \quad (\text{B.26})$$

further simplifies equation (B.24) to

$$\left( -\frac{\hbar^2}{2m} \frac{\partial^2}{\partial r^2} + \frac{L(L+1)\hbar^2}{2mr^2} + U(r) \right) u_L(r) = Eu_L(r) \quad (\text{B.27})$$

$$\implies \frac{\partial^2}{\partial r^2} u_L(r) + \left( \frac{2mE}{\hbar^2} - \frac{2m}{\hbar^2} U(r) - \frac{L(L+1)}{r^2} \right) u_L(r) = 0. \quad (\text{B.28})$$

### B.2.1 The Coulomb Potential

The Coulomb potential for a charge  $q$  in the field of a second charge  $Q$  is given by

$$U(r) = \frac{qQ}{r}. \quad (\text{B.29})$$

The functions  $u_L(r)$  are then defined by the differential equation obtained from (B.28)

$$\frac{\partial^2}{\partial r^2} u_L(r) + \left( \frac{2mE}{\hbar^2} - \frac{2mqQ}{\hbar^2 r} - \frac{L(L+1)}{r^2} \right) u_L(r) = 0. \quad (\text{B.30})$$

By the substitution

$$k = \frac{1}{\hbar} \sqrt{2mE}, \quad \rho = kr \quad \eta = \frac{mqQ}{\hbar^2 k} \quad (\text{B.31})$$

this reduces to the *Coulomb wave equation*

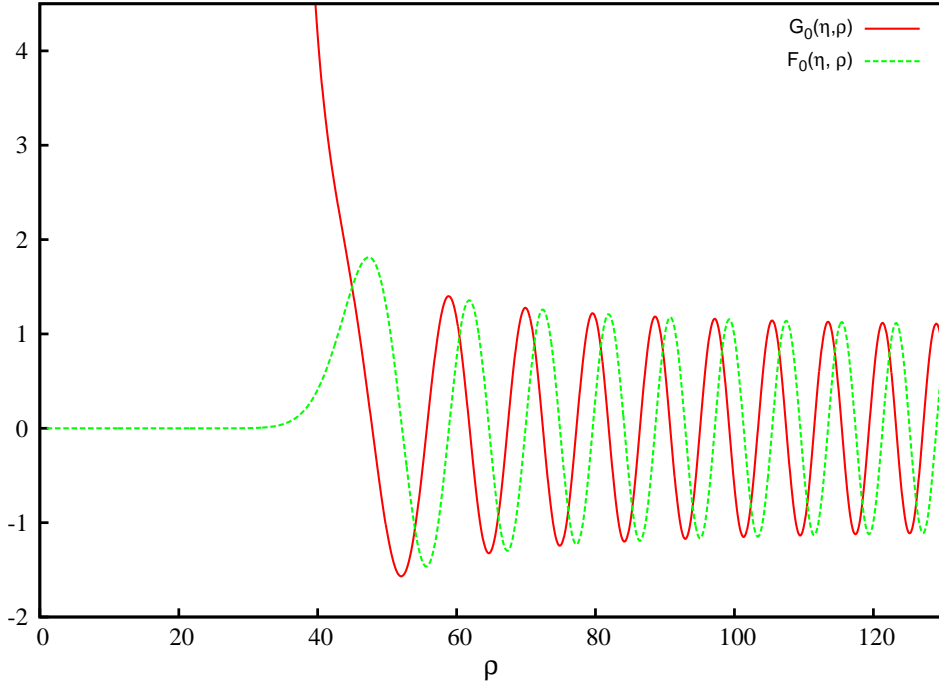


**Figure B.1:** Coulomb wave functions  $G_0(\eta, \rho)$  and  $F_0(\eta, \rho)$  with a realistic  $\eta = 22.0079$ .

$$\frac{\partial^2}{\partial \rho^2} u_L(\rho) + \left(1 - \frac{2\eta}{\rho} - \frac{L(L+1)}{\rho^2}\right) u_L(\rho) = 0. \quad (\text{B.32})$$

The general solutions of this differential equation are given by

$$u_L(\rho) = c_1 F_L(\eta, \rho) + c_2 G_L(\eta, \rho) \quad (\text{B.33})$$

where  $F_L(\eta, \rho)$  is the *regular Coulomb wave function* and  $G_L(\eta, \rho)$  is the *irregular Coulomb wave function* [64]. Figure B.1 shows the functions  $F_0(\eta, \rho)$  and  $G_0(\eta, \rho)$  for  $\eta = 22.0079$ , relevant in the case of  $^{210}\text{Po}$ .

The asymptotic behaviour of the Coulomb wave functions is given by

$$F_L(\eta, \rho) \xrightarrow{\rho \rightarrow \infty} \sin\left(\rho - \eta \ln 2\rho - L\frac{\pi}{2} + \sigma_L\right) \quad (\text{B.34})$$

$$G_L(\eta, \rho) \xrightarrow{\rho \rightarrow \infty} \cos\left(\rho - \eta \ln 2\rho - L\frac{\pi}{2} + \sigma_L\right) \quad (\text{B.35})$$

where

$$\sigma_L = \arg \Gamma(L+1+i\eta). \quad (\text{B.36})$$

Further holds the *Wronskian Relation*

$$\left(\frac{\partial}{\partial \rho} F_L(\eta, \rho)\right) G_L(\eta, \rho) - F_L(\eta, \rho) \frac{\partial}{\partial \rho} G_L(\eta, \rho) = 1. \quad (\text{B.37})$$

Let  $u_L = F_L(\eta, \rho)$  or  $u_L = G_L(\eta, \rho)$  then following *recurrence relations* hold

$$L \frac{\partial}{\partial \rho} u_L = \sqrt{L^2 + \eta^2} u_{L-1} - \left( \frac{L^2}{\rho} + \eta \right) u_L \quad (\text{B.38})$$

$$(L+1) \frac{\partial}{\partial \rho} u_L = \left( \frac{(L+1)^2}{\rho} + \eta \right) u_L - \sqrt{(L+1)^2 + \eta^2} u_{L+1} \quad (\text{B.39})$$

$$\begin{aligned} L \sqrt{(L+1)^2 + \eta^2} u_{L+1} &= (2L+1) \left( \eta + \frac{L(L+1)}{\rho} \right) u_L \\ &\quad - (L+1) \sqrt{L^2 + \eta^2} u_{L-1}. \end{aligned} \quad (\text{B.40})$$

### B.2.2 Constant Potential

If we take the potential  $U(r)$  to be constant

$$U(r) = V_0 \quad (\text{B.41})$$

the differential equation for the radial functions  $R_L(r)$  (B.24) has the form

$$\left( \frac{1}{r} \frac{\partial^2}{\partial r^2} r - \frac{L(L+1)}{r^2} + \frac{2m(E-V_0)}{\hbar^2} \right) R_L(r) = 0 \quad (\text{B.42})$$

or by using the relation

$$\frac{1}{r} \frac{\partial^2}{\partial r^2} r R_L = \frac{\partial^2}{\partial r^2} R_L + \frac{2}{r} \frac{\partial}{\partial r} R_L \quad (\text{B.43})$$

this can also be written as

$$\left( \frac{\partial^2}{\partial r^2} + \frac{2}{r} \frac{\partial}{\partial r} - \frac{L(L+1)}{r^2} + \frac{2m(E-V_0)}{\hbar^2} \right) R_L(r) = 0. \quad (\text{B.44})$$

By substituting

$$\kappa = \frac{1}{\hbar} \sqrt{2m(E-V_0)}, \quad \sigma = \kappa r \quad (\text{B.45})$$

one obtains

$$\left[ \frac{\partial^2}{\partial \sigma^2} + \frac{2}{\sigma} \frac{\partial}{\partial \sigma} + \left( 1 - \frac{L(L+1)}{\sigma^2} \right) \right] R_L(\sigma) = 0. \quad (\text{B.46})$$

This differential equation is solved by the *spherical Bessel functions*  $j_L(\sigma)$  and  $n_L(\sigma)$ :

$$R_L(\sigma) = a_1 j_L(\sigma) + a_2 n_L(\sigma). \quad (\text{B.47})$$

The spherical Bessel functions can also be written as

$$j_L(\sigma) = (-\sigma)^L \left( \frac{1}{\sigma} \frac{\partial}{\partial \sigma} \right) \frac{\sin \sigma}{\sigma} \quad (\text{B.48})$$

$$n_L(\sigma) = -(-\sigma)^L \left( \frac{1}{\sigma} \frac{\partial}{\partial \sigma} \right) \frac{\cos \sigma}{\sigma}. \quad (\text{B.49})$$

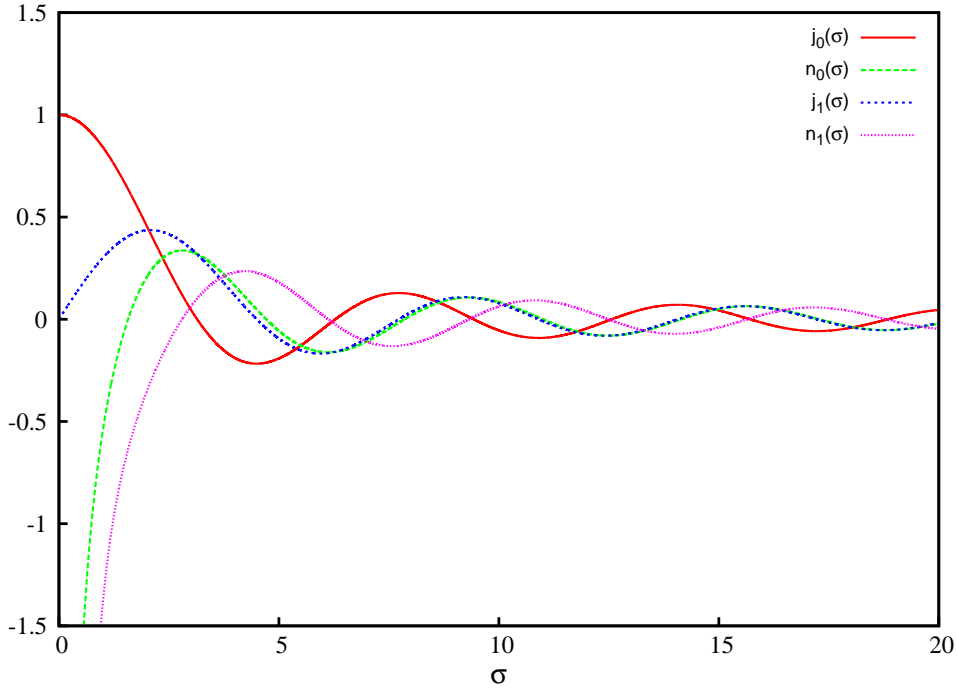


**Figure B.2:** spherical Bessel functions  $j_0(\sigma)$ ,  $j_1(\sigma)$ ,  $n_0(\sigma)$  and  $n_1(\sigma)$

For the asymptotic behaviour we have

$$j_L(\sigma) \xrightarrow{\sigma \rightarrow \infty} \frac{1}{\sigma} \sin \left( \sigma - L \frac{\pi}{2} \right) \quad n_L(\sigma) \xrightarrow{\sigma \rightarrow \infty} \frac{1}{\sigma} \cos \left( \sigma - L \frac{\pi}{2} \right) \quad (\text{B.50})$$

and

$$j_L(\sigma) \xrightarrow{\sigma \rightarrow 0} \frac{\sigma^L}{(2L+1)!!} \quad n_L(\sigma) \xrightarrow{\sigma \rightarrow 0} \frac{(2L-1)!!}{\sigma^{L+1}}. \quad (\text{B.51})$$

In figure B.2 the functions  $j_0(\sigma)$ ,  $j_1(\sigma)$ ,  $n_0(\sigma)$  and  $n_1(\sigma)$  are plotted

$$\begin{aligned} j_0(\sigma) &= \frac{\sin \sigma}{\sigma} & n_0(\sigma) &= -\frac{\cos \sigma}{\sigma} \\ j_1(\sigma) &= \frac{\sin \sigma}{\sigma^2} - \frac{\cos \sigma}{\sigma} & n_1(\sigma) &= -\frac{\cos \sigma}{\sigma^2} - \frac{\sin \sigma}{\sigma}. \end{aligned} \quad (\text{B.52})$$

### B.3 Description of the $\alpha$ Decay using Gamow Vectors

The potential experienced by the  $\alpha$  decay is usually approximated by (see figure 2.1)

$$U(r) = \frac{Z_\alpha Z_d e^2}{r} \Theta(r - r_0) + V_0 \Theta(r_0 - r) \quad (\text{B.53})$$

with the charge of the  $\alpha$  particle  $Z_\alpha$ , the charge of the daughter nucleus  $Z_d$ , and the distance  $r$  between the two particles. The function  $\Theta(x)$  is called the Heaviside step function and is defined as

$$\Theta(x) = \begin{cases} 0 & \text{for } x < 0 \\ \frac{1}{2} & \text{for } x = 0 \\ 1 & \text{for } x > 0 \end{cases} \quad (\text{B.54})$$

The unknown values for the radius of the nucleus  $r_0$  and the potential inside the nucleus  $V_0$  are chosen to describe the measured  $\alpha$  decay width and energy for a given initial state  $|\Phi_i\rangle$ .

### B.3.1 Gamow Vectors

For the quantum mechanical description of a decaying particle the formalism of Gamow vectors is used, first proposed by Gamow [32] and only shortly later by Gurney and Condon [33]. For a more detailed description see also reference [65, 66].

For a decaying system the number of particles  $N(t)$  that have not decayed satisfy the condition:

$$N(t) = N(0)e^{-\lambda t} \quad (\text{B.55})$$

where  $\lambda$  is called the *decay rate*, which is connected to the *lifetime*  $\tau$  by  $\tau = 1/\lambda$  and to the *half-life*  $T_{1/2}$  of the state by  $T_{1/2} = \ln 2/\lambda$ .

We denote the wave function of the decaying state as  $|\varphi^G(t)\rangle$  (where  $G$  refers to Gamow). For the evolution in time we have the usual equation

$$|\varphi^G(t)\rangle = e^{-iHt/\hbar} |\varphi^G(0)\rangle , \quad (\text{B.56})$$

and for the survival probability  $P_S$  we get

$$P_S = \frac{N(t)}{N(0)} = |\langle \varphi^G(0) | \varphi^G(t) \rangle|^2 \quad (\text{B.57})$$

$$= \left| \langle \varphi^G(0) | \left( e^{-iHt/\hbar} |\varphi^G(0)\rangle \right) \right|^2 \quad (\text{B.58})$$

If we claim the expression for the survival probability to be equal with the decay law in equation (B.55), we get the relation

$$\left| \langle \varphi^G(0) | \left( e^{-iHt/\hbar} |\varphi^G(0)\rangle \right) \right|^2 = e^{-\lambda t} . \quad (\text{B.59})$$

This equality can be achieved if  $|\varphi^G(0)\rangle$  is an eigenvector of the Hamiltonian  $H^G$  with a complex eigenvalue

$$H^G |\varphi^G(0)\rangle = \left( E_0 - i \frac{\Gamma}{2} \right) |\varphi^G(0)\rangle \quad (\text{B.60})$$

where  $E$  and  $\Gamma$  are both real and positive. If we postulate this we get from equation (B.59)

$$\left| \langle \varphi^G(0) | \left( e^{-iH^G t/\hbar} | \varphi^G(0) \rangle \right) \right|^2 = e^{-\lambda t} \quad (\text{B.61})$$

$$|\langle \varphi^G(0) | \varphi^G(0) \rangle e^{-i(E_0 - i(\Gamma/2))t/\hbar}|^2 = e^{-\lambda t} \quad (\text{B.62})$$

$$e^{-\Gamma t/\hbar} = e^{-\lambda t} \quad (\text{B.63})$$

$$\lambda = \frac{\Gamma}{\hbar} \quad (\text{B.64})$$

using the normalisation  $\langle \varphi^G(0) | \varphi^G(0) \rangle = 1$ . It is important to note that the introduced "Hamiltonian"  $H^G$  has a complex eigenvalue and therefore cannot be hermitian [67].

### B.3.2 Gamow Vector and Decay Rate for the $\alpha$ Decay

The Hamiltonian of the stable system with the potential (B.53) is given by

$$H_0 := \frac{\mathbf{p}^2}{2\mu} + \frac{Z_\alpha Z_d e^2}{r} \Theta(r - r_0) + V_0 \Theta(r_0 - r). \quad (\text{B.65})$$

The initial state  $|\Phi_i\rangle$  can be found by solving the Schrödinger equation for the space regions  $r < r_0$  and  $r > r_0$ , respectively

$$\left( \frac{\mathbf{p}^2}{2\mu} + V_0 \right) |\varphi_1\rangle = Q_\alpha |\varphi_1\rangle \quad \text{for } r < r_0 \quad (\text{B.66})$$

$$\left( \frac{\mathbf{p}^2}{2\mu} + \frac{Z_\alpha Z_d e^2}{r} \right) |\varphi_2\rangle = Q_\alpha |\varphi_2\rangle \quad \text{for } r > r_0. \quad (\text{B.67})$$

From section B.2 we know the general solutions for the radial equations

$$\Phi_1(r) = A_1 j_L(\kappa_0 r) + A_2 n_L(\kappa_0 r) \quad (\text{B.68})$$

$$\Phi_2(r) = \frac{C_1 F_L(\eta_0, k_0 r) + C_2 G_L(\eta_0, k_0 r)}{r} \quad (\text{B.69})$$

where  $\eta_0$  and  $k_0$  and  $\kappa_0$  are given by equation (B.31) and (B.45) and the energy  $E_0$  is given by the decay energy  $Q_\alpha$

$$k_0 = \frac{1}{\hbar} \sqrt{2\mu Q_\alpha} \quad \kappa_0 = \frac{1}{\hbar} \sqrt{2\mu(Q_\alpha - V_0)} \quad \eta_0 = \frac{\mu Z_\alpha Z_d e^2}{\hbar^2 k_0}. \quad (\text{B.70})$$

In the following we consider the case of angular momentum  $L = 0$ . Since  $\Phi_1(r)$  must be finite for  $r = 0$  we find  $A_2 = 0$ . For large  $r$  we require  $\Phi_2(r)$  to have the limit of a spherical outgoing wave. Therefore we write

$$\Phi_2(r) = C_2 \frac{G_0(\eta_0, k_0 r) + iF_0(\eta_0, k_0 r)}{r} \quad (\text{B.71})$$

and get for the asymptotic behaviour from equations (B.34) and (B.35)

$$\Phi_2(r) \xrightarrow{r \rightarrow \infty} \frac{\cos(k_0 r - \delta) + i \sin(k_0 r - \delta)}{r} = \frac{e^{ik_0 r - \delta}}{r} \quad (\text{B.72})$$

Hence we get for the wave function of the initial state

$$\Phi_i(r) = \begin{cases} A_1 j_0(\kappa_0 r) & \text{for } r < r_0 \\ C_2 (G_0(\eta_0, k_0 r) + i F_0(\eta_0, k_0 r)) / r & \text{for } r > r_0 \end{cases} \quad (\text{B.73})$$

We now define the analogous Gamow vector  $|\Phi_i^G\rangle$  by

$$\Phi_i^G(r) = \begin{cases} A_1 j_0(\kappa r) & \text{for } r < r_0 \\ C_2 (G_0(\eta, kr) + i F_0(\eta, kr)) / r & \text{for } r > r_0 \end{cases} \quad (\text{B.74})$$

with

$$k = \frac{1}{\hbar} \sqrt{2\mu E} \quad \kappa = \frac{1}{\hbar} \sqrt{2\mu(E - V_0)} \quad \eta = \frac{\mu Z_\alpha Z_d e^2}{\hbar^2 k} \quad E = Q_\alpha - i \frac{\Gamma}{2}. \quad (\text{B.75})$$

and the Hamiltonian  $H^G$  as in equation (B.60)

$$H^G |\Phi_i^G\rangle = \left( Q_\alpha - i \frac{\Gamma}{2} \right) |\Phi_i^G\rangle \quad (\text{B.76})$$

with

$$H^G := H_0 + W^G. \quad (\text{B.77})$$

Because of  $\Gamma \ll 1$  the "Hamiltonian"  $W^G$  can be viewed as a perturbation of the Hamiltonian of the stable system  $H_0$ .

To simplify the further calculations we write

$$A := A_1 \quad C := k C_2 \quad (\text{B.78})$$

and get

$$\Phi_i^G(r) = \begin{cases} A j_0(\kappa r) & \text{for } r < r_0 \\ C \frac{G_0(\eta, kr) + i F_0(\eta, kr)}{kr} & \text{for } r > r_0 \end{cases} \quad (\text{B.79})$$

For the matching of the wave functions  $\Phi_1(r)$  and  $\Phi_2(r)$  at  $r = r_0$  we get following conditions:

$$\Phi_1(r_0) = \Phi_2(r_0) \quad (\text{B.80})$$

$$\frac{\Phi'_1(r_0)}{\Phi_1(r_0)} = \frac{\Phi'_2(r_0)}{\Phi_2(r_0)} \quad (\text{B.81})$$

Equation (B.80) leads to the condition

$$\sin(\kappa r_0) = \frac{C}{A} \frac{\kappa}{k} (G_0(kr_0) + iF_0(kr_0)) \quad (\text{B.82})$$

where the  $j_0$  from equation (B.52) was used.

For the derivative of  $\Phi_1(r)$  and  $\Phi_2(r)$  we get

$$\frac{\partial}{\partial r} \Phi_1(r) = A \left( \frac{\cos(\kappa r)}{r} - \frac{1}{\kappa} \frac{\sin(\kappa r)}{r^2} \right) \quad (\text{B.83})$$

$$\frac{\partial}{\partial r} \Phi_2(r) = C \left( \frac{G'_0(\eta, kr) + iF'_0(\eta, kr)}{r} - \frac{1}{k} \frac{G_0(\eta, kr) + iF_0(\eta, kr)}{r^2} \right) \quad (\text{B.84})$$

with leads to

$$\frac{\Phi'_1(r)}{\Phi_1(r)} = \kappa \cot(\kappa r) - \frac{1}{r} \quad (\text{B.85})$$

$$\frac{\Phi'_2(r)}{\Phi_2(r)} = k \frac{G'_0(\eta, kr) + iF'_0(\eta, kr)}{G_0(\eta, kr) + iF_0(\eta, kr)} - \frac{1}{r}. \quad (\text{B.86})$$

So finally the condition (B.81) can be written as

$$\kappa \cot(\kappa r_0) = k \frac{G'_0(\eta, kr_0) + iF'_0(\eta, kr_0)}{G_0(\eta, kr_0) + iF_0(\eta, kr_0)}. \quad (\text{B.87})$$

This equation is call the *energy relation*. Using identity (B.37) we get

$$\kappa \cot(\kappa r_0) = k \frac{G'_0 + iF'_0}{G_0 + iF_0} \cdot \frac{G_0 - iF_0}{G_0 - iF_0} \quad (\text{B.88})$$

$$\kappa \cot(\kappa r_0) = k \frac{G'_0 G_0 + F'_0 F_0 + i(F'_0 G_0 - G'_0 F_0)}{G_0^2 - F_0^2} \quad (\text{B.89})$$

$$\kappa \cot(\kappa r_0) = k \left( \frac{G'_0 G_0 + F'_0 F_0}{G_0^2 - F_0^2} + \frac{i}{G_0^2 - F_0^2} \right) \quad (\text{B.90})$$

Expanding  $k$  and  $\kappa$  in a Taylor series gives

$$k = k_0 \sqrt{1 - i \frac{\Gamma}{2Q_\alpha}} \quad (\text{B.91})$$

$$\approx k_0 \left( 1 - i \frac{1}{4} \frac{\Gamma}{Q_\alpha} + \frac{1}{32} \frac{\Gamma^2}{Q_\alpha^2} + \dots \right) \quad (\text{B.92})$$

$$= k_0 \left( 1 - i \frac{1}{4} \Delta + O(\Delta^2) \right) \quad (\text{B.93})$$

with

$$\Delta = \frac{\Gamma}{Q_\alpha} = \frac{\hbar\lambda}{Q_\alpha} = \frac{\hbar}{\tau Q_\alpha}. \quad (\text{B.94})$$

In the case of  $^{210}\text{Po}$  we get  $\Delta = 7.1 \cdot 10^{-30}$ . Because  $\Delta \ll 1$  we may neglect the terms of order  $O(\Delta^2)$  and higher and get

$$k \approx k_0 - i \frac{\mu}{2\hbar^2 k_0} \Gamma = k_0 - i \frac{\varepsilon \Gamma}{k_0} + O(\Delta^2) \quad (\text{B.95})$$

$$\kappa \approx \kappa_0 - i \frac{\mu}{2\hbar^2 \kappa_0} \Gamma = \kappa_0 - i \frac{\varepsilon \Gamma}{\kappa_0} + O(\Delta^2) \quad (\text{B.96})$$

with  $\varepsilon = \mu/(2\hbar^2)$ . Now using also the Taylor expansion

$$\cot(x) \approx \cot(x_0) - \frac{1}{\sin^2(x_0)}(x - x_0) + \dots \quad (\text{B.97})$$

we get for the left hand side of equation (B.90)

$$\kappa \cot(\kappa r_0) \approx \left( \kappa_0 - i \frac{\varepsilon \Gamma}{\kappa_0} \right) \left( \cot(\kappa_0 r_0) - \frac{1}{\sin^2(\kappa_0 r_0)} \left( -i \frac{\varepsilon \Gamma}{\kappa_0} r_0 \right) \right) \quad (\text{B.98})$$

$$= \kappa_0 \cot(\kappa_0 r_0) - i \frac{\varepsilon \Gamma}{\kappa_0} \cot(\kappa_0 r_0) + i \frac{\varepsilon \Gamma r_0}{\sin^2(\kappa_0 r_0)} + O(\Delta^2) \quad (\text{B.99})$$

$$= \kappa_0 \cot(\kappa_0 r_0) + i \frac{\varepsilon \Gamma}{\kappa_0} \left( \frac{\kappa_0 r_0}{\sin^2(\kappa_0 r_0)} - \cot(\kappa_0 r_0) \right) + O(\Delta^2). \quad (\text{B.100})$$

We use the approximation  $G_0^2 - F_0^2 \approx G_0^2$  for  $r = r_0$  (see figure B.1) and  $F'_0 F_0 \ll 1$  (for  $r = r_0$ ), the right hand side of equation (B.90) can then be written as

$$k \left( \frac{G'_0 G_0 + F'_0 F_0}{G_0^2 - F_0^2} + \frac{i}{G_0^2 - F_0^2} \right) \approx k \left( \frac{G'_0}{G_0} + \frac{i}{G_0^2} \right) \quad (\text{B.101})$$

Employing the Taylor expansions for the functions  $G'_0/G_0$  and  $1/G_0^2$  (see also B.9.3):

$$\frac{G'_0(\eta, kr_0)}{G_0(\eta, kr_0)} \approx \frac{G'_0(\eta, k_0 r_0)}{G_0(\eta, k_0 r_0)} + \left( -i \frac{\varepsilon \Gamma}{k_0} \right) \frac{\partial}{\partial k} \left( \frac{G'_0}{G_0} \right) (\eta, k_0 r_0) + O(\Delta^2) \quad (\text{B.102})$$

$$\approx \frac{G'_0(\eta, k_0 r_0)}{G_0(\eta, k_0 r_0)} - i \frac{r_0 \varepsilon \Gamma}{k_0} \frac{\partial}{\partial \rho} \left( \frac{G'_0}{G_0} \right) (\eta, k_0 r_0) + O(\Delta^2) \quad (\text{B.103})$$

$$\frac{1}{G_0^2(\eta, kr_0)} \approx \frac{1}{G_0^2(\eta, k_0 r_0)} + \left( -i \frac{\varepsilon \Gamma}{k_0} \right) \frac{\partial}{\partial k} \left( \frac{1}{G_0^2} \right) (\eta, k_0 r_0) + O(\Delta^2) \quad (\text{B.104})$$

$$\approx \frac{1}{G_0^2(\eta, k_0 r_0)} - i \frac{r_0 \varepsilon \Gamma}{k_0} \frac{\partial}{\partial \rho} \left( \frac{1}{G_0^2} \right) (\eta, k_0 r_0) + O(\Delta^2) \quad (\text{B.105})$$

and write for the right hand side of equation (B.90)

$$\begin{aligned} k \left( \frac{G'_0}{G_0} + \frac{i}{G_0^2} \right) &\approx \left( k_0 - i \frac{\varepsilon \Gamma}{k_0} \right) \left[ \frac{G'_0}{G_0} - i \frac{\partial}{\partial \rho} \left( \frac{G'_0}{G_0} \right) \frac{\varepsilon \Gamma}{k_0} r_0 + i \frac{1}{G_0^2} + \frac{\partial}{\partial \rho} \left( \frac{1}{G_0^2} \right) \frac{\varepsilon \Gamma}{k_0} r_0 \right] \\ &= k_0 \frac{G'_0}{G_0} - i \frac{\partial}{\partial \rho} \left( \frac{G'_0}{G_0} \right) \varepsilon \Gamma r_0 + \frac{ik_0}{G_0^2} \\ &\quad + \frac{\partial}{\partial \rho} \left( \frac{1}{G_0^2} \right) \varepsilon \Gamma r_0 - i \frac{G'_0}{G_0} \frac{\varepsilon \Gamma}{k_0} + \frac{\varepsilon \Gamma}{k_0 G_0^2} + O(\Delta^2) \end{aligned} \quad (\text{B.106})$$

$$\begin{aligned} &= k_0 \frac{G'_0}{G_0} + \frac{\partial}{\partial \rho} \left( \frac{1}{G_0^2} \right) \varepsilon \Gamma r_0 + \frac{\varepsilon \Gamma}{k_0 G_0^2} \\ &\quad + i \left[ \frac{k_0}{G_0^2} - \frac{\partial}{\partial \rho} \left( \frac{G'_0}{G_0} \right) \varepsilon \Gamma r_0 - \frac{G'_0}{G_0} \frac{\varepsilon \Gamma}{k_0} \right] \end{aligned} \quad (\text{B.107})$$

$$= k_0 \frac{G'_0}{G_0} + \frac{\partial}{\partial \rho} \left( \frac{1}{G_0^2} \right) \varepsilon \Gamma r_0 + \frac{\varepsilon \Gamma}{k_0 G_0^2} + i \left( \frac{k_0}{G_0^2} - \frac{\varepsilon \Gamma}{k_0} \frac{\mathcal{G}}{G_0^2} \right) \quad (\text{B.108})$$

For simplicity we introduced the function  $\mathcal{G}(\eta, \rho)$ , defined as

$$\mathcal{G}(\eta, \rho) := G'_0(\eta, \rho)G_0(\eta, \rho) + \frac{\partial}{\partial \rho} \left( \frac{G'_0}{G_0} \right)(\eta, \rho)G_0^2(\eta, \rho)\rho \quad (\text{B.109})$$

$$= G'_0(\eta, \rho)G_0(\eta, \rho) + (G''_0(\eta, \rho)G_0(\eta, \rho) - G'^2_0(\eta, \rho))\rho \quad (\text{B.110})$$

Using relation (B.39) we write

$$G''_0 = \frac{\partial}{\partial \rho} G'_0 \quad (\text{B.111})$$

$$= \frac{\partial}{\partial \rho} \left[ \left( \frac{1}{\rho} + \eta \right) G_0 - \sqrt{1 + \eta^2} G_1 \right] \quad (\text{B.112})$$

$$= -\frac{1}{\rho^2} G_0 + \left( \frac{1}{\rho} + \eta \right) G'_0 - \sqrt{1 + \eta^2} G'_1 \quad (\text{B.113})$$

So we get

$$\mathcal{G} = G'_0 G_0 + \left[ -\frac{1}{\rho^2} G_0^2 + \left( \frac{1}{\rho} + \eta \right) G'_0 G_0 - \sqrt{1 + \eta^2} G'_1 G_0 - G_0^2 \right] \rho \quad (\text{B.114})$$

$$= (2 + \eta \rho) G'_0 G_0 - \left( \rho + \frac{1}{\rho} \right) G_0^2 - \rho \sqrt{1 + \eta^2} G'_1 G_0 \quad (\text{B.115})$$

Comparing the imaginary part of equation (B.100) and equation (B.108) leads to

$$\frac{k_0}{G_0^2(\eta, k_0 r_0)} \approx \frac{\varepsilon \Gamma}{\kappa_0} \left( \frac{\kappa_0 r_0}{\sin^2(\kappa_0 r_0)} - \cot(\kappa_0 r_0) \right) + \frac{\varepsilon \Gamma}{k_0} \frac{\mathcal{G}(\eta, k_0 r_0)}{G_0^2(\eta, k_0 r_0)} \quad (\text{B.116})$$

$$\frac{k_0^2}{2\varepsilon\Gamma} \approx \frac{k_0 G_0^2(\eta, k_0 r_0)}{2\kappa_0} \left( \frac{\kappa_0 r_0}{\sin^2(\kappa_0 r_0)} - \cot(\kappa_0 r_0) \right) + \frac{1}{2} \mathcal{G}(\eta, k_0 r_0) \quad (\text{B.117})$$

$$\frac{k_0^2}{2\varepsilon\Gamma} \approx \frac{k_0 r_0}{2} \frac{G_0^2(\eta, k_0 r_0)}{\sin^2(\kappa_0 r_0)} \left( 1 - \frac{\cot(\kappa_0 r_0) \sin^2(\kappa_0 r_0)}{\kappa_0 r_0} \right) + \frac{1}{2} \mathcal{G}(\eta, k_0 r_0) \quad (\text{B.118})$$

$$\frac{k_0^2}{2\varepsilon\Gamma} \approx \frac{k_0 r_0}{2} \frac{G_0^2(\eta, k_0 r_0)}{\sin^2(\kappa_0 r_0)} \left( 1 - \frac{\sin(2\kappa_0 r_0)}{2\kappa_0 r_0} \right) + \frac{1}{2} \mathcal{G}(\eta, k_0 r_0) \quad (\text{B.119})$$

where we used the relation

$$\cot \alpha \sin^2 \alpha = \cos \alpha \sin \alpha = \frac{\sin(2\alpha)}{2}. \quad (\text{B.120})$$

If we substitute the expression for  $\varepsilon$  and use equation (B.64) for  $\Gamma$  we get

$$\frac{k_0^2}{2\varepsilon\Gamma} = \frac{2Q_\alpha}{\hbar\lambda} = \frac{2Q_\alpha\tau}{\hbar} \quad (\text{B.121})$$

and get finally the relation for the decay rate,  $r_0$  and  $V_0$

$$\frac{2Q_\alpha\tau}{\hbar} \approx \frac{k_0 r_0}{2} \frac{G_0^2(\eta, k_0 r_0)}{\sin^2(\kappa_0 r_0)} \left( 1 - \frac{\sin(2\kappa_0 r_0)}{2\kappa_0 r_0} \right) + \frac{1}{2} \mathcal{G}(\eta, k_0 r_0). \quad (\text{B.122})$$

Comparison the real part of equation (B.100) and equation (B.108) leads to

$$\kappa_0 \cot(\kappa_0 r_0) = k_0 \frac{G'_0}{G_0} + \frac{\partial}{\partial \rho} \left( \frac{1}{G_0^2} \right) \varepsilon \Gamma r_0 + \frac{\varepsilon \Gamma}{k_0 G_0^2} \quad (\text{B.123})$$

$$\kappa_0 \cot(\kappa_0 r_0) - k_0 \frac{G'_0}{G_0} = \varepsilon \Gamma \left( \frac{1}{k_0 G_0^2} - 2r_0 \frac{G'_0}{G_0^3} \right) \quad (\text{B.124})$$

$$\frac{k_0^2}{\varepsilon \Gamma} \left( \frac{\kappa_0 \cot(\kappa_0 r_0)}{k_0} - \frac{G'_0}{G_0} \right) = \frac{1}{G_0^2} \left( 1 - 2k_0 r_0 \frac{G'_0}{G_0} \right) \quad (\text{B.125})$$

$$\frac{k_0^2}{2\varepsilon\Gamma} = \frac{k_0}{2G_0^2} \frac{1 - 2k_0 r_0 \frac{G'_0}{G_0}}{\kappa_0 \cot(\kappa_0 r_0) - k_0 \frac{G'_0}{G_0}} \quad (\text{B.126})$$

With  $k_0^2/(2\varepsilon\Gamma) \gg 1$ ,  $k_0/(2G_0^2(\eta, k_0 r_0)) \ll 1$  and because  $G_0(\eta, k_0 r_0)$  and  $G'_0(\eta, k_0 r_0)$  are of the same order, equation (B.126) becomes true for

$$\kappa_0 \cot(\kappa_0 r_0) - k_0 \frac{G'_0(\eta, k_0 r_0)}{G_0(\eta, k_0 r_0)} \approx 0 \quad (\text{B.127})$$

$$\kappa_0 \cot(\kappa_0 r_0) \approx k_0 \frac{G'_0(\eta, k_0 r_0)}{G_0(\eta, k_0 r_0)} \quad (\text{B.128})$$

order	1	2	3	4	5	6	7	8
$r_0$ [fm]	8.4528	8.1684	8.0519	7.9952	7.9644	7.9461	7.9344	7.9266
$V_0$ [MeV]	4.7505	2.5884	-1.1477	-6.4766	-13.417	-21.986	-32.200	-44.069

**Table B.1:** For the case of  $^{210}\text{Po}$  (life time  $\tau = 199.7$  d, decay energy  $Q_\alpha = 5.407$  MeV) the first eight sets of solutions  $(r_0, V_0)$  of the imaginary and real part of the energy relation (B.129) and (B.130) has been evaluated numerically.

which is the real part of the energy relation (B.90) with the simplifications  $F'_0 F_0 \ll 1$  and  $F_0^2 \ll 1$  for  $k_0, \kappa_0$  and  $r_0$ .

So we get the equations

$$\frac{k_0 r_0}{2} \frac{G_0^2(\eta, k_0 r_0)}{\sin^2(k_0 r_0)} \left( 1 - \frac{\sin(2\kappa_0 r_0)}{2\kappa_0 r_0} \right) + \frac{1}{2} \mathcal{G}(\eta, k_0 r_0) - \frac{2Q_\alpha \tau}{\hbar} \approx 0 \quad (\text{B.129})$$

$$k_0 \frac{G'_0(\eta, k_0 r_0)}{G_0(\eta, k_0 r_0)} - \kappa_0 \cot(\kappa_0 r_0) \approx 0. \quad (\text{B.130})$$

For a given life time  $\tau$  and decay energy  $Q_\alpha$  these equations are solved by an endless number of sets  $(r_0, V_0)$ . The first eight sets of solutions for the case of  $^{210}\text{Po}$  have been evaluated numerically and are listed in table B.1. The left hand side of equation (B.129) and (B.130) is plotted versus the depth of the inner potential in figure B.3 for the first six solutions  $r_0$ .

## B.4 The Initial Wave Function $|\Phi_i\rangle$

The initial wave function is given by the radial part  $\Phi_i(r)$  and the spherical harmonic  $Y_0^0(\theta, \varphi)$ :

$$|\Phi_i\rangle = \Phi_i(r) Y_0^0(\theta, \varphi) \quad (\text{B.131})$$

where the radial part is given by equation (B.79)

$$\Phi_i(r) = \begin{cases} A j_0(\kappa r) & \text{for } r < r_0 \\ C \frac{G_0(\eta, kr) + iF_0(\eta, kr)}{kr} & \text{for } r > r_0 \end{cases} \quad (\text{B.79})$$

with

$$k = \frac{1}{\hbar} \sqrt{2\mu E} \quad \kappa = \frac{1}{\hbar} \sqrt{2\mu(E - V_0)} \quad \eta = \frac{\mu Z_\alpha Z_d e^2}{\hbar^2 k} \quad E = Q_\alpha - i \frac{\Gamma}{2} \quad (\text{B.132})$$

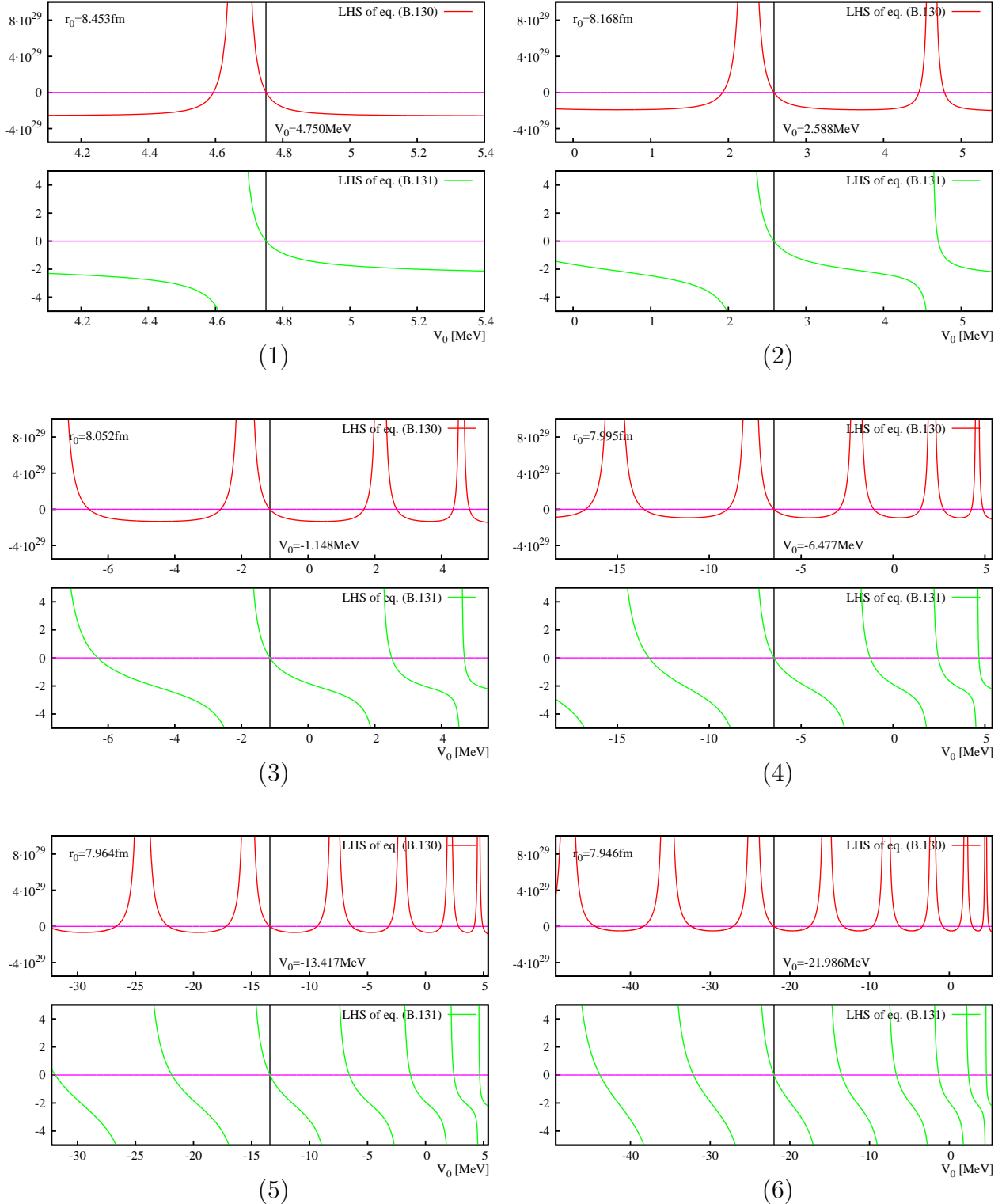


**Figure B.3:** For the case of  ${}^{210}\text{Po}$  the left hand side of equation (B.129) (red) and (B.130) (green) is plotted versus the depth of the inner potential  $V_0$  for the first six solutions  $r_0$

For  $r > r_0$  the particle flux is given by

$$\mathbf{j} = \frac{\hbar}{2\mu i} \left[ \Phi_i^*(\nabla \Phi_i) - (\nabla \Phi_i^*) \Phi_i \right] \quad (\text{B.133})$$

$$\begin{aligned} &= \frac{\hbar}{2\mu i} \left[ C^* \frac{G_0(\eta, kr) - iF_0(\eta, kr)}{kr} \frac{\partial}{\partial r} \left( C \frac{G_0(\eta, kr) + iF_0(\eta, kr)}{kr} \right) \right. \\ &\quad \left. - \frac{\partial}{\partial r} \left( C^* \frac{G_0(\eta, kr) - iF_0(\eta, kr)}{kr} \right) C \frac{G_0(\eta, kr) + iF_0(\eta, kr)}{kr} \right] \quad (\text{B.134}) \end{aligned}$$

$$\begin{aligned} &= \frac{\hbar}{2\mu i} \left[ |C|^2 \frac{G_0 - iF_0}{kr} \left( \frac{G'_0 + iF'_0}{r} - \frac{1}{k} \frac{G_0 + iF_0}{r^2} \right) \right. \\ &\quad \left. - |C|^2 \left( \frac{G'_0 - iF'_0}{r} - \frac{1}{k} \frac{G_0 - iF_0}{r^2} \right) \frac{G_0 + iF_0}{kr} \right] \quad (\text{B.135}) \end{aligned}$$

$$= |C|^2 \frac{\hbar}{2\mu k i} \left[ \frac{(G_0 - iF_0)(G'_0 + iF'_0)}{r^2} - \frac{(G'_0 - iF'_0)(G_0 + iF_0)}{r^2} \right] \quad (\text{B.136})$$

$$= |C|^2 \frac{\hbar}{2\mu k i} \frac{2i(F'_0 G_0 - F_0 G'_0)}{r^2} \quad (\text{B.137})$$

$$= |C|^2 \frac{\hbar}{\mu k} \frac{1}{r^2} \quad (\text{B.138})$$

where we used the Wronskian relation (B.37).

Integrating the flux  $\mathbf{j}$  over a sphere with radius  $R$  with  $R > r_0$  we get for the integrated flux  $J_R$

$$J_R = |C|^2 \frac{\hbar}{\mu k} . \quad (\text{B.139})$$

We normalise the initial wave function to an outgoing flux of 1 and get for  $|C|$ :

$$|C| = \sqrt{\frac{\mu k}{\hbar}} \quad (\text{B.140})$$

We introduce the global phase  $\varphi_G$

$$C = |C| e^{i\varphi_G} = \sqrt{\frac{\mu k}{\hbar}} e^{i\varphi_G} \quad (\text{B.141})$$

and write

$$\tilde{A} = A e^{i\varphi_G} . \quad (\text{B.142})$$

Then  $\tilde{A}$  is defined by the matching condition (B.82)

$$\sin(\kappa r_0) = \frac{C}{A} \frac{\kappa}{k} (G_0(kr_0) + iF_0(kr_0)) \quad (\text{B.143})$$

$$\sin(\kappa r_0) = \frac{|C|}{\tilde{A}} \frac{\kappa}{k} (G_0(kr_0) + iF_0(kr_0)) \quad (\text{B.144})$$

$$\tilde{A} = \sqrt{\frac{mk}{\hbar k}} \frac{\kappa}{k} \frac{G_0(kr_0) + iF_0(kr_0)}{\sin(\kappa r_0)} \quad (\text{B.145})$$

$$\tilde{A} = \sqrt{\frac{m}{\hbar k}} \kappa \frac{G_0(kr_0) + iF_0(kr_0)}{\sin(\kappa r_0)} \quad (\text{B.146})$$

In figure B.4 the initial wave function is plotted for the first six solution sets  $(r_0, V_0)$  for the case of  $^{210}\text{Po}$ .

## B.5 The Final Wave Function $|\Phi_f\rangle$

In the dipole approximation an E1 photon is emitted, so the final wave function has an angular momentum of  $L = 1$ . So it can be written as an radial part  $\Phi_f(r)$  and a sum over the spherical harmonics  $Y_1^m(\theta, \varphi)$ :

$$|\Phi_f\rangle = \sum_{m=-1}^1 \Phi_f(r) Y_1^m(\theta, \varphi). \quad (\text{B.147})$$

The radial part is again given by the solutions of the Schrödinger equation inside and outside  $r_0$

$$\Phi_f(r) = \begin{cases} aj_1(\kappa' r) & \text{for } r < r_0 \\ \frac{c_1 G_1(\eta', k' r) + c_2 F_1(\eta', k' r)}{k' r} & \text{for } r > r_0 \end{cases} \quad (\text{B.148})$$

with

$$k' = \frac{1}{\hbar} \sqrt{2\mu(Q_\alpha - E_\gamma)} \quad \kappa' = \frac{1}{\hbar} \sqrt{2\mu(Q_\alpha - E_\gamma - V_0)} \quad \eta' = \frac{\mu Z_\alpha Z_d e^2}{\hbar^2 k'} \quad (\text{B.149})$$

where  $E_\gamma$  is the energy of the emitted bremsstrahlung photon.

The matching condition of the function values at  $r_0$  leads to

$$aj_1(\kappa' r_0) = \frac{c_1 G_1(\eta', k' r_0) + c_2 F_1(\eta', k' r_0)}{k' r_0} \quad (\text{B.150})$$

$$a \left( \frac{\sin(\kappa' r_0)}{\kappa'^2 r_0^2} - \frac{\cos(\kappa' r_0)}{\kappa' r_0} \right) = \frac{c_1 G_1(\eta', k' r_0) + c_2 F_1(\eta', k' r_0)}{k' r_0} \quad (\text{B.151})$$

$$a \left( \frac{\sin(\kappa' r_0)}{\kappa' r_0} - \cos(\kappa' r_0) \right) = \frac{\kappa'}{k'} (c_1 G_1(\eta', k' r_0) + c_2 F_1(\eta', k' r_0)). \quad (\text{B.152})$$

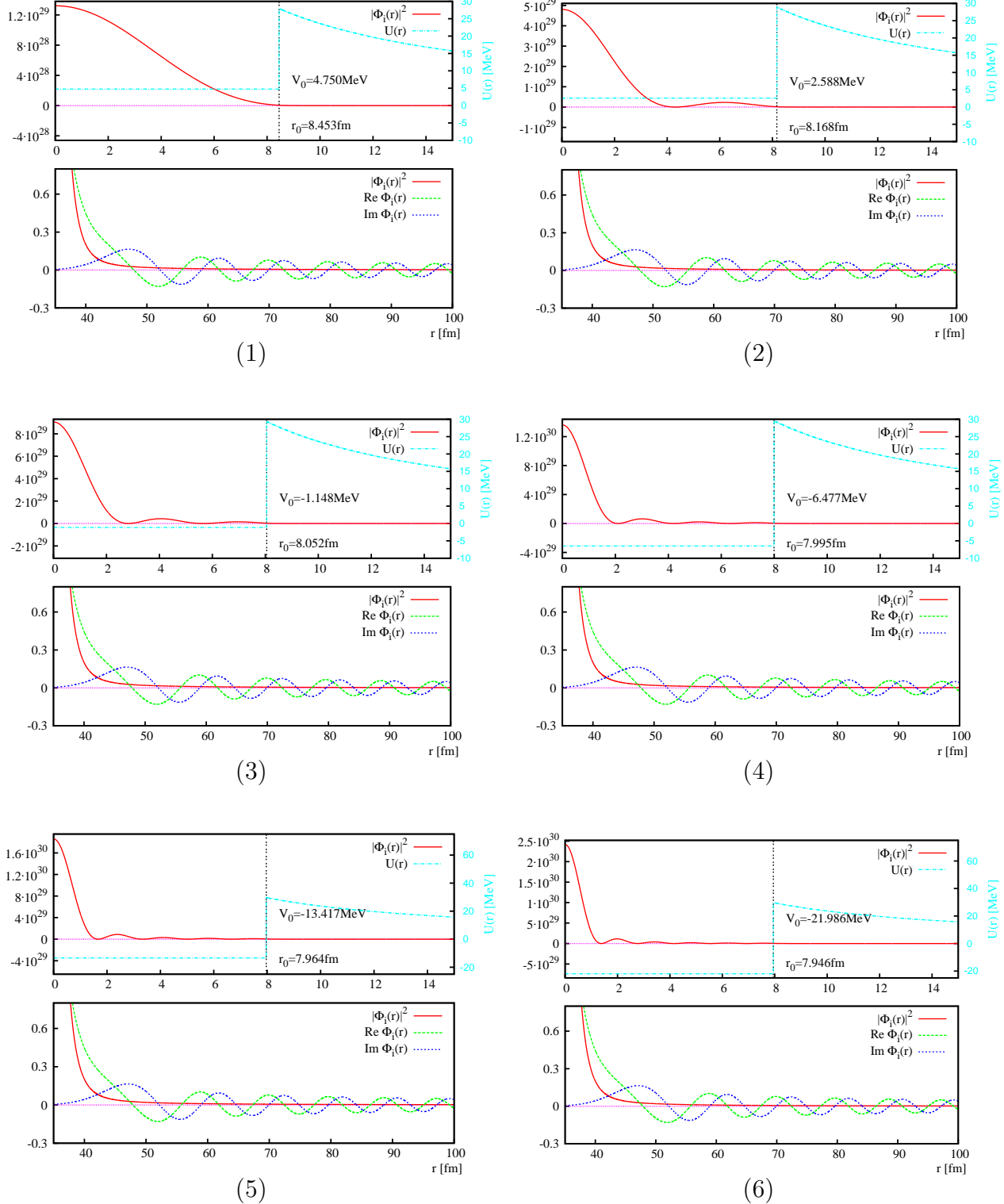


**Figure B.4:** The radial part of the initial wave function  $\Phi_i$  is plotted for the first six solution sets  $(r_0, V_0)$  for the case of  $^{210}\text{Po}$ .

The derivatives at  $r_0$  are given by

$$\frac{\partial}{\partial r} \Phi_f(r) \Big|_{r \rightarrow r_0, r < r_0} = \frac{\partial}{\partial r} (aj_1(\kappa' r)) \Big|_{r=r_0} \quad (\text{B.153})$$

$$= a \left( -\frac{2}{\kappa'^2} \frac{\sin(\kappa' r_0)}{r_0^3} + \frac{1}{\kappa'} \frac{\cos(\kappa' r_0)}{r_0^2} + \frac{\sin(\kappa' r_0)}{r_0} \right) \quad (\text{B.154})$$

$$= \frac{a \sin(\kappa' r_0)}{r_0} \left( 1 - \frac{1}{\kappa'^2 r_0^2} \right) - \frac{a}{r_0} \left( \frac{\sin(\kappa' r_0)}{\kappa'^2 r_0^2} - \frac{\cos(\kappa' r_0)}{\kappa' r_0} \right) \quad (\text{B.155})$$

$$= \frac{a \sin(\kappa' r_0)}{r_0} \left( 1 - \frac{1}{\kappa'^2 r_0^2} \right) - \frac{1}{r_0} aj_1(\kappa' r_0) \quad (\text{B.156})$$

$$\frac{\partial}{\partial r} \Phi_f(r) \Big|_{r \rightarrow r_0, r > r_0} = \frac{\partial}{\partial r} \left( \frac{c_1 G_1(\eta', k'r) + c_2 F_1(\eta', k'r)}{k'r} \right) \Big|_{r=r_0} \quad (\text{B.157})$$

$$= \frac{c_1 G'_1(\eta', k'r_0) + c_2 F'_1(\eta', k'r_0)}{r_0} - \frac{1}{r_0} \frac{c_1 G_1(\eta', k'r_0) + c_2 F_1(\eta', k'r_0)}{k'r_0} \quad (\text{B.158})$$

So we get for the logarithmic derivatives

$$\frac{\Phi'_f(r)}{\Phi_f(r)} \Big|_{r \rightarrow r_0, r < r_0} = \frac{1}{r_0} \frac{\sin(\kappa' r_0)(\kappa'^2 r_0^2 - 1)}{\sin(\kappa' r_0) - \kappa' r_0 \cos(\kappa' r_0)} - \frac{1}{r_0} \quad (\text{B.159})$$

$$= \frac{1}{r_0} \frac{\kappa'^2 r_0^2 - 1}{1 - \kappa' r_0 \cot(\kappa' r_0)} - \frac{1}{r_0} \quad (\text{B.160})$$

$$\frac{\Phi'_f(r)}{\Phi_f(r)} \Big|_{r \rightarrow r_0, r > r_0} = k' \frac{c_1 G'_1(\eta', k'r_0) + c_2 F'_1(\eta', k'r_0)}{c_1 G_1(\eta', k'r_0) + c_2 F_1(\eta', k'r_0)} - \frac{1}{r_0} \quad (\text{B.161})$$

The matching of the logarithmic derivatives leads then to

$$\frac{1}{r_0} \frac{\kappa'^2 r_0^2 - 1}{1 - \kappa' r_0 \cot(\kappa' r_0)} - \frac{1}{r_0} = k' \frac{c_1 G'_1(\eta', k'r_0) + c_2 F'_1(\eta', k'r_0)}{c_1 G_1(\eta', k'r_0) + c_2 F_1(\eta', k'r_0)} - \frac{1}{r_0} \quad (\text{B.162})$$

$$\frac{1}{k'r_0} \frac{\kappa'^2 r_0^2 - 1}{1 - \kappa' r_0 \cot(\kappa' r_0)} = \frac{c_1 G'_1(\eta', k'r_0) + c_2 F'_1(\eta', k'r_0)}{c_1 G_1(\eta', k'r_0) + c_2 F_1(\eta', k'r_0)} \quad (\text{B.163})$$

$$(B.164)$$

The final state is stable, therefore  $\eta'$ ,  $k'$  and  $\kappa'$  are real and the right hand side of equation (B.163) must also be real.  $c_1$  and  $c_2$  may be complex so we write

$$\frac{c_2}{c_1} = x + iy \quad (\text{B.165})$$

so we get for the right hand side of equation (B.163)

$$\frac{G'_1 + \frac{c_2}{c_1} F'_1}{G_1 + \frac{c_2}{c_1} F_1} = \frac{G'_1 + (x + iy)F'_1}{G_1 + (x + iy)F_1} \quad (\text{B.166})$$

$$= \frac{G'_1 + (x + iy)F'_1}{G_1 + (x + iy)F_1} \cdot \frac{G_1 + (x - iy)F_1}{G_1 + (x - iy)F_1} \quad (\text{B.167})$$

$$= \frac{(G'_1 + xF'_1)(G_1 + xF_1) + yF'_1F_1}{(G_1 + xF_1)^2 + (yF_1)^2} \\ + i \frac{yF'_1(G_1 + xF_1) - yF_1(G'_1 + xF'_1)}{(G_1 + xF_1)^2 + (yF_1)^2} \quad (\text{B.168})$$

$$= \frac{(G'_1 + xF'_1)(G_1 + xF_1) + yF'_1F_1}{(G_1 + xF_1)^2 + (yF_1)^2} + i \frac{y(F'_1G_1 - F_1G'_1)}{(G_1 + xF_1)^2 + (yF_1)^2} \quad (\text{B.169})$$

$$= \frac{(G'_1 + xF'_1)(G_1 + xF_1) + yF'_1F_1}{(G_1 + xF_1)^2 + (yF_1)^2} + i \frac{y}{(G_1 + xF_1)^2 + (yF_1)^2} \quad (\text{B.170})$$

using again the Wronskian relation (B.37). So it follow  $y = 0$  and therefore  $c_2/c_1$  must be real. So we can write

$$\frac{c_1 G_1(\eta', k'r_0) + c_2 F_1(\eta', k'r_0)}{k'r_0} = \tilde{c} \frac{G_1(\eta', k'r_0) + dF_1(\eta', k'r_0)}{k'r_0} \quad (\text{B.171})$$

where  $\tilde{c}$  is a global complex factor and  $d$  is real. This is usually written as

$$\frac{c_1 G_1(\eta', k'r_0) + c_2 F_1(\eta', k'r_0)}{k'r_0} = c \frac{\sin(\alpha) G_1(\eta', k'r_0) + \cos(\alpha) F_1(\eta', k'r_0)}{k'r_0} \quad (\text{B.172})$$

where  $c$  is a global complex factor and  $\alpha$  is real.

We then write the final wave function as

$$\Phi_f(r) = \begin{cases} aj_1(\kappa'r) & \text{for } r < r_0 \\ c \frac{\sin(\alpha) G_1(\eta', k'r) + \cos(\alpha) F_1(\eta', k'r)}{k'r} & \text{for } r > r_0 \end{cases} \quad (\text{B.173})$$

and have the two matching conditions

$$\frac{\sin(\kappa'r_0)}{\kappa'r_0} - \cos(\kappa'r_0) = \frac{c}{a} \frac{\kappa'}{k'} \left( \sin(\alpha) G_1(\eta', k'r_0) + \cos(\alpha) F_1(\eta', k'r_0) \right) \quad (\text{B.174})$$

$$\frac{\kappa'^2 r_0^2 - 1}{1 - \kappa'r_0 \cot(\kappa'r_0)} = k'r_0 \frac{\sin(\alpha) G'_1(\eta', k'r_0) + \cos(\alpha) F'_1(\eta', k'r_0)}{\sin(\alpha) G_1(\eta', k'r_0) + \cos(\alpha) F_1(\eta', k'r_0)}. \quad (\text{B.175})$$

We define

$$\mathcal{F}(\sigma) := \frac{\sigma^2 - 1}{1 - \sigma \cot(\sigma)} \quad (\text{B.176})$$

and derive  $\tan(\alpha)$  from equation (B.175)

$$\mathcal{F}(\kappa'r_0) = k'r_0 \frac{\sin(\alpha) G'_1 + \cos(\alpha) F'_1}{\sin(\alpha) G_1 + \cos(\alpha) F_1} \quad (\text{B.177})$$

$$\mathcal{F}(\kappa'r_0)(\tan(\alpha) G_1 + F_1) = k'r_0(\tan(\alpha) G'_1 + F'_1) \quad (\text{B.178})$$

$$\tan(\alpha)(\mathcal{F}(\kappa'r_0)G_1 - k'r_0G'_1) = k'r_0F'_1 - \mathcal{F}(\kappa'r_0)F_1 \quad (\text{B.179})$$

$$\tan(\alpha) = \frac{k'r_0F'_1 - \mathcal{F}(\kappa'r_0)F_1}{\mathcal{F}(\kappa'r_0)G_1 - k'r_0G'_1} \quad (\text{B.180})$$

In the case of  $^{210}\text{Po}$   $\tan(\alpha)$  is of order of  $10^{-28}$  therefore we have  $\sin(\alpha) \ll 1$  and  $\cos(\alpha) \approx 1$ , so the final wave function is dominated by the contribution of the regular Coulomb wave function  $F_1$ .

For the normalisation constant  $c$  we require the completeness relation for the  $F_1$  functions (see B.9.1)

$$\int_0^\infty \sqrt{\frac{2\mu k'}{\pi\hbar^2}} \frac{F_1(\eta, k'r)}{k'r} \sqrt{\frac{2\mu k'}{\pi\hbar^2}} \frac{F_1(\eta, k'r')}{k'r'} dE = \frac{1}{r^2} \delta(r - r') \quad (\text{B.181})$$

and get

$$|c| = \sqrt{\frac{2\mu k'}{\pi\hbar^2}}. \quad (\text{B.182})$$

We use again a global phase  $\varphi_g$  and write:

$$c = |c| e^{i\varphi_g} \quad a = \tilde{a} e^{i\varphi_g} \quad (\text{B.183})$$

and get  $\tilde{a}$  from the matching condition (B.174)

$$\frac{\sin(\kappa'r_0)}{\kappa'r_0} - \cos(\kappa'r_0) = \frac{c}{a} \frac{\kappa'}{k'} \left( \sin(\alpha) G_1(\eta', k'r_0) + \cos(\alpha) F_1(\eta', k'r_0) \right) \quad (\text{B.184})$$

$$\frac{\sin(\kappa'r_0)}{\kappa'r_0} - \cos(\kappa'r_0) = \frac{|c|}{\tilde{a}} \frac{\kappa'}{k'} \left( \sin(\alpha) G_1(\eta', k'r_0) + \cos(\alpha) F_1(\eta', k'r_0) \right) \quad (\text{B.185})$$

$$\tilde{a} = |c| \frac{\kappa'}{k'} \kappa'r_0 \frac{\sin(\alpha) G_1(\eta', k'r_0) + \cos(\alpha) F_1(\eta', k'r_0)}{\sin(\kappa'r_0) - \kappa'r_0 \cos(\kappa'r_0)} \quad (\text{B.186})$$

$$\tilde{a} = \sqrt{\frac{2m\kappa'^2}{\pi\hbar k'}} \kappa'r_0 \frac{\sin(\alpha) G_1(\eta', k'r_0) + \cos(\alpha) F_1(\eta', k'r_0)}{\sin(\kappa'r_0) - \kappa'r_0 \cos(\kappa'r_0)} \quad (\text{B.187})$$

In figure B.5 the radial part of the final wave function  $\Phi_f$  is plotted for the first six sets of solutions  $(r_0, V_0)$  for the case of  $^{210}\text{Po}$  for the photon energies  $E_\gamma = 150$  keV and 300 keV.

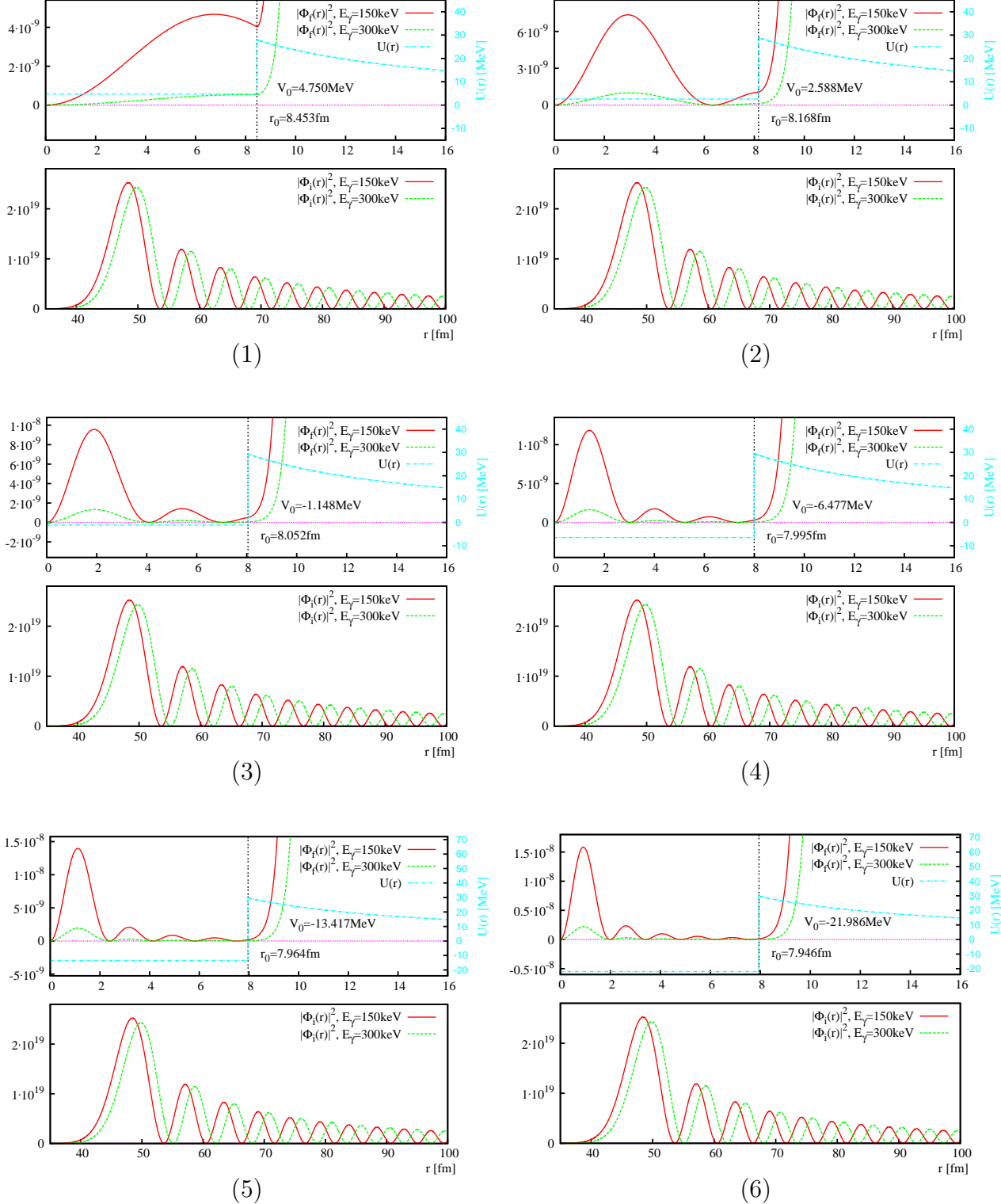


**Figure B.5:** The radial part of the final wave function  $\Phi_f$  is plotted for the first six solution sets ( $r_0, V_0$ ) for the case of  $^{210}\text{Po}$  (for energies  $E_\gamma = 150\text{ keV}$  and  $300\text{ keV}$ )

## B.6 The Matrix Element $\langle \Phi_f | \partial_r U(r) | \Phi_i \rangle$

The derivative of the potential  $U(r)$  for  $r < r_0$  is 0 because  $U(r)$  is constant there. For  $r > r_0$  the derivative is given by

$$\frac{\partial}{\partial r} U(r) = \frac{Z_\alpha Z_d e^2}{r^2}, \quad r > r_0 \quad (\text{B.188})$$

With the derivative of the step function

$$\frac{\partial}{\partial x} \Theta(x) = \delta(x) \quad (\text{B.189})$$

we get for the derivative at the point  $r_0$

$$\left. \frac{\partial}{\partial r} U(r) \right|_{r=r_0} = \frac{Z_\alpha Z_d e^2}{r_0} \delta(r - r_0) + V_0(-\delta(r_0 - r)) \quad (\text{B.190})$$

$$= \left( \frac{Z_\alpha Z_d e^2}{r_0} - V_0 \right) \delta(r - r_0). \quad (\text{B.191})$$

So the derivative of the potential  $U(r)$  can be written as

$$\frac{\partial}{\partial r} U(r) = \left( \frac{Z_\alpha Z_d e^2}{r_0} - V_0 \right) \delta(r - r_0) - \frac{Z_\alpha Z_d e^2}{r^2} \Theta(r - r_0) \quad (\text{B.192})$$

From (B.4) and (B.5) we have for the initial wave function

$$\Phi_i(r) = \begin{cases} A j_0(\kappa r) & \text{for } r < r_0 \\ \sqrt{\frac{\mu k}{\hbar}} \frac{G_0(\eta, kr) + i F_0(\eta, kr)}{kr} & \text{for } r > r_0 \end{cases} \quad (\text{B.193})$$

and for the final wave function

$$\Phi_f(r) = \begin{cases} a j_1(\kappa' r) & \text{for } r < r_0 \\ \sqrt{\frac{2\mu k'}{\pi\hbar^2}} \frac{\sin(\alpha) G_1(\eta', k'r) + \cos(\alpha) F_1(\eta', k'r)}{k'r} & \text{for } r > r_0 \end{cases} \quad (\text{B.194})$$

The matrix element  $\langle \Phi_f | \partial_r U(r) | \Phi_i \rangle$  is given by

$$\langle \Phi_f | \partial_r U(r) | \Phi_i \rangle = \int_0^\infty dr r^2 \Phi_f^*(r) \partial_r U(r) \Phi_i(r) \quad (\text{B.195})$$

There is no contribution from the internal part of the wave functions with  $r < r_0$  due to the the  $\delta$ -distribution and the Heaviside  $\Theta$  function in  $\partial_r U(r)$ . The matrix element is then

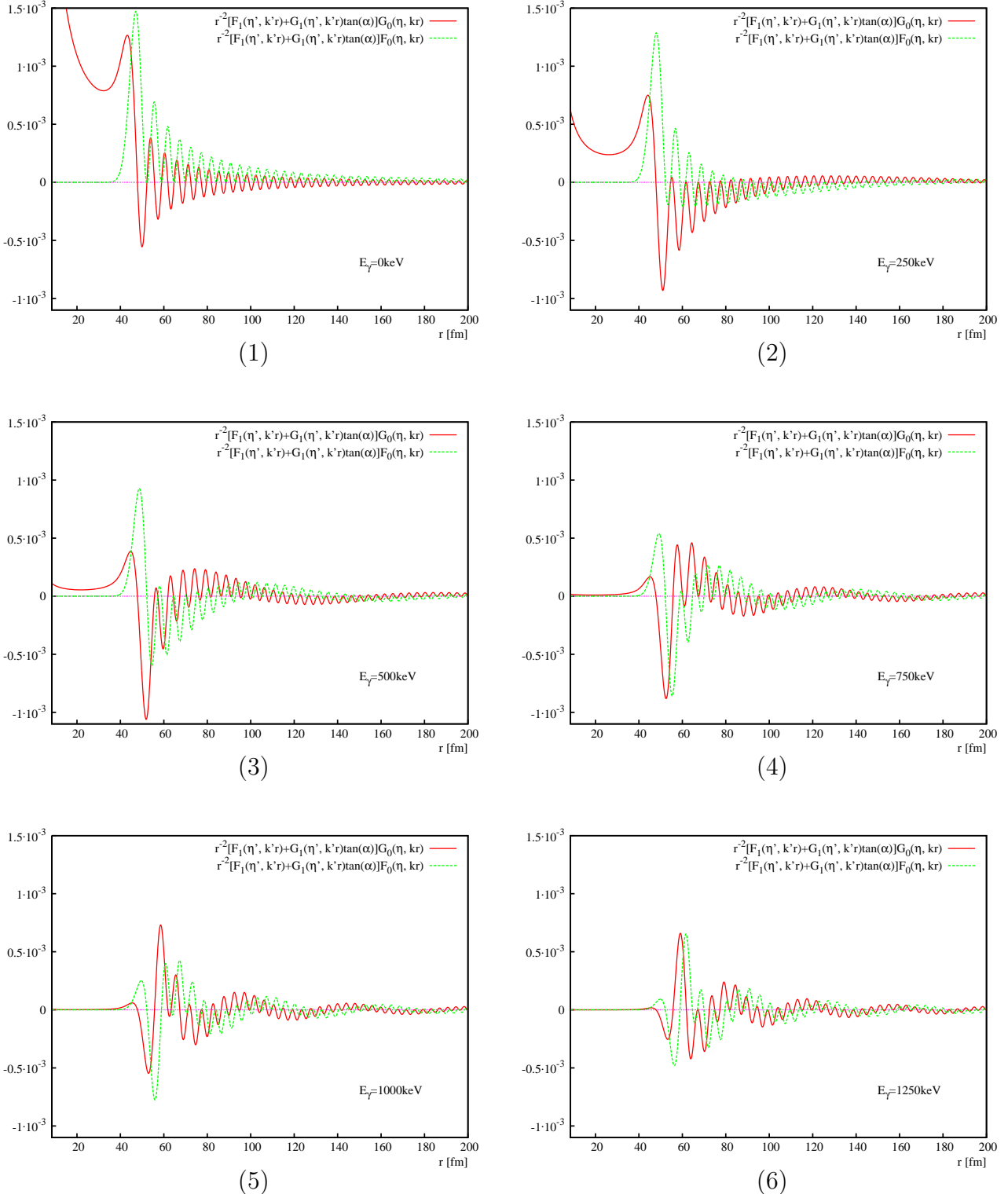


**Figure B.6:** The real part (red-solid line) and the imaginary part (green-dotted line) of the integrant of equation (B.197) is plotted for different  $\gamma$  energies  $E_\gamma$ .

given by:

$$\begin{aligned} \langle \Phi_f | \partial_r U(r) | \Phi_i \rangle &= \sqrt{\frac{2\mu^2}{\pi\hbar^3 k k'}} \\ &\left[ \left( \frac{Z_\alpha Z_d e^2}{r_0} - V_0 \right) \left( G_0(\eta, kr_0) + iF_0(\eta, kr_0) \right) \left( \sin(\alpha) G_1(\eta', k'r_0) + \cos(\alpha) F_1(\eta', k'r_0) \right) \right. \\ &\left. Z_\alpha Z_d e^2 \int_{r_0}^{\infty} dr \frac{1}{r^2} \left( G_0(\eta, kr) + iF_0(\eta, kr) \right) \left( \sin(\alpha) G_1(\eta', k'r) + \cos(\alpha) F_1(\eta', k'r) \right) \right] \end{aligned} \quad (\text{B.196})$$

Because  $\tan(\alpha) \ll 1$  we can use the approximations  $\cos(\alpha) \approx 1$  and  $\sin(\alpha) \approx \tan(\alpha)$  and neglect  $F_0(\eta, kr_0)$  in the sum  $G_0(\eta, kr_0) + iF_0(\eta, kr_0)$  because  $G_0(\eta, kr_0) \gg 1$  and  $F_0(\eta, kr_0) \ll 1$ . So equation (B.196) can be written as (see also [3])

$$\begin{aligned} \langle \Phi_f | \partial_r U(r) | \Phi_i \rangle &\approx \sqrt{\frac{2\mu^2}{\pi\hbar^3 k k'}} \left[ \left( \frac{Z_\alpha Z_d e^2}{r_0} - V_0 \right) \left( F_1(\eta', k'r_0) + G_1(\eta', k'r_0) \tan(\alpha) \right) G_0(\eta, kr_0) \right. \\ &\left. - Z_\alpha Z_d e^2 \int_{r_0}^{\infty} dr \frac{1}{r^2} \left( F_1(\eta', k'r) + G_1(\eta', k'r) \tan(\alpha) \right) \left( G_0(\eta, kr) + iF_0(\eta, kr) \right) \right] \end{aligned} \quad (\text{B.197})$$

Figure B.6 shows the real and the imaginary part of the integrant in equation (B.197).

Though the equation (B.197) depends on the choice of  $r_0$  and  $V_0$  directly and indirectly through the value of  $\tan(\alpha)$ , their influence on the value of the matrix element is small (see section B.8 for more details).

## B.7 Bremsstrahlung Emission Probability

In the dipole approximation the emission probability for bremsstrahlung accompanying the  $\alpha$  decay can be derived from equation (B.16) by replacing  $q$  by the effective dipole charge  $Z_{\text{eff}}^{E1}e$  from equation (A.76) and  $m$  by the reduced mass  $\mu$

$$\frac{dP}{dE_\gamma d\Omega} = \frac{(Z_{\text{eff}}^{E1}e)^2}{2\pi\mu^2 c^3} \left| \langle \Phi_f | \partial_r U(r) | \Phi_i \rangle \right|^2 \frac{1}{E_\gamma} \cdot \sin^2 \vartheta. \quad (\text{B.198})$$

with the matrix element

$$\begin{aligned} \langle \Phi_f | \partial_r U(r) | \Phi_i \rangle &\approx \sqrt{\frac{2\mu^2}{\pi\hbar^3 k k'}} \left[ \left( \frac{Z_\alpha Z_d e^2}{r_0} - V_0 \right) \left( F_1(\eta', k'r_0) + G_1(\eta', k'r_0) \tan(\alpha) \right) G_0(\eta, kr_0) \right. \\ &\left. - Z_\alpha Z_d e^2 \int_{r_0}^{\infty} dr \frac{1}{r^2} \left( F_1(\eta', k'r) + G_1(\eta', k'r) \tan(\alpha) \right) \left( G_0(\eta, kr) + iF_0(\eta, kr) \right) \right] \end{aligned} \quad (\text{B.199})$$

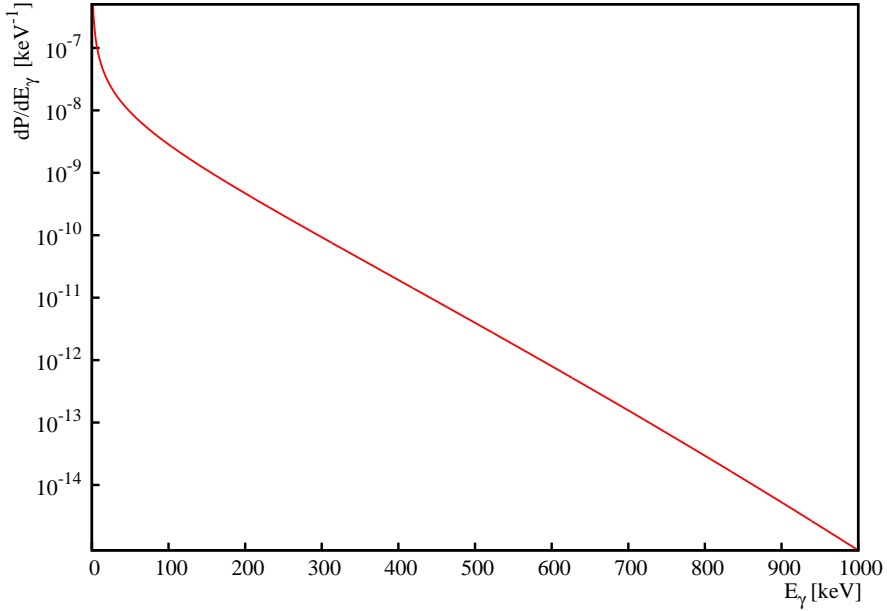


**Figure B.7:** The angle-integrated Bremsstrahlung emission probability in the  $\alpha$  decay of  $^{210}\text{Po}$  in the quantum mechanical model (for solution set  $r_0 = 7.9644 \text{ fm}$  and  $V_0 = -13.42 \text{ MeV}$ ).

where  $k$ ,  $\kappa$ ,  $\eta$  and the primed quantities are given by

$$k = \frac{1}{\hbar} \sqrt{2\mu Q_\alpha} \quad \kappa = \frac{1}{\hbar} \sqrt{2\mu(Q_\alpha - V_0)} \quad \eta = \frac{m Z_\alpha Z_d e^2}{\hbar^2 k} \quad (\text{B.200})$$

and

$$k' = \frac{1}{\hbar} \sqrt{2\mu(Q_\alpha - E_\gamma)} \quad \kappa' = \frac{1}{\hbar} \sqrt{2\mu(Q_\alpha - E_\gamma - V_0)} \quad \eta' = \frac{\mu Z_\alpha Z_d e^2}{\hbar^2 k'} \quad (\text{B.201})$$

with the charge of the  $\alpha$  particle  $Z_\alpha$ , the charge of the daughter nucleus  $Z_d$ , the decay energy  $Q_\alpha$ , and the energy  $E_\gamma$  of the emitted bremsstrahlung photon.

The final result of the angle-integrated bremsstrahlung emission probability of  $^{210}\text{Po}$  is plotted in figure B.7. For the numerical evaluation the solution set  $r_0 = 7.9644 \text{ fm}$  and  $V_0 = -13.42 \text{ MeV}$  has been chosen as it results in a reasonable depth  $V_0$  of the potential  $U(r)$  inside the nucleus. In figure B.8 the matrix element, its real part and its imaginary part and their relative contributions to the square of the matrix element are presented.

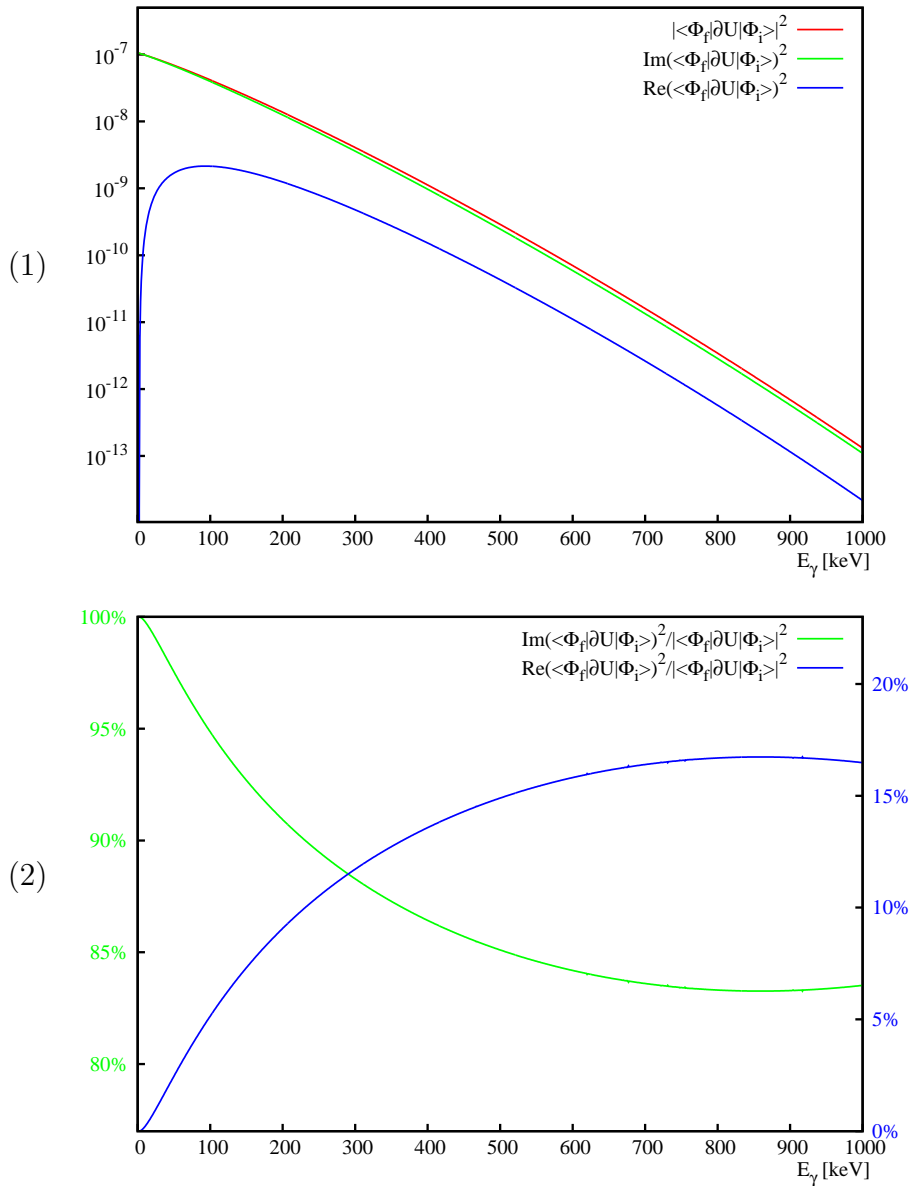


**Figure B.8:** In panel (1) the matrix element, its real part and its imaginary part are plotted. The relative contributions of the real and the imaginary part to the square of the matrix element is shown in panel (2).

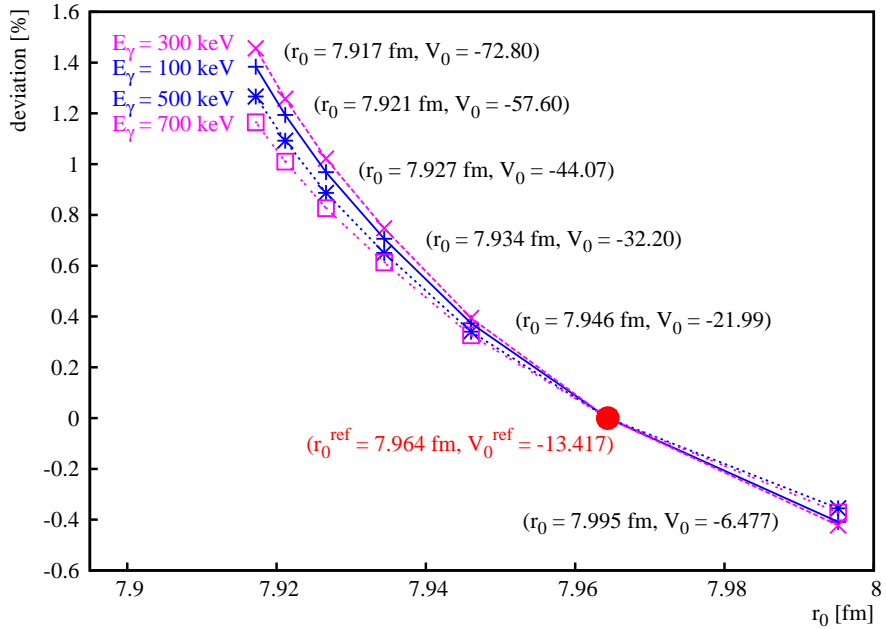


**Figure B.9:** The deviation of the bremsstrahlung emission probability for the first seven sets of solutions  $(r_0, V_0)$  from the reference solution  $(r_0^{ref} = 7.964 \text{ fm}, V_0^{ref} = -13.417 \text{ MeV})$  is plotted for the bremsstrahlung photon energies  $E_\gamma = 100 \text{ keV}$ ,  $300 \text{ keV}$ ,  $500 \text{ keV}$  and  $700 \text{ keV}$ .

## B.8 Dependence of the Bremsstrahlung Emission Probability on the Choice of $r_0$ and $V_0$

The choice of the radius  $r_0$  and the potential  $V_0$  is restricted to discrete sets of solutions  $(r_0, V_0)$  by the energy relation (B.87)

$$\kappa \cot(\kappa r_0) = k \frac{G'_0(\eta, kr_0) + iF'_0(\eta, kr_0)}{G_0(\eta, kr_0) + iF_0(\eta, kr_0)}. \quad (\text{B.87})$$

In this section the dependence of the final bremsstrahlung emission probability on the choice of  $r_0$  and  $V_0$  is discussed.

In figure B.9 the total bremsstrahlung emission probability for different sets of solutions  $(r_0, V_0)$  of the energy relation (B.87) are compared (the solution set  $r_0^{ref} = 7.964 \text{ fm}$  and  $V_0^{ref} = -13.42 \text{ MeV}$  is used as a reference). The deviations between these sets of solutions are in the range of  $\pm 1.5\%$ .

Though the parameter  $r_0$  and  $V_0$  vary considerably (in particular the depth of the inner potential  $V_0$ ) for different sets of solutions  $(r_0, V_0)$  there is only a slight variation in the resulting bremsstrahlung emission probability. In table B.2 the different parts of the matrix element (B.197) are evaluated numerically for two bremsstrahlung  $\gamma$ -energies ( $E_\gamma = 150 \text{ keV}$  and  $450 \text{ keV}$ ) to illuminate this behaviour.

n	$r_0$ [fm]	$V_0$ [MeV]	$\tan(\alpha)$	$\frac{Z_\alpha Z_d e^2}{r_0} - V_0$ [MeV]	$F_1(\eta', k'r_0)$	$G_1(\eta', k'r_0)$ $\tan(\alpha)$
3	8.0518	-1.148	$1.806 \cdot 10^{-30}$	30.48	$8.831 \cdot 10^{-16}$	$4.760 \cdot 10^{-16}$
4	7.9952	-6.477	$8.327 \cdot 10^{-31}$	36.01	$7.807 \cdot 10^{-16}$	$2.473 \cdot 10^{-16}$
5	7.9644	-13.42	$2.503 \cdot 10^{-31}$	43.07	$7.298 \cdot 10^{-16}$	$7.931 \cdot 10^{-17}$
6	7.9461	-21.99	$-1.538 \cdot 10^{-31}$	51.71	$7.012 \cdot 10^{-16}$	$-5.065 \cdot 10^{-17}$
7	7.9344	-32.20	$-4.519 \cdot 10^{-31}$	61.96	$6.835 \cdot 10^{-16}$	$-1.525 \cdot 10^{-16}$
8	7.9266	-44.07	$-6.790 \cdot 10^{-31}$	73.86	$6.719 \cdot 10^{-16}$	$-2.330 \cdot 10^{-16}$

$E_\gamma = 150\text{ keV}$	n	$\mathcal{R}_0$	$-Z_\alpha Z_d e^2 \text{Re}(\mathcal{I})$	$-Z_\alpha Z_d e^2 \text{Im}(\mathcal{I})$	$\text{Re}(\mathcal{M})$	$\text{Im}(\mathcal{M})$	$ \mathcal{M} ^2$
	3	3.896	-3.243	-2.466	$3.970 \cdot 10^{-5}$	$-1.498 \cdot 10^{-4}$	$1.096 \cdot 10^{-9}$
	4	3.919	-3.245	-2.466	$4.097 \cdot 10^{-5}$	$-1.498 \cdot 10^{-4}$	$1.100 \cdot 10^{-9}$
	5	3.935	-3.239	-2.466	$4.226 \cdot 10^{-5}$	$-1.498 \cdot 10^{-4}$	$1.105 \cdot 10^{-9}$
	6	3.947	-3.232	-2.466	$4.340 \cdot 10^{-5}$	$-1.498 \cdot 10^{-4}$	$1.110 \cdot 10^{-9}$
	7	3.956	-3.225	-2.466	$4.439 \cdot 10^{-5}$	$-1.498 \cdot 10^{-4}$	$1.114 \cdot 10^{-9}$
	8	3.962	-3.219	-2.466	$4.516 \cdot 10^{-5}$	$-1.498 \cdot 10^{-4}$	$1.117 \cdot 10^{-9}$

$E_\gamma = 450\text{ keV}$	n	$r_0$ [fm]	$V_0$ [MeV]	$\tan(\alpha)$	$\frac{Z_\alpha Z_d e^2}{r_0} - V_0$ [MeV]	$F_1(\eta', k'r_0)$	$G_1(\eta', k'r_0)$ $\tan(\alpha)$
	3	8.0519	-1.148	$2.299 \cdot 10^{-32}$	30.48	$1.148 \cdot 10^{-16}$	$4.502 \cdot 10^{-17}$
	4	7.9952	-6.477	$8.725 \cdot 10^{-33}$	36.01	$1.014 \cdot 10^{-16}$	$1.926 \cdot 10^{-17}$
	5	7.9644	-13.42	$5.166 \cdot 10^{-35}$	43.07	$9.474 \cdot 10^{-17}$	$1.217 \cdot 10^{-19}$
	6	7.9461	-21.99	$-6.036 \cdot 10^{-33}$	51.71	$9.099 \cdot 10^{-17}$	$-1.479 \cdot 10^{-17}$
	7	7.9344	-32.20	$-1.056 \cdot 10^{-32}$	61.96	$8.869 \cdot 10^{-17}$	$-2.652 \cdot 10^{-17}$
	8	7.9266	-44.07	$-1.403 \cdot 10^{-32}$	73.86	$8.718 \cdot 10^{-17}$	$-3.581 \cdot 10^{-17}$

$E_\gamma = 450\text{ keV}$	n	$\mathcal{R}_0$	$-Z_\alpha Z_d e^2 \text{Re}(\mathcal{I})$	$-Z_\alpha Z_d e^2 \text{Im}(\mathcal{I})$	$\text{Re}(\mathcal{M})$	$\text{Im}(\mathcal{M})$	$ \mathcal{M} ^2$
	3	0.4580	-0.3140	-0.3592	$8.874 \cdot 10^{-6}$	$-2.214 \cdot 10^{-5}$	$8.655 \cdot 10^{-12}$
	4	0.4599	-0.3145	-0.3592	$8.963 \cdot 10^{-6}$	$-2.214 \cdot 10^{-5}$	$8.679 \cdot 10^{-12}$
	5	0.4613	-0.3140	-0.3592	$9.081 \cdot 10^{-6}$	$-2.214 \cdot 10^{-5}$	$8.711 \cdot 10^{-12}$
	6	0.4624	-0.3133	-0.3592	$9.192 \cdot 10^{-6}$	$-2.214 \cdot 10^{-5}$	$8.742 \cdot 10^{-12}$
	7	0.4632	-0.3125	-0.3592	$9.291 \cdot 10^{-6}$	$-2.214 \cdot 10^{-5}$	$8.770 \cdot 10^{-12}$
	8	0.4637	-0.3118	-0.3592	$9.367 \cdot 10^{-6}$	$-2.214 \cdot 10^{-5}$	$8.792 \cdot 10^{-12}$

with  $\mathcal{R}_0 := \left( \frac{Z_\alpha Z_d e^2}{r_0} - V_0 \right) (F_1(\eta', k'r_0) + G_1(\eta', k'r_0) \tan(\alpha)) G_0(\eta, kr_0)$

$$\mathcal{I} := \int_{r_0}^{\infty} dr \frac{1}{r^2} (F_1(\eta', k'r) + G_1(\eta', k'r) \tan(\alpha)) (G_0(\eta, kr) + iF_0(\eta, kr))$$

$$\mathcal{M} := \langle \Phi_f | \partial_r U(r) | \Phi_i \rangle$$

**Table B.2:** Values of different parts of equation (B.197) for  $E_\gamma = 150\text{ keV}$  and  $450\text{ keV}$  and the first six sets of solutions ( $r_0, V_0$ ).

The parameter  $V_0$  goes directly into the surface term

$$\mathcal{R}_0 := \left( \frac{Z_\alpha Z_d e^2}{r_0} - V_0 \right) \left( F_1(\eta', k'r_0) + G_1(\eta', k'r_0) \tan(\alpha) \right) G_0(\eta, kr_0). \quad (\text{B.202})$$

While term  $Z_\alpha Z_d e^2/r_0 - V_0$  grows considerably for lower values of  $V_0$ , the decrease of  $\tan(\alpha)$  nearly compensates this behaviour resulting in only a small growth in the surface term  $\mathcal{R}_0$  for rising order number  $n$  of the solution set.

To examine the behaviour of the integral

$$\mathcal{I} := \int_{r_0}^{\infty} dr \frac{1}{r^2} \left( F_1(\eta', k'r) + G_1(\eta', k'r) \tan(\alpha) \right) \left( G_0(\eta, kr) + iF_0(\eta, kr) \right) \quad (\text{B.203})$$

we discuss the real part and the imaginary part separately. As illustrated in figure B.6 the real part of the integrand is small for  $r \approx r_0$  and therefore the value of the lower limit  $r_0$  has hardly any effect on the imaginary part  $\text{Im}(\mathcal{I})$  of the integral. This is not the case for the real part of the integrand, resulting in a small decrease of  $\text{Re}(\mathcal{I})$  with  $n$  which partly compensates the increase in  $\mathcal{R}_0$ . Therefore the resulting value of the matrix element  $\mathcal{M}$  depends only weakly on the choice of the solution set  $(r_0, V_0)$ .

In the following we will look at the behaviour of equation (B.198) when evaluated for "unphysical" values of  $r_0$  and  $V_0$  which not fulfil the energy relation (B.87) (the solution set  $r_0^{ref} = 7.9644 and  $V_0^{ref} = -13.42 will be used as a reference).$$

Figure B.10 shows that the numerical value of equation (B.198) changes dramatically when the parameter  $r_0$  ( $V_0$ ) is changed to "unphysical" values while the parameter  $V_0 = V_0^{ref} = -13.42 ( $r_0 = r_0^{ref} = 7.9644) is kept stable. A 2-dimensional plot of the numerical results of equation (B.198) in the parameter plane  $r_0$  versus  $V_0$  is shown in figure B.11 with the physical solutions sets for  $n = 4, 5, 6$ , and  $7$  marked by red points.$$

It is illuminative to further look at the behaviour of equation (B.198) for parameters  $r_0$  and  $V_0$  which fulfil the energy relation (B.87) "partly". As derived in section B.3 the energy relation (B.87) can be split into a condition for the imaginary part, which leads to

$$\frac{k_0 r_0}{2} \frac{G_0^2(\eta, k_0 r_0)}{\sin^2(\kappa_0 r_0)} \left( 1 - \frac{\sin(2\kappa_0 r_0)}{2\kappa_0 r_0} \right) + \frac{1}{2} \mathcal{G}(\eta, k_0 r_0) - \frac{2E_0 \tau}{\hbar} \approx 0 \quad (\text{B.129})$$

and a condition for the real part, which leads to the relation

$$k_0 \frac{G'_0(\eta, k_0 r_0)}{G_0(\eta, k_0 r_0)} - \kappa_0 \cot(\kappa_0 r_0) \approx 0. \quad (\text{B.130})$$

In figure B.12 the behaviour of equation (B.198) is investigated when  $r_0$  and  $V_0$  are changed continuously along the path of the solutions of equation (B.129) and (B.130), respectively.

In panel (1) of figure B.12 the solution of the real part of the energy relation (B.130) is plotted in red in a  $V_0$  versus  $r_0$  plot and the solution of the imaginary part (B.129) is plotted

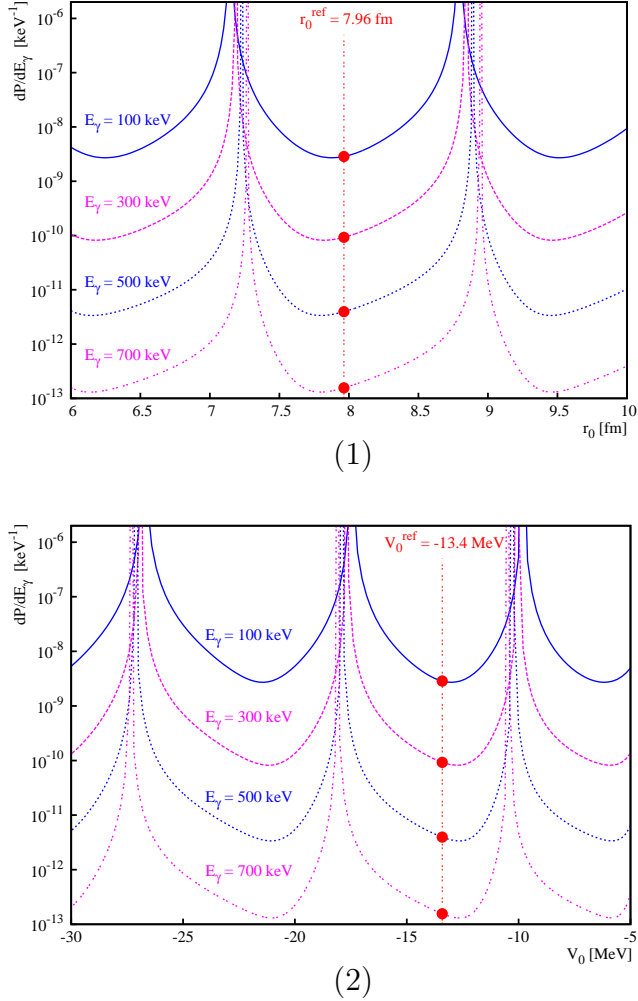


**Figure B.10:** The behaviour of equation (B.198) for "unphysical" values for the parameter  $r_0$  is shown with the parameter  $V_0 = V_0^{\text{ref}} = -13.42 \text{ MeV}$  kept stable in panel (1) and for the parameter  $V_0$  with  $r_0 = r_0^{\text{ref}} = 7.9644 \text{ fm}$  kept stable in panel (2). Panel (3) shows the resulting values of equation (B.198) for "unphysical"  $r_0$  and  $V_0$  values in a 2-dimensional  $r_0$  versus  $V_0$  plot. The physical solution sets  $(r_0, V_0)$  for  $n = 4, 5, 6$ , and 7 are marked by red points.

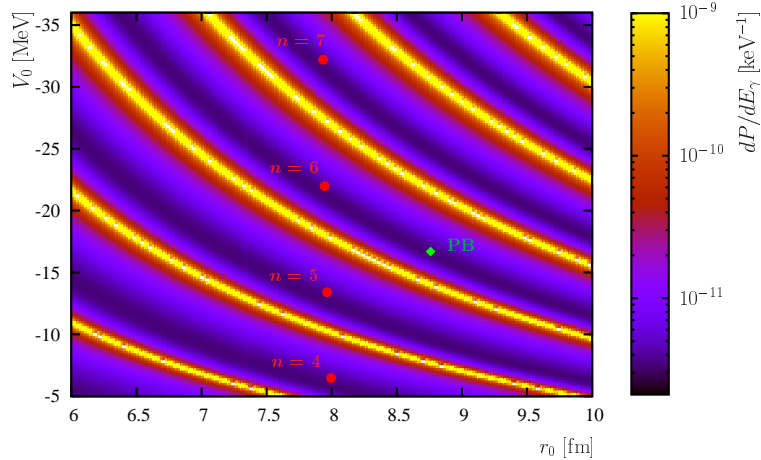


**Figure B.11:** The behaviour of equation (B.198) for "unphysical" values of the parameters  $r_0$  and  $V_0$  is illustrated in a 2-dimensional  $r_0$  versus  $V_0$  plot ( $E_\gamma = 500$  keV). The physical solution sets  $(r_0, V_0)$  for  $n = 4, 5, 6$ , and  $7$  are marked by red points, the parameter set  $(r_0, V_0)$  published by Papenbrock and Bertsch [3] is shown as a green diamond (PB).

in green. We start at the reference solution set ( $r_0^{ref} = 7.964$  fm,  $V_0^{ref} = -13.417$  MeV) and analyse solutions of the real and the imaginary part of the energy relation which are connect to the reference solution by a continuous path. The behaviour of equation (B.198) for the solutions of the real part (B.130) is plotted in panel (2) of figure B.12 and for the imaginary part (B.129) in panel (3). Along the path of solutions of the real part of the energy relation (B.130) the result of equation (B.198) changes only slightly; in contrast, along the path of solutions of the imaginary part of the energy relation (B.129) the change is dramatic.

To interpret this result we recall that the basic energy relation (B.87) approaches equation (B.130) (neglecting  $F_0(\eta, kr_0) \ll 1$  and  $F'_0(\eta, kr_0) \ll 1$ ) in the limit of a vanishing imaginary energy  $\Gamma \rightarrow 0$ , i.e. the limit of a stable state  $\tau \rightarrow \infty$ . Furthermore equation (B.130) is independent of  $\Gamma$  and therefore independent of the lifetime  $\tau$  of the initial state. Thus the result of equation (B.198) as discussed above only depends weakly on the lifetime  $\tau$  (for solution sets  $(r_0, V_0)$  of equation (B.130)). The imaginary part of the energy relation (B.129) constrains the solutions of (B.130) to the physical solution sets  $(r_0, V_0)$  according to the physical lifetime  $\tau$ .

Therefore the resulting bremsstrahlung emission probability only depends weakly on the choice of the parameter set  $(r_0, V_0)$  as long as these parameters fulfil the condition of the real part of the energy relation (B.130) or in other words fulfil the basic energy relation (B.87) in the limit of a stable nucleus ( $\tau \rightarrow \infty$ ). This is the reason why parameter sets  $(r_0, V_0)$  published in literature, e.g. in [3] (green diamond in figure B.11), lead to the almost the same numerical result for the bremsstrahlung energy spectrum as the solution sets  $(r_0, V_0)$  presented in this work.

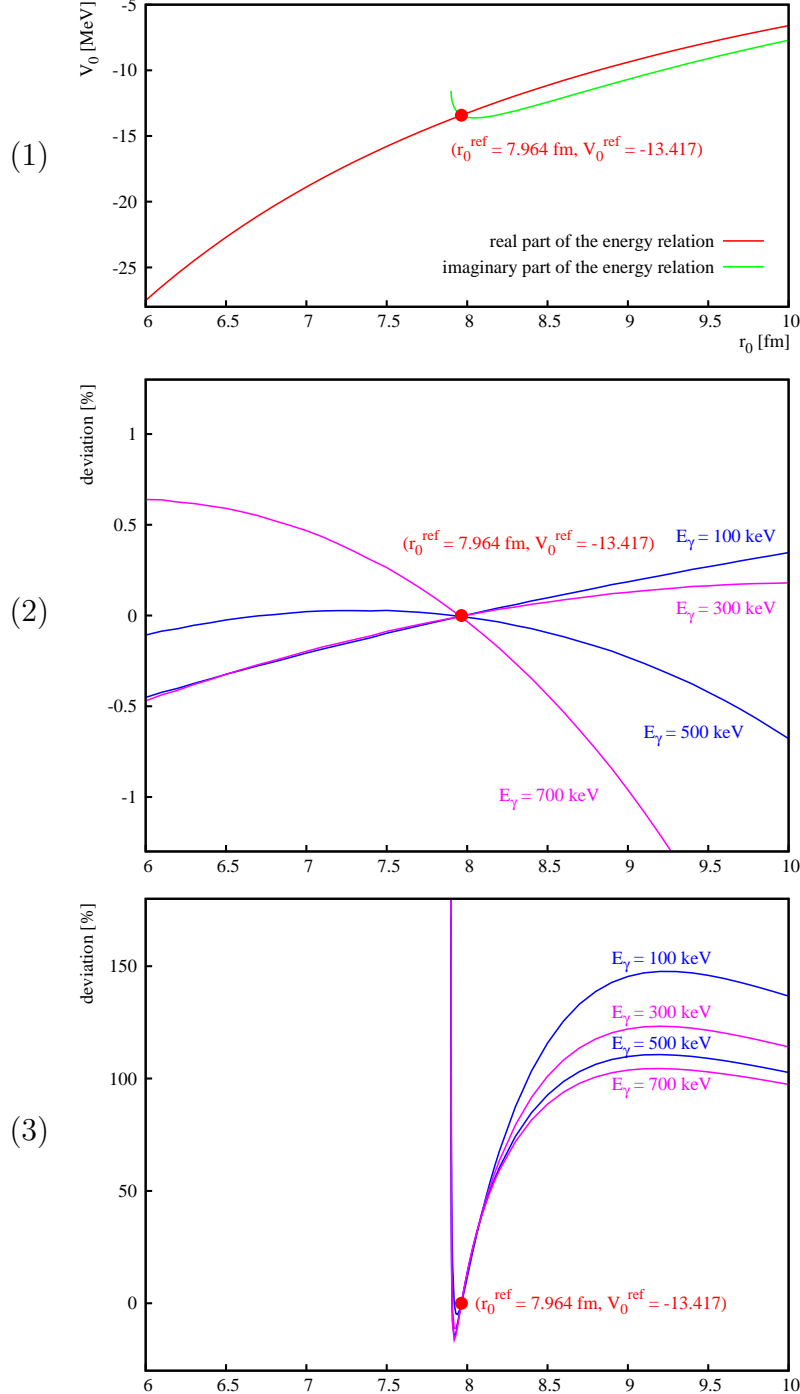


**Figure B.12:** The behaviour of equation (B.198) is analysed along the solutions of the real part (equation (B.130)) and the imaginary part (equation (B.129)) of the energy relation, respectively. The solutions of the real (red) and imaginary (green) part of the energy relation are plotted in a  $V_0$  versus  $r_0$  plot in panel (1). The deviation of the resulting value from the reference solution is plotted in panel (2) for the solutions of the real part and in panel (3) for the solutions of the imaginary part of the energy relation.

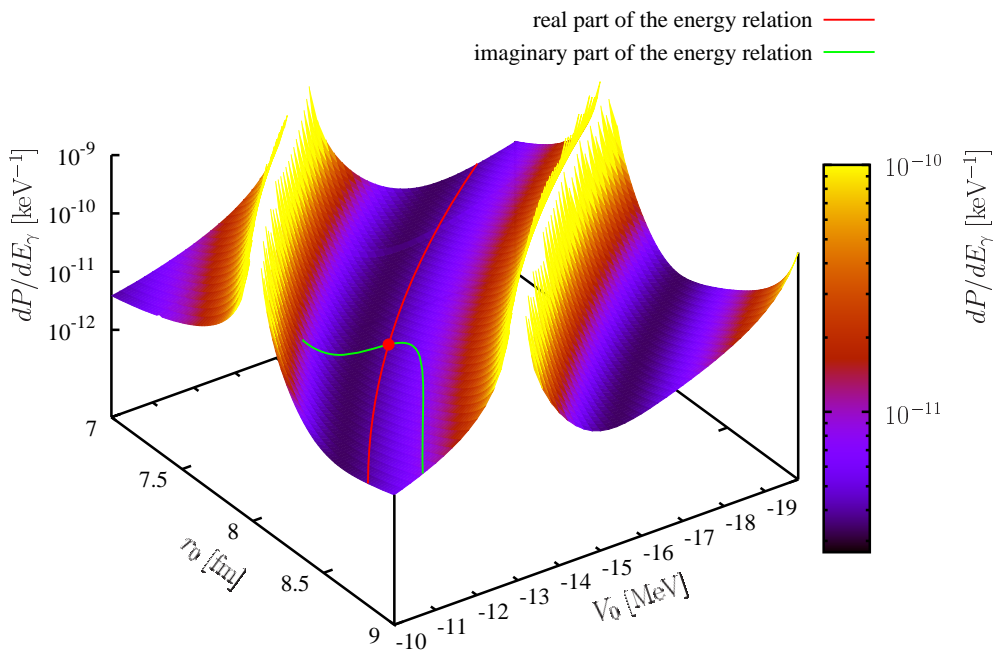


**Figure B.13:** 2-dimensional surface plot of the  $r_0$  and  $V_0$  dependence of equation (B.198) ( $E_\gamma = 500 \text{ keV}$ ). The reference solution set ( $r_0^{ref} = 7.964 \text{ fm}, V_0^{ref} = -13.417 \text{ MeV}$ ) is marked by a red point. The red and green paths show the solutions of the real and imaginary part of the energy relation (equations (B.130), red, and equation (B.129), green).

## B.9 Annotations

### B.9.1 Completeness of the Coulomb Wave Functions

The completeness of the Coulomb wave functions has been shown explicitly by Mukunda in [68]. He defines the functions  $R_L(k, r)$  by

$$\begin{aligned} R_L(k, r) = & \sqrt{\frac{\pi}{2}} \frac{k}{(2L+1)!} e^{-\pi/2ak} |\Gamma(L+1-i/ak)| \\ & \times (2kr)^L e^{ikr} M(L+1+i/ak, 2L+2, -2ikr) \end{aligned} \quad (\text{B.204})$$

with

$$a = \frac{\hbar^2}{qQm} \implies \eta = \frac{1}{ak}. \quad (\text{B.205})$$

(Note that in [68] an attractive Coulomb potential is considered, so the representation of  $R_L(k, r)$  differs slightly.) The function  $M$  is the *confluent hypergeometric function* (see also [64]) defined by

$$M(a, b, z) = 1 + \sum_{n=1}^{\infty} \frac{(a)_n z^n}{(z)_n n!} \quad (\text{B.206})$$

with the standard abbreviation

$$(a)_n = a(a+1)(a+2)\cdots(a+n-1). \quad (\text{B.207})$$

The completeness relation for the continuum is then given by

$$\int_0^{\infty} R_L(k, r) R_L(k, r') dk = \frac{1}{r^2} \delta(r - r'). \quad (\text{B.208})$$

In this text we use the definition of Coulomb wave function  $F_L(\eta, kr)$  according to [64]

$$\begin{aligned} F_L(\eta, kr) = & \frac{2^L}{\Gamma(2L+2)} e^{-\pi\eta/2} |\Gamma(L+1+i\eta)| \\ & \times kr^{L+1} e^{-ikr} M(L+1-i\eta, 2L+2, 2ikr). \end{aligned} \quad (\text{B.209})$$

Comparing equation (B.204) and (B.209) we get

$$\begin{aligned} & r \sqrt{\frac{\pi}{2}} R_L(k, r) \\ &= \frac{kr}{(2L+1)!} e^{-\pi/2ak} |\Gamma(L+1-i/ak)| (2kr)^L e^{ikr} M(L+1+i/ak, 2L+2, -2ikr) \\ &= \frac{2^L}{\Gamma(2L+2)} e^{-\pi/2ak} |\Gamma(L+1-i/ak)| (kr)^{L+1} e^{-ikr} M(L+1-i/ak, 2L+2, 2ikr) \\ &= \frac{2^L}{\Gamma(2L+2)} e^{-\pi/2ak} |\Gamma(L+1+i/ak)| (kr)^{L+1} e^{-ikr} M(L+1-i/ak, 2L+2, 2ikr) \\ &= F_L(1/ak, kr) = F_L(\eta, kr) \end{aligned} \quad (\text{B.210})$$

where we used the Kummer transformation

$$M(a, b, z) = e^z M(b - a, b, -z) \quad (\text{B.211})$$

and the relation

$$|\Gamma(\bar{z})| = |\overline{\Gamma(z)}| = |\Gamma(z)|. \quad (\text{B.212})$$

With the relation (B.210) the completeness relation for the functions  $F_L(1/ak, rk)$  can be derived from (B.208)

$$\begin{aligned} \int_0^\infty R_L(k, r) R_L(k, r') dk &= \frac{1}{r^2} \delta(r - r') \\ \int_0^\infty \sqrt{\frac{2}{\pi}} \frac{F_L(1/ak, kr)}{r} \sqrt{\frac{2}{\pi}} \frac{F_L(1/ak, kr')}{r} dk &= \frac{1}{r^2} \delta(r - r') \\ \int_0^\infty \sqrt{\frac{2}{\pi}} \frac{F_L(\eta, kr)}{r} \sqrt{\frac{2}{\pi}} \frac{F_L(\eta, kr')}{r} \frac{m}{\hbar^2 k} dE &= \frac{1}{r^2} \delta(r - r') \\ \int_0^\infty \sqrt{\frac{2mk}{\pi\hbar^2}} \frac{F_L(\eta, kr)}{kr} \sqrt{\frac{2mk}{\pi\hbar^2}} \frac{F_L(\eta, kr')}{kr} dE &= \frac{1}{r^2} \delta(r - r') \end{aligned} \quad (\text{B.213})$$

### B.9.2 Numerical Integration of $\langle \Phi_f | \partial_r U(r) | \Phi_i \rangle$

For the numerical evaluation of the integral in equation (B.197) it is important to analyse the behaviour of the integrant. With the approximation (B.34) and (B.35) we find

$$\begin{aligned} F_1(\eta', k'r) G_0(\eta, kr) &\xrightarrow{r \rightarrow \infty} \sin\left(k'r - \eta' \ln(2k'r) - \frac{\pi}{2} + \sigma'_1\right) \cos\left(kr - \eta \ln(2kr) + \sigma_0\right) \\ F_1(\eta', k'r) F_0(\eta, kr) &\xrightarrow{r \rightarrow \infty} \sin\left(k'r - \eta' \ln(2k'r) - \frac{\pi}{2} + \sigma'_1\right) \sin\left(kr - \eta \ln(2kr) + \sigma_0\right) \end{aligned}$$

with

$$\sigma'_1 = \arg \Gamma(2 + i\eta') \quad \sigma_0 = \arg \Gamma(1 + i\eta)$$

Using the relations

$$\sin(\alpha) \cos(\beta) = \frac{1}{2} (\sin(\alpha - \beta) + \sin(\alpha + \beta)) \quad (\text{B.214})$$

$$\sin(\alpha) \sin(\beta) = \frac{1}{2} (\cos(\alpha - \beta) - \cos(\alpha + \beta)) \quad (\text{B.215})$$

we get

$$F_1(\eta', k'r) G_0(\eta, kr) \xrightarrow{r \rightarrow \infty} \frac{1}{2} (\sin(\omega_s r - \varphi_s) + \sin(\omega_f r - \varphi_f)) \quad (\text{B.216})$$

$$F_1(\eta', k'r) F_0(\eta, kr) \xrightarrow{r \rightarrow \infty} \frac{1}{2} (\cos(\omega_s r - \varphi_s) - \cos(\omega_f r - \varphi_f)) \quad (\text{B.217})$$

with

$$\omega_s = k' - k \quad (\text{B.218})$$

$$\omega_f = k' + k \quad (\text{B.219})$$

$$\varphi_s = \frac{\pi}{2} + \eta' \ln(2k'r) - \eta \ln(2kr) - \sigma'_1 + \sigma_0 \quad (\text{B.220})$$

$$\varphi_f = \frac{\pi}{2} + \eta' \ln(2k'r) + \eta \ln(2kr) - \sigma'_1 - \sigma_0 \quad (\text{B.221})$$

For  $r \gg 1$  the change in  $\varphi_s$  and  $\varphi_f$  is small compared with the change in  $\omega_s r$  and  $\omega_f r$ . So the behaviour of the real and the imaginary part of the integrant is approximated by the sum of two sinusoidal functions, one oscillating fast with  $\omega_f$  and one oscillating slow with  $\omega_s$ . To get a good approximation of the value of the integral it is necessary to use an upper limit of integration which has a maximum in of both oscillations.

### B.9.3 Taylor-Expansion with a Complex Argument

Let  $f(x)$  be a real function

$$x \mapsto f(x) \quad \mathbb{R} \longrightarrow \mathbb{R}$$

and  $x_0 \in \mathbb{R}$ . Let  $D_{\mathbb{R}}$  be an interval in  $\mathbb{R}$  with

$$D_{\mathbb{R}} := \{x \in \mathbb{R}, |x - x_0| < \varepsilon\}$$

with  $\varepsilon \ll 1$ . We get for the Taylor expansion about  $x_0$

$$f(x) = \sum_{n=0}^{\infty} a_n (x - x_0)^n \quad \forall x \in D_{\mathbb{R}}$$

with the Taylor coefficients

$$a_n := \frac{\left(\frac{\partial}{\partial x}\right)^n f(x_0)}{n!}$$

We define  $D \subset \mathbb{C}$  by the condition

$$D := \{z \in \mathbb{C}, |z - z_0| < \varepsilon\}$$

with  $z_0 = x_0 \in \mathbb{R}$  and find  $D_{\mathbb{R}} \in D$ . The function  $F(z)$  defined by

$$F(z) := \sum_{n=0}^{\infty} a_n (z - z_0)^n \quad \forall z \in D$$

is called the complex continuation of  $f$  on  $D$ .

We now consider the value of  $F(z)$  at the point  $z = x_0 + i\delta$  where  $\delta < \varepsilon \ll 1$  and get

$$\begin{aligned} F(x_0 + i\delta) &\approx a_0 + ia_1\delta + O(\delta^2) \\ &\approx f(x_0) + i\delta \frac{\partial}{\partial x} f(x_0) + O(\delta^2) \end{aligned}$$



# Appendix C

## $\alpha$ - and $\gamma$ -Lineshape

### C.1 The $\alpha$ -Lineshape

Several methods to fit an  $\alpha$  spectrum have been proposed in the literature [55–58]. In this work a fit function  $f(x)$  is used consisting out of a Gaussian  $g(x)$ , a function for the approximation of the low energy tail  $t_l(x)$  and one for the high energy tail  $t_h(x)$ . For the fitting procedure a non-linear least square fit is used (provided by the gnuplot<sup>1</sup> software).

The exact fit function is defined by

$$f(x, x_0) = g(x, x_0) + t_l(x, x_0) + t_h(x, x_0) \quad (\text{C.1})$$

with a Gaussian  $g(x, x_0)$

$$g(x, x_0) = \frac{A_{ref}}{\sigma\sqrt{2\pi}} \exp\left(-\frac{1}{2} \frac{(x - x_0)^2}{\sigma^2}\right). \quad (\text{C.2})$$

The low energy tail  $t_l(x, x_0)$  is approximated by two exponential tails  $t_{la}(x, x_0)$  and  $t_{lb}(x, x_0)$ , a smoothed step function  $s_l(x, x_0)$  and an additional Gaussian  $g_s(x, x_0)$

$$t_l(x, x_0) = t_{la}(x, x_0) + t_{lb}(x, x_0) + g_s(x, x_0) + s_l(x, x_0) \quad (\text{C.3})$$

$$t_{la}(x, x_0) = B_{la} e^{C_{la}(x-x_0)} \left(1 - \exp\left(-\frac{1}{2} \frac{(x - x_0)^2}{\sigma^2}\right)\right) \Theta(x_0 - x) \quad (\text{C.4})$$

$$t_{lb}(x, x_0) = B_{lb} e^{C_{lb}(x-x_0)} \left(1 - \exp\left(-\frac{1}{2} \frac{(x - x_0)^2}{\sigma^2}\right)\right) \Theta(x_0 - x) \quad (\text{C.5})$$

$$s_l(x, x_0) = \frac{B_{sl}}{2} \left(1 + \operatorname{erf}\left(\frac{x_0 - x}{\sigma\sqrt{2}}\right)\right) \quad (\text{C.6})$$

$$g_s(x, x_0) = \frac{A_{gs}}{\sigma_{gs}\sqrt{2\pi}} \exp\left(-\frac{1}{2} \frac{(x - x_0 - x_{gs})^2}{\sigma_{gs}^2}\right). \quad (\text{C.7})$$

---

<sup>1</sup><http://www.gnuplot.info/>

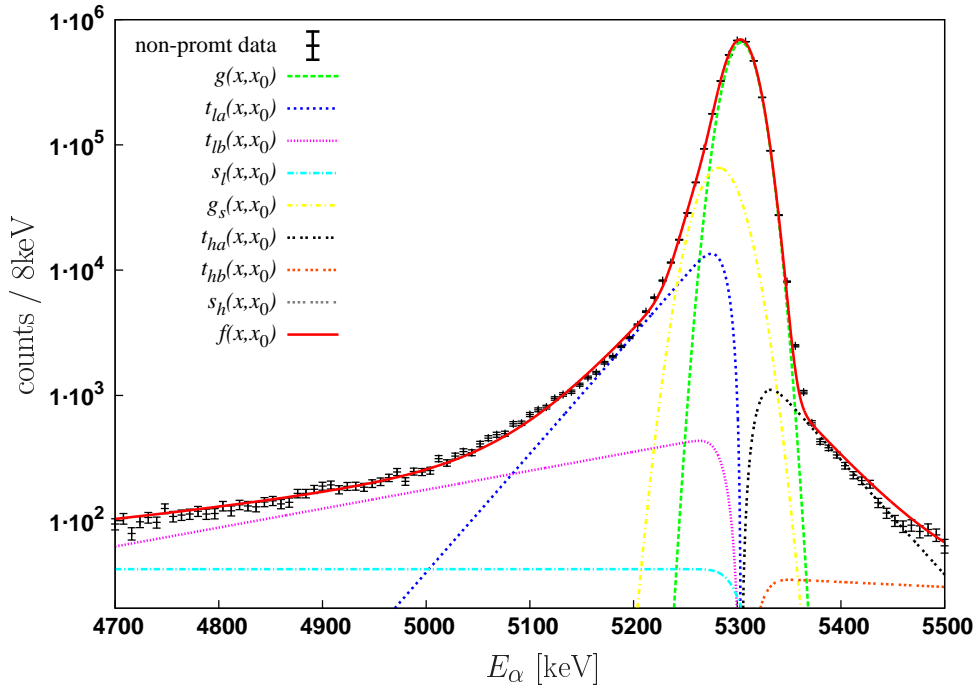


**Figure C.1:** As a reference for the structure of the  $\alpha$ -lineshape the  $\alpha$ -energy spectrum of random gate is fitted. The main contribution to the fit function  $f(x, x_0)$  is the Gaussian  $g(x, x_0)$ . The low energy tail is approximated by the function  $t_l(x, x_0)$  consisting of an additional Gaussian  $g_s(x, x_0)$ , two exponential tails  $t_{la}(x, x_0)$  and  $t_{lb}(x, x_0)$  and a smoothed step function  $s_l(x, x_0)$ . The fit function for the high energy tails  $t_h(x, x_0)$  is similarly composed of two exponential tail  $t_{ha}(x, x_0)$  and  $t_{hb}(x, x_0)$  and a smoothed step function  $s_h(x, x_0)$ .

The structure of the high energy tail fit function  $t_h(x, x_0)$  is similarly given by two exponential tails  $t_{ha}(x, x_0)$  and  $t_{hb}(x, x_0)$  and a smoothed step function  $s_h(x, x_0)$

$$t_h(x, x_0) = t_{ha}(x, x_0) + t_{hb}(x, x_0) + s_h(x, x_0) \quad (\text{C.8})$$

$$t_{ha}(x, x_0) = B_{ha} e^{C_{ha}(x_0-x)} \left( 1 - \exp \left( -\frac{1}{2} \frac{(x_0-x)^2}{\sigma^2} \right) \right) \Theta(x - x_0) \quad (\text{C.9})$$

$$t_{hb}(x, x_0) = B_{hb} e^{C_{hb}(x_0-x)} \left( 1 - \exp \left( -\frac{1}{2} \frac{(x_0-x)^2}{\sigma^2} \right) \right) \Theta(x - x_0) \quad (\text{C.10})$$

$$s_h(x, x_0) = \frac{B_{sh}}{2} \left( 1 + \operatorname{erf} \left( \frac{x - x_0}{\sigma \sqrt{2}} \right) \right). \quad (\text{C.11})$$

Figure C.1 shows a fit of the random  $\alpha$ -energy spectrum. The fit function reproduces the peak form very well.

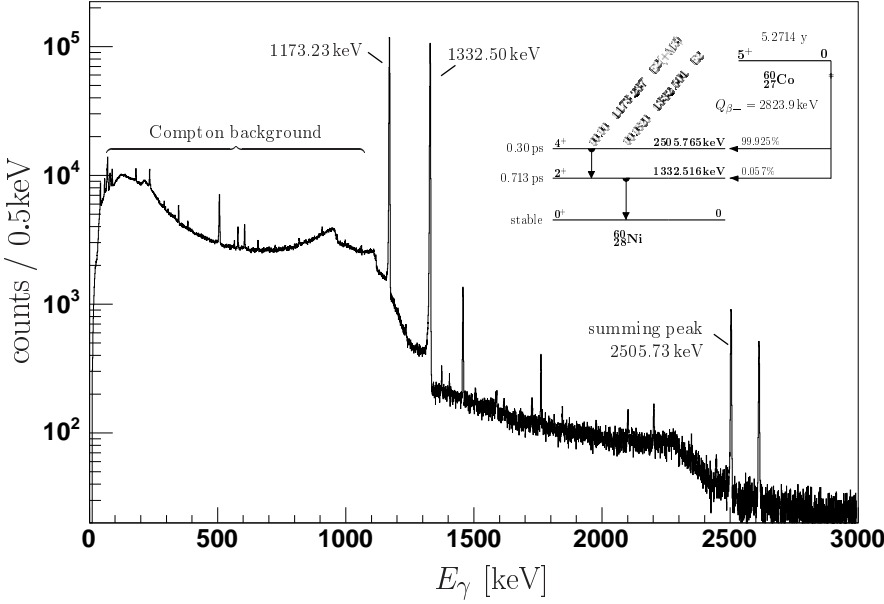


**Figure C.2:** The  $\gamma$ -energy spectrum of a  $^{60}\text{Co}$  reference source recorded with crystal C is plotted.

## C.2 The $\gamma$ -Lineshape

A typical  $\gamma$ -energy spectrum of a  $^{60}\text{Co}$  source is shown in figure C.2 (recorded with module C of the cluster detector). The two full energy peaks at 1173.23 keV and 1332.50 keV are prominent. If a photon is Compton scattered in the active volume of the detector and then escapes only part of the original energy of the photon is detected. This effect gives rise to the Compton background. Another prominent feature is the summing peak at 2505.73 keV where both photons from the source are recorded with full energy in the detector. The remaining peaks in the spectrum are due to the room background. A detailed analysis of the room background can be found in the appendix D.

Various analytical fit functions for the full energy peak in the  $\gamma$ -energy spectrum have been proposed in the literature [69, 70]. The peak form is mainly Gaussian like. For the fitting procedure of the peaks in the  $\gamma$  spectra a fit function  $f^G(x)$  is used which is the sum of a Gaussian  $g^G(x)$ , two low energy tails  $t_{la}^G(x)$  and  $t_{lb}^G(x)$ , a high energy tail  $t_h^G(x)$ , a step function  $s^G(x)$  and a linear background  $b_l^G(x)$

$$f^G(x) = g^G(x, x_0) + t_{la}^G(x, x_0) + t_{lb}^G(x, x_0) + t_h^G(x, x_0) + s^G(x, x_0) + b_l^G(x, x_0). \quad (\text{C.12})$$

The function  $g^G(x, x_0)$  is defined by

$$g^G(x, x_0) = \frac{A^G}{\tau\sqrt{2\pi}} \exp\left(-\frac{1}{2} \frac{(x - x_0)^2}{\tau^2}\right) \quad (\text{C.13})$$

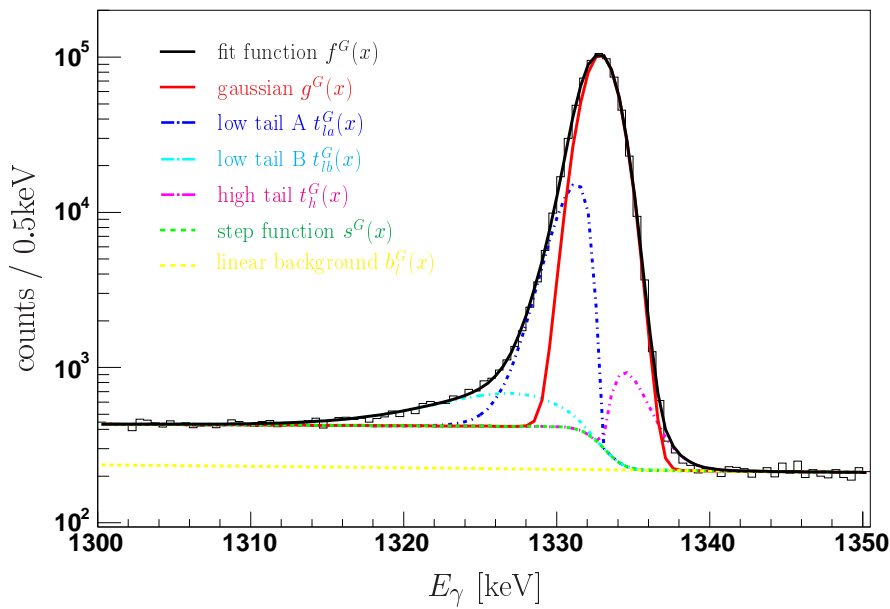


**Figure C.3:** For the fit of the full-energy peak in the  $\gamma$ -energy spectrum a fit function  $f^G(x)$  is used which is the sum of a Gaussian  $g^G(x)$ , two low energy tails  $t_{la}^G(x)$  and  $t_{lb}^G(x)$ , a high energy tail  $t_h^G(x)$ , a step functions  $s^G(x)$  and a linear background  $b_l^G(x)$ . Here the 1332.50 keV line in the spectrum of the  $^{60}\text{Co}$  reference source recorded with detector C is shown.

crystal	FWHM @ 1173.23 keV	FWHM @ 1332.50 keV
A	2.4 keV	2.5 keV
B	2.7 keV	2.7 keV
C	2.5 keV	2.6 keV

**Table C.1:** The resolution of the three HPGe-crystal of the cluster detector were measured with a  $^{60}\text{Co}$  reference source.

with the peak position  $x_0$ , the width  $\tau$  and the area  $A^G$ . The low energy tails  $t_{la}^G(x, x_0)$  and  $t_{lb}^G(x, x_0)$  and the high energy tail  $t_h^G(x, x_0)$  are defined by

$$t_{la}^G(x, x_0) = B_{la}^G e^{C_{la}^G(x-x_0)} \left( 1 - \exp \left( -D_{la}^G \frac{(x-x_0)^2}{\tau^2} \right) \right) \Theta(x_0 - x) \quad (\text{C.14})$$

$$t_{lb}^G(x, x_0) = B_{lb}^G e^{C_{lb}^G(x-x_0)} \left( 1 - \exp \left( -D_{lb}^G \frac{(x-x_0)^2}{\tau^2} \right) \right) \Theta(x_0 - x) \quad (\text{C.15})$$

$$t_h^G(x, x_0) = B_h^G e^{C_h^G(x_0-x)} \left( 1 - \exp \left( -D_h^G \frac{(x_0-x)^2}{\tau^2} \right) \right) \Theta(x - x_0) \quad (\text{C.16})$$

where the values  $B_*^G$ ,  $C_*^G$  and  $D_*^G$  are free parameters. For the step function  $s^G(x, x_0)$  the error function is used

$$s^G(x, x_0) = \frac{B_s^G}{2} \left( 1 + \operatorname{erf} \left( \frac{x_0 - x}{\tau \sqrt{2}} \right) \right). \quad (\text{C.17})$$

The linear background is described by the linear function  $b^G(x, x_0)$

$$b_l^G(x, x_0) = B_{bl}^G (x - x_0) + C_{bl}^G. \quad (\text{C.18})$$

Figure C.3 shows the fit function with its components fitted to the 1332.50 keV line in the spectrum of the  $^{60}\text{Co}$  reference source recorded with detector C. The chosen fit functions reproduces the peak form in the data very well.

The resolution of the three HPGe crystals measured with the  $^{60}\text{Co}$  source is shown in table C.1.



## Appendix D

### $\gamma$ Spectra

In the figures D.1-D.4 the  $\gamma$ -energy spectra of the room background are shown up to an  $\gamma$ -energy of 3220 keV with the classification of the background lines. The spectrum was recorded with crystal C of the MINIBALL cluster detector over the whole period of data taking ( $\sim 270$  days).

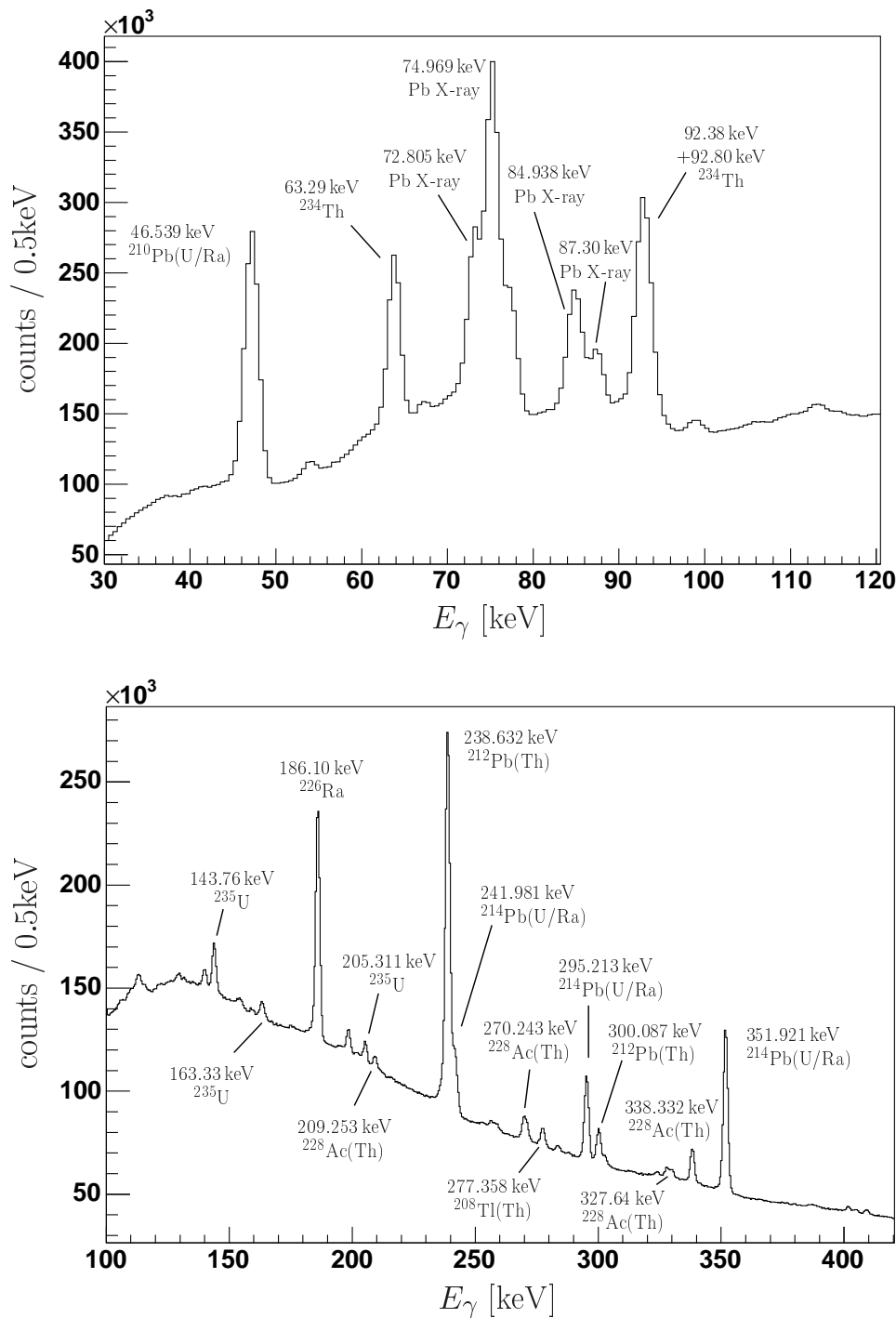


**Figure D.1:**  $\gamma$ -energy spectrum of the room background in the energy region from 30 keV to 420 keV with the classification of the background lines.

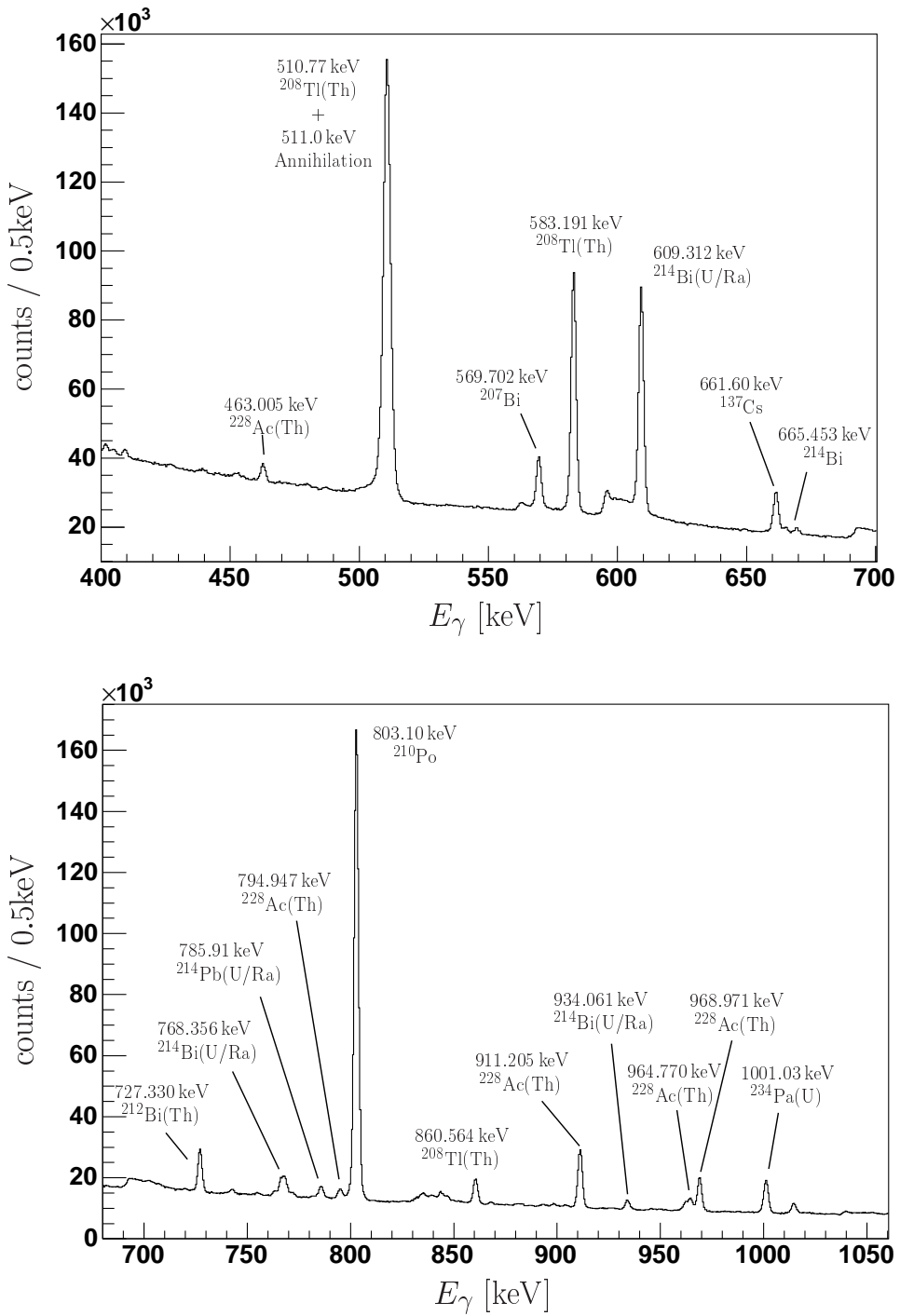


**Figure D.2:**  $\gamma$ -energy spectrum of the room background in the energy region from 400 keV to 1060 keV with the classification of the background lines.

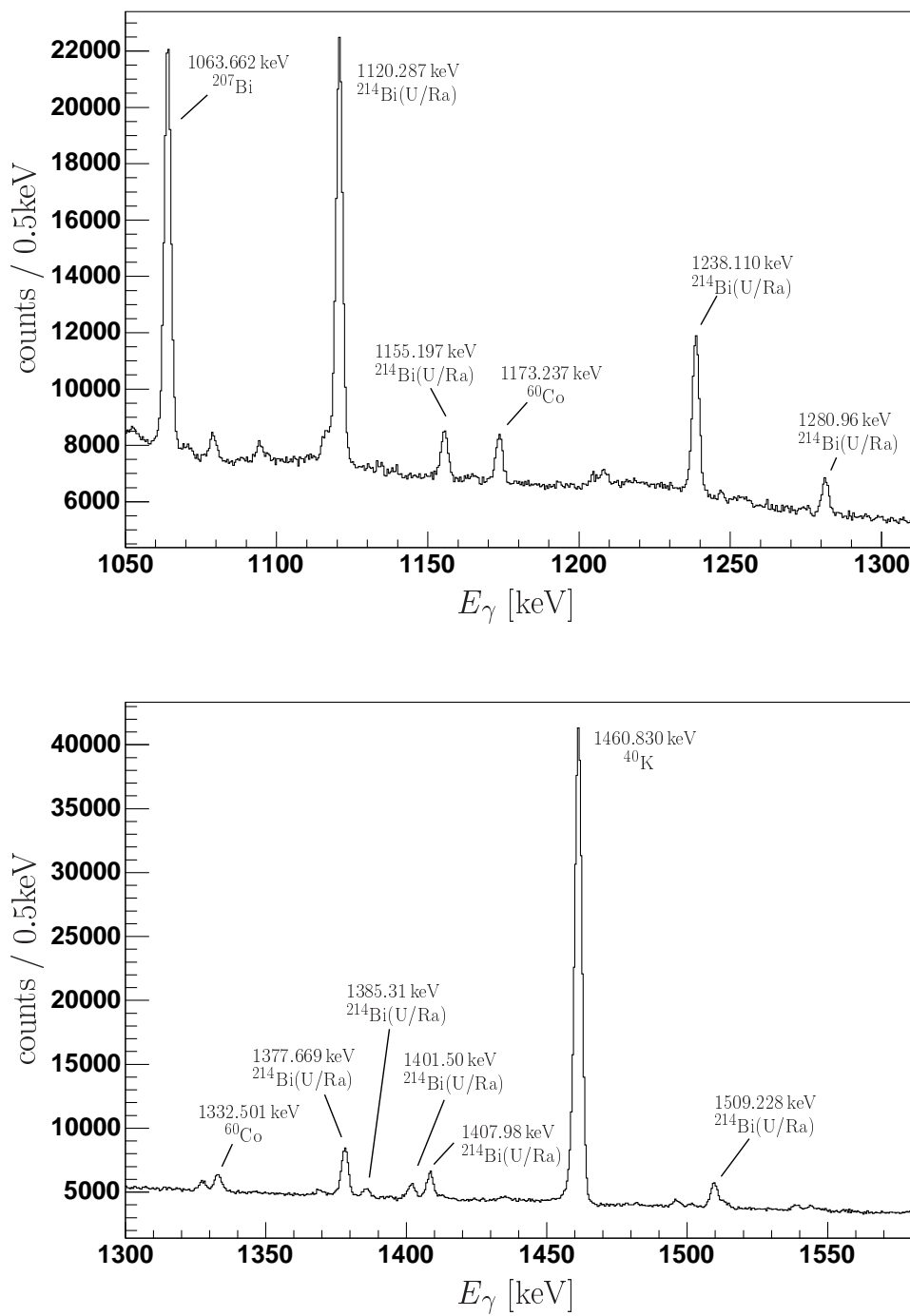


**Figure D.3:**  $\gamma$ -energy spectrum of the room background in the energy region from 1050 keV to 1580 keV with the classification of the background lines.

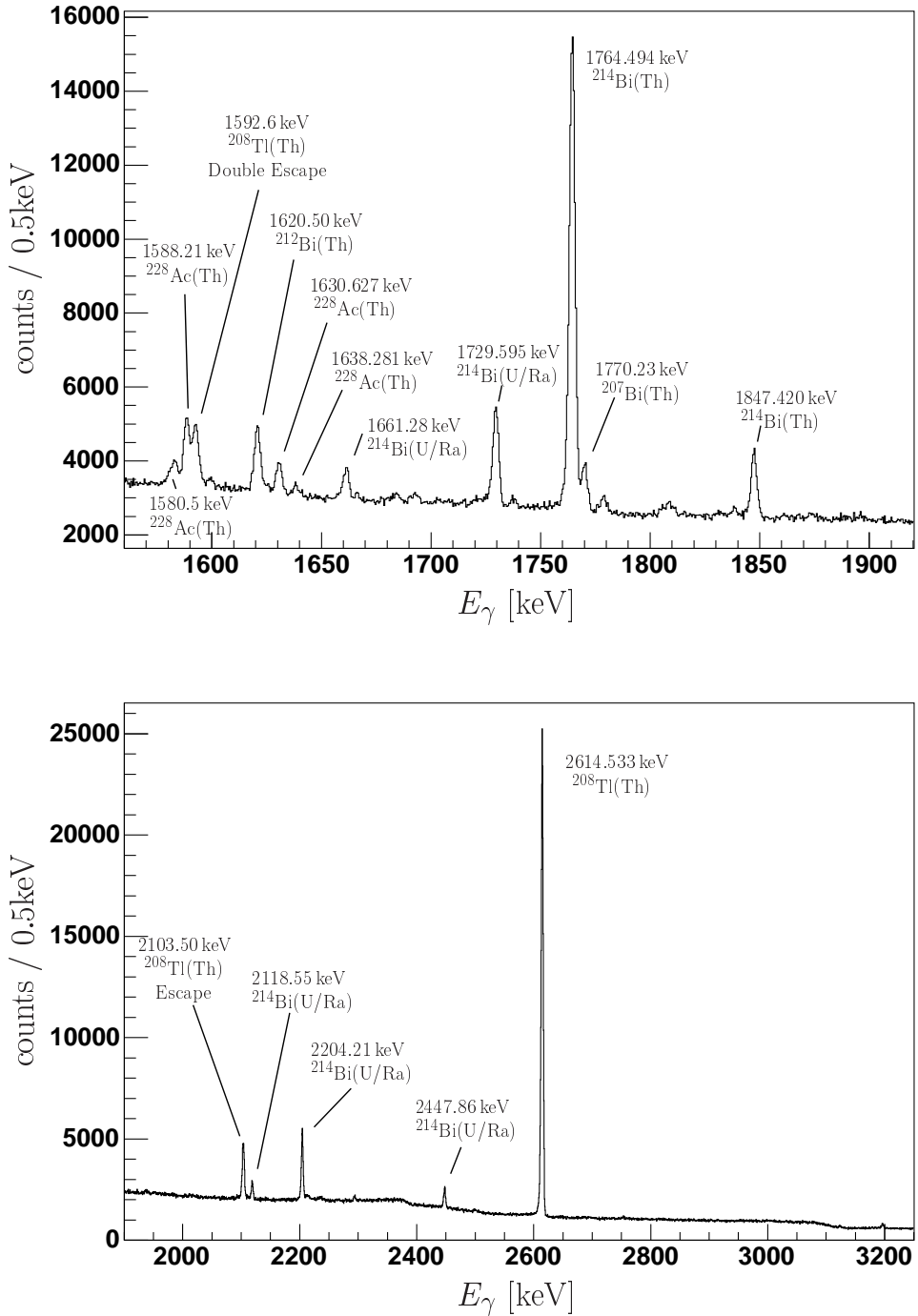


**Figure D.4:**  $\gamma$ -energy spectrum of the room background in the energy region from 1560 keV to 3220 keV with the classification of the background lines.



# List of Figures

1.1	Previous measurements and theoretical predictions . . . . .	2
2.1	Schematic potential for a decaying nucleus . . . . .	6
2.2	Overview over theoretical predictions . . . . .	8
2.3	Interference term $\Lambda_{\text{CA}}(E_\gamma)$ as function of the photon energy $E_\gamma$ . . . . .	9
2.4	Contribution from the tunneling region in the QM model . . . . .	13
2.5	Deviation of the semiclassical JMT model from the quantum mechanical model . . . . .	14
3.1	Schematic structure of the 2-dimensional $E_\alpha$ versus $E_\gamma$ plot . . . . .	19
3.2	Coincident background in the 2-dimensional $E_\alpha$ versus $E_\gamma$ plot . . . . .	19
3.3	Decay scheme of $^{210}\text{Po}$ . . . . .	20
3.4	Dimensions of the $^{210}\text{Po}$ source . . . . .	21
3.5	Autoradiography of the $\alpha$ source . . . . .	22
3.6	Picture of the silicon strip detector . . . . .	22
3.7	Picture of MINIBALL cluster detector . . . . .	24
3.8	Dimensions and segmentation of the HPGe crystals . . . . .	25
3.9	Pictures of an encapsulated HPGe crystal . . . . .	25
3.10	Schematic drawing of the experimental setup . . . . .	26
3.11	Distances between sources and detectors . . . . .	27
3.12	Picture of the silicon detector mounted in the vacuum chamber . . . . .	27
3.13	Schematic drawing of the vacuum chamber . . . . .	28
3.14	Shielding of the experimental setup . . . . .	29
4.1	Simulation of a MINIBALL Cluster Detector . . . . .	32

---

4.2	Simulation of a standard setup of MINIBALL . . . . .	32
4.3	Simulation of the Experimental Setup . . . . .	34
4.4	Simulation of the Experimental Setup Zoomed . . . . .	35
4.5	Comparison of the 803 keV $\gamma$ -branch from the data and the simulation . . . . .	37
4.6	Comparison between simulation and $^{60}\text{Co}$ reference source . . . . .	39
4.7	Comparison between simulation and $^{152}\text{Eu}$ reference source . . . . .	40
4.8	Comparison of the measured and simulated X-rays from the source . . . . .	41
4.9	Comparison of the acceptance of the setup with an isotropic, a dipole and a quadrupole distribution . . . . .	43
4.10	Coincident photon detection efficiency of the setup for isotropic, dipole and quadrupole distribution . . . . .	43
4.11	Angular Distribution generated in the simulation for $2\Lambda = 0$ and $2\Lambda = 2$ . . . . .	44
4.12	Coincident photon detection efficiency for $\Lambda(E_\gamma) = 0$ , $\Lambda_{\text{JMT}}^{E2}(E_\gamma)$ and 0.26 . . . . .	46
4.13	Contributions to the relative error of the simulated efficiency. . . . .	47
4.14	Variation of the coincident detection efficiency over the active area of the source . . . . .	48
4.15	Coincident photon detection efficiency with error band . . . . .	49
5.1	$\alpha$ -energy spectrum of down-scaled $\alpha$ -singles and $\alpha$ - $\gamma$ coincidences . . . . .	52
5.2	Energy resolution and count rates of the silicon detectors . . . . .	53
5.3	$\gamma$ -energy spectrum of the $\alpha$ -branch to $^{206}\text{Pb}(2^+)$ . . . . .	54
5.4	Spectrum of $t_\alpha$ for a single strip . . . . .	56
5.5	2-dimensional $E_\gamma$ versus $t_\alpha - t_\gamma^{\text{CFD}}$ (analog timing branch) plot . . . . .	57
5.6	2-dimensional $E_\gamma$ versus $t_\alpha - t_\gamma^{\text{XFT}}$ (XIA Fast Trigger time) plot . . . . .	58
5.7	Charge pulse trace of a 2.4 MeV photon with fitted response function $R(t)$	59
5.8	Fitted charge pulse trace of a 240 keV photon with slow rise in the beginning	60
5.9	2-dimensional $E_\gamma$ versus $t_\alpha - t_\gamma^{\text{XTC}}$ (corrected XIA time) plot . . . . .	61
5.10	Spectrum of $t_\alpha - t_\gamma$ with time-cut and chance gate . . . . .	63
5.11	2-dimensional $E_\alpha$ versus $E_\gamma$ plot with coincidence time-cut $-50 \text{ ns} < \Delta t < 50 \text{ ns}$ . . . . .	64
5.12	2-dimensional $E_\alpha$ versus $E_\gamma$ plot with chance gate . . . . .	64
5.13	Prompt data projected along the expected bremsstrahlung diagonal . . . . .	66
5.14	Random data projected along the expected bremsstrahlung diagonal . . . . .	67

5.15	Modelling of the background for the projected prompt data . . . . .	69
5.16	Simulation of Compton background from higher energy bremsstrahlung . .	71
5.17	Fit of the bremsstrahlung . . . . .	73
5.18	Fitted time spectrum for the energy bin $130 \text{ keV} < E_\gamma < 150 \text{ keV}$ . . . . .	74
5.19	Time-cut widths used for the analysis . . . . .	75
5.20	Area of the bremsstrahlung peak versus the prompt time gate width . . . .	76
5.21	Fit of down-scaled $\alpha$ -singles . . . . .	78
5.22	Deduction of the angle $\vartheta$ between $\alpha$ particle and the photon . . . . .	79
5.23	Simulated $\vartheta$ -distribution and average angle $\vartheta^{sim}$ for two segment-strip pairs	80
5.24	Number of segment-strip pairs per $\vartheta$ -bin . . . . .	81
5.25	Angular resolution for four segment-strip bins . . . . .	81
5.26	Selection of the data for the analysis of the angular correlation . . . . .	82
5.27	Measured angular correlation of the X-rays following the $\alpha$ decay of $^{210}\text{Po}$ .	83
5.28	Measured angular correlation of the 803 keV $\gamma$ -branch compared to a simulated quadrupole distribution . . . . .	83
5.29	Subtraction of room background . . . . .	85
5.30	Angular correlation of bremsstrahlung compare to the simulation . . . .	86
5.31	$\chi^2_{red}$ on dependence of $\Lambda$ . . . . .	86
5.32	Angular correlation correction parameter $\Lambda$ . . . . .	87
5.33	Fit of the angular correlation correction parameter $\Lambda$ . . . . .	88
5.34	Coincident photon detection efficiency for the fitted $\Lambda$ value . . . . .	91
6.1	The measured energy differential bremsstrahlung emission probability accompanying the $\alpha$ decay of $^{210}\text{Po}$ . . . . .	94
6.2	Experimental result compared to theory . . . . .	95
6.3	Deviation of the experimental data evaluated with $\Lambda_{exp}$ and $\Lambda_{JMT}$ from theory	96
A.1	Definition of the angle $\vartheta$ . . . . .	103
A.2	Definition of the angle $\vartheta_1$ and $\vartheta_2$ . . . . .	108
A.3	Velocity, acceleration and time as a function of $r$ in the CA model . . . .	114
A.4	Bremsstrahlung emission probability of $^{210}\text{Po}$ in the CA and SCA model .	115
A.5	Correction of the angular distribution in the CA and SCA model . . . . .	116

B.1	Coulomb wave functions $G_0(\eta, \rho)$ and $F_0(\eta, \rho)$	122
B.2	Spherical Bessel functions $j_0(\sigma), j_1(\sigma), n_0(\sigma)$ and $n_1(\sigma)$	124
B.3	Imaginary part of the energy relation versus $V_0$	133
B.4	Initial wave functions $\Phi_i(r)$ for the first six orders	136
B.5	Final wave functions $\Phi_f(r)$ for the first six orders	140
B.6	Real and imaginary part of the integrant of the matrix element	142
B.7	Bremsstrahlung emission probability of $^{210}\text{Po}$ in the QM model	144
B.8	Matrix element with its contributions	145
B.9	Comparison between different set of solutions $(r_0, V_0)$	146
B.10	$r_0$ and $V_0$ dependence of equation (B.198)	149
B.11	$r_0$ and $V_0$ dependence of equation (B.198)	150
B.12	Behaviour of $dP/dE_\gamma$ along the real and imag. part of the energy relation	151
B.13	2-dimensional surface plot of the $r_0$ and $V_0$ dependence of $dP/dE_\gamma$	152
C.1	Fit of the reference $\alpha$ peak form	158
C.2	$\gamma$ -energy spectrum of a $^{60}\text{Co}$ reference source	159
C.3	Fit of the full-energy peak in the $\gamma$ -energy spectrum	160
D.1	Background $\gamma$ spectrum $30\text{ keV} < E_\gamma < 420\text{ keV}$	164
D.2	Background $\gamma$ spectrum $400\text{ keV} < E_\gamma < 1060\text{ keV}$	165
D.3	Background $\gamma$ spectrum $1050\text{ keV} < E_\gamma < 1580\text{ keV}$	166
D.4	Background $\gamma$ spectrum $1560\text{ keV} < E_\gamma < 3220\text{ keV}$	167

# List of Tables

3.1	Lengths, weights and relative efficiencies of the HPGe crystals . . . . .	23
4.1	Input data adapted in the simulation . . . . .	36
4.2	Calibration of the simulated absolute detection efficiency for the 803 keV $\gamma$ -branch . . . . .	36
4.3	X-ray energies and intensities for lead . . . . .	38
4.4	Simulated coincident photon detection efficiencies $\varepsilon_{\gamma,2\Lambda=0}^c$ and $\varepsilon_{\gamma,2\Lambda=1}^c$ . . . . .	45
5.1	Comparison of the timing for $t_\gamma^{\text{CFD}}$ and $t_\gamma^{\text{XTC}}$ . . . . .	62
5.2	Binning of the data in $E_\gamma$ . . . . .	65
5.3	Fitted bremsstrahlung area for each energy bin . . . . .	77
5.4	Number of $\alpha$ particles recorded by the silicon detectors . . . . .	78
5.5	Bremsstrahlung emission probability evaluated for $\Lambda_{exp}$ . . . . .	89
5.6	Statistical and systematic error estimation . . . . .	90
B.1	First eight solutions sets $(r_0, V_0)$ of the energy relation . . . . .	132
B.2	Constituents of matrix element for $E_\gamma = 150$ keV and 450 keV . . . . .	147
C.1	Resolution of the three HPGe-crystals of the cluster detector . . . . .	161



# Glossary

## Notations

$\mathbf{A}(\mathbf{x}, t)$	<i>vector potential at the point of the observer <math>\mathbf{x}</math> and at time <math>t</math></i>
$\beta = \vec{v}/c$	<i>velocity</i>
$E_\alpha$	<i>energy of an <math>\alpha</math> particle</i>
$E_\gamma$	<i>energy of a photon</i>
$E_{\alpha,0}$	<i>energy of the <math>\alpha</math> particle in the <math>\alpha</math> decay of <math>^{210}\text{Po}</math> into the ground state of <math>^{206}\text{Pb}</math></i>
$E_{\alpha,803}$	<i>energy of the <math>\alpha</math> particle in the <math>\alpha</math> decay of <math>^{210}\text{Po}</math> into the first excited <math>2^+</math> state of <math>^{206}\text{Pb}</math> at 803.1 keV</i>
$\mu$	<i>reduced mass</i>
$M_\alpha$	<i>mass of the <math>\alpha</math> particle</i>
$M_d$	<i>mass of the daughter nucleus</i>
$\eta$	<i>Sommerfeld parameter</i>
$\Phi_i$	<i>initial wave function</i>
$\Phi_f$	<i>final wave function</i>
$Q_\alpha$	<i>decay energy in the <math>\alpha</math>-decay</i>
$r_n$	<i>radius of the nucleus</i>
$r_0$	<i>classical turning point</i>
$U_C^{(\max)} = U(r_n)$	<i>height of the Coulomb-barrier</i>
$V_0$	<i>depth of the potential inside the nucleus</i>
$Z_{\text{eff}}^{E1}$	<i>effective dipole charge</i>
$Z_{\text{eff}}^{E2}$	<i>effective quadrupole charge</i>
$Z_\alpha$	<i>charge of the <math>\alpha</math> particle</i>
$Z_d$	<i>charge of the daughter nucleus</i>

## Abbreviations

ADC	<i>analog-to-digital converter</i>
ASC	<i>analog signal conditioning</i>
CA	<i>Coulomb acceleration [model]</i>
CFD	<i>constant fraction discriminator</i>
CM	<i>centre of mass</i>
DGF	<i>digital gamma finder</i>
DSP	<i>digital signal processor</i>
FIFO	<i>first-in first-out memory</i>
FPGA	<i>field programmable gate array</i>
FWHM	<i>full width half maximum</i>
HPGe	<i>high-purity germanium</i>
LE	<i>leading edge discriminator</i>
LN <sub>2</sub>	<i>liquid nitrogen</i>
PECL	<i>positive emitter collector logic</i>
SCA	<i>strict Coulomb acceleration [model]</i>
SSS(S)D	<i>single sided segmented silicon detector</i>
TDC	<i>time-to-digital converter</i>

## Constants

$\alpha$	1/137.03598	<i>fine structure constant</i>
$c$	$2.99792458 \cdot 10^8$ m/s	<i>velocity of light</i>
$e^2 = \alpha \hbar c$	1.43997 MeV fm	
$\hbar$	$6.582122 \cdot 10^{-22}$ MeV s	<i>Planck's constant</i>
$\hbar c$	197.327 MeV fm	
$u$	931.49432 MeV/c <sup>2</sup>	<i>unified atomic mass unit</i>
$M_\alpha$	4.00260325 u	<i>mass of an <math>\alpha</math> particle</i>
$M_{(^{210}\text{Po})}$	209.982857 u	<i>mass of <math>{}^{210}\text{Po}</math></i>
$M_d = M_{(^{206}\text{Pb})}$	205.974449 u	<i>mass of <math>{}^{206}\text{Pb}</math></i>

# Bibliography

- [1] J. D. Jackson, *Classical Electrodynamics* (John Wiley & Sons, New York, 1975), 2nd ed.
- [2] L. D. Landau and E. M. Lifschitz, *Klassische Feldtheorie*, vol. 2 of *Lehrbuch der Theoretischen Physik* (Akademie Verlag, 1992), 12th ed.
- [3] T. Papenbrock and G. F. Bertsch, Phys. Rev. Lett. **80**, 4141 (1998).
- [4] W. van Dijk and Y. Nogami, Phys. Rev. Lett. **83**, 2867 (1999).
- [5] W. van Dijk and Y. Nogami, Phys. Rev. C **65**, 024608 (2002).
- [6] W. van Dijk and Y. Nogami, Few-Body Sys. Suppl. **14**, 229 (2003).
- [7] E. V. Tkalya, Phys. Rev. C **60**, 054612 (1999).
- [8] E. V. Tkalya, J. Exp. Theo. Phys. **89**, 208 (1999).
- [9] C. Bertulani, D. de Paula, and V. Zelevinsky, Phys. Rev. C **60**, 031602 (1999).
- [10] M. Dyakonov, Phys. Rev. C **60**, 037602 (1999).
- [11] N. Takigawa, K. Nozawa, K. Hagino, A. Ono, and D. Brink, Phys. Rev. C **59**, R593 (1999).
- [12] W. So and Y. Kim, J. Korean Phys. Soc. **37**, 202 (2000).
- [13] D. Brink, in *Proceedings of the International Workshop "Fission Dynamics of Atomic Clusters and Nuclei"* (Luso, Portugal, 2000).
- [14] S. Misicu, M. Rizea, and W. Greiner, J. Phys. G **27**, 993 (2001).
- [15] I. Batkin, I. Kopytin, and T. Churakova, Sov. J. Nucl. Phys. **44**, 946 (1986).
- [16] S. Kurgalin, Y. Chuvilsky, and T. Churakova, Bull. Russ. Ac. Sc. Phys. **65**, 715 (2001).
- [17] S. Maydanyuk, V. Olkhovsky, and S. Omelchenko, Bull. Russ. Ac. Sc. Phys. **12**, 2026 (2002).

- [18] S. P. Maydanyuk and V. S. Olkhovsky, Prog. Theo. Phys. **109**, 203 (2003).
- [19] S. P. Maydanyuk and S. V. Belchikov, Prob. At. Science and Technology **5**, 19 (2004).
- [20] S. P. Maydanyuk and V. S. Olkhovsky, Eur. Phys. J. A **28**, 283 (2006).
- [21] U. Jentschura, A. Milstein, I. Terekhov, H. Boie, H. Scheit, and D. Schwalm, Phys. Rev. C **77**, 014611 (2008).
- [22] A. D'Arrigo, N. Eremin, G. Fazio, G. Giardina, M. Glotova, T. Klochko, M. Sacchi, and A. Taccone, Phys. Lett. B **332**, 25 (1994).
- [23] J. Kasagi, H. Yamazaki, N. Kasajima, T. Ohtsuki, and H. Yuki, Phys. Rev. Lett. **79**, 371 (1997).
- [24] J. Kasagi, H. Yamazaki, N. Kasajima, T. Ohtsuki, and H. Yuki, J. Phys. G **23(10)**, 1451 (1997).
- [25] T. Ohtsuki, J. Kasagi, N. Kasajima, H. Yamazaki, H. Yuki, and M. Yukishima, J. Radioanalyt. Nucl. Chem. **239**, 123 (1999).
- [26] N. Eremin, S. Klimov, D. Smirnov, and A. Tulinov, Moscow Univ. Phys. Bul. **55**, 62 (2000).
- [27] G. Giardina, N. Eremin, S. Klimov, D. Smirnov, and A. Tulinov, Bull. Russ. Ac. Sc. Phys. **65**, 45 (2001).
- [28] G. Giardina, G. Fazio, G. Mandaglio, M. Manganaro, C. Saccá, N. Eremin, A. Paskhalov, D. Smirnov, S. Maydanyuk, and V. Olkhovsky, Eur. Phys. J. A **36**, 31 (2008).
- [29] G. Giardina, G. Fazio, G. Mandaglio, M. Manganaro, S. Maydanyuk, V. Olkhovsky, N. Eremin, A. Paskhalov, D. Smirnov, and C. Saccá, Mod. Phys. Lett. A **23**, 2651 (2008).
- [30] H. Boie, H. Scheit, U. D. Jentschura, F. Köck, M. Lauer, A. I. Milstein, I. S. Terekhov, and D. Schwalm, Phys. Rev. Lett. **99**, 022505 (2007).
- [31] B. Povh, K. Rith, C. Scholz, and F. Zetsche, *Teilchen und Kerne* (Springer-Verlag, 1999), 5th ed.
- [32] G. Gamow, Zeitschr. f. Physik **37**, 204 (1928).
- [33] R. Gurney and E. Condon, Nature **122**, 439 (1928).
- [34] R. Gurney and E. Condon, Phys. Rev. **33**, 127 (1929).
- [35] O. Nachtmann, private communication (2008).

- [36] H. Boie, Diplomarbeit, Universität Heidelberg (2002), URL <http://www.mpi-hd.mpg.de/cb/theses.html>.
- [37] R. B. Firestone, *Table of Isotopes* (John Wiley & Sons, New York, 1996), 8th ed.
- [38] J. Eberth, G. Pascovici, H. Thomas, N. Warr, D. Weisshaar, D. Habs, P. Reiter, P. Thirolf, D. Schwalm, C. Gund, et al., Prog. Part. Nucl. Phys. **46**, 389 (2001).
- [39] G. F. Knoll, *Radiation Detection and Measurement* (John Wiley & Sons, 2000), 3rd ed.
- [40] G. Heusser, Nucl. Instr. Meth. B **83**, 223 (1993).
- [41] M. Lauer, Diplomarbeit, Universität Heidelberg (2001), URL <http://www.mpi-hd.mpg.de/cb/theses.html>.
- [42] M. Lauer, Dissertation, Universität Heidelberg (2004), URL <http://www.mpi-hd.mpg.de/cb/theses.html>.
- [43] F. Köck, Ph.D. thesis, MPI-K Heidelberg (1994).
- [44] S. Agostinelli, J. Allison, K. Amako, J. Apostolakis, H. Araujo, P. Arce, M. Asai, D. Axen, S. Banerjee, G. Barrand, et al., Nucl. Instr. Meth. A **506**, 250 (2003).
- [45] H. Boie, *g4miniball - the MINIBALL simulation package*, <http://www.mpi-hd.mpg.de/mbwiki/wiki/MiniballSimulation>.
- [46] R. Brun and F. Rademakers, Nucl. Instr. Meth. A **389**, 81 (1997).
- [47] H. Fischbeck and M. Freedman, Phys. Rev. Lett. **34**, 173 (1975).
- [48] J. Law, Nucl. Phys. A **286**, 339 (1977).
- [49] R. Anholt and P. Amundsen, Phys. Rev. **25**, 169 (1982).
- [50] F. Hanser and B. Sellers, Rev. Sci. Instr. **41**, 780 (1970).
- [51] R. Siegele, G. Weatherly, H. Haugen, D. Lockwood, and L. Howe, Appl. Phys. Lett **66**, 1319 (1995).
- [52] J. Fitting, Diplomarbeit, Universität Heidelberg (2002), URL <http://www.mpi-hd.mpg.de/cb/theses.html>.
- [53] W. Gast, R. Lieder, L. Mihailescu, M. Rossewij, H. Brands, A. Georgiev, J. Stein, and T. Kröll, IEEE Trans. Nucl. Sci. **48**, 2380 (2001).
- [54] L. Mihailescu, Ph.D. thesis, Rheinische Friedrich-Wilhelms-Universität Bonn (2000).
- [55] E. García-Toraño and M. Aceña, Nucl. Instr. Meth. **185**, 261 (1981).

- [56] W. Wätzig and W. Westmeier, Nucl. Instr. Meth. **153**, 517 (1978).
- [57] E. García-Toranño, Nucl. Instr. Meth. A **369**, 608 (1996).
- [58] M. Aceña and E. García-Torano, Nucl. Instr. Meth. **223**, 346 (1984).
- [59] C. Gund, Dissertation, Universität Heidelberg (2000), URL <http://www.mpi-hd.mpg.de/cb/theses.html>.
- [60] D. Cline and P. M. S. Lesser, Nucl. Instr. Meth. **82**, 291 (1970).
- [61] F. E. Low, Phys. Rev. **110**, 974 (1958).
- [62] S. Luke, C. Gossett, and R. Vandenbosch, Phys. Rev. C **44**, 1548 (1991).
- [63] F. Schwabl, *Quantenmechanik: QM I* (Springer-Verlag, 1998), 5th ed.
- [64] M. Abramowitz and I. A. Stegun, eds., *Handbook of Mathematical Functions* (Dover Publications, Inc., New York, 1965), 5th ed.
- [65] A. Bohm, M. Gadella, and G. B. Mainland, Am. J. Phys. **57**, 1103 (1989).
- [66] D. Delion and A. Săndulescu, J. Phys. G **28**, 617 (2002).
- [67] C. Cohen-Tannoudji, B. Diu, and F. Laloë, *Quantenmechanik*, vol. 1 (de Gruyter, Berlin, 1997).
- [68] N. Mukunda, Am. J. Phys. **46**, 910 (1978).
- [69] K. Debertin and R. Helmer, *Gamma- and X-Ray Spectrometry with Semiconductor Detectors* (North-Holland, Amsterdam, 1988).
- [70] R. Helmer and M. Lee, Nucl. Instr. Meth. **178**, 499 (1980).

## Danksagung

An dieser Stelle möchte ich allen danken, die mich während dieser Arbeit unterstützt und begleitet haben und zum Gelingen beigetragen haben. Besonders danken möchte ich:

- Herrn Prof.Dr. Dirk Schwalm, für die Möglichkeit diese Arbeit in seiner Gruppe durchzuführen, für seine Unterstützung, seine Motivation, für seine Anleitung und Führung, seine Anregungen, für seine Ausdauer und Beharrlichkeit auf dem langen Weg – kurzum für seine hervorragende Betreuung.
- Herrn Dr. Heiko Scheit, für die hervorragende Betreuung, für seine Unterstützung, seine Anregungen, viele Idee und anregende Diskussionen.
- Herrn Prof.Dr. Otto Nachtmann für seine Unterstützung im Bereich der relativistischen Quantenmechanik.
- Herrn Prof. Alexander Milstein, Herrn Dr. Ulrich Jentschura und Herrn Terekhov für ihren Einsatz bei der Entwicklung eines semi-klassischen Modells.
- Den ehemaligen Kollegen aus der CB-Gruppe für ein angenehmes, fröhliches und inspirierendes Arbeitsklima, hierbei gilt mein Dank besonders Herrn Dr. Jörg Fitting, Herrn Dr. Martin Lauer und Herrn Dr. Oliver Niedermaier.
- Herr Dr. Frank Köck für seine Unterstützung, für sein offenes Ohr und sein offenes Zimmer, für viele nette Gespräche und lustige Stunden.
- Frau Helga Krieger für ihre Hilfe und Unterstützung und ihr Engagement für unsere Gruppe.
- Allen Kollegen aus der Arbeitsgruppe von Herrn Prof. Schwalm, vor allem meinen Zimmerkollegen für die immer angenehme Atmosphäre.
- Den Mitarbeitern der Werkstätten am MPI-K für ihre hervorragende Arbeit, hierbei gilt mein Dank besonders Herrn Oliver Koschorreck für sein Interesse und seine Unterstützung, nicht nur in der Physik.
- Den Mitarbeitern der Boie GmbH, besonders meinem Bruder Herrn Stefan Boie für die Möglichkeit einen großen Teile dieser Arbeit parallel zu meinem Beruf verwirklichen zu können.
- Meinen Eltern für ihre Unterstützung und alles das, was sie mir in meinem Leben geschenkt haben.
- Meiner geliebten Frau Claudia und meinen geliebten Töchtern Emily, Giulia und Hanna – Ihnen möchte ich diese Arbeit widmen.